

ABSTRACT

SONG, YOUNG JUN. Ratcheting Fatigue Failure of Welded Stainless Steel Pipe and Dislocation Microstructure. (Under the direction of Drs. K.L. Murty and T. Hassan).

Fatigue failures of welded piping joints are continued to be the majority of the failures in the nuclear power plants (NPPTs), resulting in unscheduled plant downtime and financial loss. This study investigates the influence of ratcheting on the fatigue failure of the welded piping joints. Many studies on the phenomenon of strain ratcheting have been conducted at the macroscale but not in the microscale. This study presents results on the microstructure evolution of the heat affected zone under cyclic loading. Four welded piping specimens are subjected to displacement-controlled cyclic loading with different number of cycles. Microstructural evolutions of the piping material coupons conditioned by various temperature cycles to simulate HAZ materials are also investigated. The coupons are subjected to three different types of fatigue loading cycles, uniaxial strain-controlled, biaxial ratcheting, and uniaxial force-controlled before the microstructural investigation.

The stress response of welded pipe specimens showed initial cyclic hardening until 20 cycles followed by softening, and strain ratcheting was observed at the weld toe. Microstructure at the weld toe showed various dislocation types under different number of cycles. More cell and wall structures were formed with changing volume fraction of each type of substructure as the number of fatigue cycles increases. Dislocation density measured at weld toe initially increased and then decreased until failure, which was attributed to cyclic hardening and softening. More heterogeneous dislocations were noted near the weld toe in contrast to more planar slip away from the weld toe.

Cyclic hardening and softening are observed during cyclic loading of coupons. Stress amplitude responses show decrease in amplitude with increase in heat-treatment temperature under uniaxial strain-controlled tests. Before fatigue, heterogeneous dislocation structures are not visible, but various dislocation structures are observed after fatigue cycles; these include planar dislocations, dislocation cells, ladder like structures, tangles, dislocation walls as well as stacking faults. Percent of cell structure increases as the planar slip and tangles decrease with increasing number of cycles in both unconditioned and 800°C heat-treated materials. However, high proportion of planar slip remains even though cell structure increases in the 1050°C heat-treatment coupons. Dislocation density increases during cyclic loading where stress amplitude initially increases followed by decrease with progressive cycles. Dislocation cell size was inversely proportional to cyclic hardening. Ratcheting strain was observed when positive mean stress applied to a coupon under uniaxial force-controlled cycles. Dislocation structures were similar for both ratcheting and non-ratcheting coupons. However, cell and wall structures were better defined in non-ratcheting specimen while higher dislocation density is noted in ratcheting specimens. Under biaxial ratcheting cycles, all specimens exhibited dislocation cell and wall structures. However, high proportion of dislocation wall structures are observed in 1050°C heat-treated specimens. Dislocation density decreased with increasing heat-treatment temperature, and cell size decreased when stress amplitude and dislocation density increased. This work clearly demonstrated that ratcheting resulted in lower dislocation density along with larger cell size.

Ratcheting Fatigue Failure of Welded Stainless Steel Pipe and Dislocation Microstructure

by
Young Jun Song

A thesis submitted to the Graduate Faculty of
North Carolina State University
in partial fulfillment of the
requirements for the Degree of
Master of Science

Nuclear Engineering

Raleigh, North Carolina

2009

APPROVED BY:

Dr. T. Hassan

Dr. J.M. Rigsbee

Dr. K.L. Murty
Chair of Advisory Committee

DEDICATION

This thesis is dedicated to my parents who always support me.

BIOGRAPHY

Young Jun Song was born on January 23, 1980, in Seoul, Korea. He attended Inha University and obtained his Bachelor of Science in Mining and Mineral Engineering in February of 2005. After finishing his BS, he was interested in new academic field, and then enrolled in Nuclear Engineering Department of North Carolina State University in Raleigh, North Carolina, USA in fall of 2006 to pursue his Master of Science.

ACKNOWLEDGMENTS

I would like to extend my sincerest thanks and appreciation to Drs. K.L. Murty and T. Hassan for their guidance, patience, and support throughout this research project. I am truly grateful for their willingness to share time, wisdom, and enthusiasm with me over the last two years.

I would also like to express my thanks to my thesis committee Dr. M.J. Rigsbee for his advice and help during the course of TEM work. Thanks are also given to Dr. T. Rawdanowicz who helped me with TEM on numerous opportunities.

In addition, I would like to thank to Dr. M.S. Yim who helped me with an academic advice and encouragement. I also wish thank to Dr. I. Charit, Mr. Pei-yuan Cheng, Mr. Jason Hescheles, and Nuclear materials group who helped me with my work.

The financial support provided through award #: DMR 0408910 of the NSF grant is gratefully acknowledged. Final thanks are given to the faculty and staff at the Department of Nuclear Engineering and Materials Science and Engineering at NCSU. Without their help and support, this would not have been a possible task.

TABLE OF CONTENTS

LIST OF TABLES.....	vii
LIST OF FIGURES.....	viii
CHAPTER 1 Introduction.....	1
1.1 Background	1
1.2 Residual Stress Effect on Fatigue Failure	2
1.3 Strain Ratcheting	3
1.4 Dislocation Structure.....	8
1.5 Overview	11
CHAPTER 2 Experimental Procedures	12
2.1 Material and specimen	12
2.1.1 Socket Welded Piping joints	12
2.1.2 Test Setup of Socket Welded Pipe.....	15
2.1.3 Coupon Specimen	18
2.1.4 Test Setup of Coupons	19
2.2 Metallography	22
2.2.1 Specimen Preparation	22
2.2.2. Optical Microscopy Observation	24
2.3 Hardness Test Preparation	24
2.4 Transmission Electron Microscopy	26
2.4.1 Transmission Electron Microscope Equipment	26
2.4.2 Transmission Electron Microscope Specimen	27
CHAPTER 3 Experimental Results and Discussions	31
3.1 Fatigue Response of the Welded Specimens	31
3.1.1 Displacement-controlled Fatigue Tests	31
3.2 Fatigue Response of the Coupon Specimens	35
3.2.1 Uniaxial Strain-Controlled Fatigue Tests.....	35
3.2.2 Uniaxial Force-Controlled Fatigue Tests	40
3.2.3 Biaxial Ratchetting Fatigue Tests	42
3.3 Optical Metallography.....	45
3.3.1 Metallographic Observation of Coupon.....	45
3.3.2 Metallographic Observations of Welded Pipe.....	48

3.4 Microhardness	51
3.4.1 Hardness Measurement.....	51
3.5 Transmission Electron Microscopy Investigation	56
3.5.1 Microstructure Observation	56
3.5.1.1 Dislocation Structures in Uniaxial Strain Controlled Coupons.....	59
3.5.1.2 Dislocation Structures in Uniaxial Force Controlled Coupons	72
3.5.1.3 Dislocation Structures in Biaxial Ratchetting Coupons	75
3.5.1.4 Dislocation Structures in Welded Pipe Specimen	80
3.5.2 Dislocation Density.....	93
3.5.2.1 Dislocation Density in Uniaxial Strain controlled Specimens	93
3.5.2.2 Dislocation Density in Biaxial Ratchetting Specimens.....	99
3.5.2.3 Dislocation Density in Unaxial Force Controlled Specimens.....	101
3.5.2.4 Dislocation Density in Welded Pipe Specimens	103
3.5.3 Dislocation Cell Size Measurement.....	105
3.5.3.1 Dislocation Cell Size in Uniaxial Strain controlled Specimens	106
3.5.3.2 Dislocation Cell Size in Biaxial Ratchetting Specimens	112
3.5.3.3 Dislocation Cell Size in Uniaxial Force Controlled Specimens	114
CHAPTER 4 Conclusions and Recommendations	116
REFERENCES	120
APPENDICES	123

LIST OF TABLES

Table 2.1 Chemical composition of 304L SS (in weight percent)	12
Table 2.2 Welded pipe specimens for test	14
Table 2.3 Coupon specimens for fatigue test	19
Table 3.1 The maximum peak stress of uniaxial strain controlled test	36
Table 3.2 Optical microscopy of coupons at different heat-treated temperatures and loading cycles (10kX magnification)	46
Table 3.3 Grain size of coupons in different heat-treated temperature	47
Table 3.4 Optical microscopy of welded pipe specimen (10kX magnitude)	50
Table 3.5 Grain size of welded pipe specimen	50
Table 3.6 VHN of coupon specimens	52
Table 3.7 VHN of welded pipe specimens	52
Table 3.8 Percentage of different structures of dislocations observed in the coupon subjected to uniaxial strain-controlled cycles	59
Table 3.9 Percentage of different structures of dislocations observed in the uniaxial force controlled test	73
Table 3.10 Percentage of different structures of dislocations observed in the biaxial ratchetting test	76
Table 3.11 The percentage of different structures of dislocations observed in welded pipe specimens	80
Table 3.12 Summary of dislocation structures of unconditioned coupons	88
Table 3.13 Summary of dislocation structures of 800°C heat-treated coupons	90
Table 3.14 Summary of dislocation structures of 1050°C heat-treated coupons	91
Table 3.15 Summary of dislocation structures of socket welded pipe specimens	92
Table 3.16 Dislocation densities in uniaxial strain-controlled coupons	94
Table 3.17 Dislocation density of biaxial ratchetting coupons	99
Table 3.18 Dislocation density of Uniaxial Force-controlled coupons	102
Table 3.19 Dislocation density in welded pipe specimens	104
Table 3.20 Data of dislocation cell diameter for uniaxial strain-controlled tests	108

LIST OF FIGURES

Figure 1.1 Chart of (a) Vibration Fatigue Socket Weld Failures and (b) Thermal Fatigue Failure [Chart from Gosselin (2008)]	2
Figure 1.2 (a) Axial ratcheting and (b) axial mean strain vs number of cycle in uniaxial ratcheting test [Humphreys (2004)]	6
Figure 1.3 (a) Biaxial ratcheting and (b) biaxial mean strain vs number of cycle in biaxial ratcheting test [Humphreys (2004)]	7
Figure 1.4 Axial ratcheting vs number of cycle in socket welded joint tests [Lu (2003)]	8
Figure 1.5 Description of heterogeneous dislocation distribution [Bocher (2001)]	10
Figure 2.1 Socket-weld piping joint specimen	13
Figure 2.2 Geometry of (a) socket and (b) socket weld specimen (figure not in scale, dimensions in inches, 1 inch = 25.4 mm) [Lu, 2003]	14
Figure 2.3 Cantilever set-up for welded piping joint fatigue tests.....	16
Figure 2.4 Cantilever set-up for welded piping joint fatigue tests--side view	17
Figure 2.5 Welded piping joint fatigue test set up on T-slot table.....	17
Figure 2.6 (a) Coupon Specimen and (b) Geometry of coupon specimen.....	18
Figure 2.7 Coupon test set-up on the MTS machine	21
Figure 2.8 Different types of cyclic loading tests; (a) Uniaxial strain-controlled, (b) Uniaxial force-controlled, and (c) Biaxial ratcheting test	21
Figure 2.9 ViewMet optical microscope	22
Figure 2.10 Orientation of specimen sectioned from coupon and welded pipe.....	23
Figure 2.11 Grinding and polishing machine.....	23
Figure 2.12 BUEHLER Vicker hardness test machine	26
Figure 2.13 JEOL 2000FX Transmission electron microscope	27
Figure 2.14 The BUEHLER Low speed diamond saw	29
Figure 2.15 The 3mm diameter disk puncher for TEM specimen	29
Figure 2.16 The FISCHIONE twin jet electropolisher	30
Figure 2.17 Schematic of a twin-jet polishing apparatus.....	30
Figure 3.1 Force (p)-Displacement (δ) response of Socket welded pipe fatigue test	32
Figure 3.2 Load responses (p) as a function of cycles (N) for displacement controlled test of	

welded pipe (Specimen failed at 2679 cycles).....	32
Figure 3.3 Axial (ϵ_x) and hoop (ϵ_θ) strain responses for displacement controlled test of welded pipe with 5 cycles.....	33
Figure 3.4 Axial (ϵ_x) and hoop (ϵ_θ) strain responses for displacement controlled test of welded pipe with 20 cycles.....	33
Figure 3.5 Axial (ϵ_x) and hoop (ϵ_θ) strain responses for displacement controlled test of welded pipe with 100 cycles.....	34
Figure 3.6 Axial (ϵ_x) and hoop (ϵ_θ) strain responses for displacement controlled test of welded pipe with 2679 cycles; (a) Axial strain and (b) Hoop strain.....	34
Figure 3.7 Stress (σ_x)-Strain (ϵ_x) response of Uniaxial strain controlled test with unconditioned coupons for 20 cycles.....	37
Figure 3.8 Amplitude (σ_{xc}) and mean (σ_{xm}) of stress responses from Uniaxial strain-controlled test on unconditioned coupons for 5, 20, and 100 cycles.....	37
Figure 3.9 Stress (σ_x)-Strain (ϵ_x) response of Uniaxial strain controlled test with 800°C heat-treated coupons for 20 cycles.....	38
Figure 3.10 Amplitude (σ_{xc}) and mean (σ_{xm}) of stress responses from Uniaxial strain-controlled test on 800°C heat-treatment coupons for 5, 20, and 100 cycles.....	38
Figure 3.11 Stress (σ_x)-Strain (ϵ_x) response of Uniaxial strain controlled test with 1050°C heat-treatment coupons for 5 cycles.....	39
Figure 3.12 Amplitude (σ_{xc}) and mean (σ_{xm}) of stress responses from Uniaxial strain-controlled test on 1050°C heat-treatment coupons for 5, 20, and 100 cycles.....	39
Figure 3.13 Stress (σ_x)-strain (ϵ_x) response of uniaxial force-controlled test with (a) positive mean stress (70cycles) and (b) zero mean stress (70 cycles).....	41
Figure 3.14 Mean of axial strain (ϵ_{xm}) responses as a function of cycles for Uniaxial force controlled test.....	42
Figure 3.15 Stress (σ_x)-strain (ϵ_x) response of biaxial ratcheting test with unconditioned temperature.....	43
Figure 3.16 Axial (ϵ_x) and hoop (ϵ_θ) strain response of biaxial ratcheting test with unconditioned temperature.....	44
Figure 3.17 Amplitude ($\epsilon_{\theta c}$) and mean ($\epsilon_{\theta m}$) of hoop strain response as a function of cycles for biaxial ratcheting test.....	44
Figure 3.18 Grain size (d) versus heat-treatment temperature (T_m)of uniaxial strain controlled coupons.....	47

Figure 3.19 Grain size (d) versus heat-treatment temperature (T_m) of biaxial ratcheting coupons	48
Figure 3.20 Illustration of different locations of socket welded specimen taken for metallographs	49
Figure 3.21 Grain size (d) at different location (l) from the weld toe of the welded pipe after 20 displacement-controlled cycles of 10mm amplitude	51
Figure 3.22 VHN vs. Number of cycles (N) of different heat-treated coupons subjected to uniaxial strain-controlled	53
Figure 3.23 VHN vs. Heat-treatment temperature (T_m) of coupons subjected to (a) uniaxial strain-controlled cycles and (b) biaxial ratcheting cycles	54
Figure 3.24 VHN as a function of (a) number of cycles (N) and (b) different distance (l) from weld toe of socket welded pipe	55
Figure 3.25 Example of the various types of dislocation structures; (a) Planar slip, (b) Tangles, (c) Uncondensed cells, (d) Ladder structure, (e) Cells, (f) Twins and cells, (g) Walls, and (h) Cells [Bocher et al. (2001)]	58
Figure 3.26 Dislocation structure of unconditioned coupon before 1% strain-controlled fatigue	60
Figure 3.27 Dislocation structure of unconditioned coupon after 5 cycles	61
Figure 3.28 Dislocation structure of unconditioned coupon after 20 cycles	62
Figure 3.29 Dislocation structure of 800°C heat-treated coupon before 1% strain-controlled fatigue	63
Figure 3.30 Dislocation structure of 800°C heat-treated coupon after 5 cycles	64
Figure 3.31 Dislocation structure of 800°C heat-treated coupon after 20 cycles	66
Figure 3.32 Dislocation structure of 800°C heat-treated coupon after 100 cycles	67
Figure 3.33 Dislocation structure of 1050°C heat-treated coupon before 1% strain-controlled fatigue	68
Figure 3.34 Dislocation structure of 1050°C heat-treated coupon after 5 cycles	69
Figure 3.35 Dislocation structure of 1050°C heat-treated coupon after 20 cycles	70
Figure 3.36 Dislocation structure of 1050°C heat-treated coupon after 100 cycles	72
Figure 3.37 Dislocation structure of non-ratcheting coupon after 400 cycles	74
Figure 3.38 Dislocation structure of ratcheting coupon after 400 cycles	75
Figure 3.39 Dislocation structure of unconditioned specimen after 2000 cycles	77
Figure 3.40 Dislocation structure of 800°C heat-treated specimen after 1482 cycles	78

Figure 3.41 Dislocation structure of 1050°C heat-treated specimen after 2000 cycles ..	79
Figure 3.42 Dislocation structure after 5cycles (SSPC4) at 3mm away in weld toe	82
Figure 3.43 Dislocation structure after 20 cycles (SSPC2) at 3mm away in weld toe ...	83
Figure 3.44 Dislocation structure after 20 cycles (SSPC2) at 9.8mm away in weld toe	84
Figure 3.45 Dislocation structure after 20 cycles (SSPC2) at 38mm away from weld toe	85
Figure 3.46 Dislocation structure after 100 cycles (SSPC3) at 3mm away from weld toe	86
Figure 3.47 Dislocation structure after crack initiation at 2679 cycles (SSPC5) at 3mm away from weld toe	87
Figure 3.48 Mean of Dislocation density (ρ_m) vs. Number of cycles (N) for different heat- treatment temperature	96
Figure 3.49 Dislocation density (ρ) as a function of axial peak stress (σ_{xp}) and heat-treatment temperature at (a) 5 cycles, (b) 20 cycles, and (c) 100 cycles	97
Figure 3.50 Linear relation between dislocation density and stress amplitude in uniaxial strain-controlled specimens	98
Figure 3.51 Mean of Dislocation density (ρ_m) vs. Heat-treatment temperature (T_m) at different cycles	98
Figure 3.52 Dislocation density (ρ) as a function of axial peak stress (σ_{xp}) and heat-treatment temperature (T_m)	100
Figure 3.53 Linear relation between dislocation density and stress amplitude in biaxial ratcheting specimens	101
Figure 3.54 Dislocation density in unaxial force-controlled (Non-ratcheting vs. Ratcheting) experiments	103
Figure 3.55 Dislocation density (ρ) as a function of the number of cycles (N).....	105
Figure 3.56 Dislocation density (ρ) vs. Location (l) from weld toe	105
Figure 3.57 Representative cell structure after (a) 5 cycles and (b) 20 cycles in unconditioned specimen	106
Figure 3.58 Representative cell structure after (a) 5 cycles, (b) 20 cycles, and (c) 100 cycles in 800°C heat-treated specimen	107
Figure 3.59 Representative cell structure after (a) 5 cycles, (b) 20 cycles, and (c) 100 cycles in 1050°C heat-treated specimen	107
Figure 3.60 Mean cell size (δ_m) vs. Number of fatigue cycles (N).....	110
Figure 3.61 Mean cell size (δ_m) as a function of dislocation density (ρ).....	110
Figure 3.62 Linear relation between stress and cell size in uniaxial strain-controlled specimen	

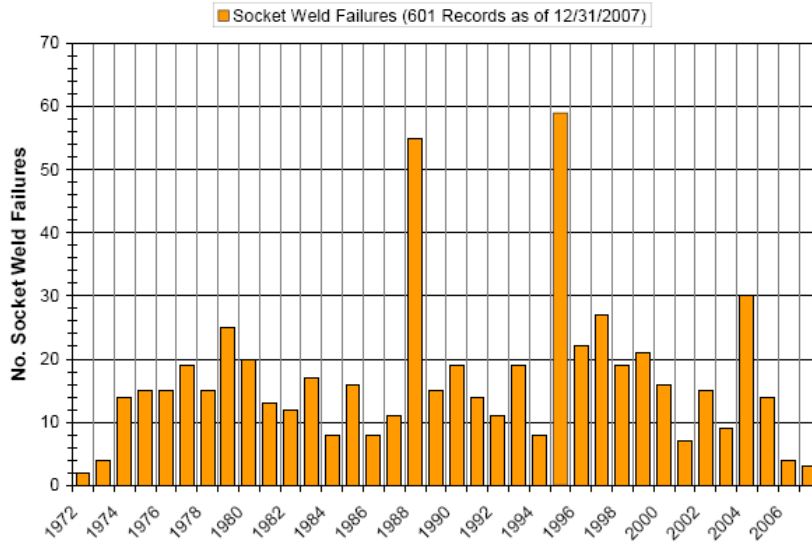
.....	111
Figure 3.63 Mean cell size (δ_m) vs. Heat-treatment temperature (T_m).....	111
Figure 3.64 Representative cell structure after 2000 cycles in (a) unconditioned material, (b) 800°C heat-treatment temperature, and (c) 1050°C heat-treatment temperature	112
Figure 3.65 Cell size (δ) vs. Heat-treatment temperature (T_m) at 2000 cycles	113
Figure 3.66 Mean cell size (δ_m) as a function of stress amplitude (σ_{xc}) and dislocation density (ρ).....	113
Figure 3.67 Linear relation between stress and reciprocal mean cell size in biaxial ratcheting specimen	114
Figure 3.68 Representative cell structure of (a) non-ratcheting and (b) ratcheting in unconditioned material.....	115
Figure 3.69 Mean cell size (δ_m) in uniaxial force-controlled (Non-ratcheting vs. Ratcheting) experiments	115

CHAPTER 1 Introduction

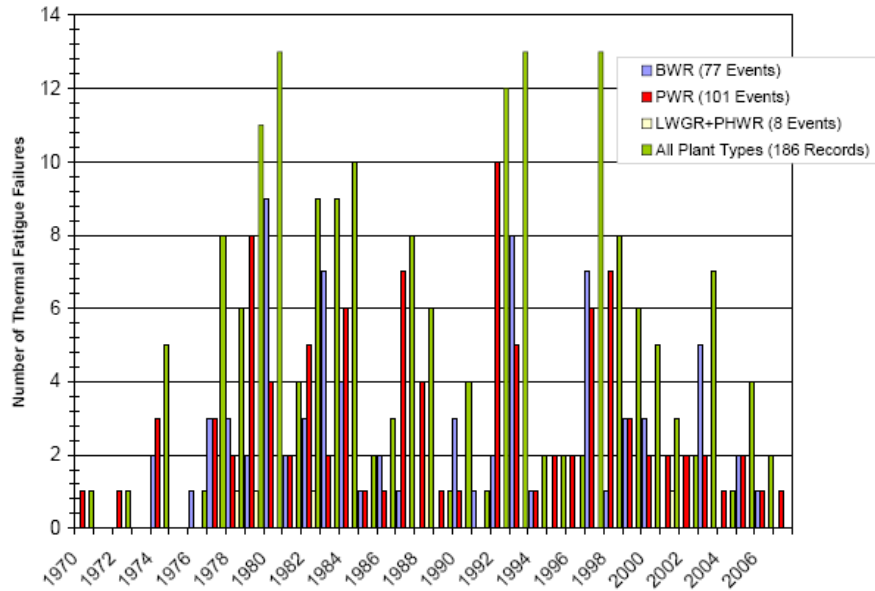
1.1 Background

Fatigue failures are continued to occur in nuclear power plants (NPPs), resulting in unscheduled plant downtime and substantial financial loss. The majority of fatigue failures are caused by vibration fatigue of socket welded joints and thermal fatigue during 1970 to 2007 in United States [Gosselin (2008)]. As shown in the Figure 1.1, vibration fatigue and thermal fatigue failures occurred over the last few decades. The vibration fatigue failure of socket weld (Figure 1.1 (a)) was suddenly increased during 1988 and 1989 as well as 1995 and 1996. For the thermal fatigue, the number of failures in nuclear power plants have been occurred that initially increased in 1980, decreased until 1992, increased in 1993 again, and then tended to decrease after 1998 (Figure 1.1 (b)).

Improvement of socket welded joints was emphasized because a substantial number of failures and leakage initiated in socket welds [EPRI (1998)]. It is reported by OPDE (OECD Piping Failure Data Exchange) database that 108 cases of socket weld failure occurred during 1970 to 2001 in the nuclear piping systems [Choi (2007)]. Fatigue failures are mostly observed at the socket welds of small diameter piping and fillet attachment [Hassan (2005)]. For unexpected failures, it is required to determine the reasons for cracking and to provide an adequate repair procedure [Vecchio (1996)]. In this work, efforts are made to understand the fatigue failure mechanism of welded piping joints with emphasis on microstructural evolution induced by fatigue loading.



(a)



(b)

Figure 1.1 Chart of (a) Vibration Fatigue Socket Weld Failures and (b) Thermal Fatigue Failure [Chart from Gosselin (2008)]

1.2 Residual Stress Effect on Fatigue Failure

Fatigue failures of welded piping joints are caused by many factors, such as, stress

concentration, environment, loading type and residual stress. Among them, residual stress has been studied as a reason of fatigue failure, because it can act as a mean stress to the external loading cycle, thereby induces ratcheting and may reduce fatigue life [Lu (2003); Humphreys (2004)]. Welding residual stress, a fabrication by-product that is not avoidable, developed in welded piping component during welding process. The welding process exposes both the base and weld materials to the heating and non-uniform cooling cycles resulting in residual stress. It is pointed out that residual stress due to welding could be approximately as high as the yield stress (Maddox [1991]; Yamashita et al. [1997]). Experimental study on the influence of residual stress and ratcheting on fatigue failure of welded joints showed that fatigue cracks initiated at the weld toe where the ratcheting strain is the largest [Lu (2003)]. He also anticipated that the ratcheting strain is induced by the residual stress. Generally, it is well known that the tensile residual stresses reduce the fatigue life of piping component by promoting early crack initiation, whereas the compressive residual stresses improve fatigue life. However, it is also reported that strain ratcheting was observed in the tensile direction even though residual stresses were compressive [Humphreys (2004)]. Now that it has not been proven clearly that residual stress is the only factor that induces ratcheting strain, interaction between ratcheting strain caused by welding process and dislocation heterogeneity will be studied in this research.

1.3 Strain Ratcheting

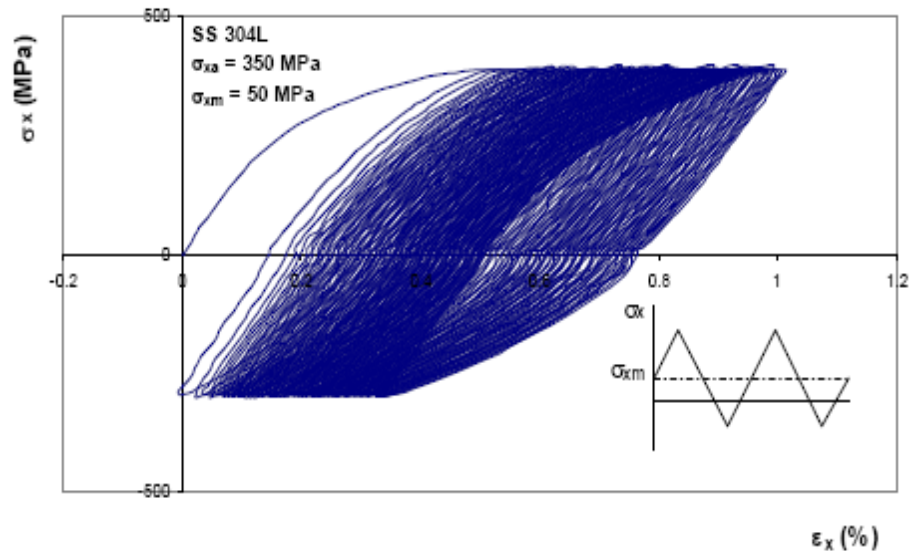
Usually, normal operation superimposed to cyclic load, such as earthquake, is considered for designing piping system of nuclear power plants [Kulkarni et al. (2003)]. The accumulation of deformation which occurs in the plastic region under cyclic loading results

in degradation and failure of the piping system. Strain ratcheting is defined as an accumulation of strain under cyclic loading which may accelerate fatigue crack initiation and leads to premature failure. Strain ratcheting usually takes place in the components subjected to presence of nonzero mean stress in the cyclic loading.

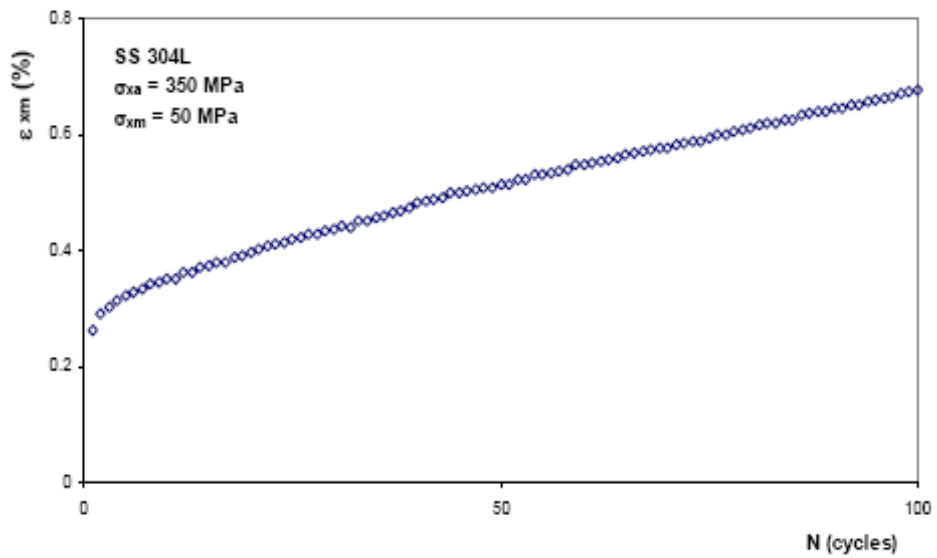
The typical phenomena of uniaxial and biaxial ratcheting are shown in Figures 1.2 and 1.3 [Humphreys (2004)]. In the case of the uniaxial ratcheting (Figure 1.2 (a)), the prescribed stress cycles were unsymmetric with a positive mean stress, and hence hysteresis loop gradually migrated to the positive strain direction, which is defined as the strain ratcheting. Figure 1.2 (b) shows increasing mean strain with cycles as a demonstration of strain ratcheting. In the biaxial ratcheting (Figure 1.3 (a)), strains cycled in the axial direction are symmetric in the presence of steady circumferential stress. This loading induces strain ratcheting in circumferential direction. The mean circumferential strain increases with cycles as shown in Figure 1.3 (b).

The cyclic fatigue life might be reduced by ratcheting strain. It is reported that the ratcheting strain produced by cyclic stress in the presence of mean stress is detrimental to fatigue life [Kang et al. (2006); Xia et al. (1996)]. It was reported by Lu (2003) that ratcheting strain at welded joint might be the primary reason of premature fatigue failures. He performed low cycle fatigue tests of socket-welded piping joints in the cantilever set-up. These tests were subjected to displacement-controlled loading cycles of 14.5 mm amplitude. The axial strain ratcheting at 5mm from the weld toe was observed with increasing cycle and continued until the crack initiated. Axial strain ratcheting with two different types of welding sequences are shown in Figure 1.4; socket welded pipe with quarter-circumferential welding

(SW1) and full-circumferential welding (SW3). It is interesting that these specimens show ratcheting strain even though fatigue tests were subjected to displacement-controlled loading cycles. Is the difference between the ratcheting strains of the two experiments the reason for the difference in their fatigue lives? This question will be addressed in this study by investigating the dislocation structure of ratcheting phenomenon of the welded joints and coupons under simulated environment and loading conditions of welded joints.

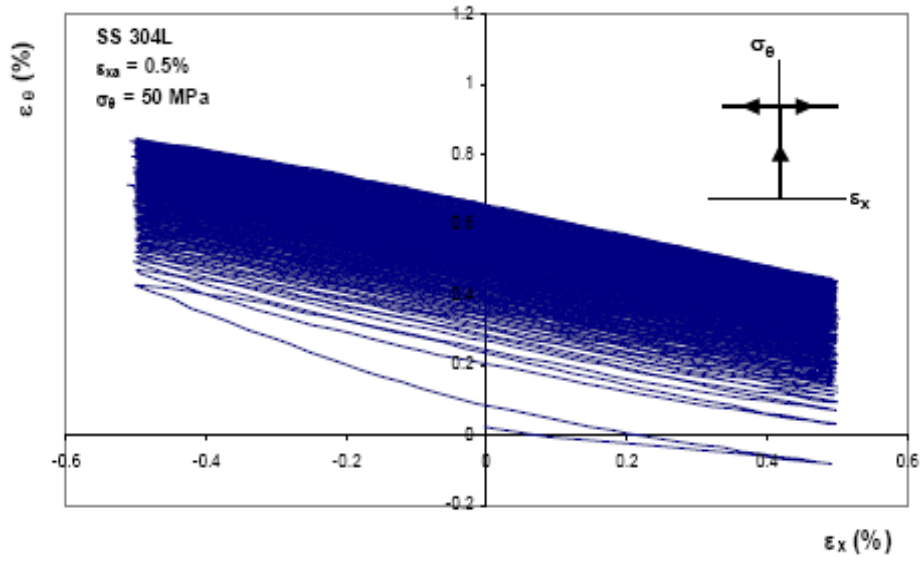


(a)

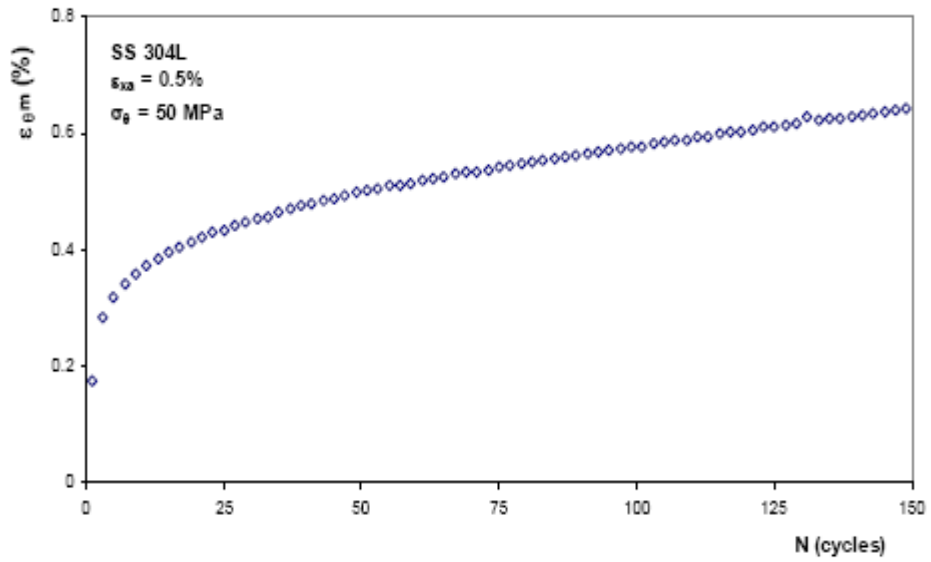


(b)

Figure 1.2 (a) Axial ratcheting and (b) axial mean strain vs number of cycle in uniaxial ratcheting test [Humphreys (2004)]



(a)



(b)

Figure 1.3 (a) Biaxial ratcheting and (b) biaxial mean strain vs number of cycle in biaxial ratcheting test [Humphreys (2004)]

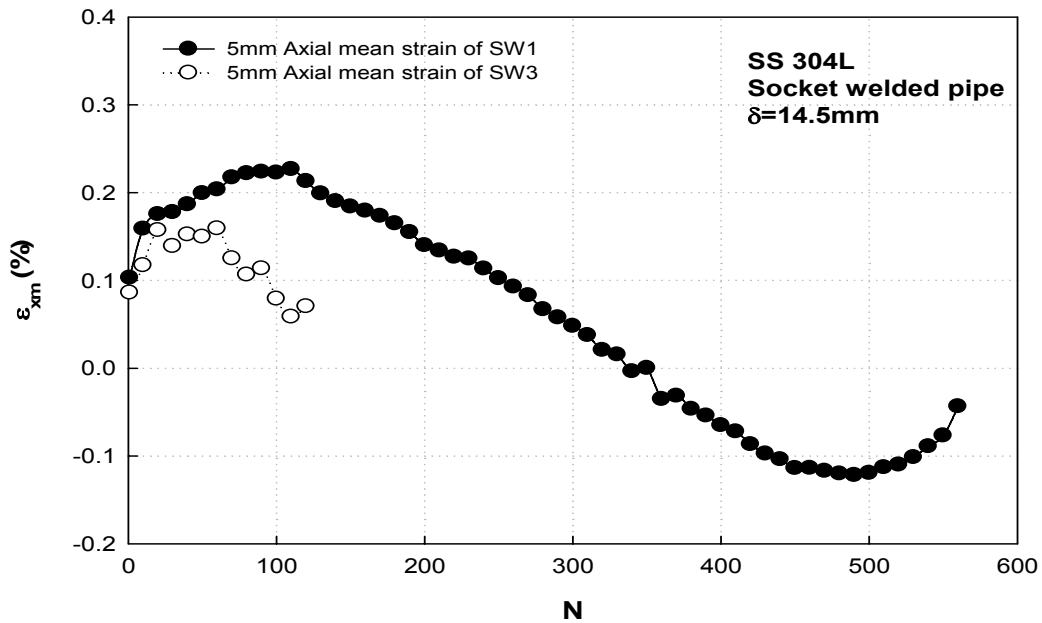


Figure 1.4 Axial ratcheting vs number of cycle in socket welded joint tests [Lu (2003)]

1.4 Dislocation Structure

Understanding the dislocation substructures of ratcheting fatigue failure of welded joints is important for developing methods of life enhancement. For this purpose, it is not enough to understand fatigue failure at macroscopic scale. The primary reason of this is that the failure mechanism is extensively affected by the dislocation structures or dislocation structure influences subsequent fatigue response [Mayama et al. (2008)]. The dislocation structures in fatigue can be separated into three types following the dislocation slip modes; 1) the wavy type of dislocations such as loop patches, vein structure, persistent slip band (PSB), dislocation walls, and dislocation cells, 2) the planar type of dislocations which remain planar during fatigue, 3) a mix of wavy and planar type [Chiu et al. (2006)]. The mixed type of

dislocations is found in stainless steel subjected to low cycle fatigue tests. The planar types of dislocations are formed at early stages of fatigue and may transform into the wavy type during later stage [Altenberger et al. (1999); Obrtlík et al. (1994)]. Dislocation structures are influenced by strain amplitude and cyclic loading in fatigue tests. Dislocation structures consist of loop patches at low cycles, become mixed with respect to wall structures at intermediate periods, and transform to cell structure at high cycle [Laird et al. (1989)]. The cell structures become equiaxed and smaller as number of fatigue cycles increases [Laird et al. (1989)]. It is also pointed out that evolution of dislocation structure from loop patches into wall and PSB, and then into cell structures is observed with increasing strain amplitude during strain-controlled tests in copper polycrystals [Laird and Llanes (1993)]. Dislocation cell structures become more uniform with larger strain amplitudes of cyclic loading [Mayama et al. (2008)]. To explain dislocation structure with hardening and softening, Xia and Wang (1992) showed that hardening stage is characterized by the formation of dislocation tangles, pile-ups, and planar arrays in the initial hardening stage, while the dislocation wall structures or poorly formed cell structures are distinctive of the softening region. In the fatigue tests on annealed specimens, dislocation tangles are transient features between the low dislocation density of the initial state and the formation of the developed cell structures [Mayama and Sasaki (2006)].

Few studies have been reported focusing on a quantitative evaluation of microstructure. Dislocation density increases with increasing stress amplitude, and decreasing cell size [Lee and Lin (2001)]. The correlation between dislocation density and stress indicates that cyclic hardening is induced by increasing dislocation density, and cyclic

softening is dependent on formation of dislocation structures. Bocher et al. (2001) and Gerland (1989) point out dislocation cell size decreases as either stress or strain amplitude increases. It is also pointed out that heterogeneous dislocation structures are hard regions with a high dislocation density compared with soft region with a low dislocation density [Mughrabi (1983)]. The heterogeneous dislocation is defined as $f_w = e/(e + \lambda)$, where f_w is the percentage of walls in the substructure, e is the thickness of the hard zone which is like dislocation walls, and λ is the thickness of the soft zone like dislocation channels and described in Figure 1.5 [Bocher et al. (2001)]. The density of heterogeneous structures such as tangles, walls, and cells increases with plastic strain, whereas their dimension e and λ decrease [Feaugas (1999)]. In this aspect, not only the macroscopic behavior and microscopic observation have correlation to some degree, but also mechanism of macroscopic deformation can be explained by microscopic point of view.

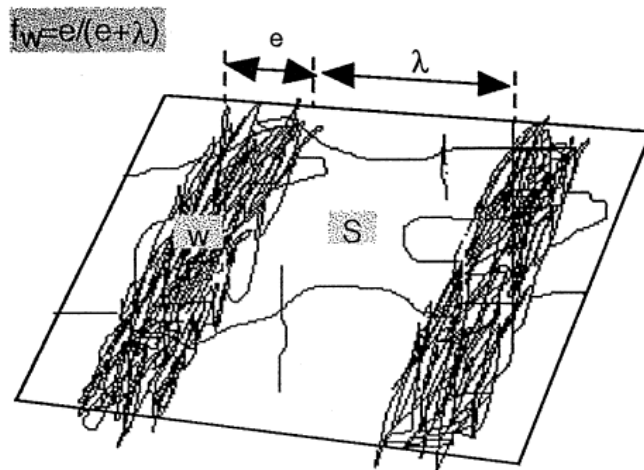


Figure 1.5 Description of heterogeneous dislocation distribution [Bocher (2001)]

1.5 Overview

In this research, the primary goal is to determine the evolution of dislocation structures near the toe of welded piping joints under the application of low-cycle fatigue loading and to understand the microstructure of ratcheting response of the welded joints. In order to gain this insight, four welded piping specimens were subjected to 10mm displacement-controlled cyclic loading with different number of cycles (5, 20, 100, and failure cycle of specimen).

Additional fatigue tests under axial strain-controlled cycle, axial force-controlled cycle, and axial strain-controlled cycle under steady internal pressure on the tubular specimen, heat-treated at 800°C and 1050°C, were conducted to simulate different locations of welded pipe specimens. The different heat-treatment temperatures were corresponding to the temperature cycle experienced by different points of the welded pipe during the welding process. The simulated influences of heat-treatment temperature and the number of fatigue cycles on the microstructures are studied.

This study focuses on both qualitative and quantitative analyses of dislocation structures of welded joints and simulated coupons subjected to various numbers of fatigue cycles. Qualitative Transmission Electron Microscopy (TEM) observation of dislocation microstructures in fatigued specimens with different conditions was carried out. Two-beam condition method for Bright Field (BF) image was applied to visualize dislocation structure in TEM images. Using this, the statistical characteristics and quantitative measurements related to dislocation substructure are presented. Finally, the influence of the ratcheting mechanism on the microstructure is investigated.

CHAPTER 2 Experimental Procedures

2.1 Material and specimen

The specimens used in this study were type 304L austenitic stainless steel (SS 304L). SS 304L was received in the cold worked (CW) condition and as tubular samples and pipes of varied sizes. SS 304L is an extra low-carbon variation of type 304 with a 0.03% maximum carbon content that eliminates carbide precipitation during welding. As a result, this alloy can be used in the “as-welded” condition even in severe corrosive conditions. It often eliminates the necessity of annealing weldments except for applications specifying stress relief. It has slightly lower mechanical properties than type 304. Chemical composition of type 304L stainless steel is shown in Table 2.1.

Table 2.1 Chemical composition of 304L SS (in weight percent)

	C	Si	Mn	P	S	Cr	Ni	Mo
wt%	0.013	0.41	1.22	0.02	0.006	18.25	10.13	0.27

Socket welded piping joints and heat treated tubular coupons are subjected to various fatigue loadings for subsequent microstructural characterization. The 304L stainless steel tubular specimens were heat treated at 800°C and 1050°C in a furnace for five minutes and allowed to cool at a room temperature in order to simulate the heat affected zone (HAZ) condition of welded joints. The welded joints, tubular specimens, and fatigue loading cycles are discussed below.

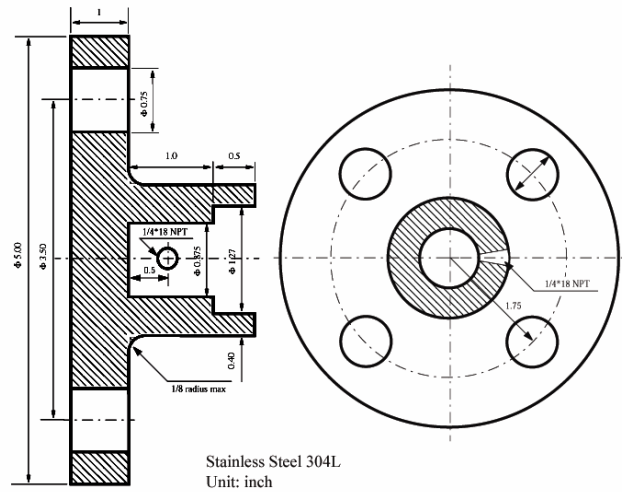
2.1.1 Socket Welded Piping joints

Figure 2.1 is a photograph of a socket welded joint for fatigue testing. As mentioned earlier, the test specimens were 304L stainless steel and the weld filler was SS 308L. Both

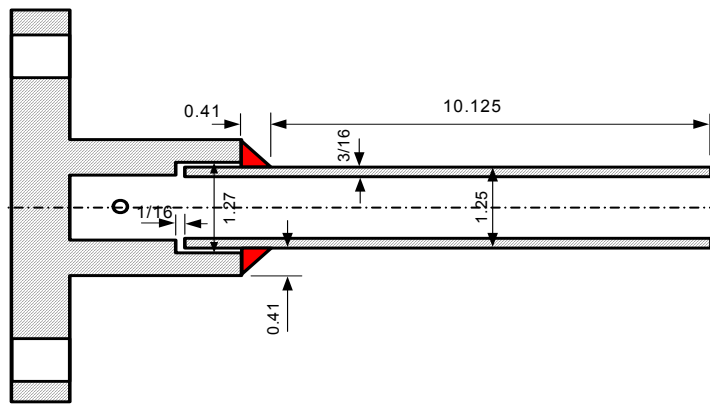
the socket and end fixtures of the weld specimen were machined from SS 304L blocks. The geometry and dimensions of socket welded pipe specimen are shown in Figure 2.2. The pipe specimen has a nominal diameter of 1.25 inches and wall thickness of 3/16 inches. The length of the pipe of socket weld specimens was set to be 10.125 inches. Table 2.2 lists welded pipe specimens used in the present work.



Figure 2.1 Socket-weld piping joint specimen



(a)



(b)

Figure 2.2 Geometry of (a) socket and (b) socket weld specimen (figure not in scale, dimensions in inches, 1 inch = 25.4 mm) [Lu, 2003]

Table 2.2 Welded pipe specimens for test

Specimen	Number of cycle	Welding type	Welding sequence	Prescribed loading amplitude, δ_c
SSPC4	5	Socket	Quarter	10mm
SSPC2	20	Socket	Quarter	10mm
SSPC3	100	Socket	Quarter	10mm
SSPC5	2679	Socket	Quarter	10mm

2.1.2 Test Setup of Socket Welded Pipe

The fatigue tests of socket-welded pipe were carried out in a cantilever set-up as shown in Figures 2.3 and 2.4. The welded joints were located near the support column, the fixed end of the cantilever set-up. As shown in the Figure 2.3, prescribed cyclic loading was applied to the end of the pipe on the other end of the welded joint. The actuator of a servo-hydraulic testing machine through a pin end fixture setup was used to transfer loading. The pin fixture is made up of a self-aligning ball bearing and a pin. The support column is rigidly tied up to the T-slot table of the testing machine (Figure 2.5). Both end fixtures of the pipe specimen had small access holes which were used to fill the pipe specimen with oil and apply an internal pressure using a pneumatic pump. A small pressure of about 100psi was prescribed for detection of through-wall fatigue crack by oil leak. Four fatigue tests of socket welded pipe specimen were conducted by the prescribed loading cycle with a displacement-controlled cyclic loading of 10 mm amplitude. Each cycle period was 4 seconds. Axial and hoop strains were recorded at five locations, 3mm, 19mm, 38mm, and 125mm from the weld toe at the top, and 3mm at the bottom were recorded using strain gages. Residual stress measurements before and following fatigue testing at each of the strain gage location were obtained using X-ray and Neutron diffraction at Oak Ridge National Laboratory.

In all of the fatigue tests, the displacement, force, and strain at various locations mentioned above were recorded. These recorded data were digitized and stored every 0.032 seconds using a LabVIEW data acquisition program developed by Glen Wheeler and Shafiqul Bari.

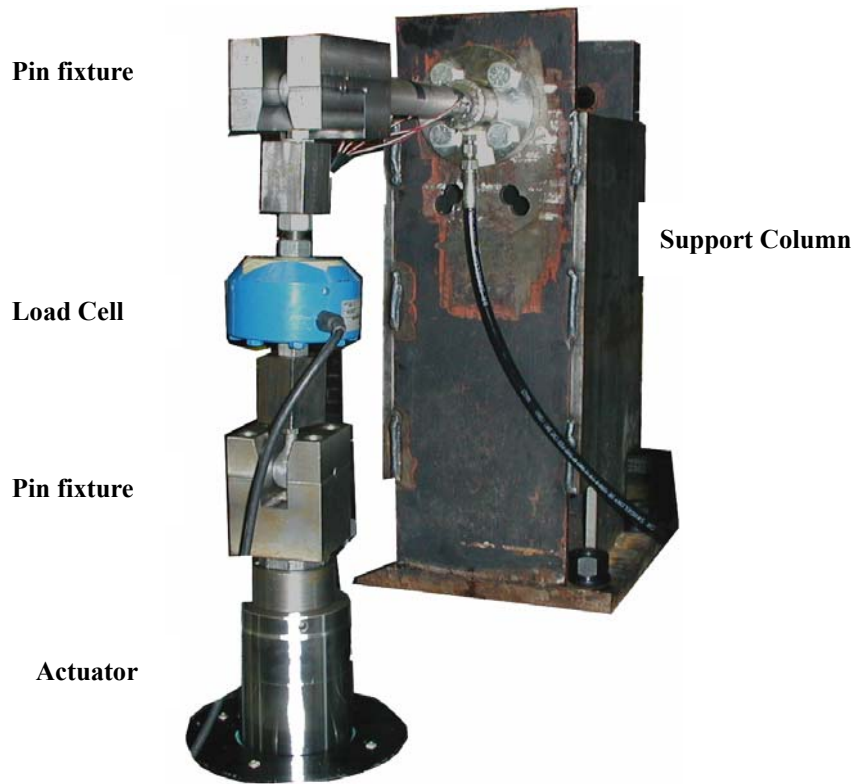


Figure 2.3 Cantilever set-up for welded piping joint fatigue tests

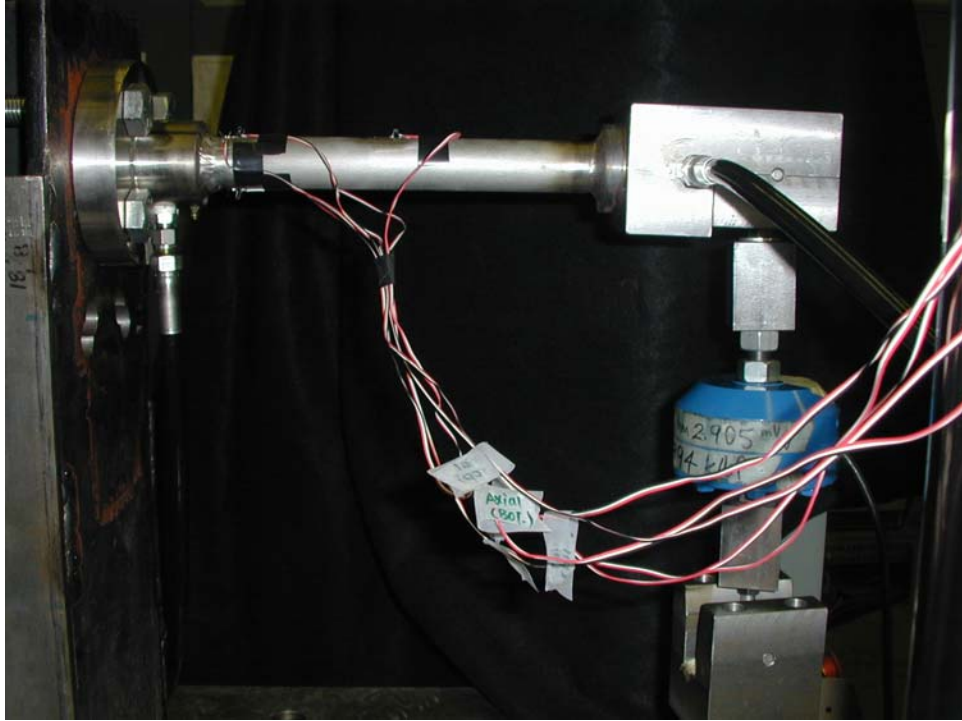


Figure 2.4 Cantilever set-up for welded piping joint fatigue tests—side view

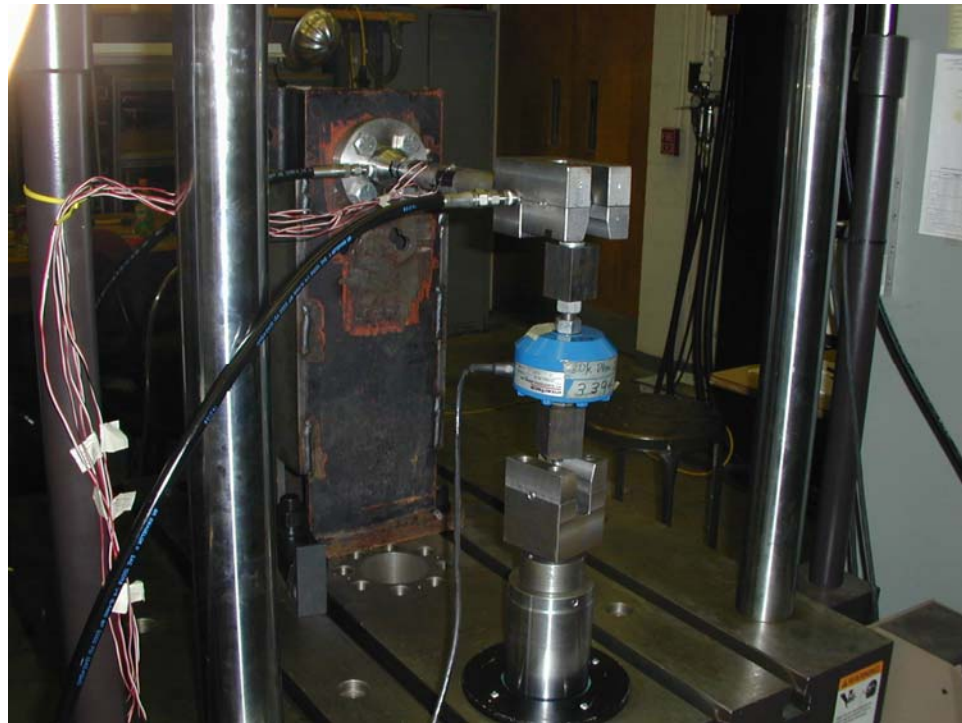


Figure 2.5 Welded piping joint fatigue test set up on T-slot table

2.1.3 Coupon Specimen

A tubular coupon was machined from the same SS 304L pipe as the socket welded pipe specimens to obtain material properties following heat treatment mimicking HAZ conditions in a weld. The machined specimen and its dimension are shown in Figure 2.6. The coupon had nominal outer diameter of 1 inch, inner diameter of 0.9 inches, and wall thickness of 0.05 inches. Some of the coupons were heat treated at 800°C and 1050°C for 5 minutes and then allowed to air cool down to room temperature to imitate the HAZ material condition. All coupon specimens tested in this work are listed in Table 2.3.

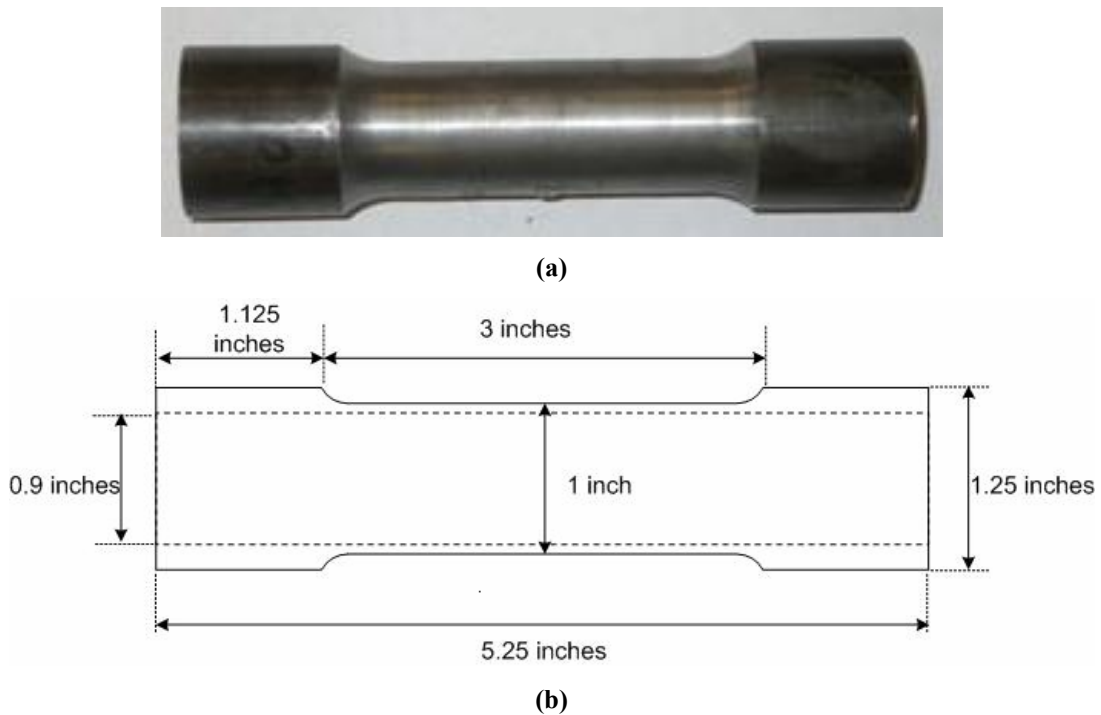


Figure 2.6 (a) Coupon Specimen and (b) Geometry of coupon specimen

Table 2.3 Coupon specimens for fatigue test

Fatigue test type	Annealing temperature	Specimen ID	Number of cycle	Prescribed loading
Uniaxial strain controlled	Unconditioned	SS_uncond	0	Before fatigue
		SS_sn11	5	$\varepsilon = 1\%$
		SS_sn12	20	$\varepsilon = 1\%$
		SS_sn01	234	$\varepsilon = 1\%$
	800C	SS_800	0	Before fatigue
		SS_sn13	5	$\varepsilon = 1\%$
		SS_sn14	20	$\varepsilon = 1\%$
		SS_sn05	100	$\varepsilon = 1\%$
	1050C	SS_1050	0	Before fatigue
		SS_sn15	5	$\varepsilon = 1\%$
		SS_sn16	20	$\varepsilon = 1\%$
		SS_sn07	100	$\varepsilon = 1\%$
Biaxial ratchetting	Unconditioned	SS_bi01	2000	P = 6.89MPa $\varepsilon_x = 0.4\%$
	800C	SS_bi04	1482	P = 6.89MPa $\varepsilon_x = 0.4\%$
	1050C	SS_bi05	2000	P = 6.89MPa $\varepsilon_x = 0.4\%$
Uniaxial force controlled	Unconditioned	SS_uni11	400	$F_m = 0$ $F_a = 0.8F_{1\%}$
		SS_uni01	400	$F_m = 0.2F_{1\%}$ $F_a = 0.8F_{1\%}$

2.1.4 Test Setup of Coupons

The fatigue tests of coupons were also performed using the same machine as for cantilever set-up. However, coupon tests were held with one more actuator on upper side of machine instead of support column and pin fixtures different from welded pipe tests as

shown in Figure 2.7. The ends of coupon were fixed in both actuators. Cyclic loading is applied to coupons through the actuator. Coupon specimens were filled with oil under internal pressure to detect fatigue crack. The coupon specimens were axially cycled under prescribed strain and force controls and in some cases with steady-state internal pressure as shown in Figure 2.8. In the uniaxial strain-controlled test, the loading cycle is symmetric, axial strain-controlled cycles of 1% amplitude at the rate of 4 seconds/cycle. Uniaxial stress-controlled cyclic experiments are conducted by prescribing constant amplitude force-controlled cycles about a positive mean stress. In the biaxial ratcheting test, symmetric, axial strain-controlled cycle in the presence of steady internal pressure is prescribed to the specimens. Extensometer and strain gage were mounted on the pipe surface. Throughout the test, force, axial strain, and hoop strain were digitized and recorded.



Figure 2.7 Coupon test set-up on the MTS machine

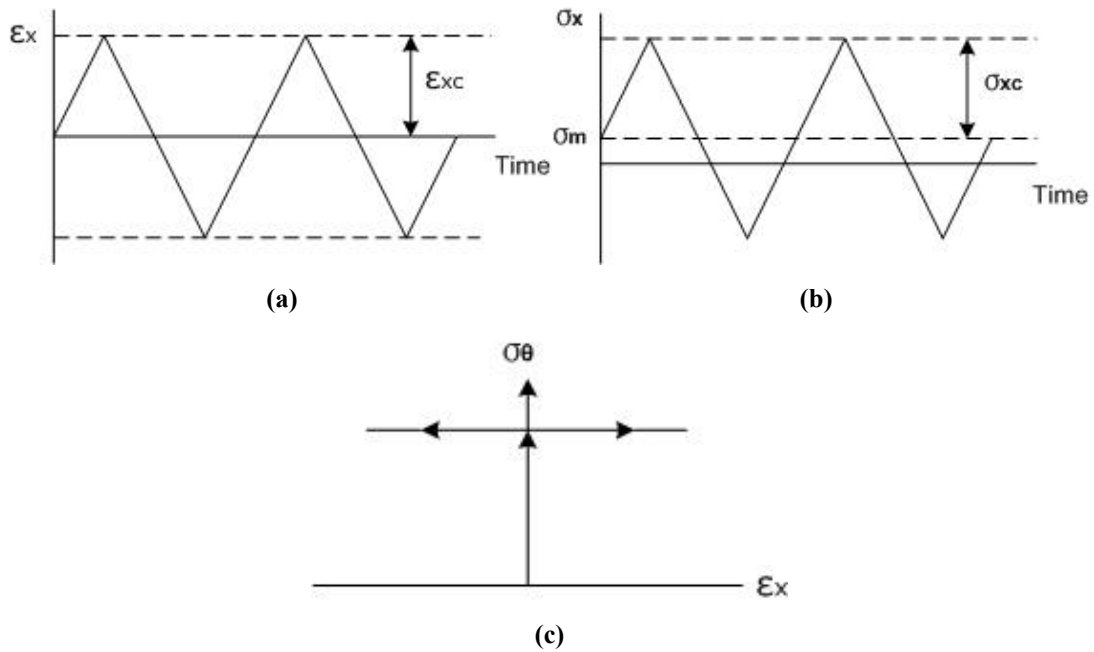


Figure 2.8 Different types of cyclic loading tests; (a) Uniaxial strain-controlled, (b) Uniaxial force-controlled, and (c) Biaxial ratcheting test

2.2 Metallography

Metallographic investigation was accomplished using ViewMet microscope in the Nuclear Material Laboratory as shown in Figure 2.9.



Figure 2.9 ViewMet optical microscope

2.2.1 Specimen Preparation

The coupons and pipes specimens were sectioned into hoop and axial orientations that will be same directions corresponding to TEM specimens to examine dislocation microstructures (Figure 2.10). The sample was mounted in acrylic powder for grinding and polishing. The grinding and polishing machine shown in Figure 2.11 was available in the Nuclear Material Laboratory. Grinding was started using 120 grit paper initially, and progressed to 600, and finally to 800 grit paper. Then, polishing was carried out using 3 μ diamond suspension to remove remained scratches. Next, the sample was etched using Aqua

Regia, mixture of 25% nitric acid and 75% hydrochloric acid by volume. The sample surface was immersed in the etching solution for 20-30 seconds and rinsed in water to stop the reaction.

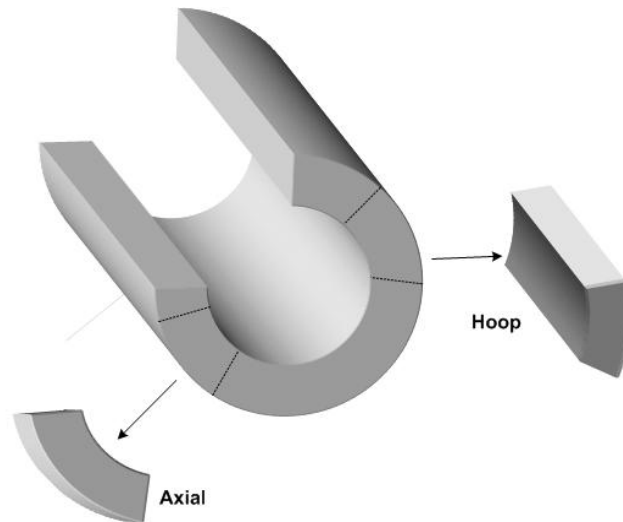


Figure 2.10 Orientation of specimen sectioned from coupon and welded pipe



Figure 2.11 Grinding and polishing machine

2.2.2. Optical Microscopy Observation

Optical microscopy is a technique to study the grain structure of materials for both qualitative and quantitative metallography. In this work, quantitative measurement of the grain size was performed. A general method of measuring grain size is to compare the grains at a fixed magnification with the ASTM grain size number. The ASTM grain size number has the following relationship with the number of grain in square inch at a magnification of 100.

$$N=2^{n-1} \quad (1)$$

where N is the number of grains per square inch, n is the ASTM grain size number. Higher the ASTM grain size number smaller is the grain size. Although a small area can be selected to count the number of grains, larger areas are selected to obtain more accurate grain size measurement.

2.3 Hardness Test Preparation

The coupon and pipe specimens were sectioned and mounted in acrylic powder for grinding and polishing in the same manner as metallography specimen. Grinding and polishing were performed until specimen surface was shiny and flat using polishing machine (Figure 2.11). The hardness measurements were made on BUEHLER Vickers hardness test machine as shown in Figure 2.12.

The Vickers hardness test technique involves indenting the test material with a diamond indenter, in the form of a right pyramid with a square base and an angle of 136 degrees between opposite faces. The full loading time is generally 10 to 15 seconds. The two diagonals of the indentation in the surface of the specimen after removal of the load are

measured and their average calculated. The area of the indented surface is calculated from the length of the diagonals. The Vickers hardness number (VHN) is obtained by dividing applied load by the surface area of the indentation. The following relationship is generally used [Dieter (1986)].

$$\text{VHN} = \frac{2P \sin\left(\frac{\theta}{2}\right)}{L^2} = \frac{1.854P}{L^2} \quad (2)$$

where P= applied load in kgf

L= the average length of the diagonals in mm

θ = the angle between opposite faces of the indenter (136°)

In this work, 0.5 kgf load was applied for 10 seconds to evaluate Vickers hardness number of 304L stainless steel material. As the test sample has a smooth surface and is held perpendicular to the indenter, these results are considered reasonably accurate.



Figure 2.12 BUEHLER Vicker hardness test machine

2.4 Transmission Electron Microscopy

2.4.1 Transmission Electron Microscope Equipment

The TEM study was performed using the microscope in the Atomic Resolution Electron Microscopy Center at the North Carolina State University. The JEOL 2000FX TEM operating at 200kV was used in this work. Bright field imaging was used to capture low magnification pictures in a two-beam condition. JEOL 2000FX is shown in Figure 2.13. This microscope consists of electron gun, column, goniometer, high tension tank, vacuum pump, CCD camera, viewing chamber, specimen holder, and power supply console.

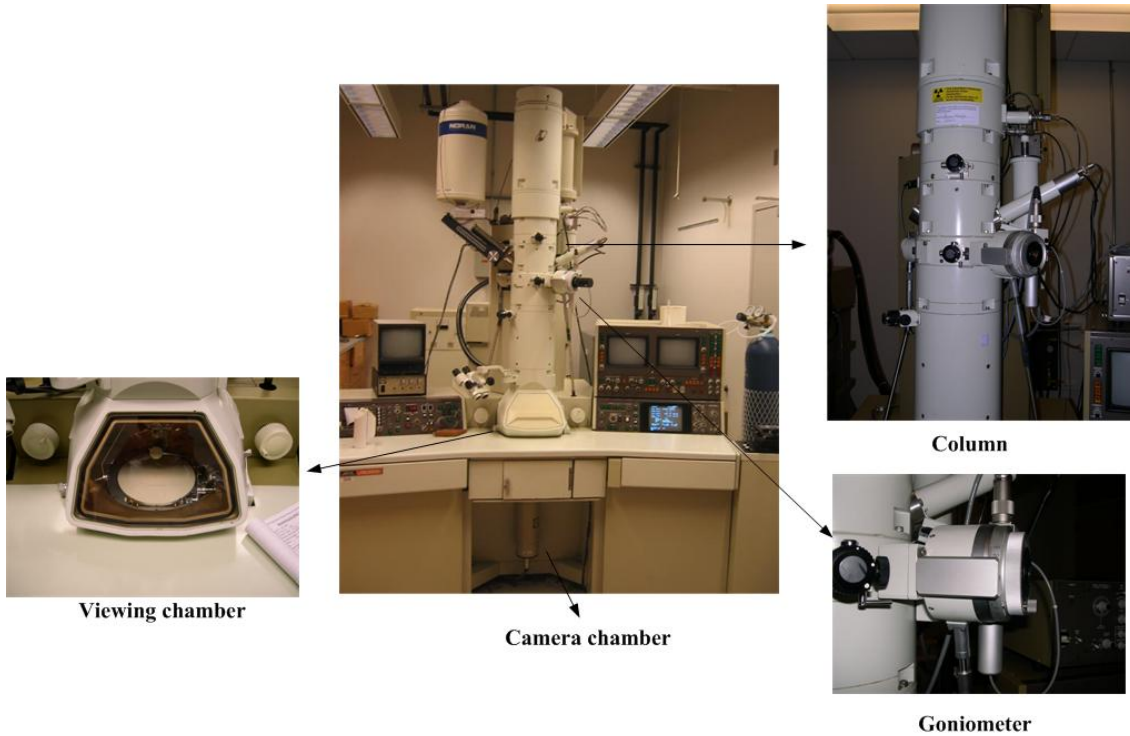


Figure 2.13 JEOL 2000FX Transmission electron microscope

2.4.2 Transmission Electron Microscope Specimen

Specimen preparation is an important aspect of the TEM analysis. Specimen preparation techniques are very material dependent, therefore, it is important to initially select the technique that is most beneficial for the specific material. In this work, the specimens were prepared using the electropolishing method which is a time-proven technology for the preparation of most metallic specimens.

The specimen preparation involves creation of a thin slice from the bulk sample, cutting the disk, and final thinning of the disk. Small samples were cut from the tested specimen by low speed diamond saw (Figure 2.14). These samples were undergone grinding on coarse polishing paper to get rid of much of the material and then on fine polishing paper.

Grinding on these polishing papers made sample thickness of around 200 μ m. These samples were then punched into 3 mm diameter disks using disk puncher shown in Figure 2.15. Each disk was then thinned down to a thickness of less than 100 μ m using fine polishing paper with a grit size of 1200. Once the disks attained a thickness smaller than 100 μ m, they were installed in the twin jet electropolisher, Fischione Model 120. A twin-jet electropolisher is shown in Figure 2.16 and consists of the electrolytic polishing cell and a separate power control. A twin-jet electropolishing apparatus can be used to pump a jet of electrolyte onto both sides of the disk. A schematic of a twin-jet electropolishing system is shown in Figure 2.17.

The electrolyte solution used in this process contained 15% perchloric acid and 85% methanol. Since the electropolishing is most effective at temperatures from -35°C to -40°C, thus polishing cell was filled with dry ice. The final thinning process was complete when a perforation occurred with tiny hole in the specimen. The samples were rinsed in methanol to protect them from more chemical reaction and oxidization. The regions around the hole are usually electron transparent and the best TEM micrographs can be obtained from these regions.



Figure 2.14 The BUEHLER Low speed diamond saw



Figure 2.15 The 3mm diameter disk puncher for TEM specimen



(a) Power control



(b) The electrolytic polishing cell

Figure 2.16 The FISCHIONE twin jet electropolisher

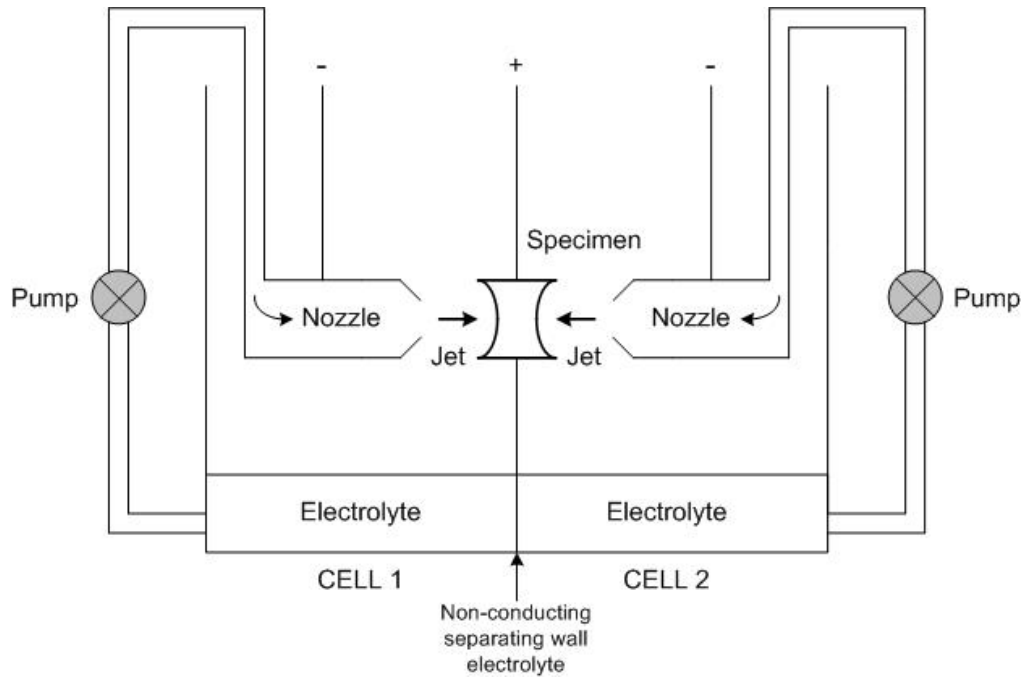


Figure 2.17 Schematic of a twin-jet polishing apparatus

CHAPTER 3 Experimental Results and Discussions

3.1 Fatigue Response of the Welded Specimens

Four socket welded stainless steel pipes were subjected to 5, 20, 100, and 2679 cycles of fatigue loading using the cantilever setup described earlier in Chapter 2. Fatigue tests were performed by prescribing 10 mm displacement-control cycles.

3.1.1 Displacement-controlled Fatigue Tests

In Fig. 3.1, the recorded load-displacement response of the socket welded specimen at the loading end is shown. The inelastic response of the pipe to the applied loading is reflected by the hysteresis loops that characterize the load-displacement response. Figure 3.2 exhibits the load response indicating hardening upto 20 fatigue cycles followed by cyclic softening through 2679 cycles. This softening is shown as decreased amplitude of the load response with cycles. This result is interesting because 304L stainless steel is known to be a cyclic hardening material. The softening seems to be occurring at the structural level of the material and the reasons for this cyclic softening response in the test will be investigated in the dislocation microstructures following fatigue.

Strain responses at the location 3mm from the weld toe of each pipe specimen are shown in Figures 3.3-3.6. Axial and hoop strain ratcheting were not observed in the 5, 20, and 100 fatigue cycle tests. However, positive axial ratcheting was observed at the location 3mm away from the weld toe in 2679 fatigue cycle test. In addition to this observation, positive ratcheting of the hoop strain was also noted. The strain amplitude in the axial direction seems to be higher than that in the hoop direction, albeit it is not clearly proven to-date. We hope to figure out by microstructure investigation which strain ratcheting

predominantly affects fatigue failure in welded pipes.

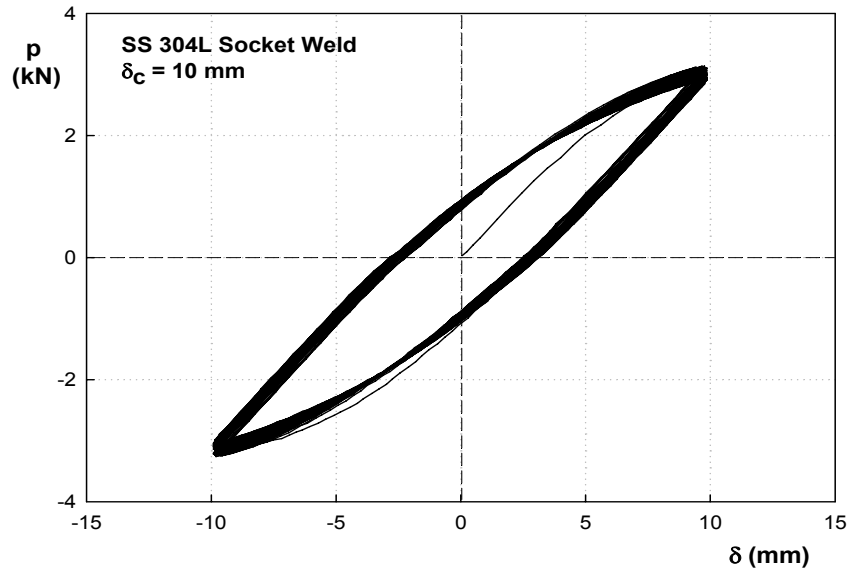


Figure 3.1 Force (p)-Displacement (δ) response of Socket welded pipe fatigue test

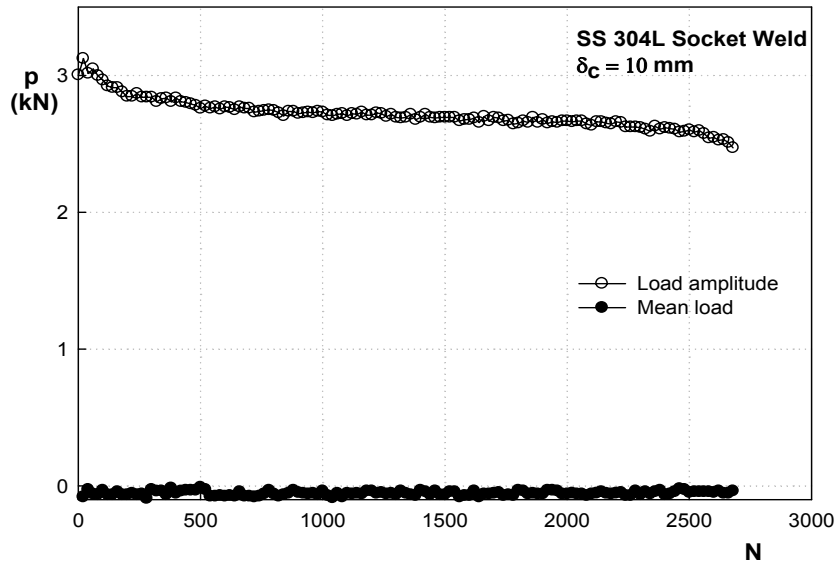


Figure 3.2 Load responses (p) as a function of cycles (N) for displacement controlled test of welded pipe (Specimen failed at 2679 cycles)

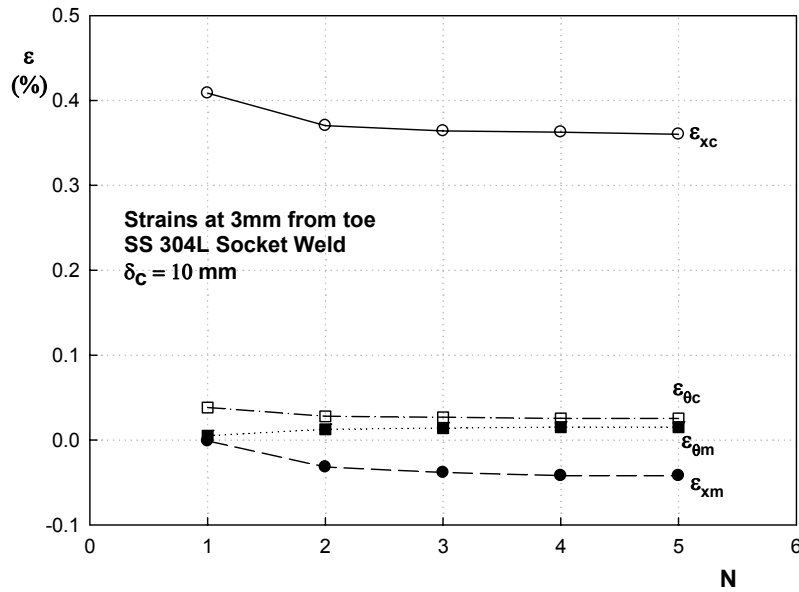


Figure 3.3 Axial (ϵ_x) and hoop (ϵ_θ) strain responses for displacement controlled test of welded pipe with 5 cycles

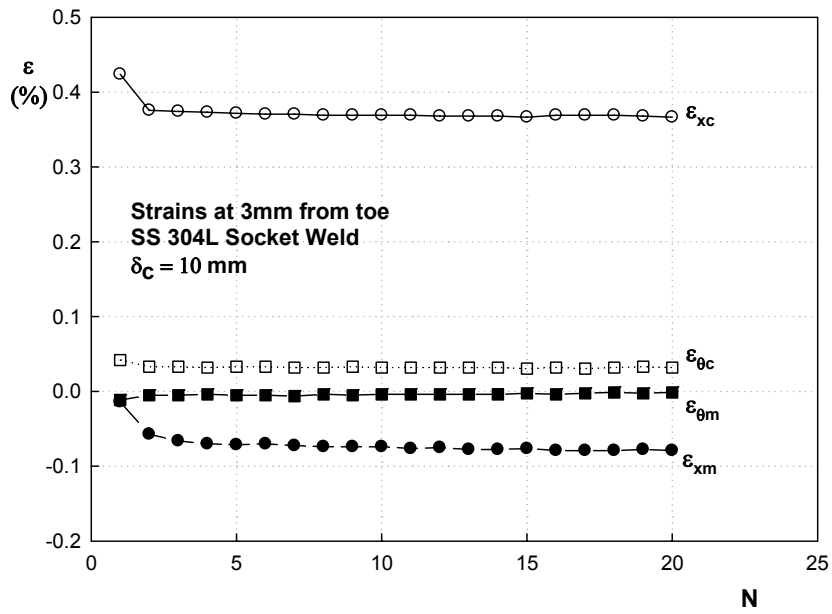


Figure 3.4 Axial (ϵ_x) and hoop (ϵ_θ) strain responses for displacement controlled test of welded pipe with 20 cycles

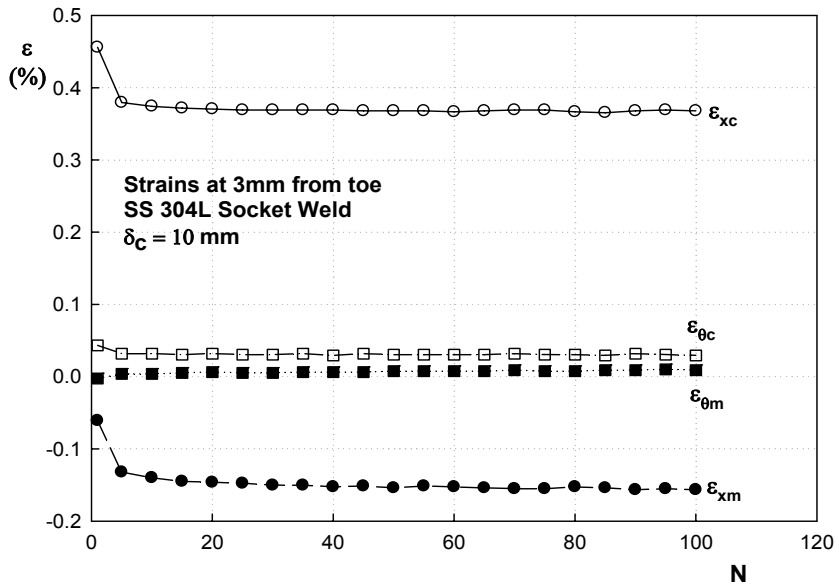


Figure 3.5 Axial (ϵ_x) and hoop (ϵ_θ) strain responses for displacement controlled test of welded pipe with 100 cycles

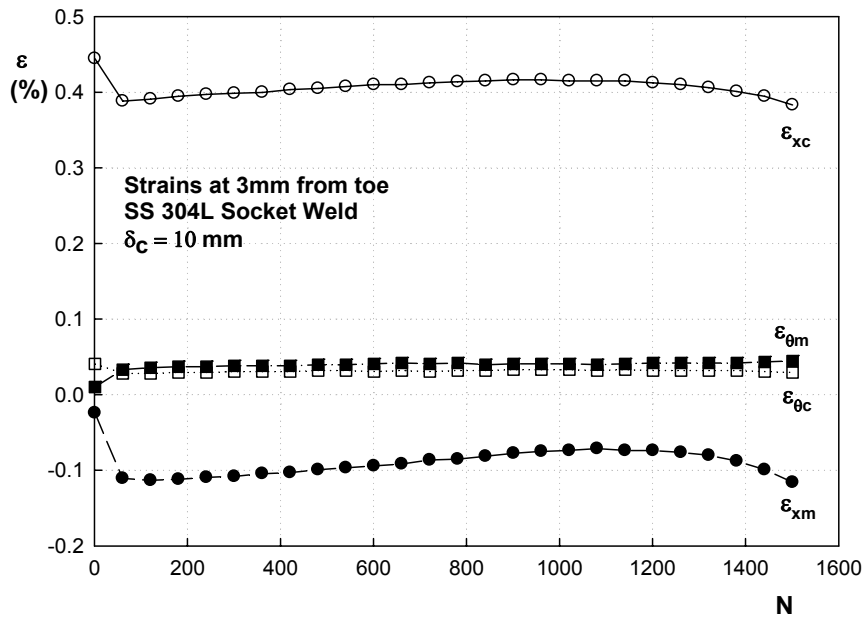


Figure 3.6 Axial (ϵ_x) and hoop (ϵ_θ) strain responses for displacement controlled test of welded pipe with 2679 cycles

3.2 Fatigue Response of the Coupon Specimens

Various fatigue tests of the tubular specimens were carried out in an attempt to simulate the fatigue of weld toe of welded piping specimens. The fatigue response data was recorded from uniaxial strain controlled, biaxial ratcheting, and uniaxial forced-controlled cyclic tests in order to understand how cyclic loading induces ratcheting failure at the weld toe.

3.2.1 Uniaxial Strain-Controlled Fatigue Tests

Uniaxial strain controlled fatigue tests were performed on coupon specimens following varied heat-treatments. Specimens following various numbers of fatigue cycles were considered for microstructural studies using TEM. 1% strain amplitude was used for these uniaxial strain cycling tests, and Figures 3.7, 3.9, and 3.11 exhibit the typical stress-strain responses of uniaxial strain controlled tests for specimens heat-treated at different temperatures. No crack initiation was observed in these fatigue tests.

The amplitude and stress responses as a function of cycles for uniaxial strain controlled tests are shown in Figures 3.8, 3.10, and 3.12. It can be concluded that the stress response is symmetric with mean stress being almost zero. The stress amplitude indicates that the cyclic softening and hardening features of 304L stainless steel coupons depend on applied fatigue cycles. The state of cyclic hardening is followed by a state of cyclic softening, and then the saturation of cyclic hardening state is observed. When the number of fatigue cycles is relatively low such as 5 cycles, the specimen initially presents cyclic hardening feature, but after about 20 cycles cyclic softening occurs and finally a stable state (saturation) is reached. The maximum peak stresses corresponding to 5, 20, and 100 cycles for different heat-treated

temperature are included in Table 3.1. The value of responded stress amplitudes decreases with increase of heat-treatment temperature, even though each stress response shows similar cyclic softening and hardening features.

The experimental results of the axial strain amplitude and a mean of strain with various heat-treatment temperatures show constant value of 1% amplitude and zero mean strain for every test. It can be explained that the axial strain amplitude and a mean of strain response do not influence the cyclic softening and hardening features.

Table 3.1 The maximum peak stress of uniaxial strain controlled test

Temperature \ Cycles	5 cycles	20 cycles	100 cycles
Unconditioned	379MPa	409MPa	444MPa
800C	361MPa	367MPa	396MPa
1050C	339MPa	324MPa	350MPa

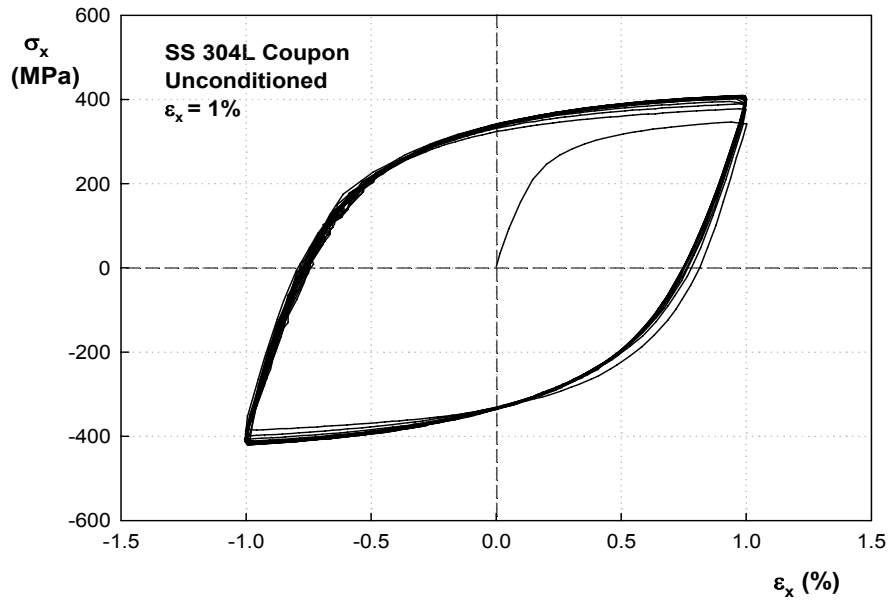


Figure 3.7 Stress (σ_x)-Strain (ϵ_x) response of Uniaxial strain controlled test with unconditioned coupons for 20 cycles

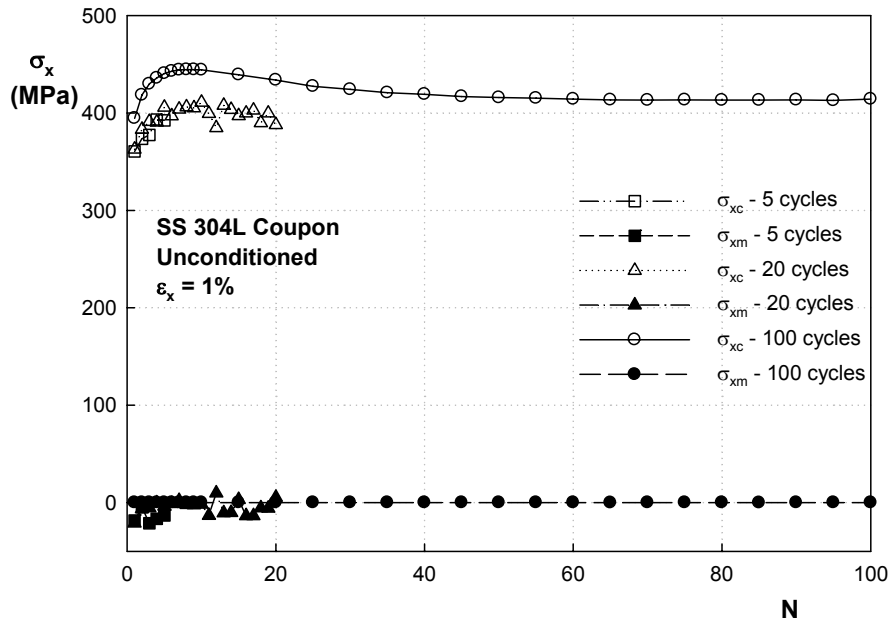


Figure 3.8 Amplitude (σ_{xc}) and mean (σ_{xm}) of stress responses from Uniaxial strain-controlled test on unconditioned coupons for 5, 20, and 100 cycles

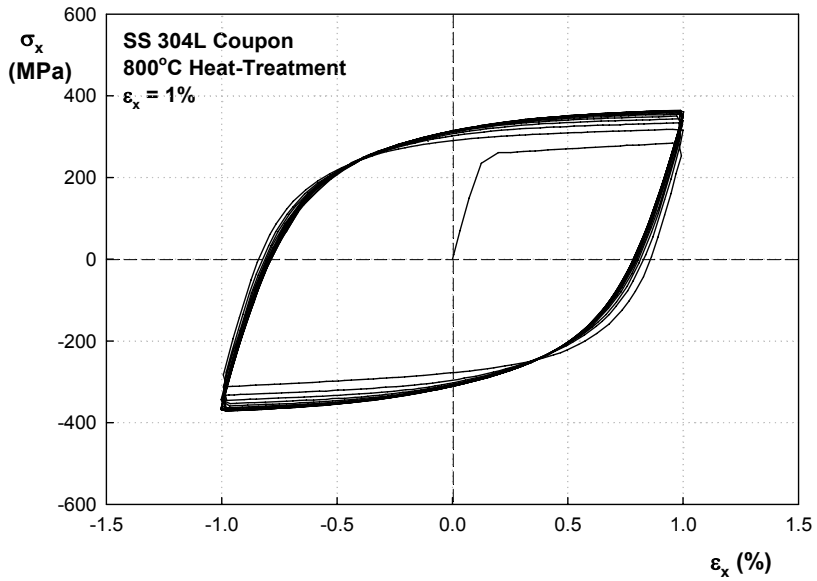


Figure 3.9 Stress (σ_x)-Strain (ϵ_x) response of Uniaxial strain controlled test with 800°C heat-treated coupons for 20 cycles

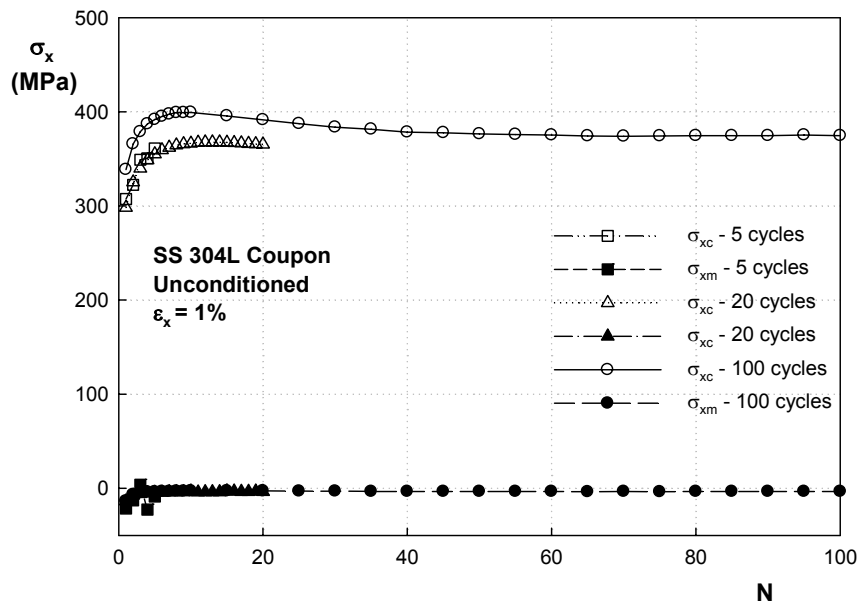


Figure 3.10 Amplitude (σ_{xc}) and mean (σ_{xm}) of stress responses from Uniaxial strain-controlled test on 800°C heat-treated coupons for 5, 20, and 100 cycles

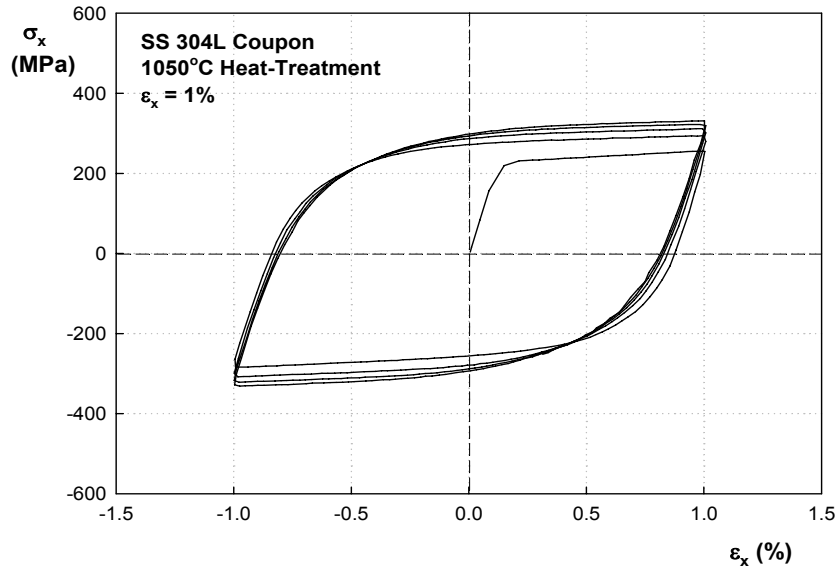


Figure 3.11 Stress (σ_x)-Strain (ϵ_x) response of Uniaxial strain controlled test with 1050°C heat-treated coupons for 5 cycles

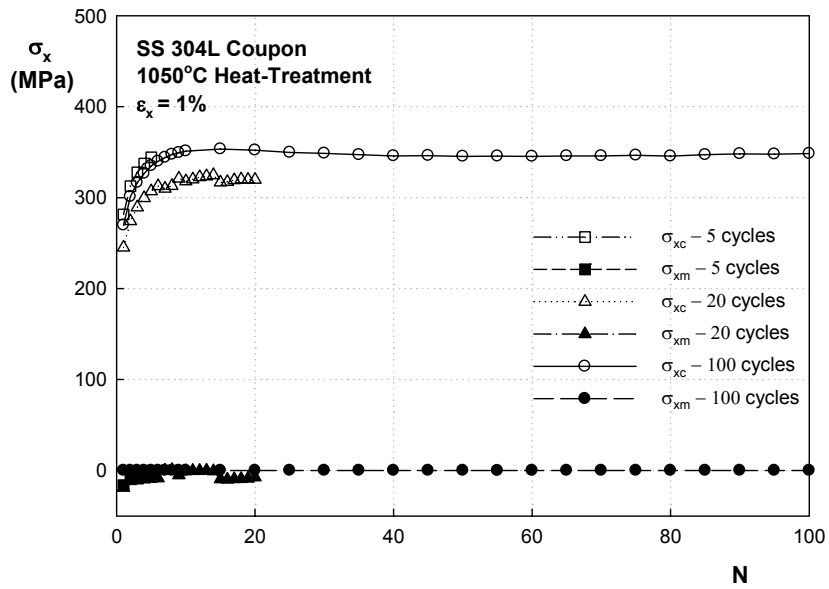
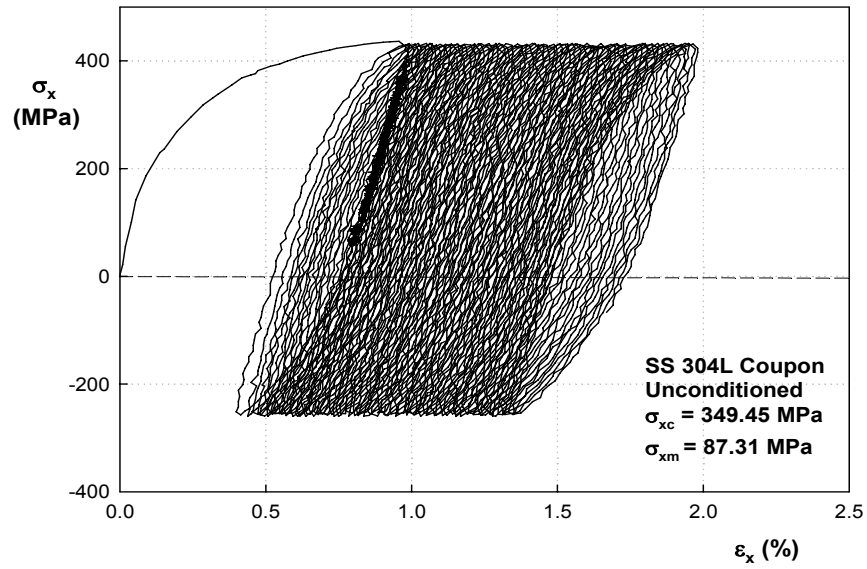


Figure 3.12 Amplitude (σ_{xc}) and mean (σ_{xm}) of stress responses from Uniaxial strain-controlled test on 1050°C heat-treated coupons for 5, 20, and 100 cycles

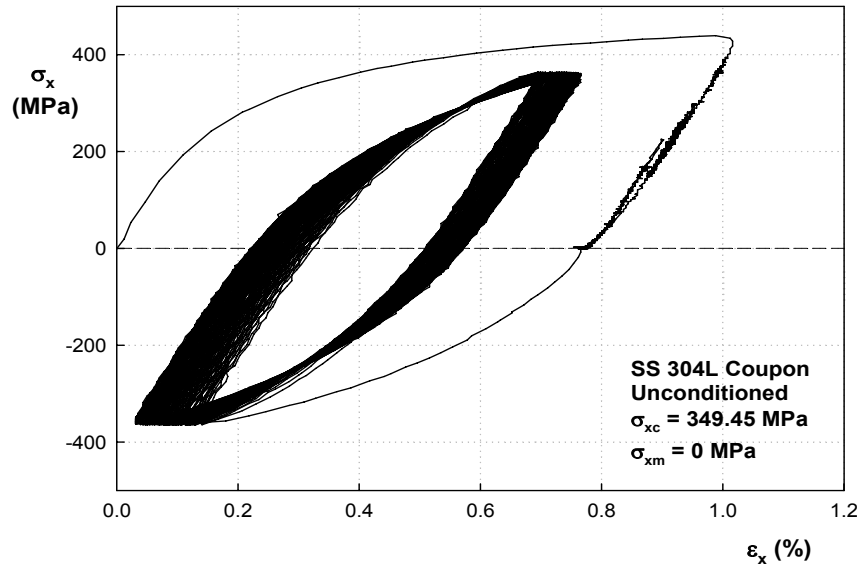
3.2.2 Uniaxial Force-Controlled Fatigue Tests

The fatigue testing of uniaxial force controlled specimen was performed with different mean stresses. The specimen was subjected to zero mean stress for no ratcheting test and positive mean stress for ratcheting test. It is shown in the Figure 3.13 (b) that no ratcheting occurs in the case of zero mean stress. However, unsymmetrical applied stress and positive mean stress causes considerable ratcheting. This results in axial strain ratcheting as depicted in Figure 3.13 (a) that hysteresis loop moves to axial strain direction. Uniaxial ratcheting in the axial direction is induced by positive mean stress in the prescribed stress cycle.

The amplitude and mean response at every 10th cycle of axial strain is shown in Figure 3.14. This figure clearly shows that mean strain increases with number of cycles only in ratcheting tests. Increasing mean strain with number of cycles is evidence of positive axial strain ratcheting. Comparison of ratcheting and no ratcheting strain response demonstrates that positive mean stress induces greater mean strain than zero mean stress.



(a)



(b)

Figure 3.13 Stress (σ_x)-Strain (ϵ_x) response of uniaxial force-controlled test with (a) positive mean stress (70cycles) and (b) zero mean stress (70 cycles)

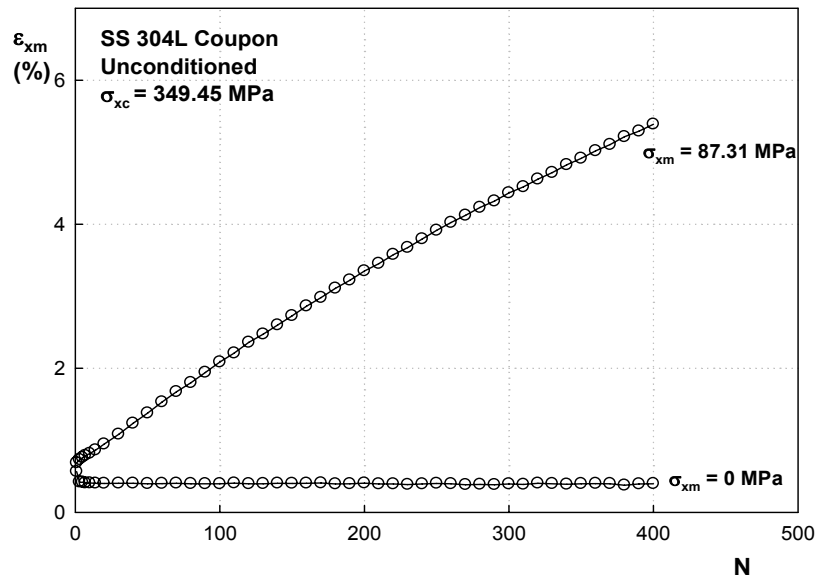


Figure 3.14 Mean of axial strain (ϵ_{xm}) responses as a function of cycles for Uniaxial force controlled test

3.2.3 Biaxial Ratchetting Fatigue Tests

The fatigue testing of biaxial ratchetting specimen was performed following different heat-treatment temperatures and the prescribed loading was 0.4% axial strain range superimposed with 1ksi internal pressure for steady hoop stress. Figure 3.15 represents stress-strain response for biaxial ratchetting test on non-heat treated (as received) specimen. Axial strain range is from -0.4% to 0.4% and stress is symmetric.

The axial-hoop strain response of unconditioned specimen is shown in Figure 3.16. It is indicated from this results that the axial strain response is reversible. However, it is also observed that significant ratchetting in the hoop direction resulted from the steady stress caused by internal pressure. As the heat-treatment temperature increases, more ratchetting occurred in the hoop direction meaning that heat treatment influences in promoting ratchetting

phenomenon.

The amplitude and mean strain responses at every 20th cycle of hoop strain is shown in Figure 3.17. The strain amplitude in the hoop direction continued almost constant as the number of fatigue cycles increased. Mean strain, however, increased with cycles, which implies that hoop strain ratcheted in the positive direction. It is demonstrated from these responses that not only mean of hoop strain increases with loading cycles, but also mean strain value at higher heat-treatment temperature is larger than that at the relatively lower annealing temperature. This result might be related to the effect of heat-treatment on the ratcheting failure inducing fatigue crack initiation.

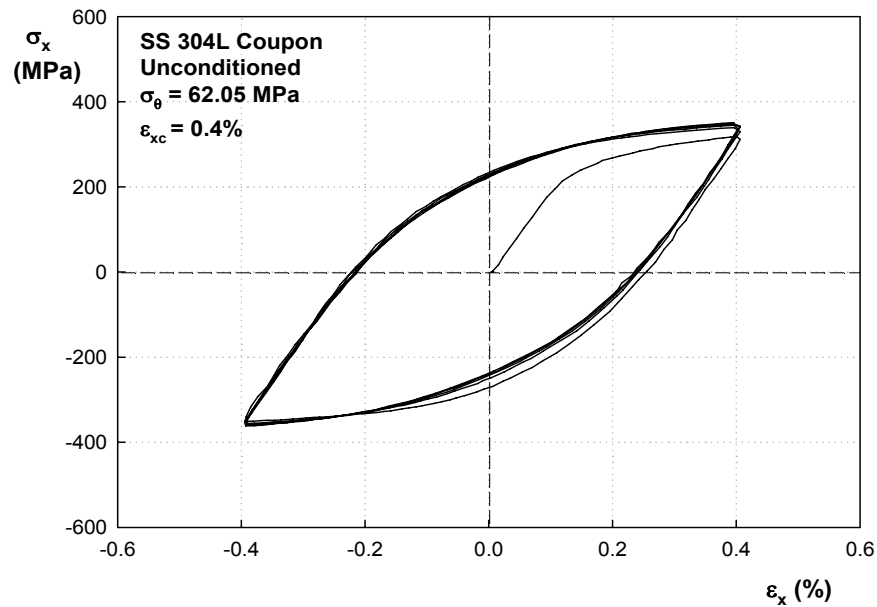


Figure 3.15 Stress (σ_x)-Strain (ϵ_x) response of biaxial ratcheting test with unconditioned temperature

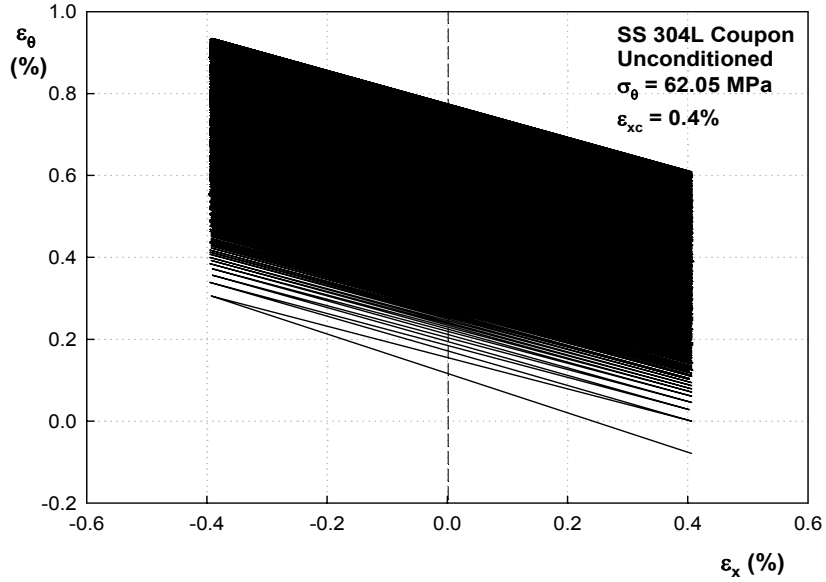


Figure 3.16 Axial (ϵ_x) and hoop (ϵ_θ) strain response of biaxial ratcheting test with unconditioned temperature

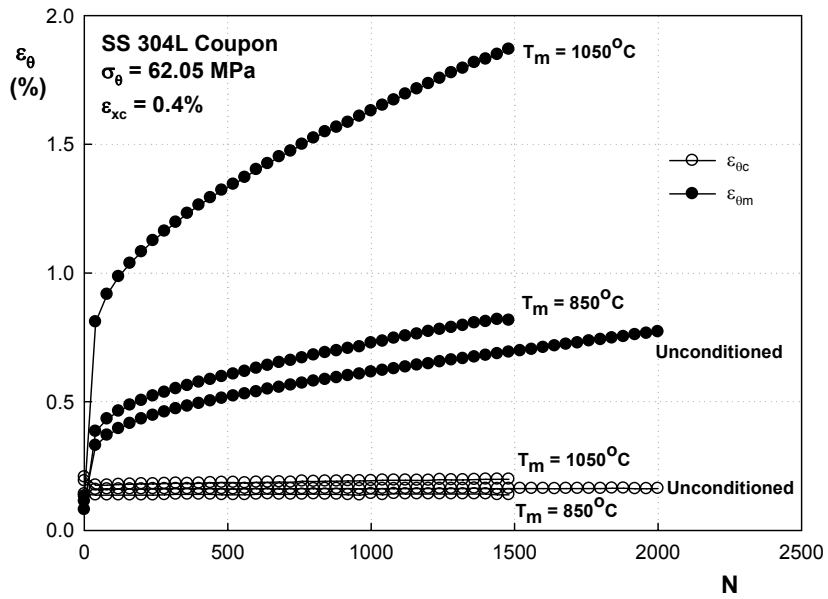


Figure 3.17 Amplitude ($\epsilon_{\theta c}$) and mean ($\epsilon_{\theta m}$) of hoop strain response as a function of cycles for biaxial ratcheting test

3.3 Optical Metallography

3.3.1 Metallographic Observation of Coupon

Optical metallographs were obtained from each coupon specimen that was subjected to different heat-treatment temperatures and fatigue cycles. The optical images at 10kX magnification of materials from coupons subjected to uniaxial strain-controlled and biaxial ratcheting loading cycles are presented in Table 3.2. Distinct increase in grain size is noted (Table 3.2) following higher temperature heat-treatment. For the 800°C there is no remarkable grain size increase compare to the unconditioned coupon, but for 1050°C grain size enlargement is clearly observed. Mean grain size becomes larger at the higher heat-treatment temperature because of the higher energy input (grain growth). The result of grain size and ASTM grain size number measurement is shown in Table 3.3. The grain size range is 28 - 38 μm for unconditioned specimen, 28 - 41 μm for 800°C, and 49 - 64 μm for 1050°C. The influence of heat-treatment temperature on the grain size is illustrated in Figure 3.18 before and after fatigue, while similar results are included in Figure 3.19 following large number (>1400) of biaxial fatigue cycles. These results indicate that grain size is mainly affected by the annealing temperature with minimal effect by the fatigue loading considered in this study.

Table 3.2 Optical microscopy of coupons at different heat-treated temperatures and loading cycles (10kX magnification)

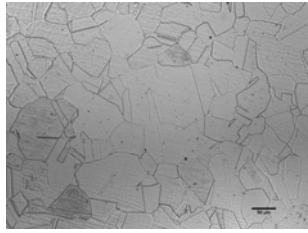
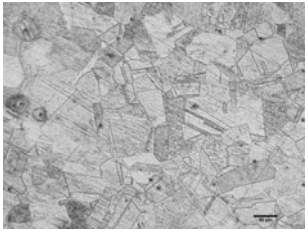
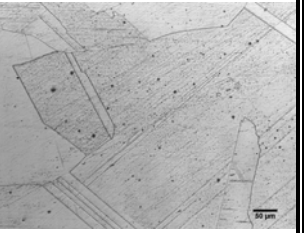
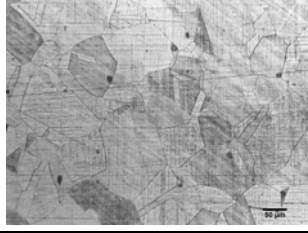
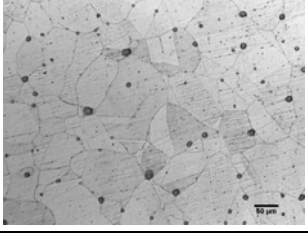
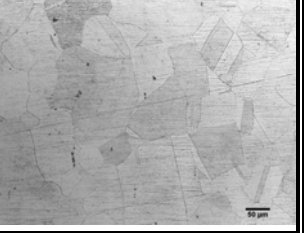
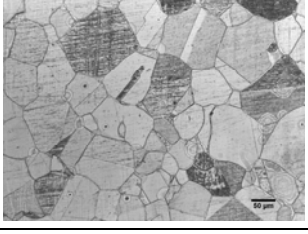
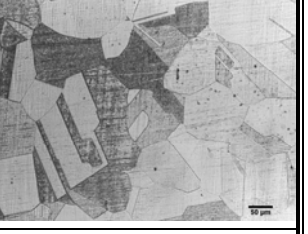
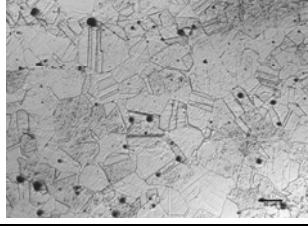
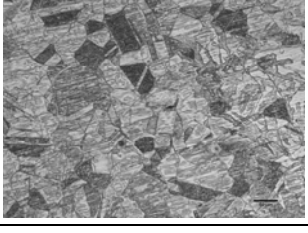
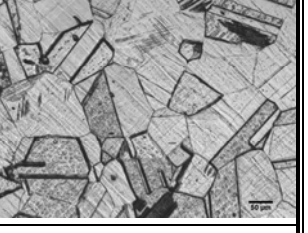
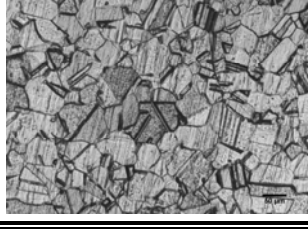
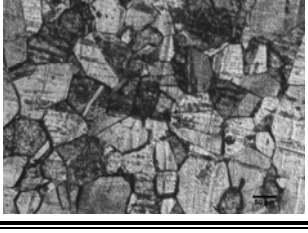
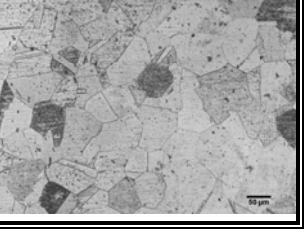
Specimen	Unconditioned	800°C	1050°C
Before fatigue (0 cycles) 50 μm			
Uniaxial strain controlled (5 cycles) 50 μm			
Uniaxial strain controlled (20 cycles) 50 μm			
Uniaxial strain controlled (100 cycles) 50 μm			
Biaxial ratcheting (2000 cycles) 50 μm			

Table 3.3 Grain size of coupons in different heat-treated temperature

Specimen		Unconditioned		800°C		1050°C	
Type	Cycles	Grain size (μm)	ASTM	Grain size (μm)	ASTM	Grain size (μm)	ASTM
Uniaxial strain-controlled	0	28.89 \pm 4.21	6.9	28.68 \pm 5.35	7	64.37 \pm 12.23	4.6
	5	38.14 \pm 8.19	6.2	41.64 \pm 5.18	5.9	52.07 \pm 6.81	5.2
	20	34.35 \pm 3.08	6.4	38.89 \pm 8.51	6.1	49.28 \pm 14.86	5.4
	100	28.13 \pm 6.18	7.2	28.34 \pm 3.47	7	56.89 \pm 14.98	5
Biaxial ratchetting	2000	28.20 \pm 5.44	7	32.93 \pm 6.61	6.6	49.04 \pm 5.77	5

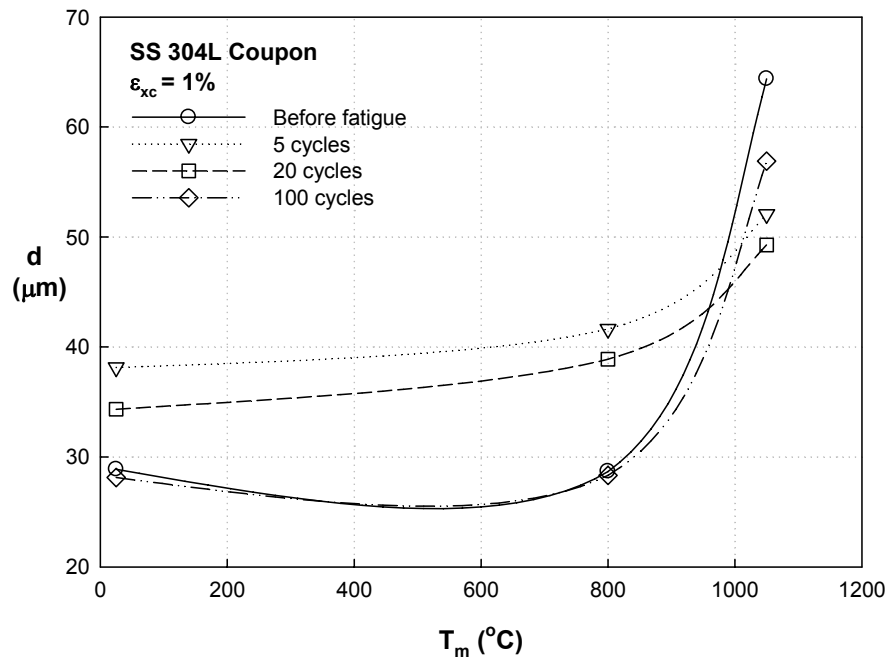


Figure 3.18 Grain size (d) versus heat-treatment temperature (T_m) of uniaxial strain controlled coupons

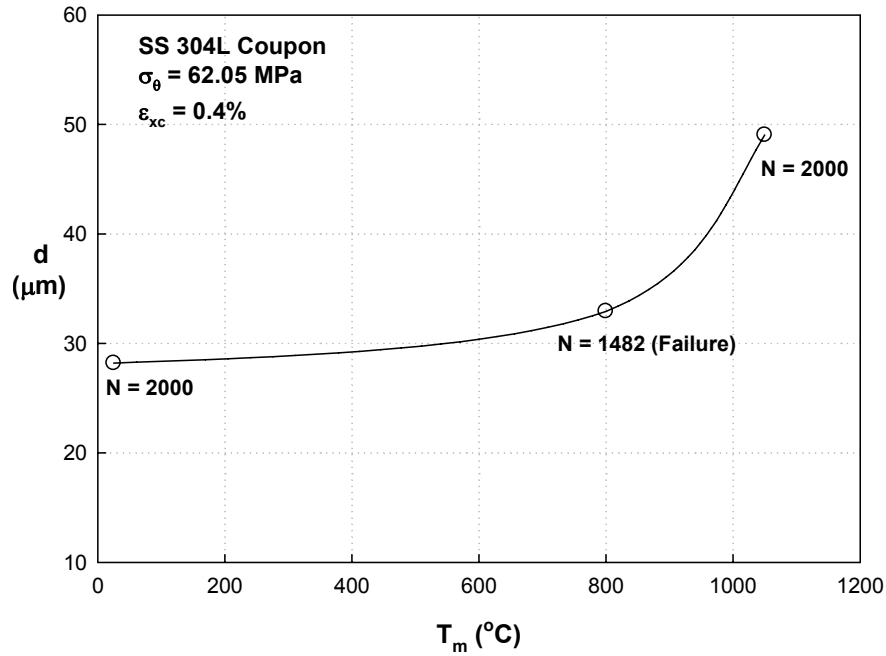


Figure 3.19 Grain size (d) versus heat-treatment temperature (T_m) of biaxial ratcheting coupons

3.3.2 Metallographic Observations of Welded Pipe

As shown in Figure 3.20, metallographs were taken at 3mm location away from the weld toe and on the top of the pipe after various fatigue loading cycles (5, 20, 100, and 2679 cycles) of the socket-welded specimen. Moreover, same metallographs at 9.8mm and 38mm location away from the weld toe and on the top of the pipe for 20 cycles tested specimen were also taken to represent the change in structure with respect to distance from the weld toe.

Microstructures at 10kX magnitude and grain size of welded pipe following different cyclic loadings are shown in Table 3.4 and 3.5. No microstructure change is visible in the welded pipe specimen. As shown in Figure 3.21, grain size is also not changed with respect to distance from the weld toe, even though location 3mm is the closest to the weld toe. It can

be concluded that the welding process does not affect directly the grain size near the weld toe.

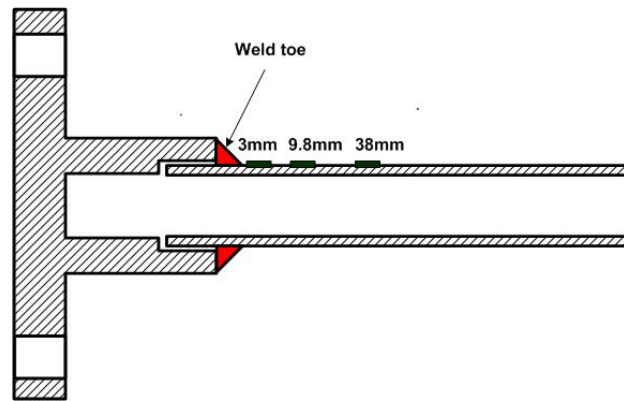


Figure 3.20 Illustration of different locations of socket welded specimen taken for metallographs

Table 3.4 Optical microscopy of welded pipe specimen (10kX magnitude)

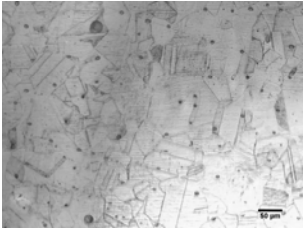
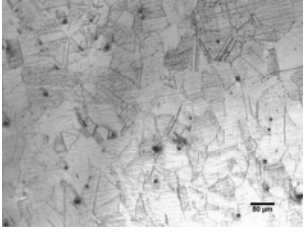
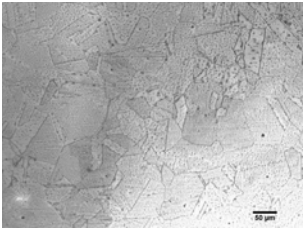
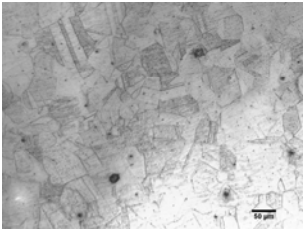
Specimen	3mm	9.8mm	38mm
SSPC4 (5 cycles) 50 μm			
SSPC2 (20 cycles) 50 μm			
SSPC3 (100 cycles) 50 μm			
SSPC5 (2679 cycles) 50 μm			

Table 3.5 Grain size of welded pipe specimen

Specimen	Cycles	3mm		9.8mm		38mm	
		Grain size (μm)	ASTM	Grain size (μm)	ASTM	Grain size (μm)	ASTM
SSPC4	5	21.09±1.88	7.8				
SSPC2	20	23.12±2.02	7.6	23.87±3.3	7.5	24.81±5.4	7.4
SSPC3	100	24.69±1.28	7.4				
SSPC5	2679	20.55±0.43	7.9				

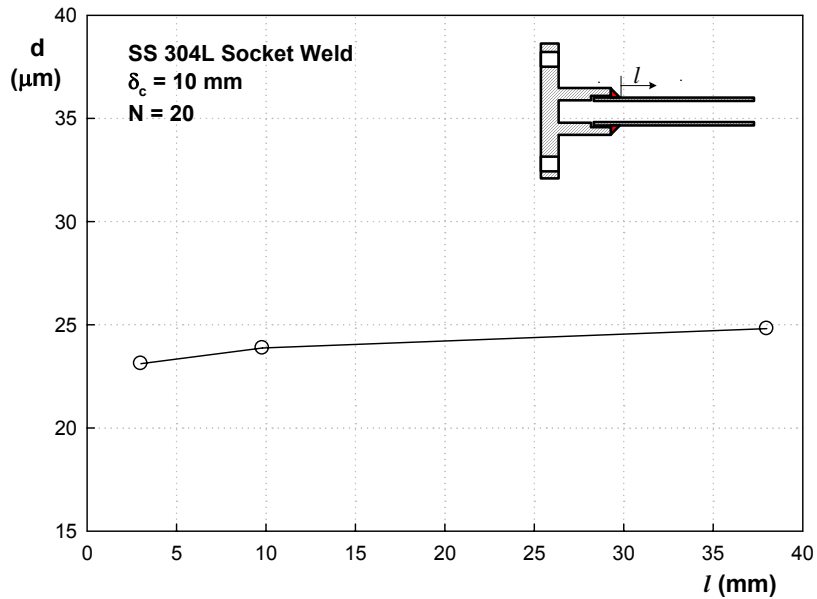


Figure 3.21 Grain size (d) at different location (l) from the weld toe of the welded pipe after 20 displacement-controlled cycles of 10mm amplitude

3.4 Microhardness

3.4.1 Hardness Measurement

The microhardness measurement were made on the coupon specimens and welded pipe specimens to study the effect of the number of fatigue cycles and heat-treatment temperature on the material strength. As previously illustrated, coupon and welded pipe specimens were sectioned into axial and hoop orientation that are the same directions corresponding to TEM specimens. Each specimen was examined on the Vickers hardness test machine, and Vickers hardness number was recorded from several locations in each sample. Average values of hardness number are shown in Tables 3.6 and 3.7 for coupon and weld

pipe specimens respectively.

Table 3.6 VHN of coupon specimens

Specimen	Cycles	Unconditioned	800°C	1050°C
Uniaxial strain controlled	0	157±3.2	161±7.1	161±7
	5	193±9.6	196±7.7	197±9.3
	20	211±8.9	211±9.7	199±6.8
	100	219±4.6	219±9.2	216±10.3
Biaxial ratchetting	2000	201±2.8	205±5.5	211±2.6

Table 3.7 VHN of welded pipe specimens

Specimen	Number of cycles	3mm away from weld toe	9.8mm away from weld toe	38mm away from weld toe
SSPC4	5	204±5.7		
SSPC2	20	198±7.9	187±12.6	187±13.3
SSPC3	100	193±8.6		
SSPC5	2679	208±11.9		

The effect of fatigue cycles and heat-treating temperature for coupon specimens was illustrated in Figures 3.22 and 3.23. In the case of welded pipe specimens, hardness number as a function of cycles and different distance from the weld toe was demonstrated in Figure 3.24.

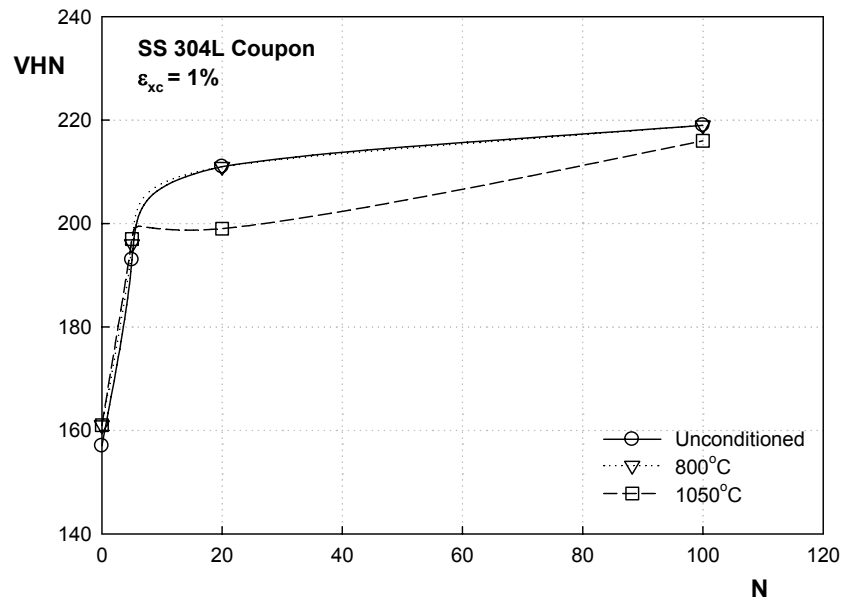
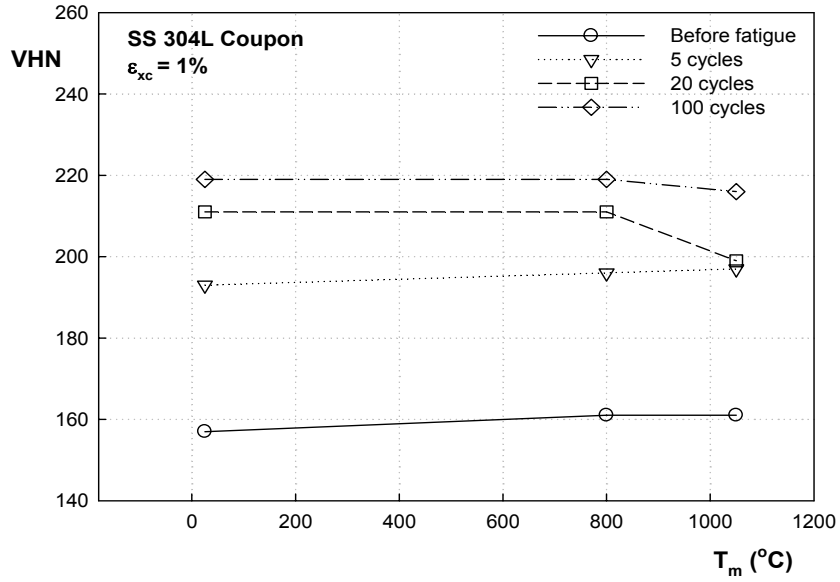
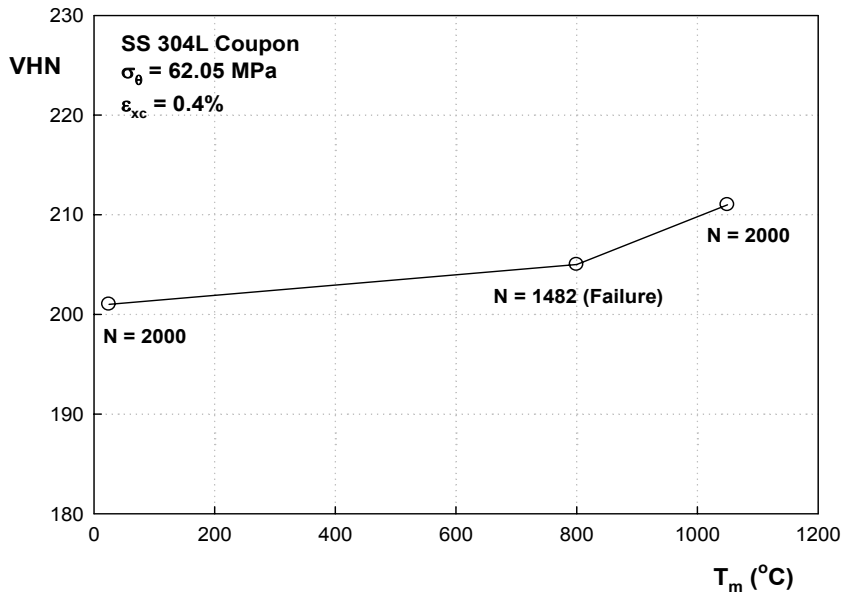


Figure 3.22 VHN vs. Number of cycles (N) of different heat-treated coupons subjected to uniaxial strain-controlled

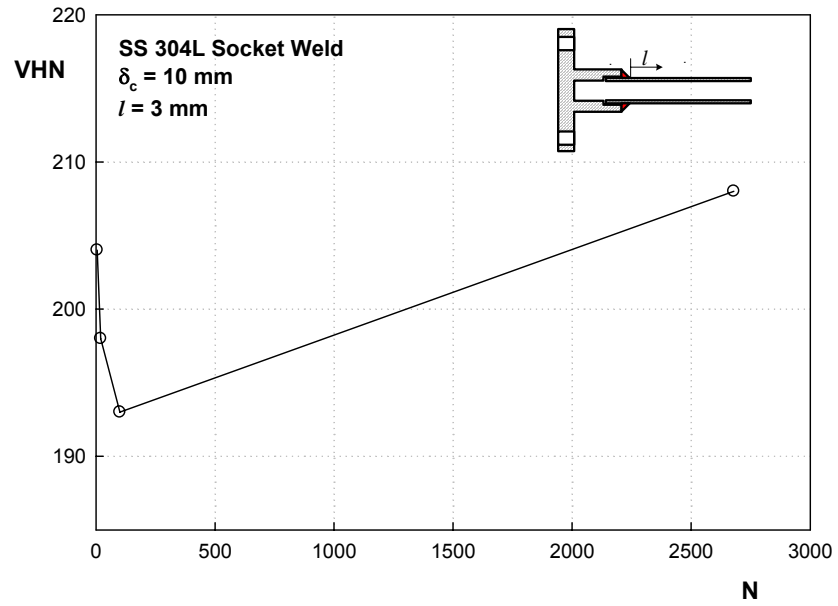


(a)

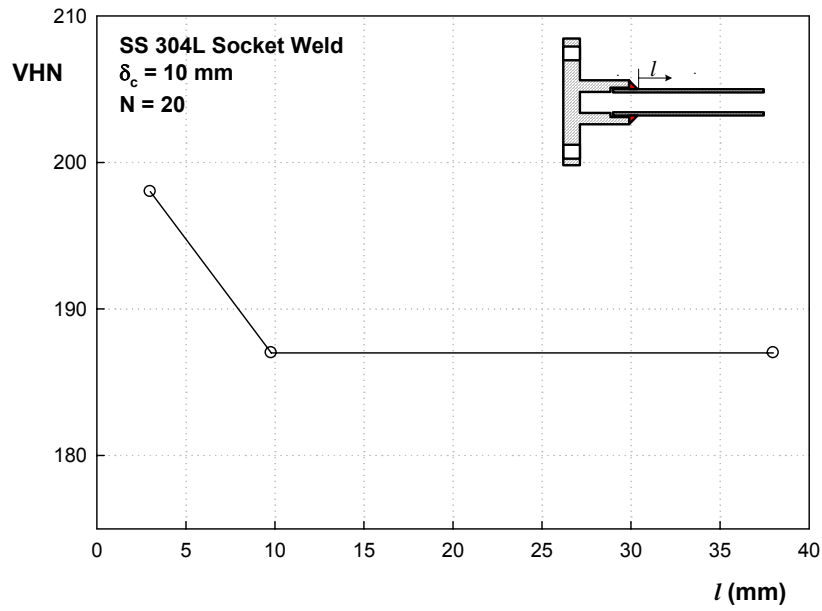


(b)

Figure 3.23 VHN vs. Heat-treatment temperature (T_m) of coupons subjected to (a) uniaxial strain-controlled cycles and (b) biaxial ratcheting cycles



(a)



(b)

Figure 3.24 VHN as a function of (a) number of cycles (N) and (b) different distance (l) from weld toe of socket welded pipe

All coupon specimens show increasing hardness as the number of cycle increases while the heat-treating temperature has negligible effect. This indicates hardening or strengthening with the number of fatigue cycles and is reflected in the increase of maximum peak stress as fatigue cycles increase (Table 3.1). However, heat-treating temperature has a minor effect on the strength although grain size increased slightly. In the case of welded pipe no significant difference of hardness was noted between both location and fatigue cycles.

3.5 Transmission Electron Microscopy Investigation

3.5.1 Microstructure Observation

The microstructure of 304L stainless steel specimen resulting from the various cyclic loadings discussed in Tables 2.1 and 2.2 was examined by transmission electron microscopy to study the relationship between fatigue-ratcheting response and microstructure. Diverse types of dislocation microstructures were observed such as planar dislocations, stacking faults, pile up, tangles, walls, and cells. Figure 3.25 is an example of the various types of dislocation structures under fatigue-ratcheting cycles reported by Bocher et al. (2001); planar slip for tensile loading and tangles, uncondensed cells, ladder structures, twins, cells, and walls for tensile-torsion loading. In this thesis, arrangement of each type of dislocation structure relies on the type of cyclic loading, number of cycles, and heat treatment condition of the specimen. It is assumed that TEM images taken from each specimen in this work represent entire region of each specimen. Percentage of different dislocation structures was calculated using all images in several regions taken from each specimen to investigate the characteristics of dislocation distribution for various cyclic loadings and heat-treatment

temperatures. The dislocation structures for coupon specimens and welded pipe specimens are summarized in Tables 3.12 - 3.15.

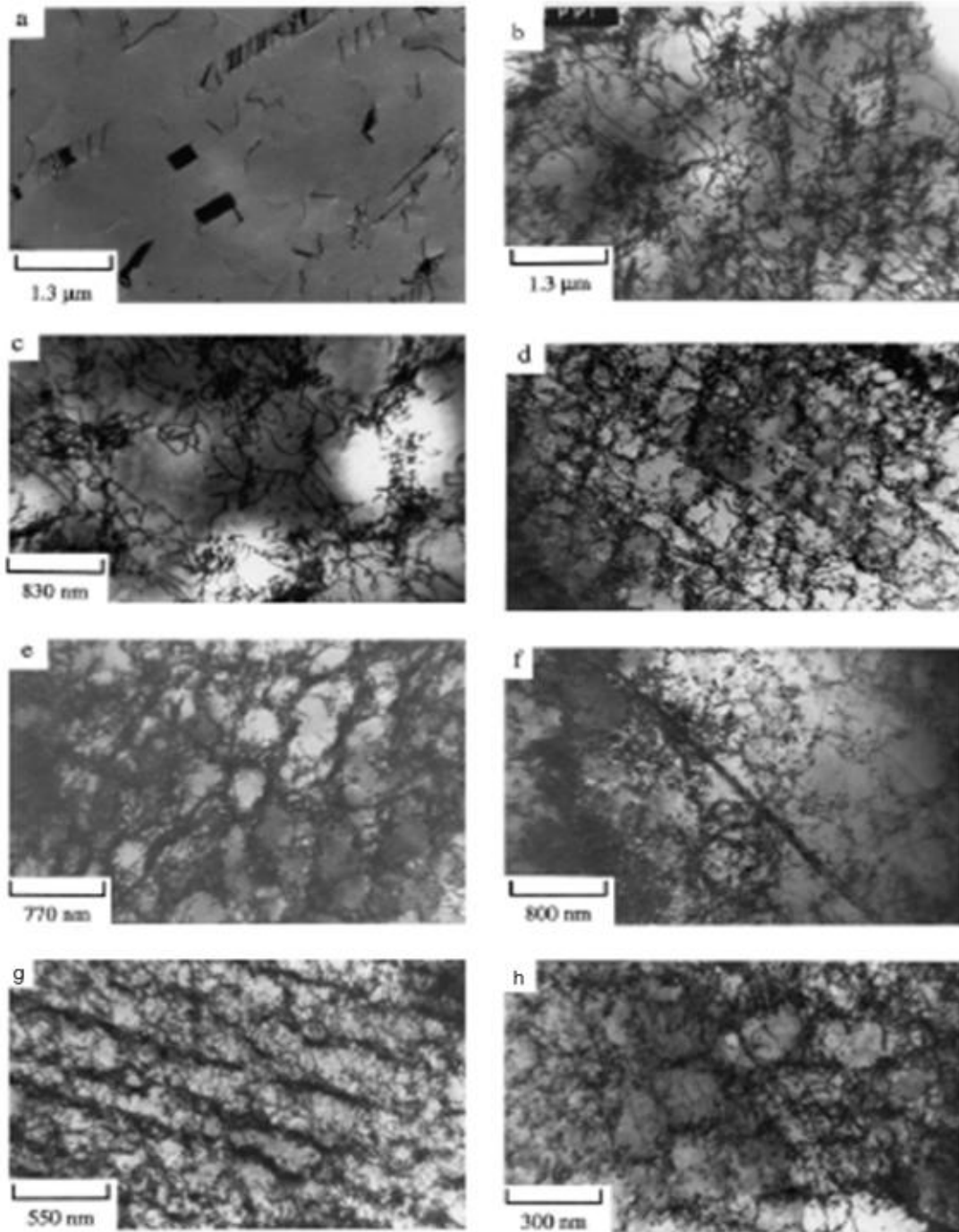


Figure 3.25 Example of the various types of dislocation structures; (a) Planar slip, (b) Tangles, (c) Uncondensed cells, (d) Ladder structure, (e) Cells, (f) Twins and cells, (g) Walls, and (h) Cells [Bocher et al. (2001)]

3.5.1.1 Dislocation Structures in Uniaxial Strain Controlled Coupons

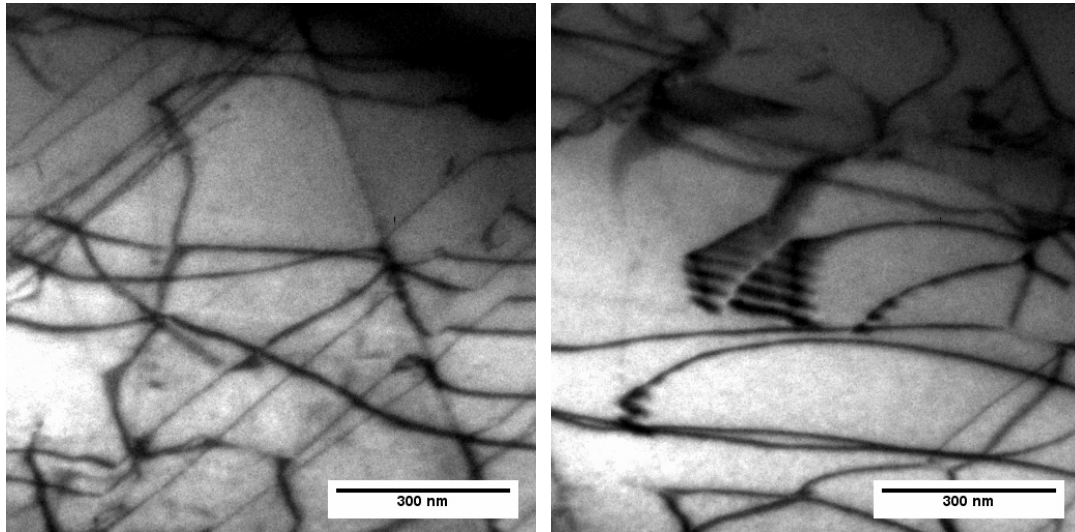
Comparison between structures after heat treatment at different temperatures reveals different microstructures. A detailed study of the evolution of structures was carried out after the coupons were subjected to strain-cycles of 1% amplitude. The specimens were fatigue tested up to 0, 5, 20, 100 number of cycles. The proportion of each structure in the specimen depended on the number of cycles for the different temperature conditions as summarized in Table 3.8.

Table 3.8 Percentage of different structures of dislocations observed in the coupon subjected to uniaxial strain-controlled cycles

Temperature	Cycle	Structures					
		Planar slip	Stacking faults	Tangles	Ladder structure	Cells	Walls
Unconditioned	0	90%	10%				
	5	17%		83%			
	20	28%		14%	14%	44%	
	100						
800°C	0	95%	5%				
	5	33%		67%			
	20	25%		56%	6%	13%	
	100					100%	
1050°C	0	89%	11%				
	5	50%	7%	14%		29%	
	20	40%		40%		20%	
	100	44%	11%	11%		34%	

First, in the case of unconditioned coupon, before fatigue planar dislocation arrays and a small portion of stacking faults are already developed as shown in Figure 3.26. The

proportion occupied by planar slip is about 90%, and no heterogeneous structure is observed in the as-received specimen.

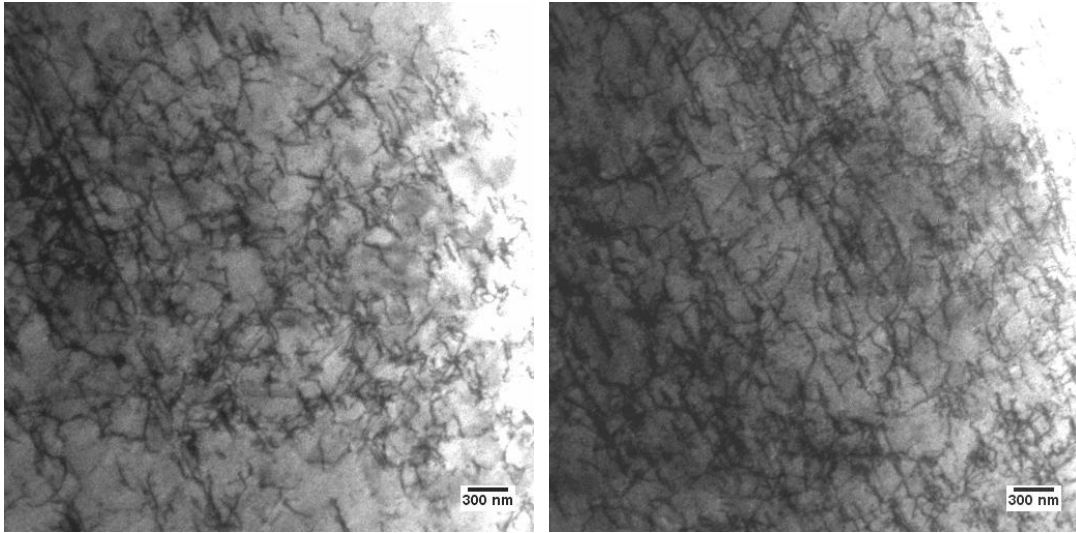


(a) Planar dislocation arrays

(b) Stacking faults

Figure 3.26 Dislocation structure of unconditioned coupon before 1% strain-controlled fatigue

Figure 3.27 shows that the dislocation structure consists of dislocation arrays and loosely tangled dislocation cells after 5 cycles. The cell walls are very thin with few dislocation loops. 304L stainless steel is an alloy with low stacking fault energy, and thus this characteristic induces structure to undergo planar slip during plastic deformation. The proportions of tangle and planar slip are 83% and 17% in volume respectively.

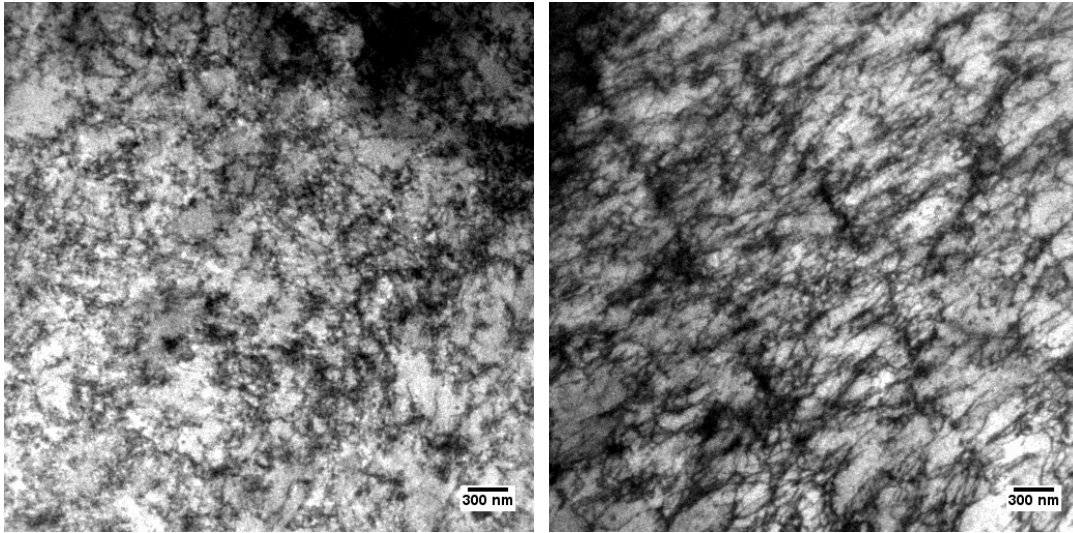


(a) Tangles

(b) Tangles

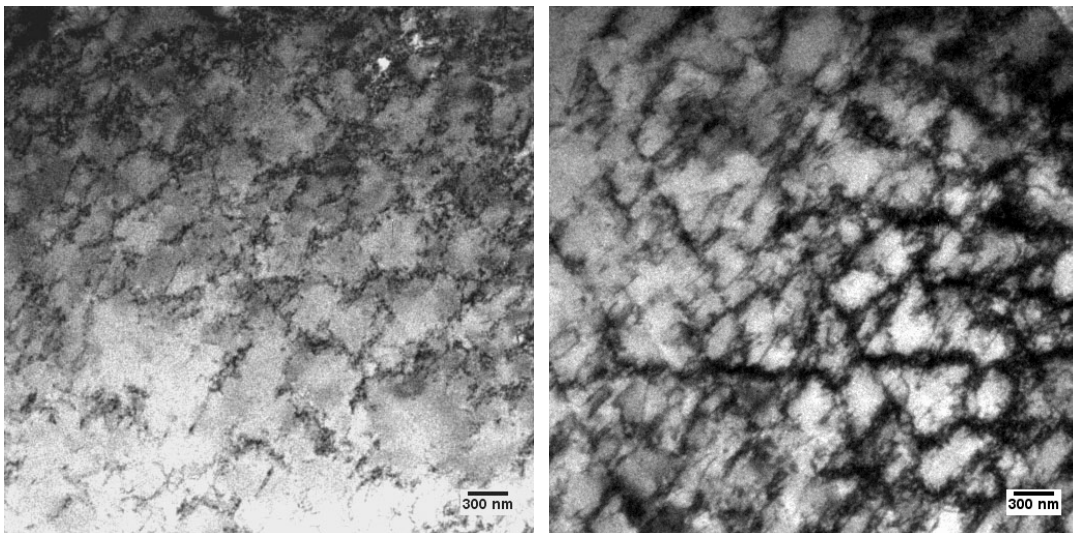
Figure 3.27 Dislocation structure of unconditioned coupon after 5 cycles

At 20 cycles, more dislocations are generated, and the dislocation cell structures are formed with more tangled dislocations present in the cell walls (Figure 3.28). The percentage occupied by cells is about 44%, but there is still ~28% of planar slip remained. Figure 3.28 (b) shows ladder structure which only covers 14% of the total region observed.



(a) Cells

(b) Ladder structure



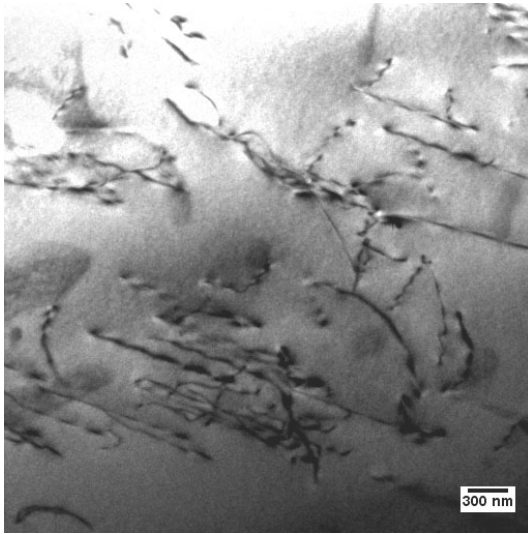
(c) Cells

(d) Cells

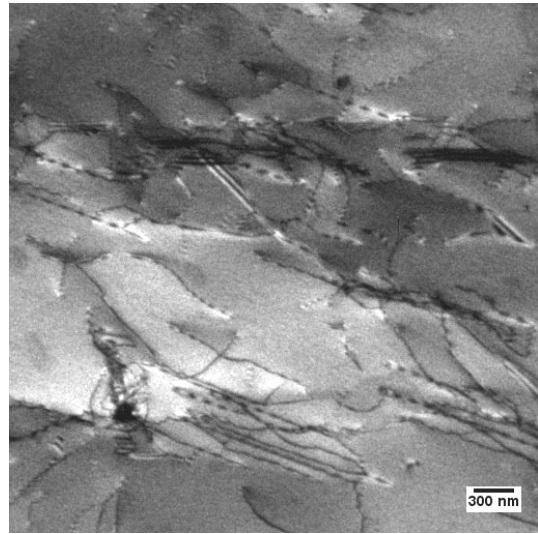
Figure 3.28 Dislocation structure of unconditioned coupon after 20 cycles

After 100 fatigue cycles, unfortunately, dislocation structures could not be observed because the TEM foil had many bend contours. For 800°C condition, dislocation structure is similar to that of unconditioned material. Figure 3.29 presents dislocation structure before

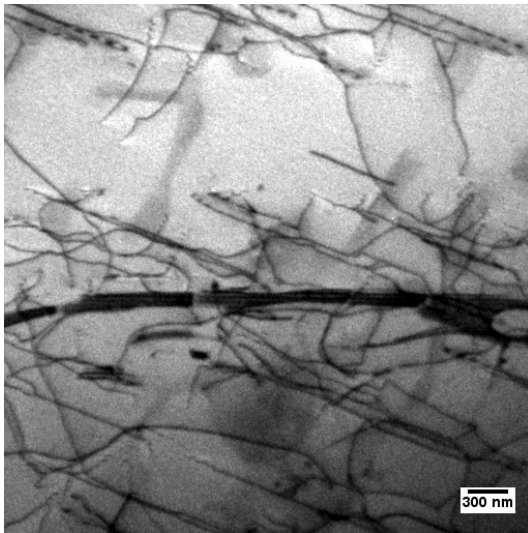
fatigue with planar dislocations occupying 95% of total area and 5% portion of stacking fault. Heterogeneous dislocation structure is also not visible without fatigue cyclic loading.



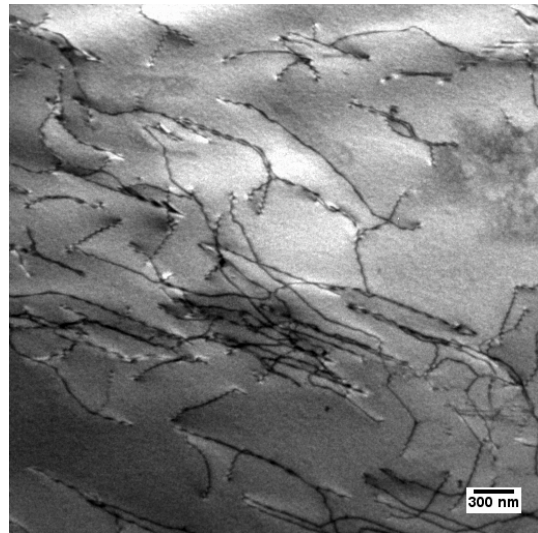
(a) Planar dislocation arrays



(b) Planar dislocation arrays



(c) Planar dislocation arrays and stacking faults

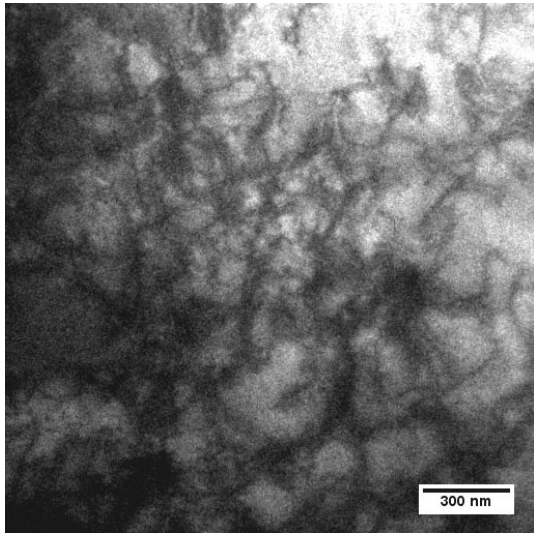


(d) Planar dislocation arrays

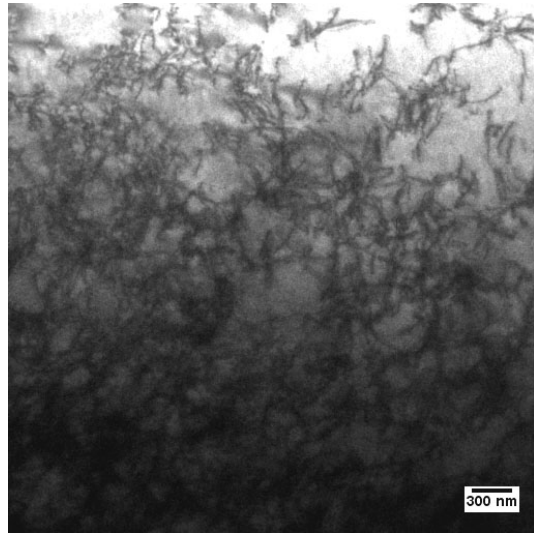
Figure 3.29 Dislocation structure of 800°C heat-treated coupon before 1% strain-controlled fatigue

After 5 cycles, dislocation tangle structures are predominant and about 33% of total

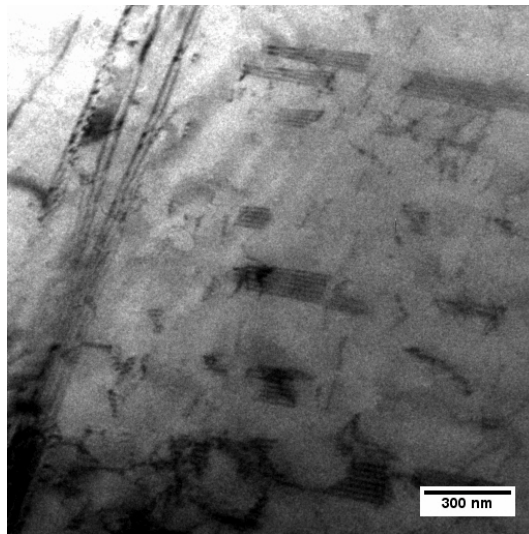
portion is covered with planar slip as shown in Figure 3.30. Comparing to 5 cycle test of unconditioned material, the structure shows that smaller portion of tangle structures and larger portion of planar slip are formed.



(a) Tangles



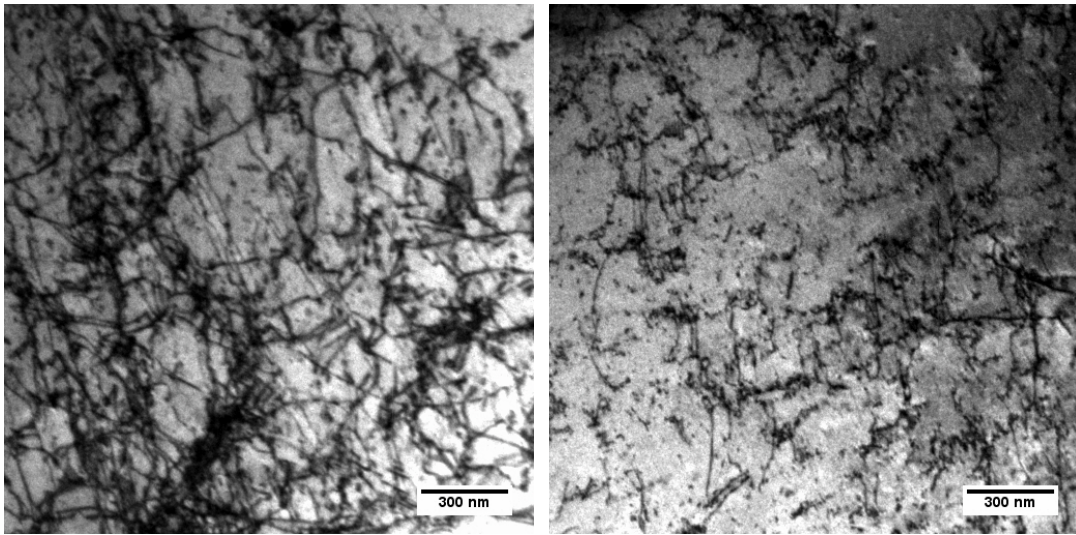
(b) Tangles



(c) Planar slip

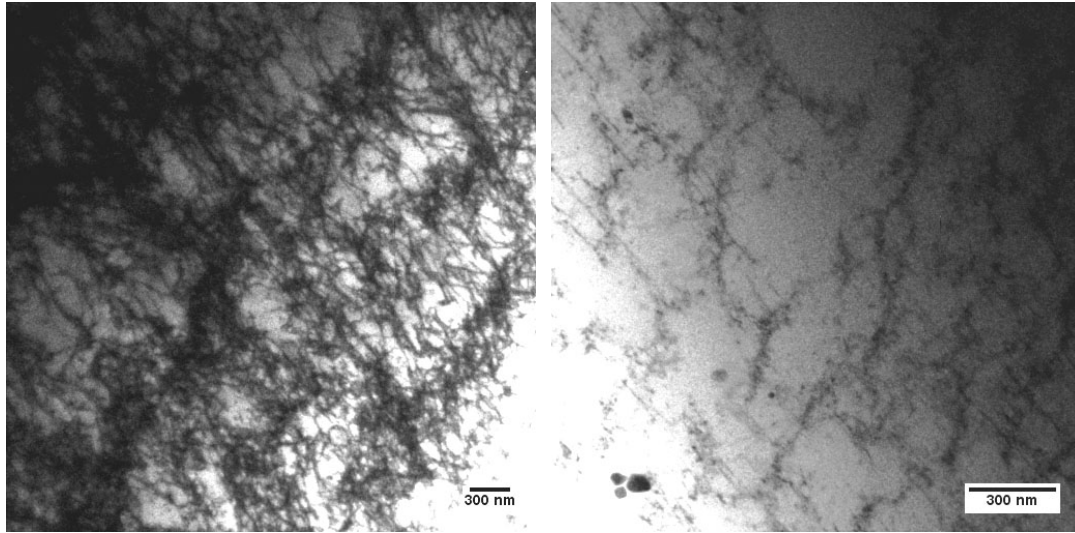
Figure 3.30 Dislocation structure of 800°C heat-treated coupon after 5 cycles

Figure 3.31 exhibits dislocation cells with tangle structures (a, b, and d) and ladder structure (c) after 20 fatigue cycles. The proportion of planar slip (25%) and tangle structure (56%) decrease, but cell structure (13%) increases. More dislocations have been produced and the cell walls become more distinct due to more tangled dislocations within the walls. In the Figure 3.31 (c), a great number of dislocations is observed, and they are trying to form small cells with tangled dislocations.



(a) Cells

(b) Cells

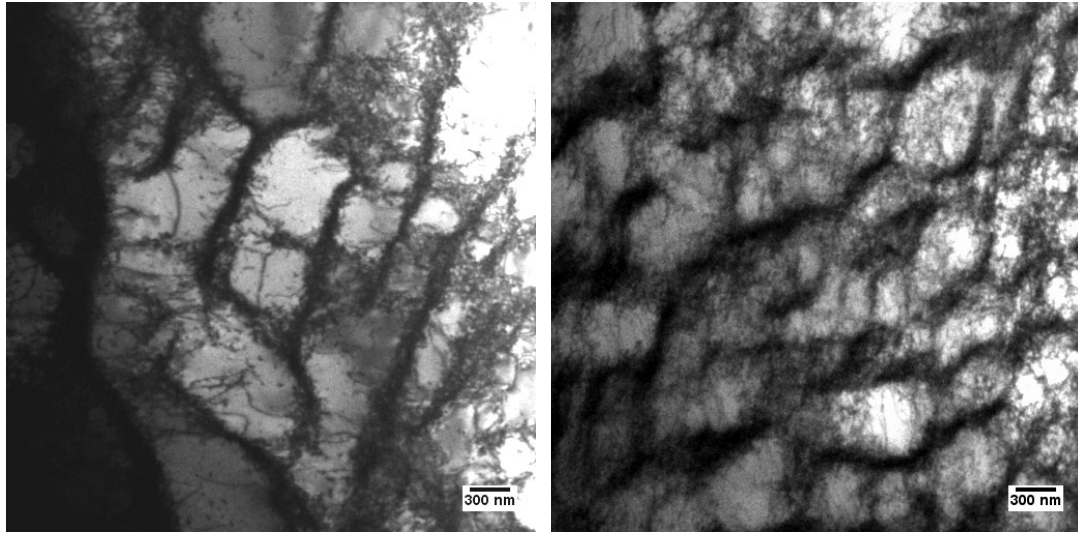


(c) Ladder structure

(d) Cells

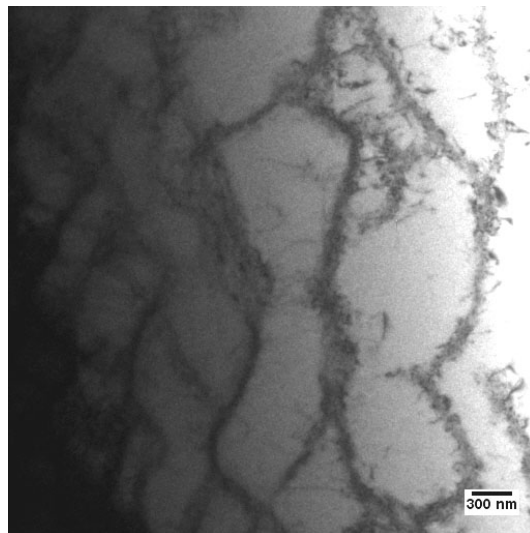
Figure 3.31 Dislocation structure of 800°C heat-treated coupon after 20 cycles

Figure 3.32 shows images of dislocation structure after 100 cycles of fatigue loading of 800°C heat-treated specimen. We note hundred percent of cell structure in this specimen (Figure 3.32). The higher cycles result in a more distinct dislocation cell structure whereas weak dislocation cell structure is noted following relatively low fatigue cycles along with insignificant accumulation of dislocations. For this specimen two types of cells are observed, either equiaxed or elongated cells (Figure 3.32).



(a) Cells

(b) Cells

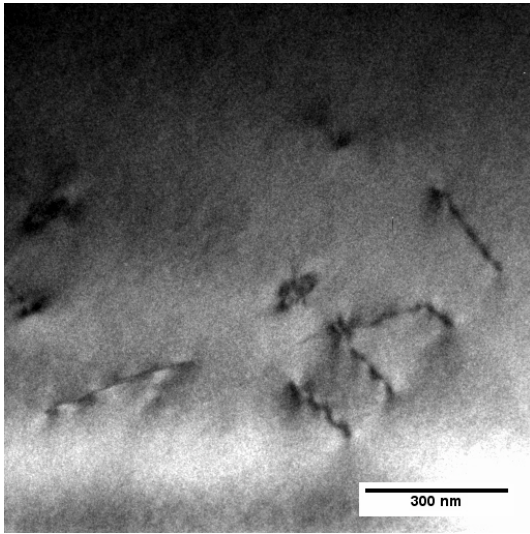


(c) Elongated cells

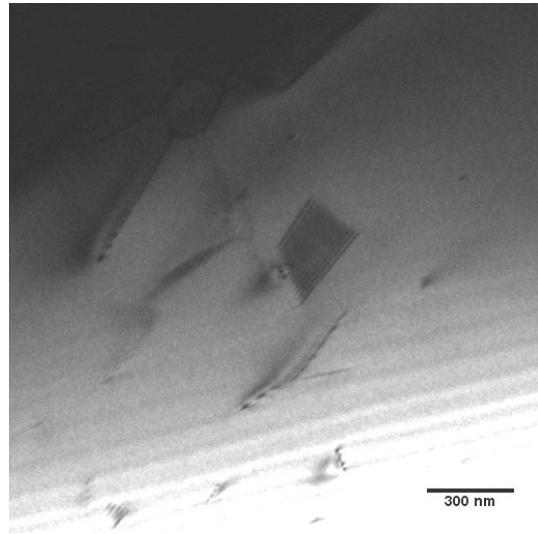
Figure 3.32 Dislocation structure of 800°C heat-treated coupon after 100 cycles

Finally, for 1050°C heat-treated coupon with different cycle are discussed below. Dislocation structure before fatigue (Figure 3.33) shows 89% of isolated dislocations and 11% of stacking faults. However, difference from unconditioned and 800°C heat-treated is

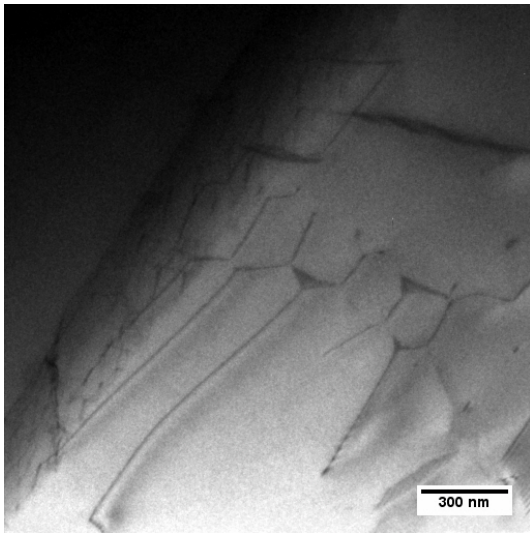
low density of dislocations. This observation is consistent with slightly larger grain size following heat treatment.



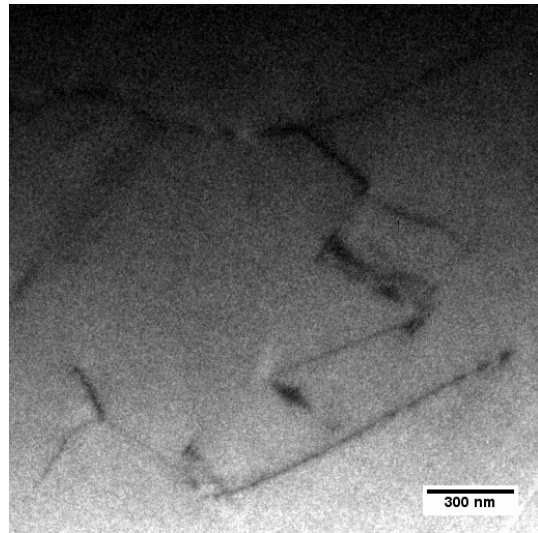
(a) Isolated dislocations



(b) Isolated dislocations



(c) Isolated dislocations

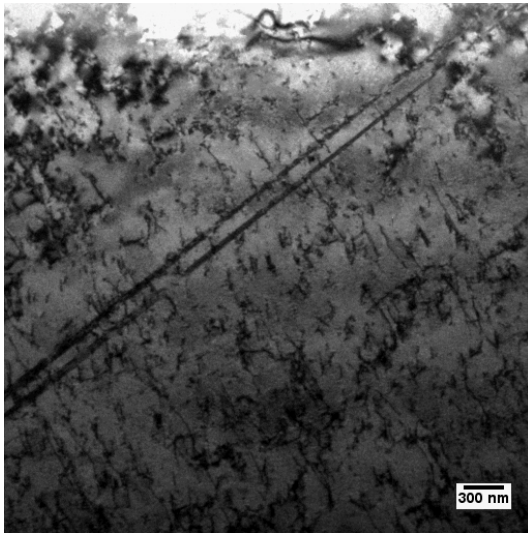


(d) Isolated dislocations

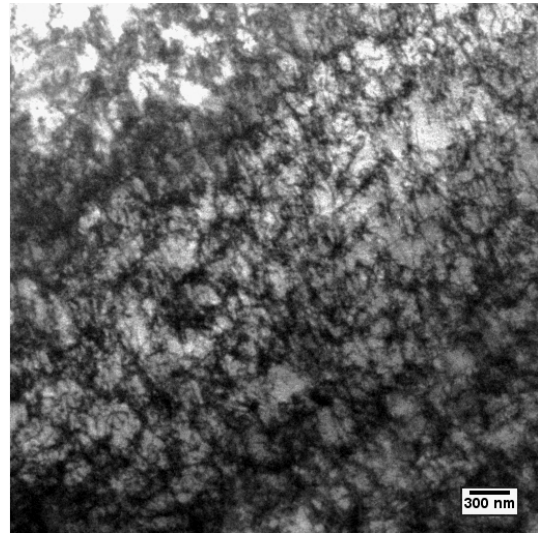
Figure 3.33 Dislocation structure of 1050°C heat-treated coupon before 1% strain-controlled fatigue

It is observed that about 50% of planar slip, 7% of stacking faults, 14% of

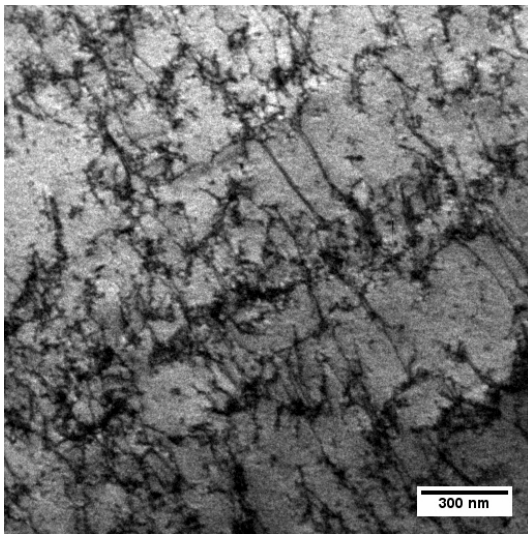
dislocation tangles, and 29% of cell structure are presented in the 1050°C heat-treated coupon specimen following 5 cycle fatigue test. In this case, Figure 3.34 shows that dislocation cells are not well formed with poor uncondensed walls.



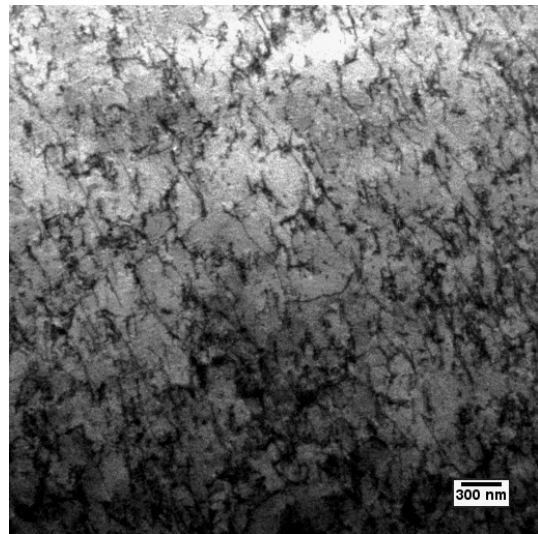
(a) Dislocation and stacking faults



(b) Cells



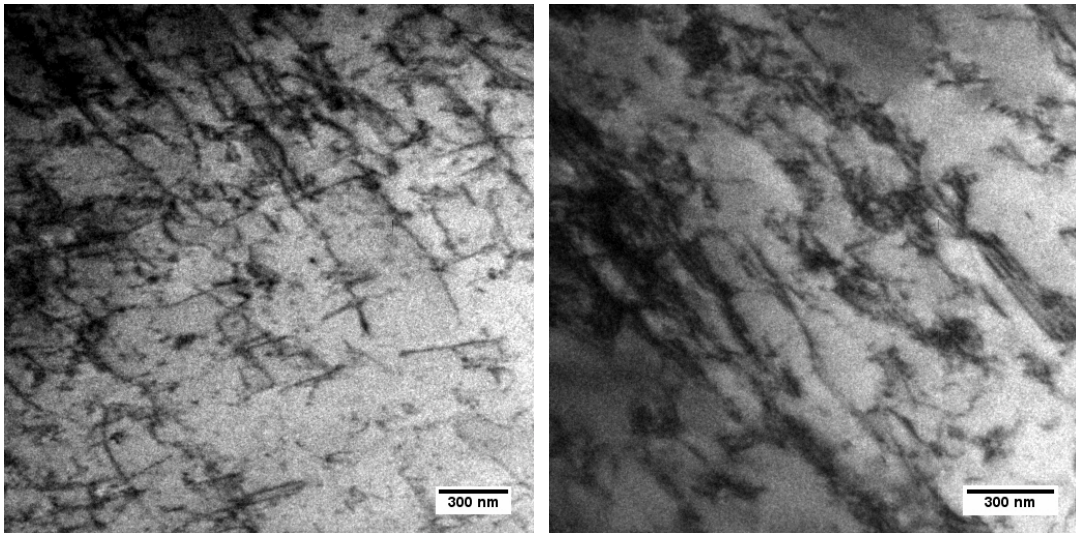
(c) Tangles



(d) Cells

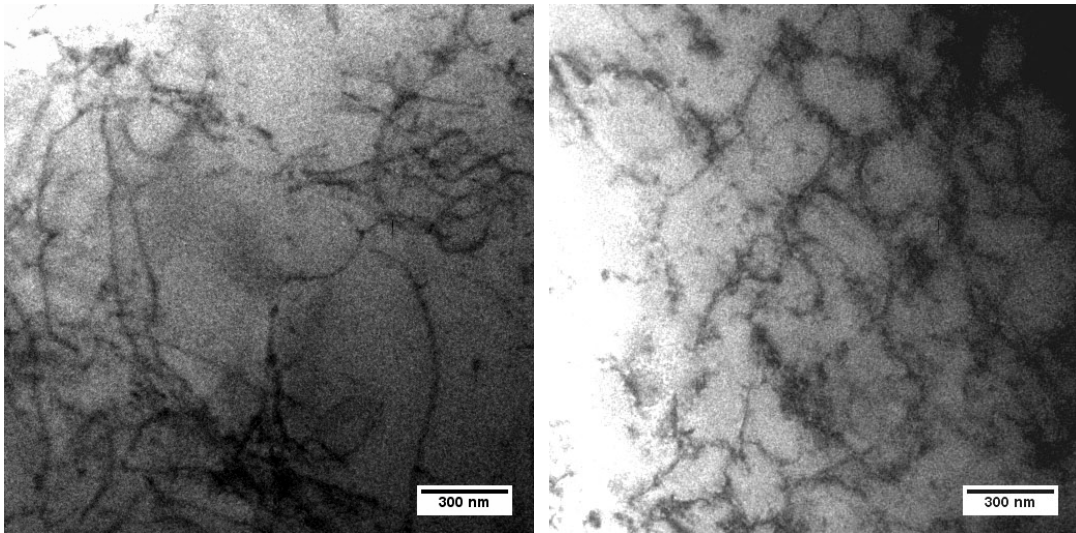
Figure 3.34 Dislocation structure of 1050°C heat-treated coupon after 5 cycles

After 20 cycles of 1050°C heat-treated sample the cell structures are not only badly formed but also rarely observed. The dislocation structure consists of 40% of planar slip, 40% of tangles, and 20% of cells. Figure 3.35 presents types of dislocation structures in this specimen with tangles (a and c), planar slip (b), and cells (d).



(a) Tangles

(b) Planar slip

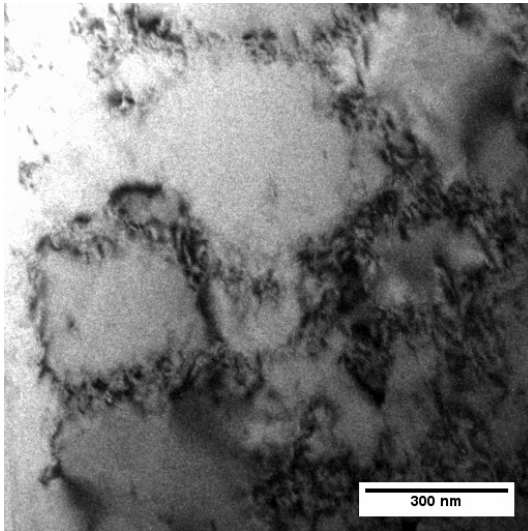


(c) Tangles

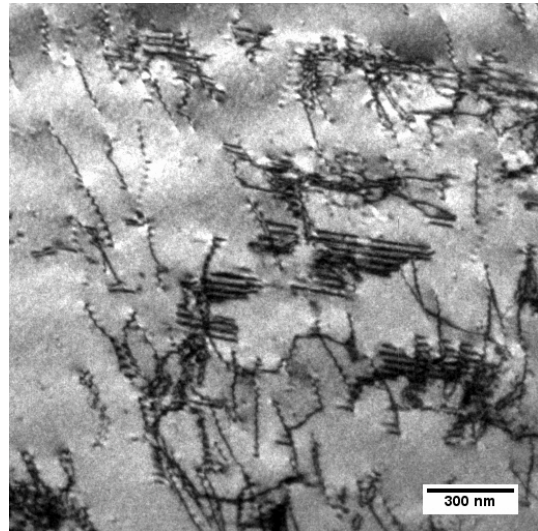
(d) Cells

Figure 3.35 Dislocation structure of 1050°C heat-treated coupon after 20 cycles

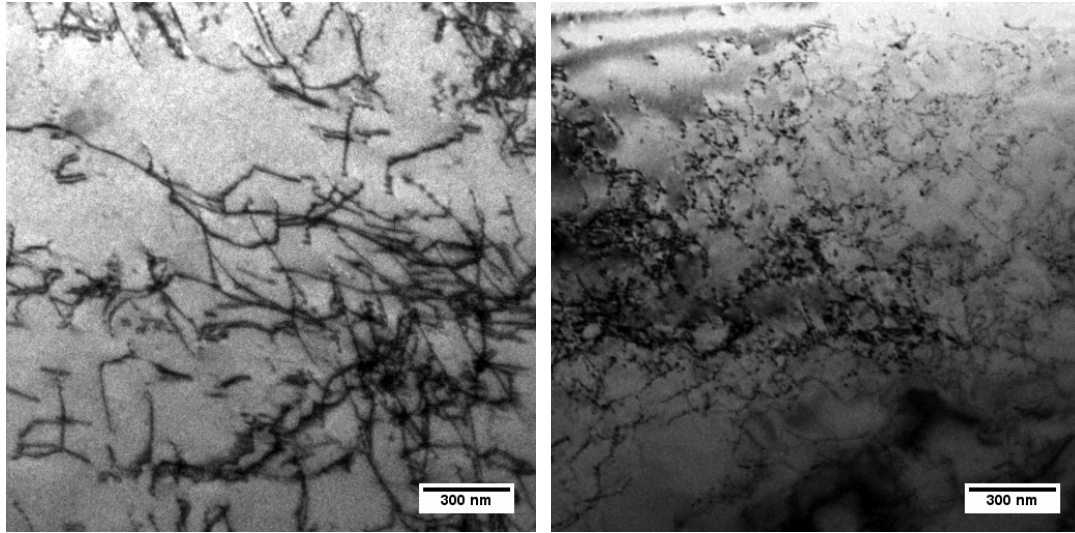
At 100 cycles in 1050°C heat-treated material the portion of cell structures increased compared to relatively low cycles. However, the proportion of planar slip remained high (44%). This result shows a relatively smaller portion of dislocation cell structure rather than the 100% of dislocation cell structure at 100 cycles with 800°C. Stacking faults (11%) and some tangles (11%) can also be noted in Figure 3.36.



(a) Cells



(b) Dislocation and stacking faults



(c) Planar dislocations

(d) Cells

Figure 3.36 Dislocation structure of 1050°C heat-treated coupon after 100 cycles

It can be seen in Table 3.8 that the proportion of planar slip tends to decrease with cycle number while the proportion of cell structure increases at the same time. The dislocation wall and channel structures are not observed in the uniaxial strain controlled test. However, part of the cell structure consists of elongated cells aligned in channels (Figure 3.32 (c)), and these cells might be formed from the wall and channel structure.

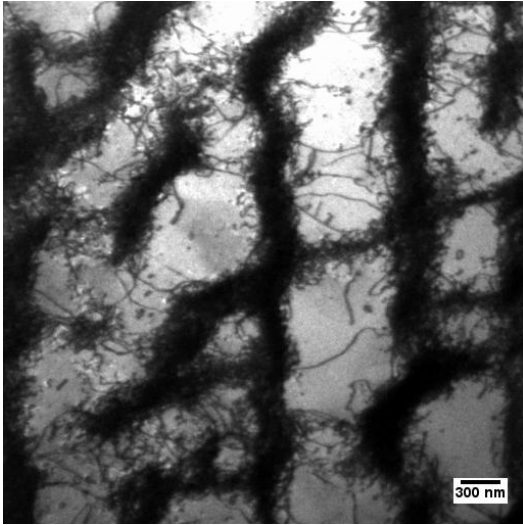
3.5.1.2 Dislocation Structures in Uniaxial Force Controlled Coupons

In order to study dislocation structures following uniaxial ratcheting, comparison between structures of non-ratchetting and ratchetting coupons (see section 3.2.2 for loading cycles prescribed) shows an evolution of each structure after 400 fatigue cycles on unconditioned material. The proportion of different dislocation structures is shown in Table 3.9.

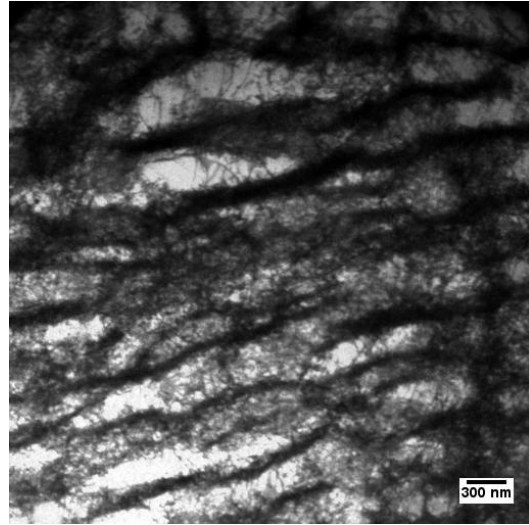
Table 3.9 Percentage of different structures of dislocations observed in the uniaxial force controlled test

Specimen	Cycle	Structures					
		Planar slip	Stacking faults	Tangles	Ladder structure	Cells	Walls
Non-Ratchetting	400	7%		21%		65%	7%
Ratchetting	400	9%		23%		59%	9%

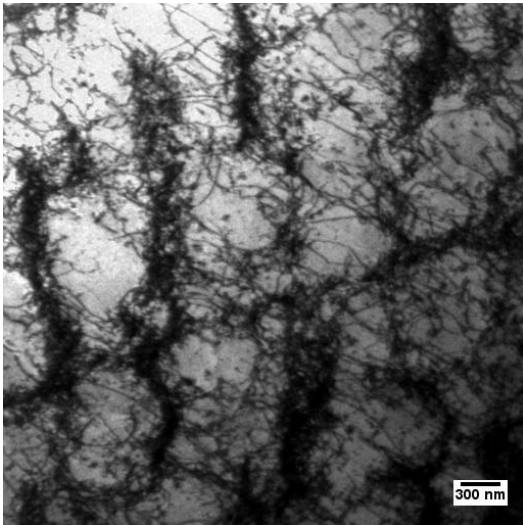
Different dislocation structures are observed in ratcheting specimens compared to those in non-ratcheting cases even though these specimens show similar distribution of each type of dislocation structures. A relatively large proportion of cell structures along with smaller proportion of wall structures distinguished the fatigue damage in ratcheting specimens. Figure 3.37 shows cell and wall structures of non-ratcheting specimen. It is seen that the dislocation structures have relatively uniform dislocation cell structures although walls or boundaries are thick, while the dislocation structures of ratcheting specimen shown in Figure 3.38 have poorly formed dislocation cell structures. In other words, difference of dislocation structure between non-ratcheting and ratcheting specimen is that there are more mobile dislocations not condensed in the cell boundaries inside the channels in ratcheting specimens than in non-ratcheting specimens.



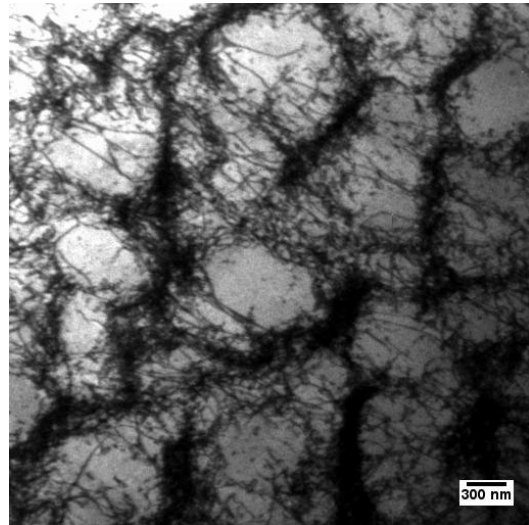
(a) Cells



(b) Walls



(c) Cells



(d) Cells

Figure 3.37 Dislocation structure of non-ratcheting coupon after 400 cycles

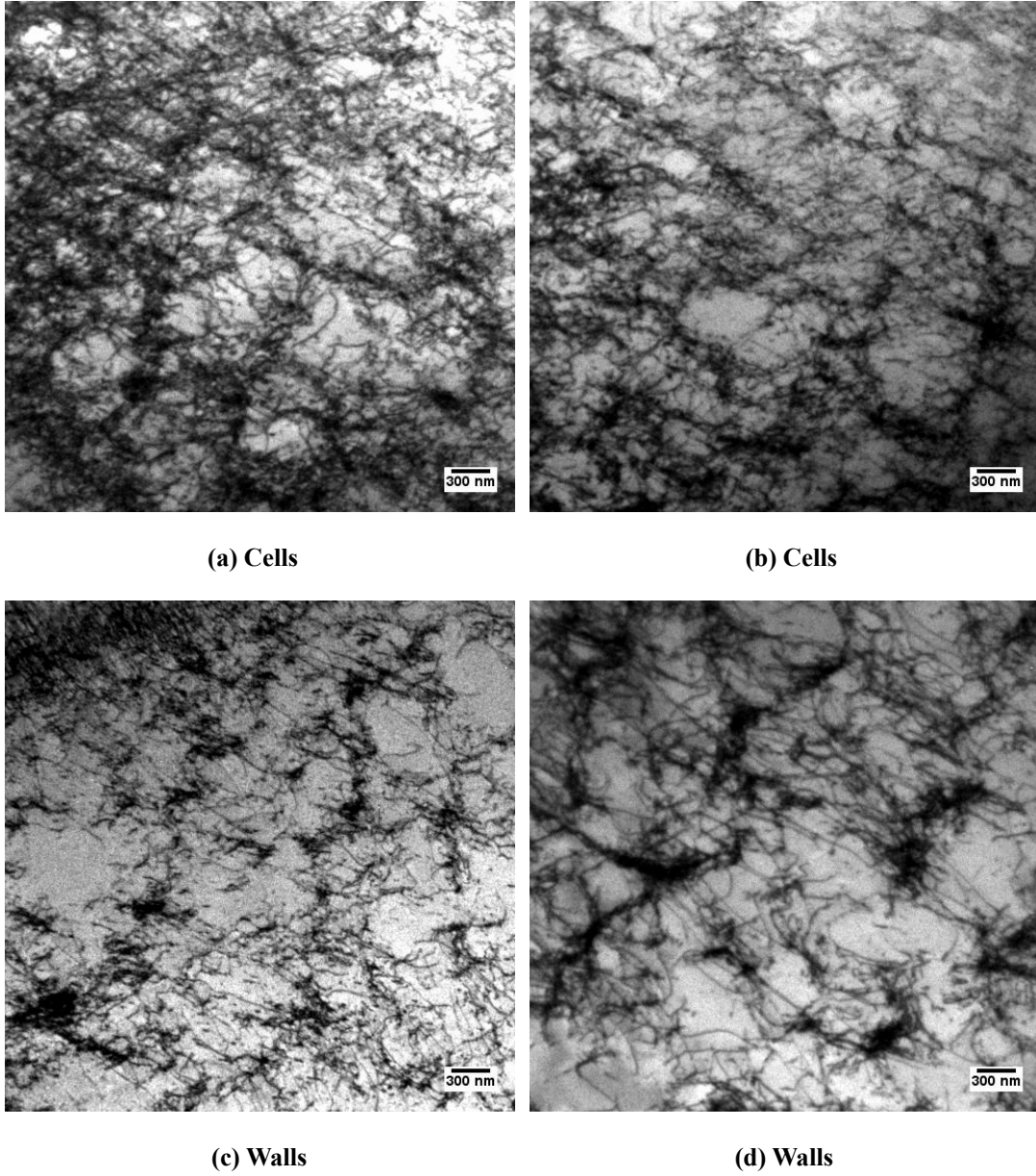


Figure 3.38 Dislocation structure of ratcheting coupon after 400 cycles

3.5.1.3 Dislocation Structures in Biaxial Ratchetting Coupons

The evolution of dislocation structures of biaxially loaded specimen with different heat-treatment temperature is investigated in this section. The coupons were subjected to

0.4% axial strain and 1ksi internal pressure of cyclic load and cycled up to 2000 number of cycles. The percentage of each type of dislocation structure of fatigued coupon material versus heat-treatment temperature is summarized in Table 3.10.

Table 3.10 Percentage of different structures of dislocations observed in the biaxial ratchetting test

Temperature	Cycle	Structures					
		Planar slip	Stacking faults	Tangles	Ladder structure	Cells	Walls
Unconditioned	2000	33%		16%		17%	34%
800°C	1482			7%		78%	15%
1050°C	2000	17%				33%	50%

Planar slip (33%), tangles (16%), cells (17%), and walls (34%) are observed in the unconditioned specimen as illustrated in Figure 3.39. Figures 3.39 (c) and (d) show that dislocation walls and channels are poorly formed although they cover about 34% in volume. Even many tangles are generated between the walls as shown in Figure 3.39 (d).

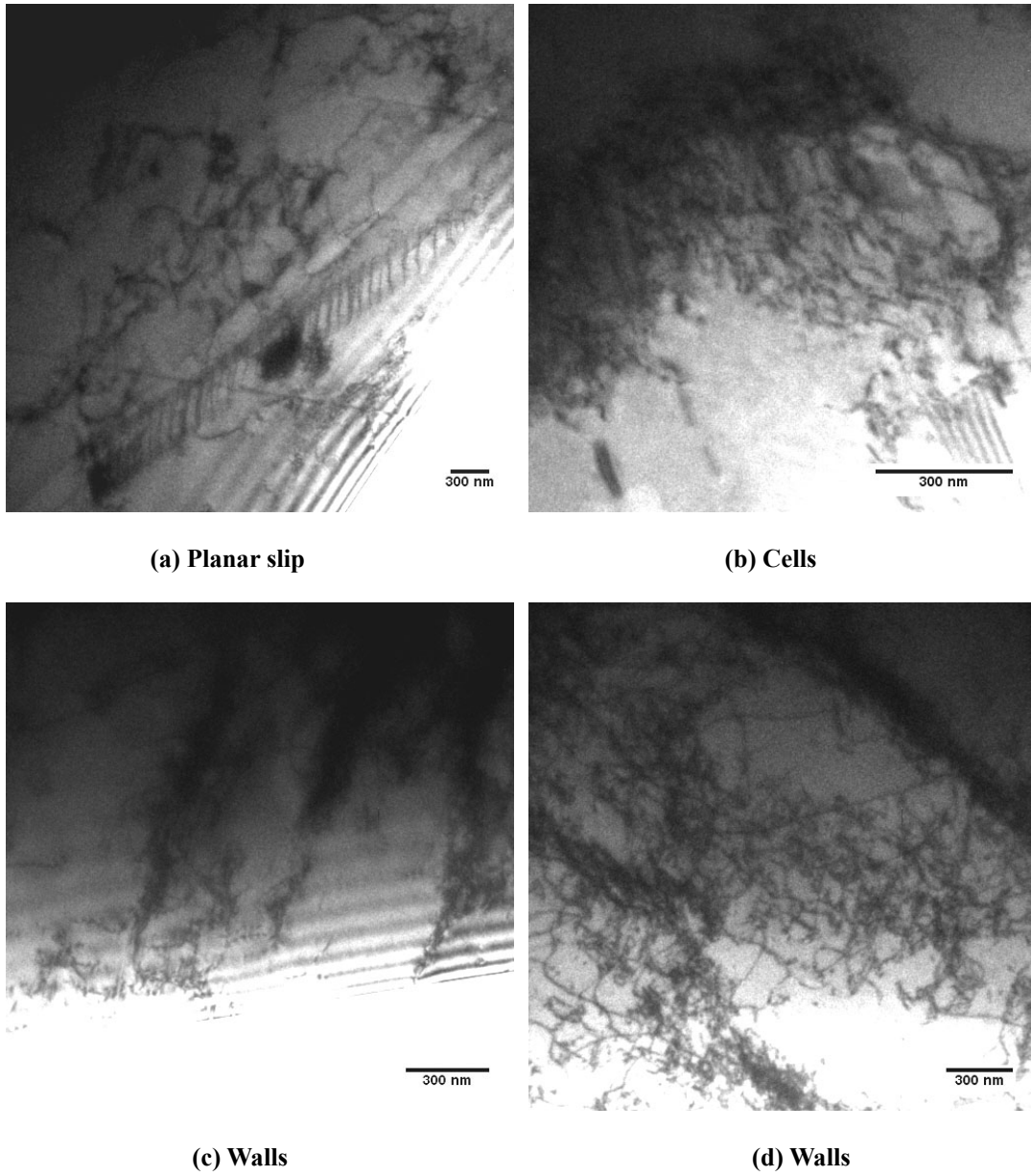


Figure 3.39 Dislocation structure of unconditioned specimen after 2000 cycles

At 800°C annealing temperature proportion of cell structures increased to 78% whereas planar slip decreases to zero. The proportion of structures is 7% of tangles, 78% of cells, and 15% of wall and channel structures. Figure 3.40 demonstrates cell and wall

structure of specimen with 1482 fatigue cycles. The walls or boundaries are thick and wavy as well as appear better defined due to more dislocations generated within the walls.

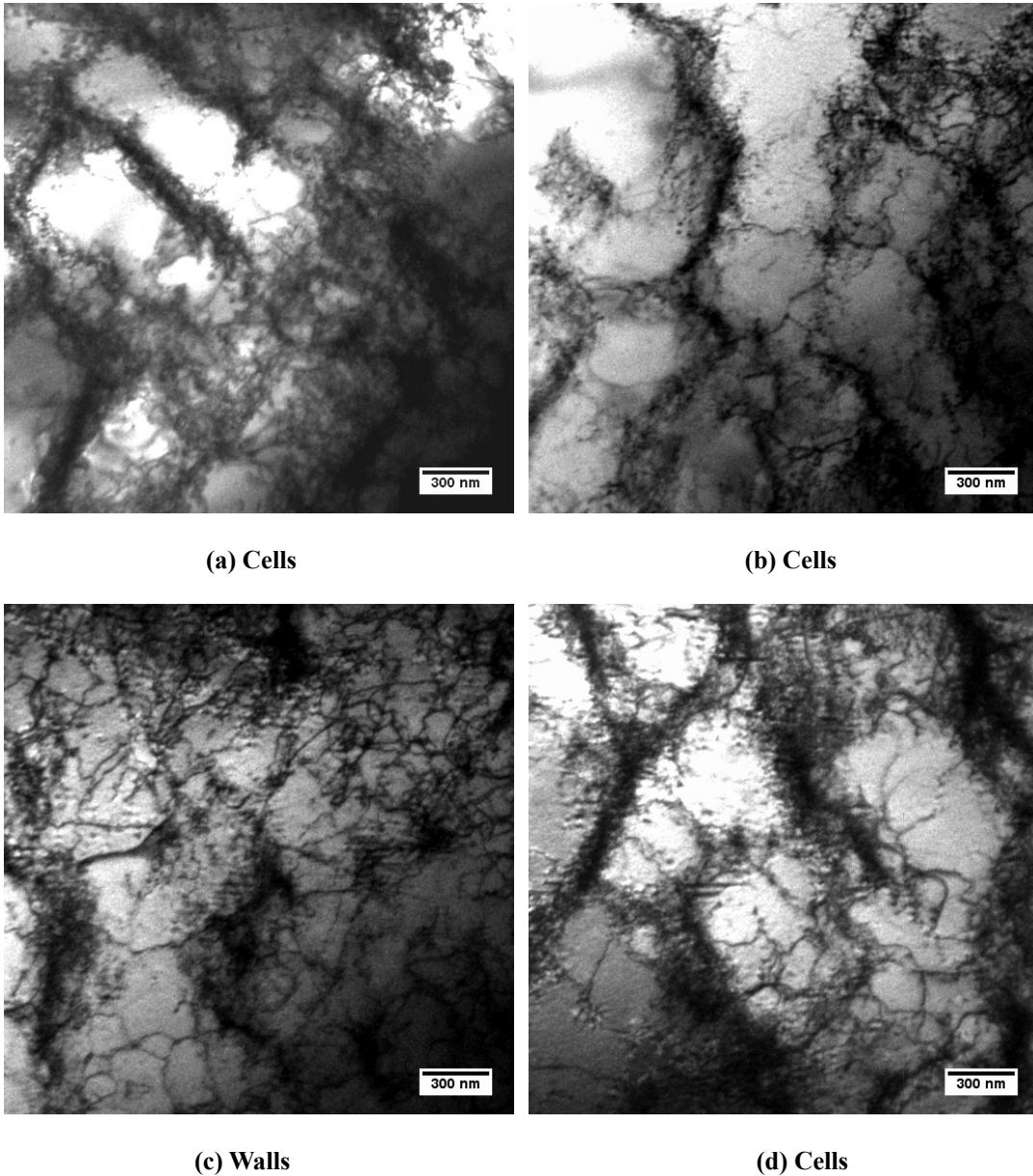


Figure 3.40 Dislocation structure of 800°C heat-treated specimen after 1482 cycles

In the specimen following 2000 fatigue cycles after 1050°C heat-treatment, it is

shown that proportion of wall structures is 50% and cell structures is 33% in volume. A small proportion of the planar slip (17%) is also observed. Figure 3.41 notes that the wall structures become predominant but remain thick and badly formed, and numerous dislocations are contained in the channels.

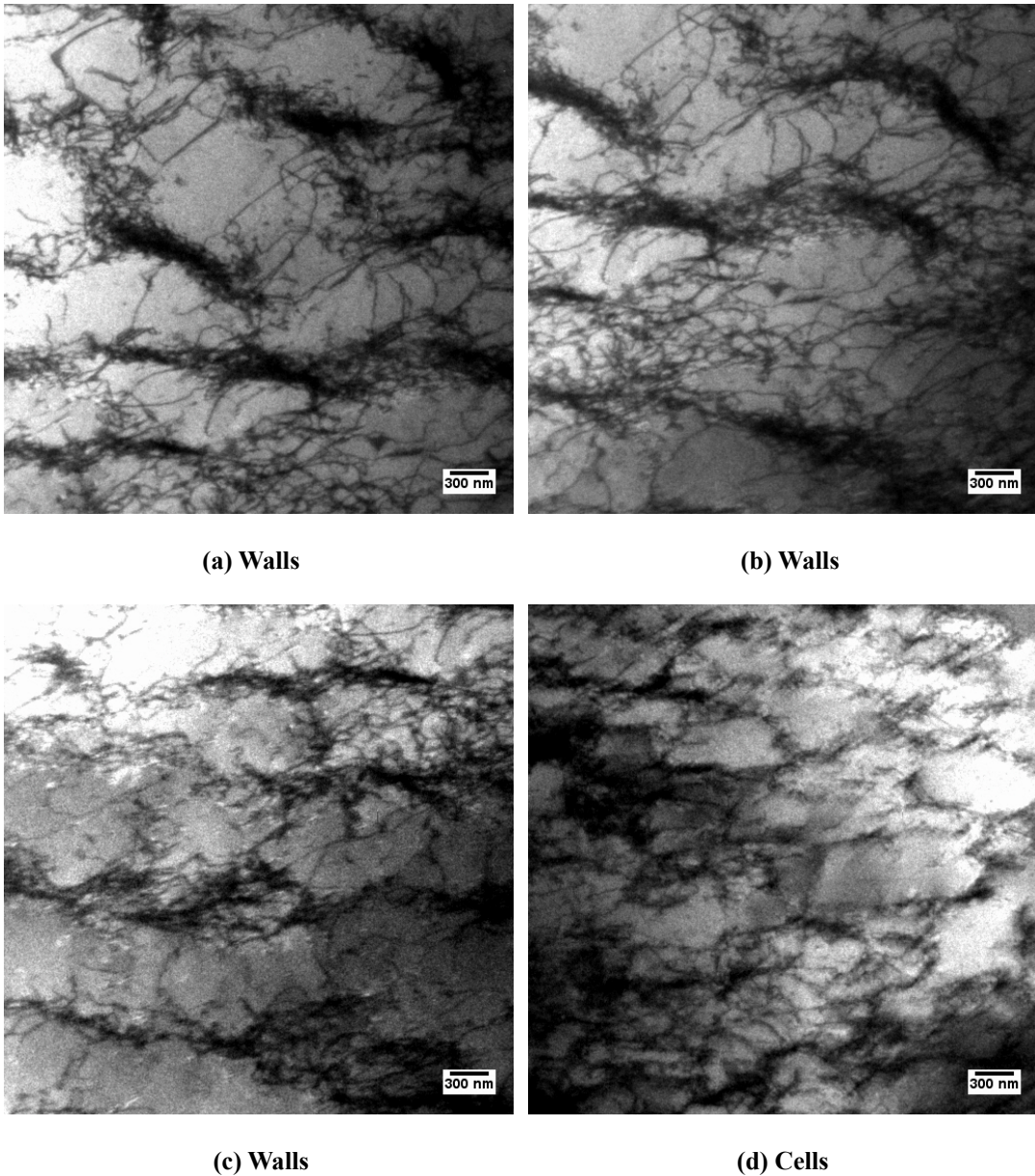


Figure 3.41 Dislocation structure of 1050°C heat-treated specimen after 2000 cycles

3.5.1.4 Dislocation Structures in Welded Pipe Specimen

The dislocation structures of welded pipe specimens resulting from displacement-controlled fatigue test are examined. A detailed study of the change of dislocation structures was performed at different cycle numbers and different positions with respect to the weld toe. The percentage of different dislocation structures observed in the welded pipe specimen according to the number of cycles and locations are recorded in Table 3.11.

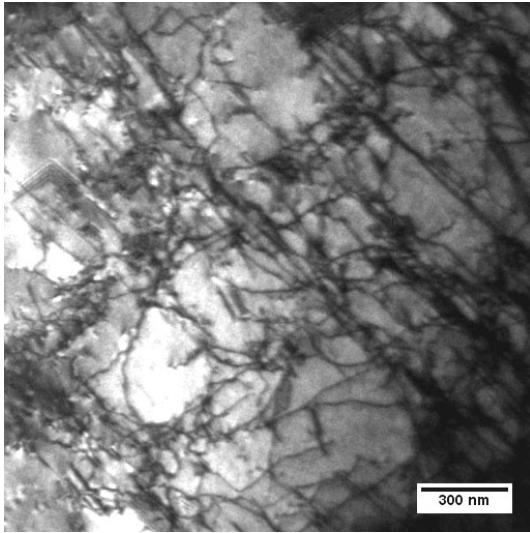
Table 3.11 The percentage of different structures of dislocations observed in welded pipe specimens

Specimen	Cycle	Location	Structures					
			Planar slip	Stacking faults	Tangles	Ladder structure	Cells	Walls
SSPC4	5	3mm	71%		29%			
SSPC2	20	3mm			89%		11%	
		9.8mm	29%		71%			
		38mm	60%		40%			
SSPC3	100	3mm	22%		56%		22%	
SSPC5	2679	3mm	9%		36%		45%	9%

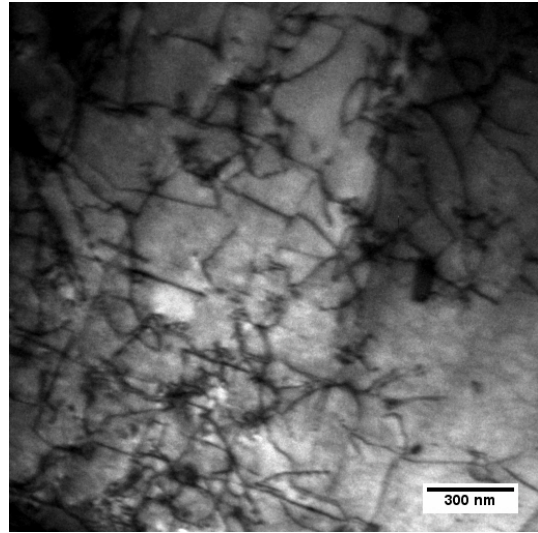
Dislocation structures of SSPC4 specimen at 3mm away from the weld toe consist of 71% of planar slip and 29% of tangles. Tangle structures are shown in Figure 3.42 (a) and planar dislocation arrays are included in Figures 3.42 (b), (c), and (d). After 5 cycles cell structures are not developed but high portion of planar dislocations remained. However, high proportion of tangles appears and a small proportion of uncondensed cell structure is developed at 3mm away from the weld toe after 20 cycles (SSPC2) as shown in Figure 3.43. Figure 3.46 demonstrates dislocation structures after 100 cycles (SSPC3). At this stage more dislocation cells are forming, but still high percentage of tangles are observed. After crack

initiation at 2679 cycles cell (Figure 3.47 a, b, d) and wall (Figure 3.47 c) structures are developed. These structures contain lots of dislocations in the channel, and walls are thick and poorly formed. The proportion covered by cell structures is about 45%. The wall structure occupies about 9% in volume which seems to be an intermediate structure between cell and wall structure at greater number of cycles. With increased number of cycles, cell and wall structure increased, but percentage of planar slip decreased.

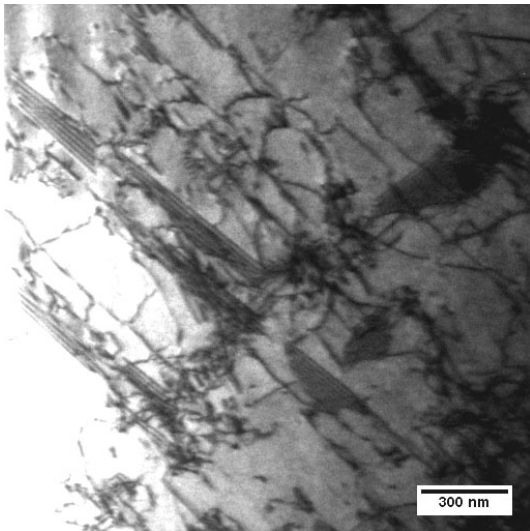
To gain a better understanding of the dislocation structures developed following fatigue cycles at different locations from the welded toe of pipe specimen, dislocation structures at 3mm, 9.8mm, and 38mm away from the welded toe after 20 cycles (SSPC2) are shown in Figures 3.43, 3.44, and 3.45. At 3mm, the observation of dislocation structures of 89% tangles and 11% cells is already mentioned. From Figure 3.44, only planar slip (29%) and tangles (71%) are observed at 9.8mm from the welded toe. It is also observed in Figure 3.45 that planar slip and tangles are produced at 38mm away from the welded toe. However, the proportion of planar slip is higher than tangle structure. More cell structures are noted near the weld toe while dispersed dislocations are observed away from weld toe.



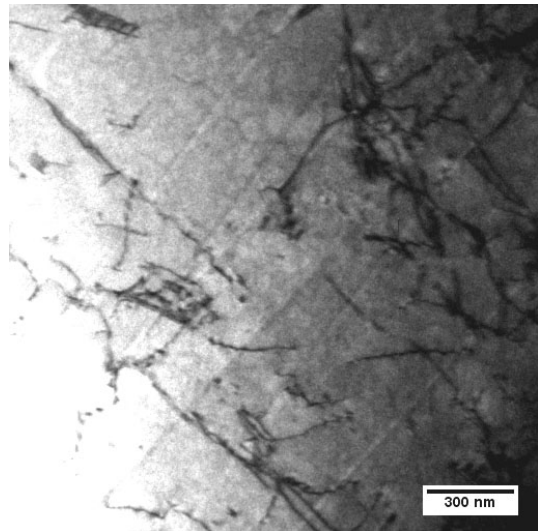
(a) Tangles



(b) Planar dislocations

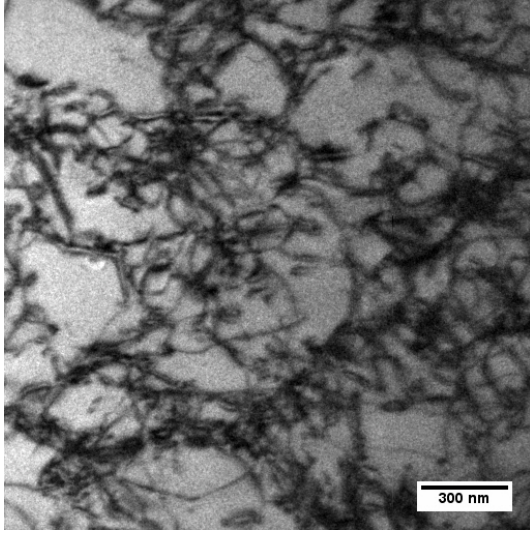


(c) Planar dislocations and stacking faults

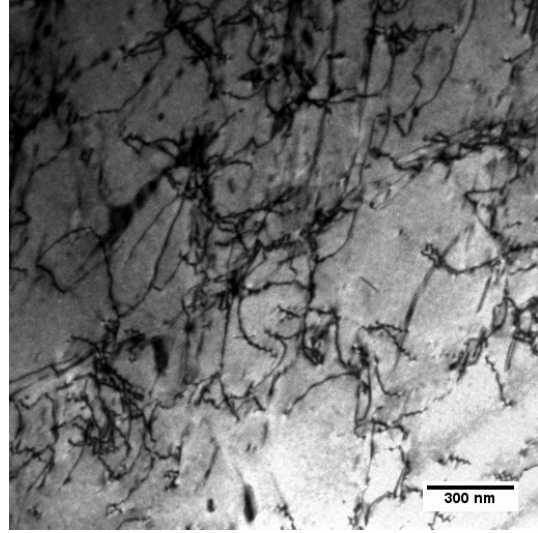


(d) Planar dislocations

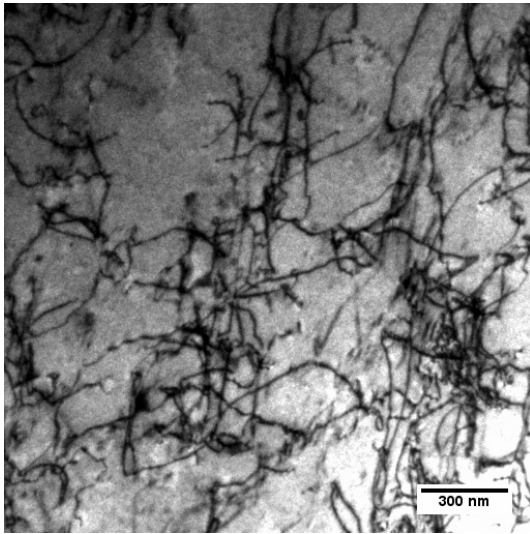
Figure 3.42 Dislocation structure after 5 cycles (SSPC4) at 3mm away in weld toe



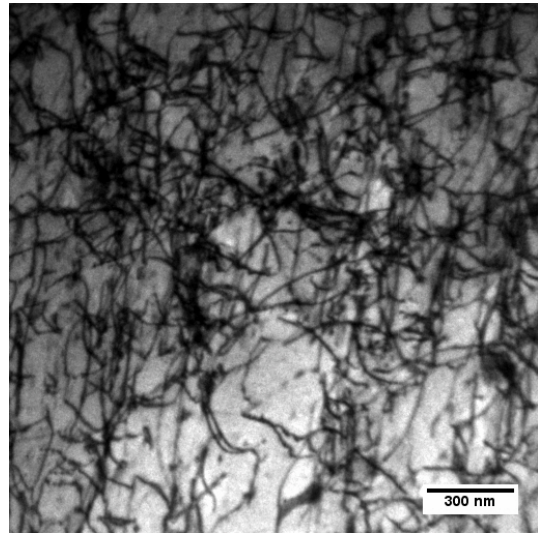
(a) Cells



(b) Tangles

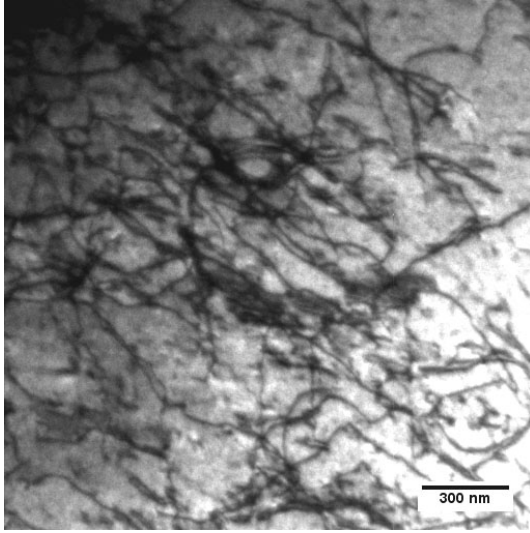


(c) Tangles

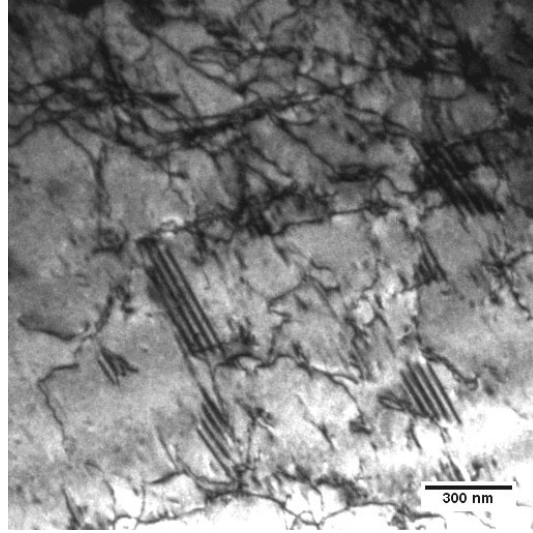


(d) Tangles

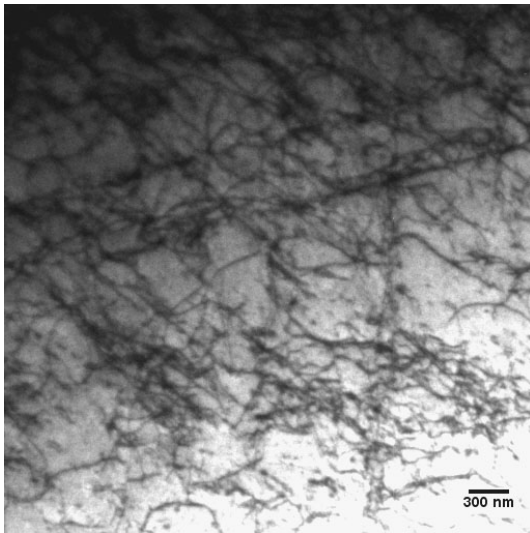
Figure 3.43 Dislocation structure after 20 cycles (SSPC2) at 3mm away in weld toe



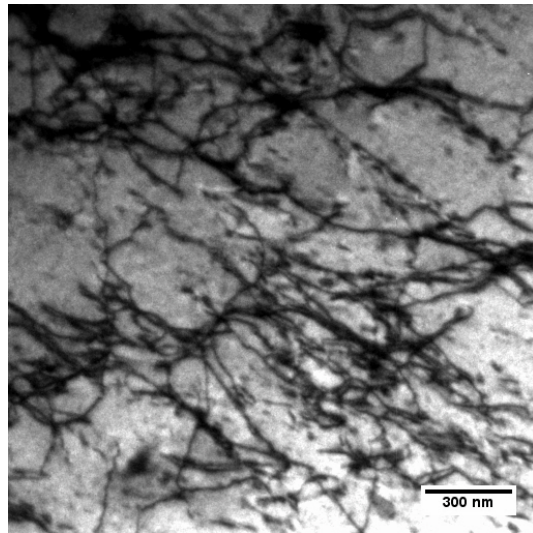
(a) Tangles



(b) Planar dislocations

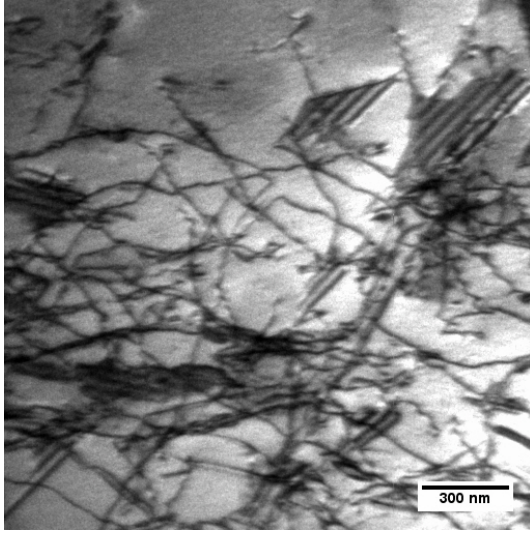


(c) Tangles

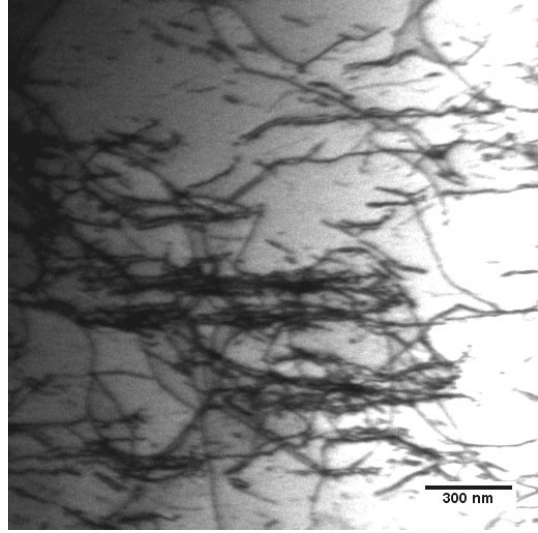


(d) Tangles

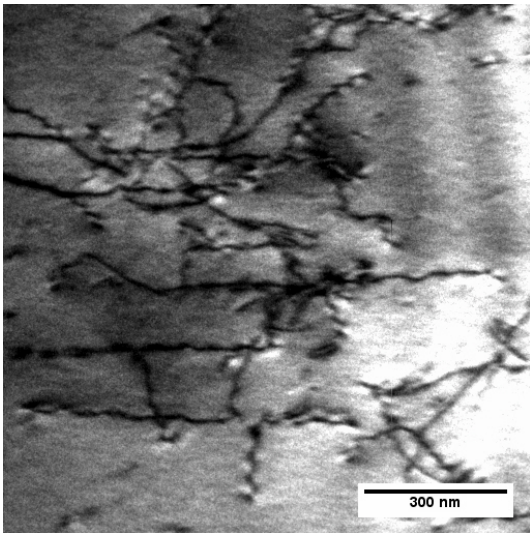
Figure 3.44 Dislocation structure after 20 cycles (SSPC2) at 9.8mm away in weld toe



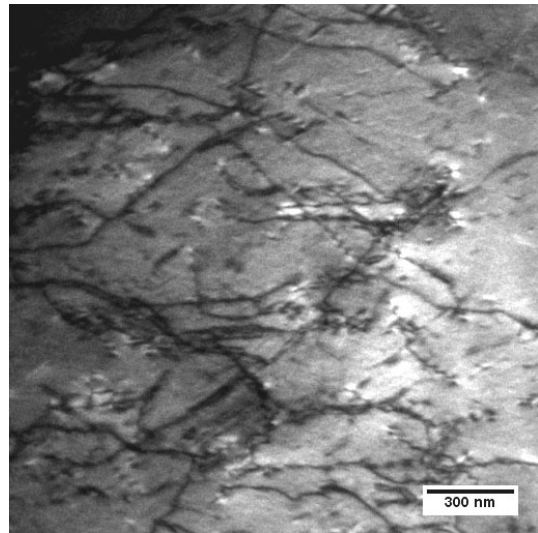
(a) Tangles



(b) Tangles

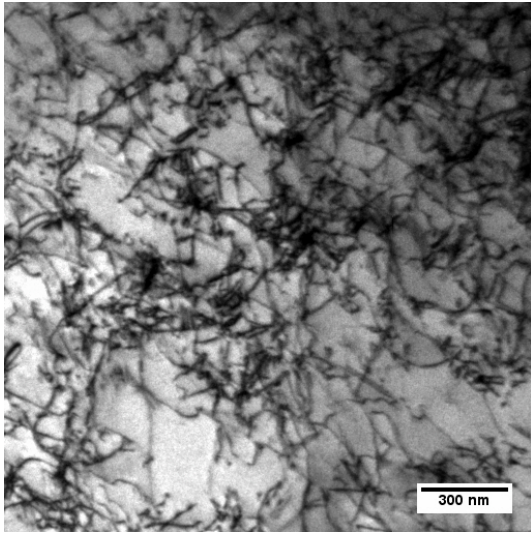


(c) Planar dislocation

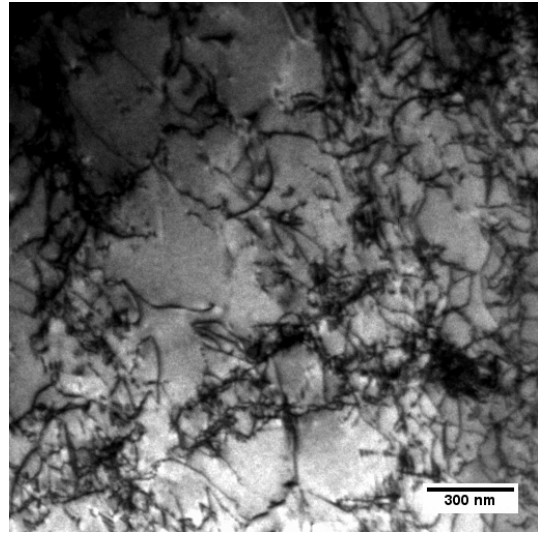


(d) Planar dislocation

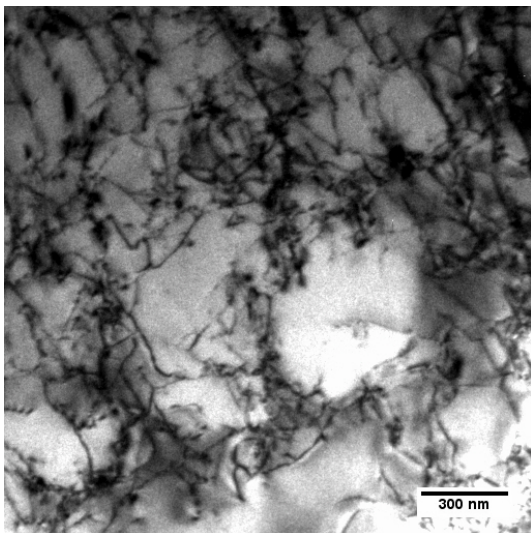
Figure 3.45 Dislocation structure after 20 cycles (SSPC2) at 38mm away from weld toe



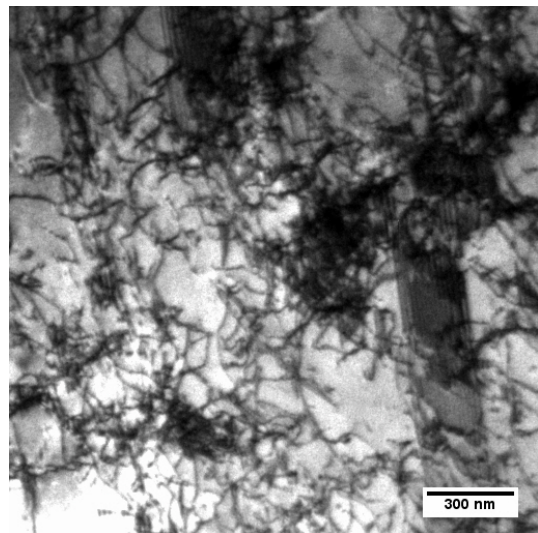
(a) Tangles



(b) Cells

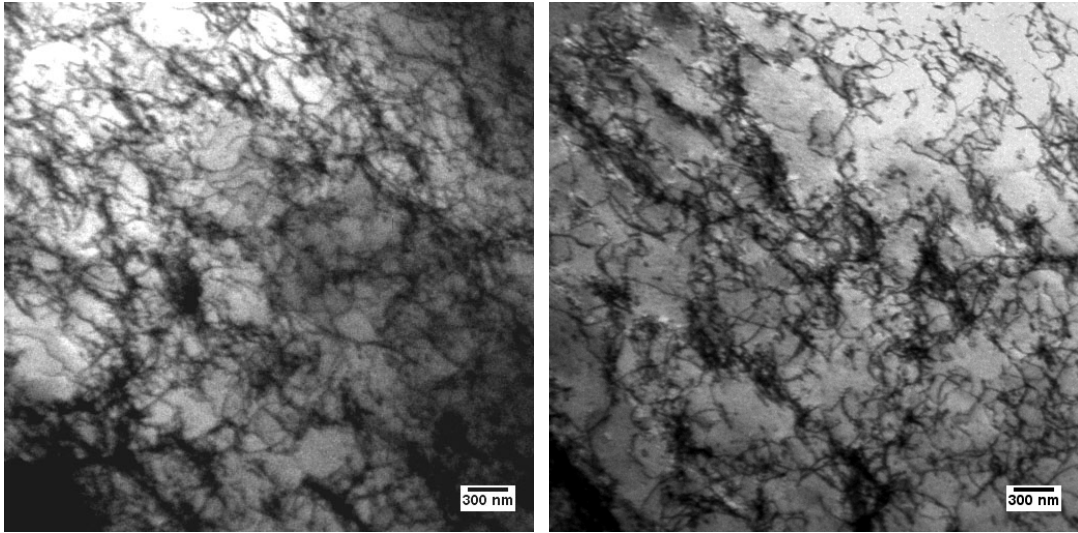


(c) Cells



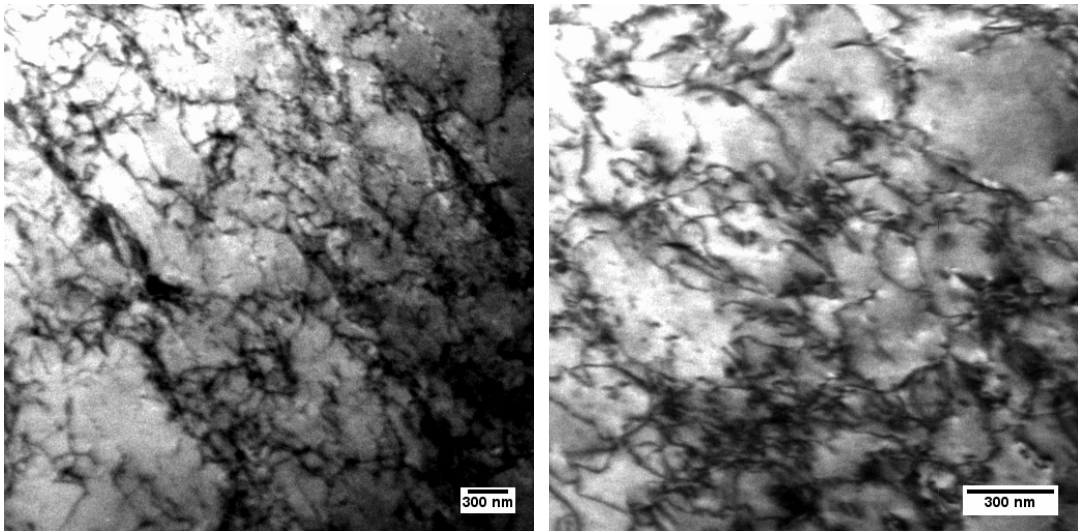
(d) Tangles

Figure 3.46 Dislocation structure after 100 cycles (SSPC3) at 3mm away from weld toe



(a) Cells

(b) Cells

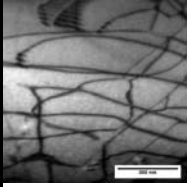
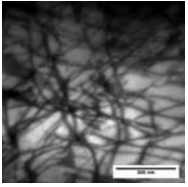
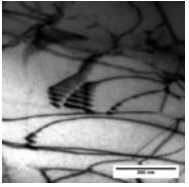
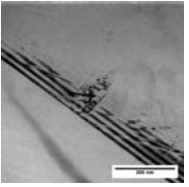
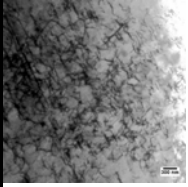
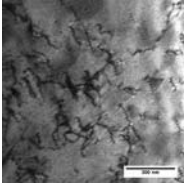
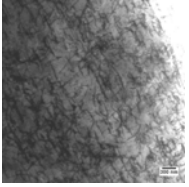
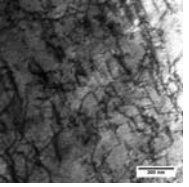
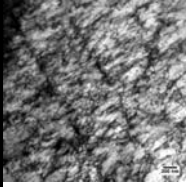
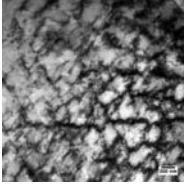
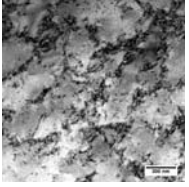
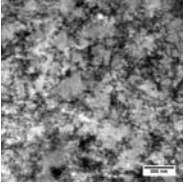
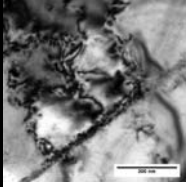
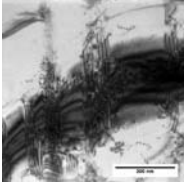
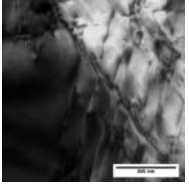
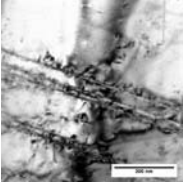
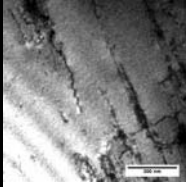
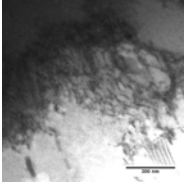
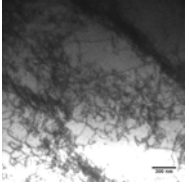
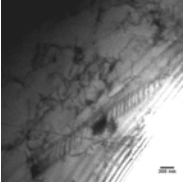
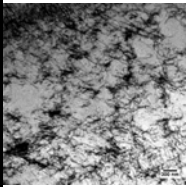
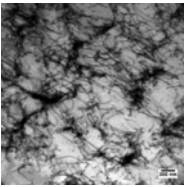
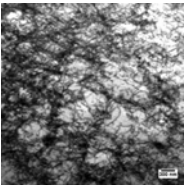
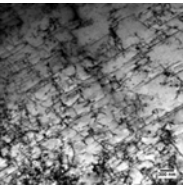


(c) Walls

(d) Cells

Figure 3.47 Dislocation structure after crack initiation at 2679 cycles (SSPC5) at 3mm away from weld toe

Table 3.12 Summary of dislocation structures of unconditioned coupons

	Specimen	Loading	Microstructure			
Before Fatigue	As-received					
			Planar dislocation arrays		Stacking faults	
Uniaxial Strain-controlled Fatigue	5 cycles	$\epsilon = 1\%$				
			Uncondensed cells ($\delta = 361\text{nm}$)		Tangles	
	20 cycles	$\epsilon = 1\%$				
			Ladder structure	Cells ($\delta = 421\text{nm}$)	Cells ($\delta = 310\text{nm}$)	Cells ($\delta = 448\text{nm}$)
	234 cycles (Crack)	$\epsilon = 1\%$				
			Stacking faults			
Biaxial Ratcheting Fatigue	2000 cycles	$P = 1\text{ksi}$ $\epsilon_x = 0.4\%$				
			Dislocation band	Cells	Tangles within the walls	Pile up
Uniaxial Force-	Ratchetting (400 cycles)	$F_m = 0.2F_{1\%}$ $F_a = 0.8F_{1\%}$				
			Walls	Cells($\delta = 563\text{nm}$)	Tangles	

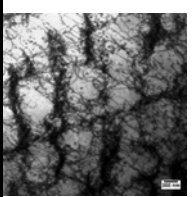
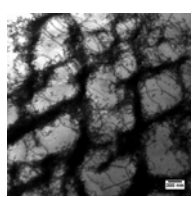
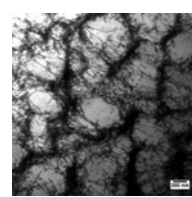
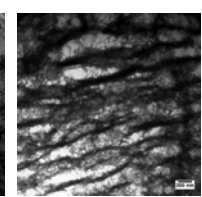
controlled Fatigue	No Ratchetting (400 cycles)	$F_m = 0$ $F_a = 0.8F_{1\%}$	 <p>Cells($\delta = 702\text{nm}$)</p>	 <p>Cells($\delta = 702\text{nm}$)</p>	 <p>Cells($\delta = 738\text{nm}$)</p>	 <p>Walls</p>
-----------------------	--------------------------------------	---------------------------------	--	---	--	--

Table 3.13 Summary of dislocation structures of 800°C heat-treated coupons

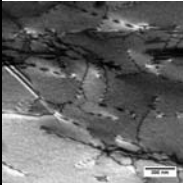
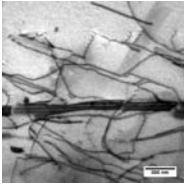
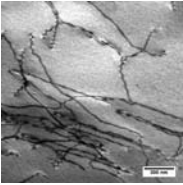
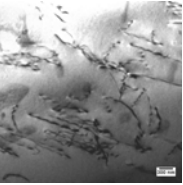
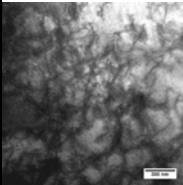
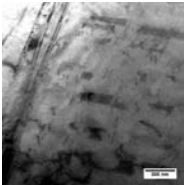
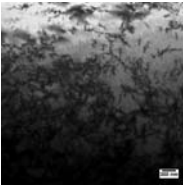
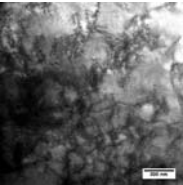
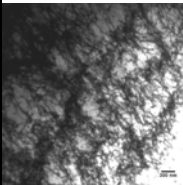
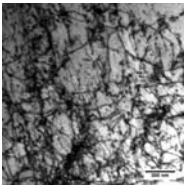
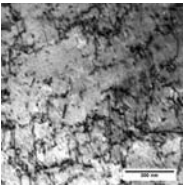
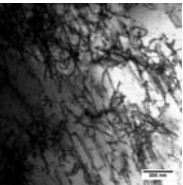
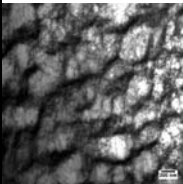
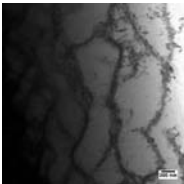
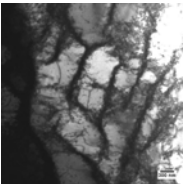
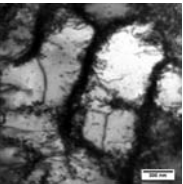
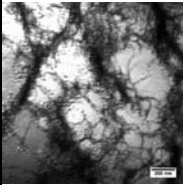
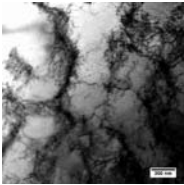
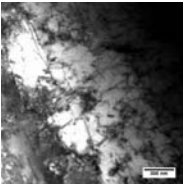
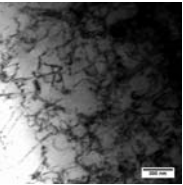
	Specimen	Loading	Microstructure				
Before Fatigue	As-received						
			Planar dislocation arrays and Stacking faults				
Uniaxial Strain-controlled Fatigue	5 cycles	$\epsilon = 1\%$					
				Uncondensed cells ($\delta = 289\text{nm}$)	Stacking faults	Uncondensed cells ($\delta = 306\text{nm}$)	
	20 cycles	$\epsilon = 1\%$					
			Ladder structure ($\delta = 305\text{nm}$)	Tangles	Uncondensed cells	Tangles	
100 cycles	$\epsilon = 1\%$						
			Cells ($\delta = 568\text{nm}$)	Elongated cells	Cells ($\delta = 688\text{nm}$)		
Biaxial Ratcheting Fatigue	1482 cycles (Crack)	$P = 1\text{ksi}$ $\epsilon_x = 0.4\%$					
			Cells ($\delta = 557\text{nm}$)	Walls	Tangles	Uncondensed cells	

Table 3.14 Summary of dislocation structures of 1050°C heat-treated coupons

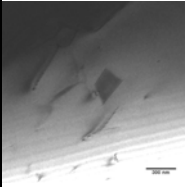
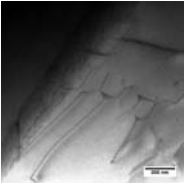
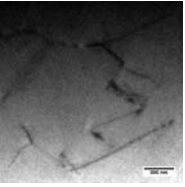
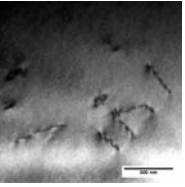
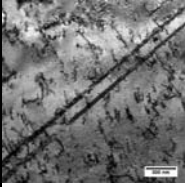
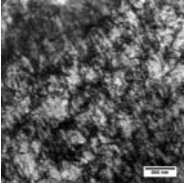
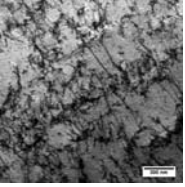
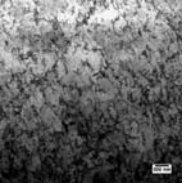
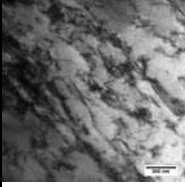
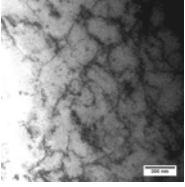
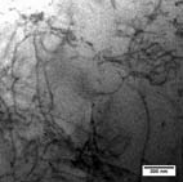
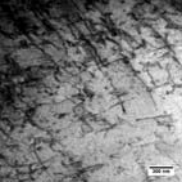
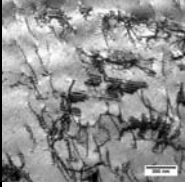
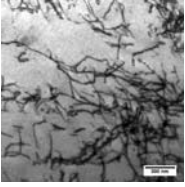
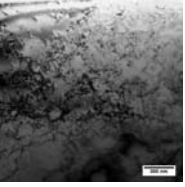
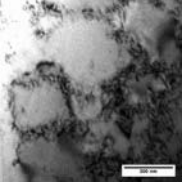
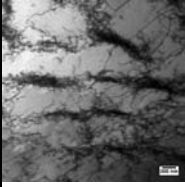
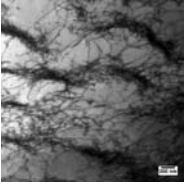
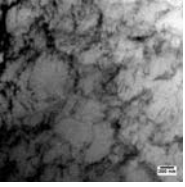
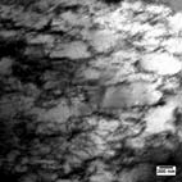
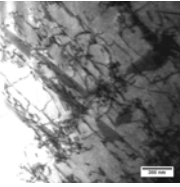
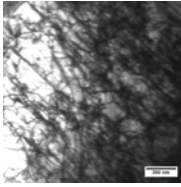
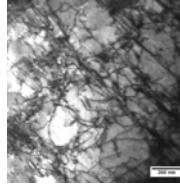
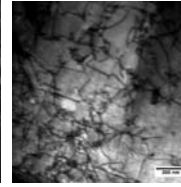
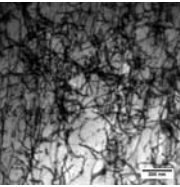
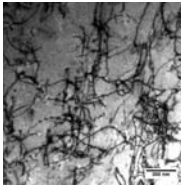
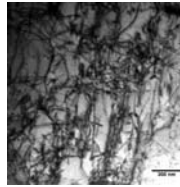
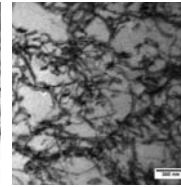
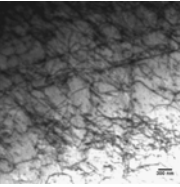
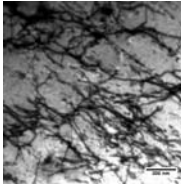
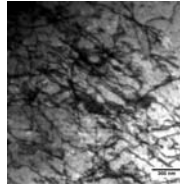
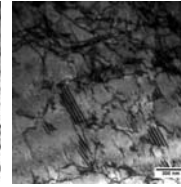
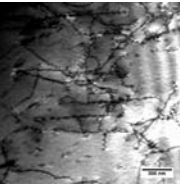
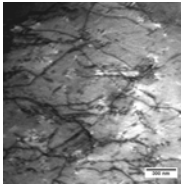
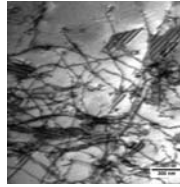
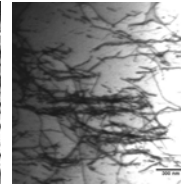
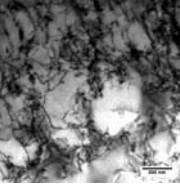
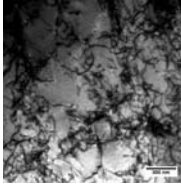
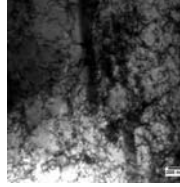
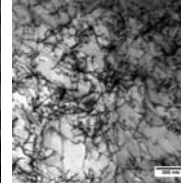
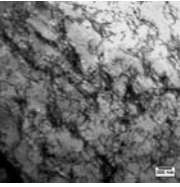
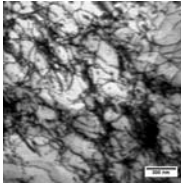
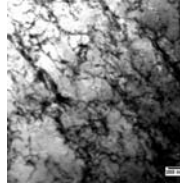
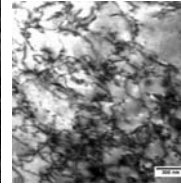
	Specimen	Loading	Microstructure				
Before Fatigue	As-received						Planar slip
Uniaxial Strain-controlled Fatigue	5 cycles	$\epsilon = 1\%$					Dislocations and SF Cells ($\delta = 191\text{nm}$) Tangles Uncondensed cells
	20 cycles	$\epsilon = 1\%$					Stacking faults Cells ($\delta = 233\text{nm}$) Tangles Tangles
	100 cycles	$\epsilon = 1\%$					Dislocations and SF Tangles Uncondensed cells Cells ($\delta = 310\text{nm}$)
Biaxial Ratcheting Fatigue	2000 cycles	P= 1ksi $\epsilon_x = 0.4\%$					Walls Walls Cells ($\delta = 694\text{nm}$) Cells ($\delta = 605\text{nm}$)

Table 3.15 Summary of dislocation structures of socket welded pipe specimens

Specimen	Loading	Location	Microstructure			
SSPC4 (5 cycles)	$\delta = 10\text{mm}$	3mm (away from the weld toe)				
			Dislocation and SF	Tangles	Planar dislocations	
SSPC2 (20 cycles)	$\delta = 10\text{mm}$	3mm (away from the weld toe)				
				Tangles	Uncondensed cells	
		9.5mm (away from the weld toe)				
			Planar dislocation arrays and tangles	Tangles and SF		
		38mm (away from the weld toe)				
			Planar dislocation arrays and SF	Tangles		
SSPC3 (100 cycles)	$\delta = 10\text{mm}$	3mm (away from the weld toe)				
			uncondensed cells	Uncondensed cells	Dislocation band and SF	Tangles
SSPC5 (2679 cycles)	$\delta = 10\text{mm}$	3mm (away from the weld toe)				
			Walls	Cells	Walls	Cells($\delta = 401\text{nm}$)

3.5.2 Dislocation Density

In order to investigate the quantitative correlation between dislocation density, cell size, flow stress, number of cycles, and annealing temperature, the dislocation density was determined using a linear intercept method and following relationship

$$\rho = \frac{2N}{Lt} \quad (3)$$

where ρ is the dislocation density, N is the number of intersections between a dislocation and a random set of lines, L is the length of the line, and t is the thickness of the specimen. Average thickness of 0.1 μ m was assumed for all of TEM foils and is reasonable to allow examination of the microstructure at the peak damage region.

3.5.2.1 Dislocation Density in Uniaxial Strain controlled Specimens

Table 3.16 shows numerical values of dislocation density for uniaxial strain-controlled coupons. A mean value of dislocation densities in several areas of each specimen is measured. Original data of dislocation density measured in every region taken from TEM are included in appendix. These results could be used in evaluation of relationship of dislocation density with stress for a given number of cycles and heat-treatment.

Table 3.16 Dislocation densities in uniaxial strain-controlled coupons

	Specimen	# of Fatigue cycle	Dislocation density (m^{-2})	Standard Deviation
Unconditioned	SS_Unconditioned	0	2.6E+14	3.44E+13
	SS_sn11	5	4.93E+14	2.92E+13
	SS_sn12	20	3.12E+14	6.23E+13
	SS_sn01	234	N/A	N/A
Annealed at 800°C	SS_800	0	1.02E+14	3.16E+13
	SS_sn13	5	2.02E+14	2.48E+13
	SS_sn14	20	3.09E+14	5.09E+13
	SS_sn05	100	2.14E+14	2.16E+13
Annealed at 1050°C	SS_1050	0	5.57E+13	9.83E+12
	SS_sn15	5	1.85E+14	2.79E+13
	SS_sn16	20	1.43E+14	4.47E+13
	SS_sn07	100	1.92E+14	3.9E+13

Figure 3.48 is a graphical representation of the dislocation density measured from uniaxial strain controlled test versus number of fatigue cycles. Dislocation density of all specimens tends to increase when cyclic load is applied, and then decrease after a certain number of cycles. This trend means distributions of the dislocation density as a function of number of cycles correspond to stress response of fatigue test which shows hardening and softening stages. Figure 3.49 shows dislocation density as a function of maximum stress amplitude (σ_{xc}) and heat-treatment temperature (T_m). Each data point in the Figure is gathered from a large number of TEM images in the same specimen. It can be seen that increasing heat-treatment temperature correlates with decreasing maximum stress amplitude and dislocation density. It is also shown that dislocation density increases with increasing

maximum stress amplitude at every cycle. Stress proportionally correlates with the square root of dislocation density as following Taylor relationship,

$$\sigma = \alpha G b \sqrt{\rho} \quad (4)$$

where σ is stress, α is dimensionless strength factor, G is shear modulus, b is burgers vector, and ρ is mobile dislocation density in channel. Figure 3.50 shows reasonable fit of this relation:

$$b\sqrt{\rho} = \frac{1}{\alpha} \left(\frac{\sigma}{G} \right) = 0.807x$$

where $G = 73\text{GPa}$

$$b = \frac{a}{\sqrt{2}} = 2.5 \times 10^{-10} \text{ m}$$

General value of shear modulus (G) of SS 304 is $7.3 \times 10^4 \text{ MPa}$, and burgers vector (b) is $2.5 \times 10^{-10} \text{ m}$ for this material which has face-center cubic structure. Using these number, the strength factor (α) is ~ 1.24 . Thus, dislocation density increases during cyclic hardening stage and decreases during cyclic softening stage. According to this result it can be drawn that (1) a specimen experiences cyclic hardening until 5 cycles and then softening until 20 cycles for unconditioned, (2) cyclic hardening up to 20 cycles and softening after 20 cycles for 800°C heat-treatment temperature, and (3) cyclic hardening until 5 cycles, softening up to 20 cycles, and then hardening again after 20 cycles for 1050°C heat-treatment temperature. Figure 3.51 represents mean value of dislocation density as a function of heat-treatment temperature and has the characteristic of dislocation density decreasing with increasing heat-treatment temperature (Figure 3.49).

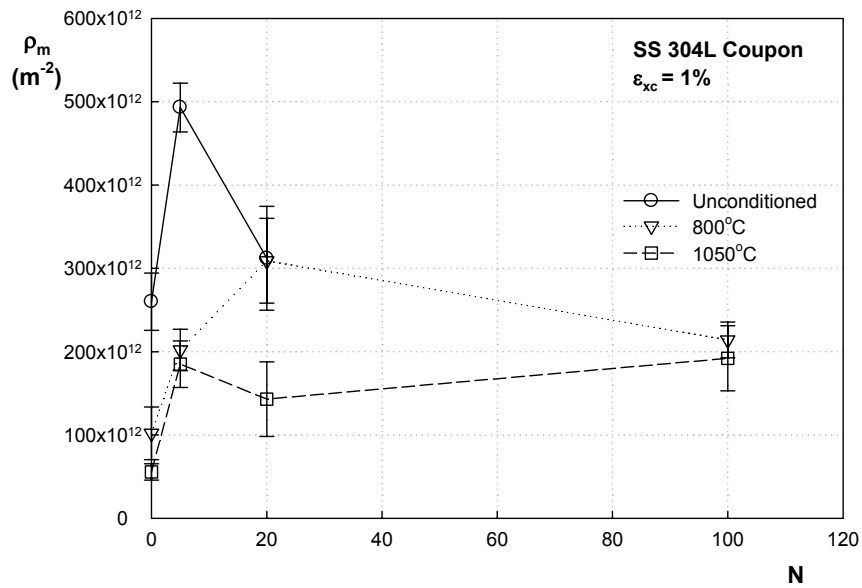
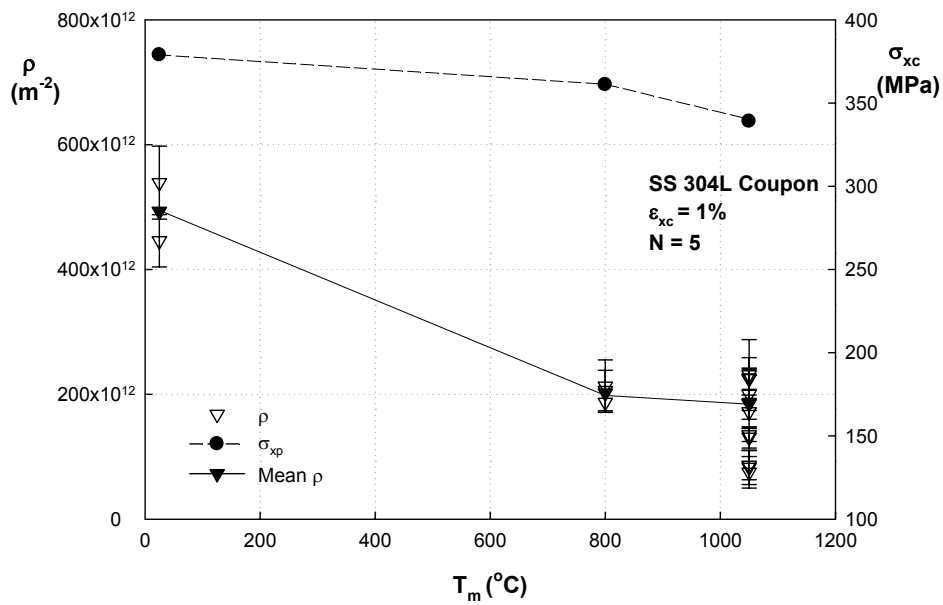
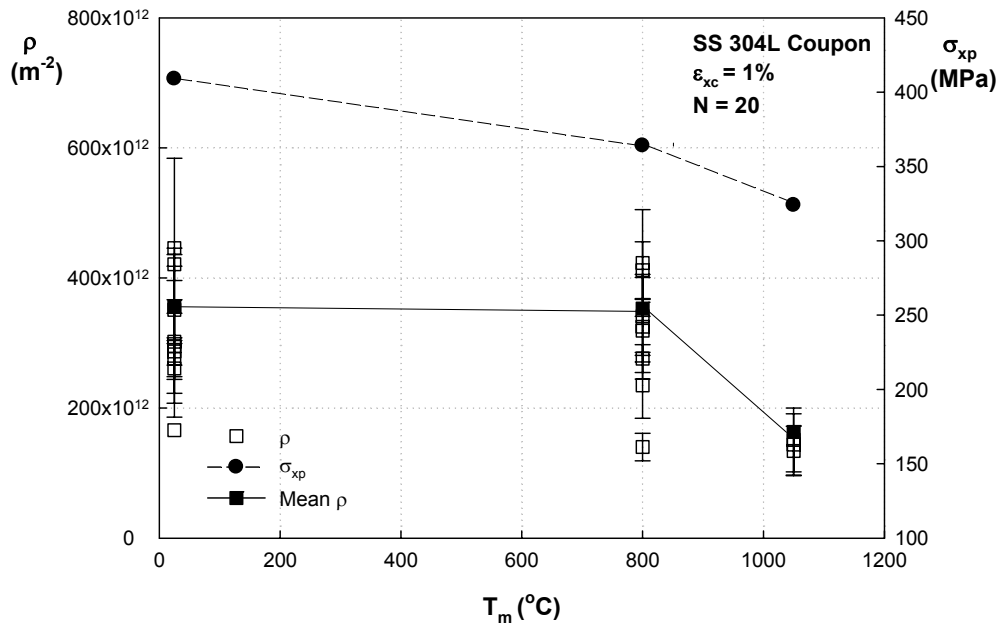


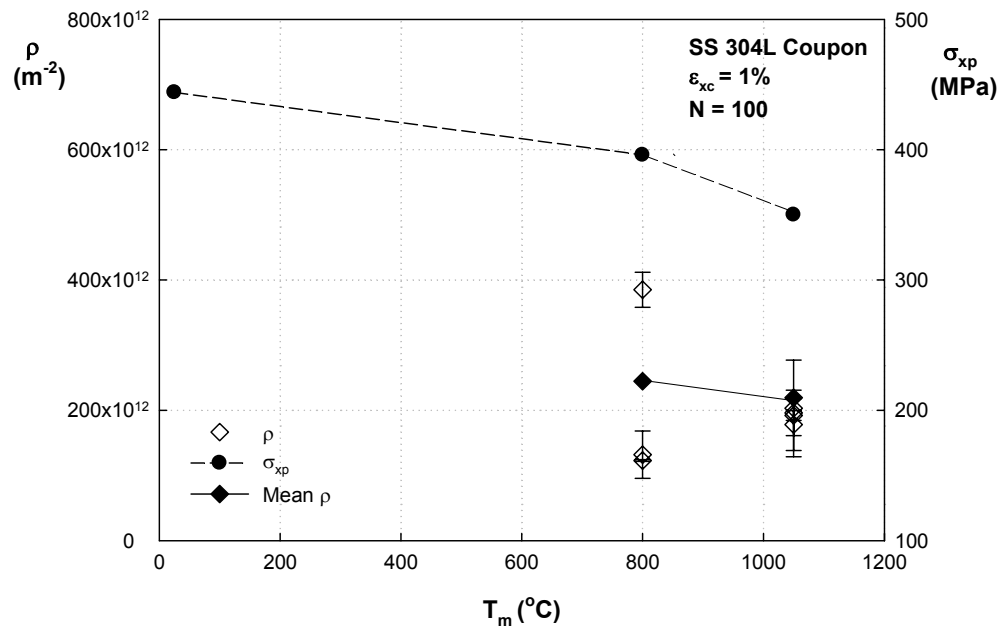
Figure 3.48 Mean of Dislocation density (ρ_m) vs. Number of cycles (N) for different heat-treatment temperature



(a)



(b)



(c)

Figure 3.49 Dislocation density (ρ) as a function of axial peak stress (σ_{xp}) and heat-treatment temperature (T_m) at (a) 5 cycles, (b) 20 cycles, and (c) 100 cycles

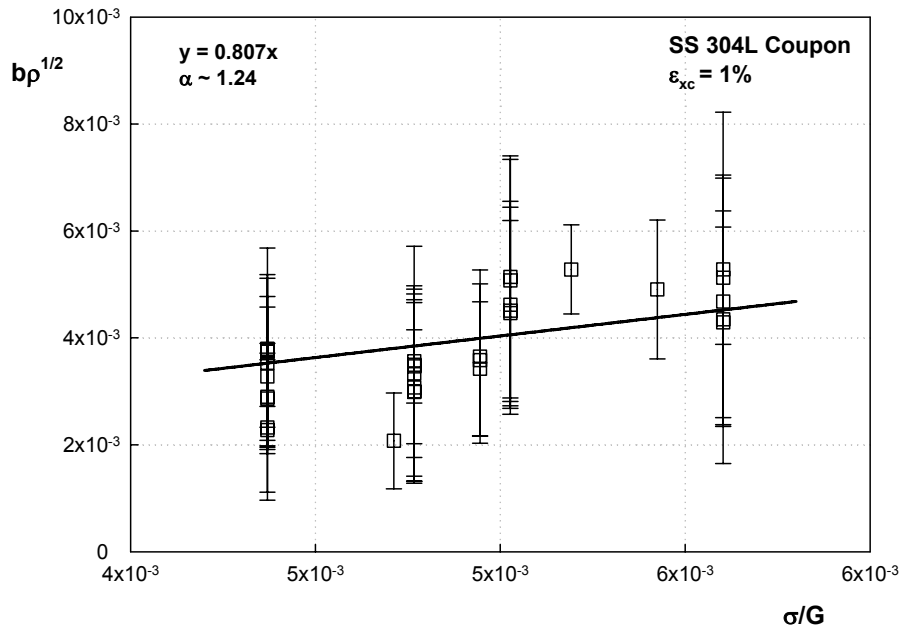


Figure 3.50 Linear relation between dislocation density and stress amplitude in uniaxial strain-controlled specimens

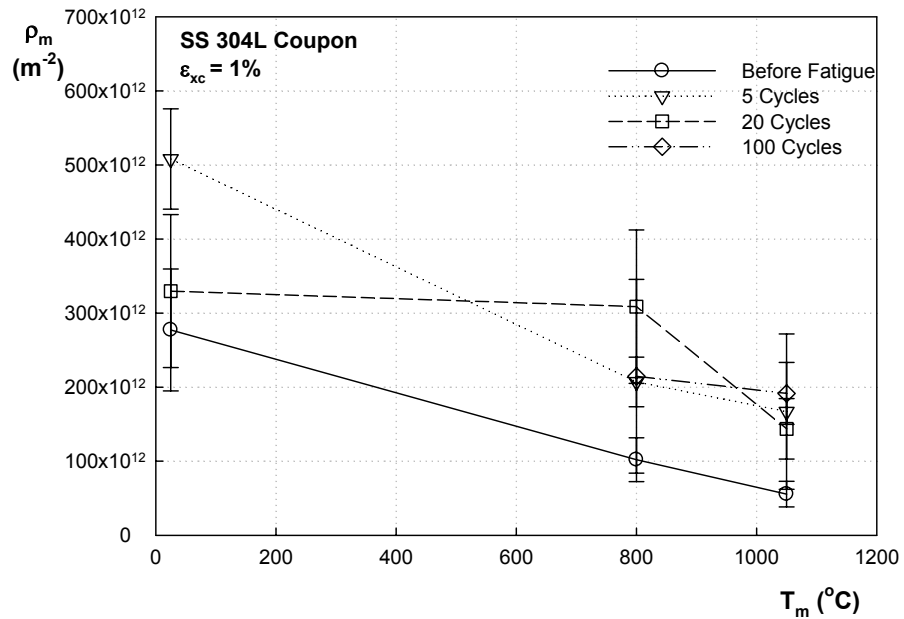


Figure 3.51 Mean of Dislocation density (ρ_m) vs. Heat-treatment temperature (T_m) at different cycles

3.5.2.2 Dislocation Density in Biaxial Ratchetting Specimens

Table 3.17 shows the data obtained for dislocation density for biaxial ratchetting specimens. Dislocation density was measured from several regions in each specimen for good statistics.

Table 3.17 Dislocation density of biaxial ratchetting coupons

Specimen	Region	Dislocation density (m^{-2})	Standard deviation
Unconditioned (2000 cycles)	2	4.41E+14	5.09E+13
	4	3.36E+14	3.46E+13
	5	1.59E+14	4.33E+13
	Mean	3.12E+14	4.29E+13
Annealed at 800°C (1482 cycles)	2	1.59E+14	2.43E+13
	3	2.82E+14	3E+13
	4	1.93E+14	5.74E+13
	1_2	9.87E+13	7.29E+12
	1_3	3.35E+14	7.17E+13
	Mean	2.14E+14	3.81E+13
Annealed at 1050°C (2000 cycles)	1	1.14E+14	4.5E+13
	2	1.2E+14	3.31E+13
	3	1.06E+14	2.18E+13
	6	8.52E+13	2.68E+12
	8	6.1E+13	1.86E+13
	5	9.21E+13	2.79E+13
	4	4.54E+13	1.78E+12
	Mean	8.92E+13	2.16E+13

Figure 3.52 shows a plot of dislocation density dependent on heat-treatment temperature and maximum stress amplitude. It is also observed that dislocation density

decreases with increasing heat-treatment temperature and decreasing maximum stress amplitude. The reason of this result is expected from the change of dislocation structure following different heat-treatment temperatures. In biaxial ratcheting specimen, it is also shown reasonable fit of relation between stress and dislocation density in Figure 3.53. The strength factor (α) is ~ 1.19 calculated by equation;

$$b\sqrt{\rho} = \frac{1}{\alpha} \left(\frac{\sigma}{G} \right) = 0.84x$$

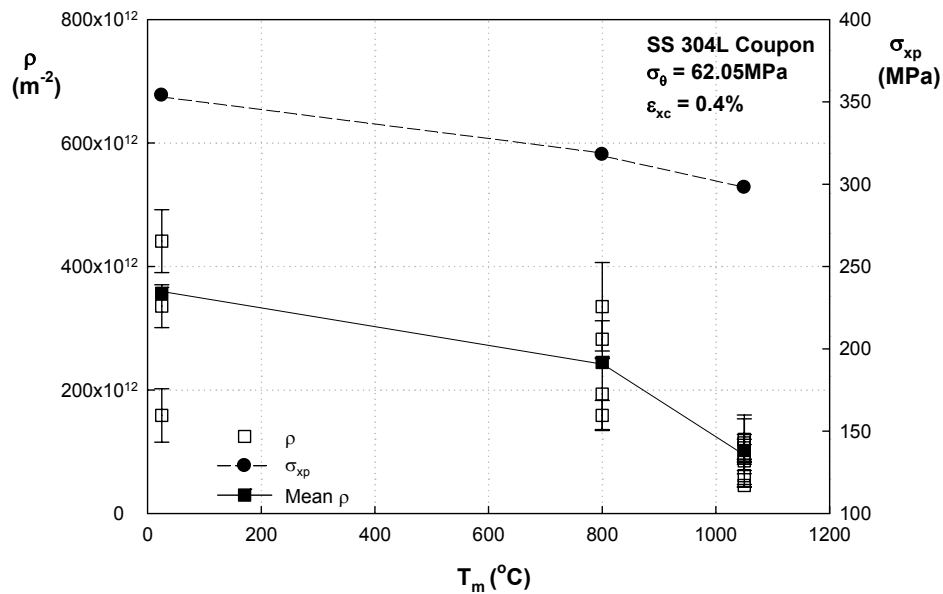


Figure 3.52 Dislocation density (ρ) as a function of axial peak stress (σ_{xp}) and heat-treatment temperature (T_m)

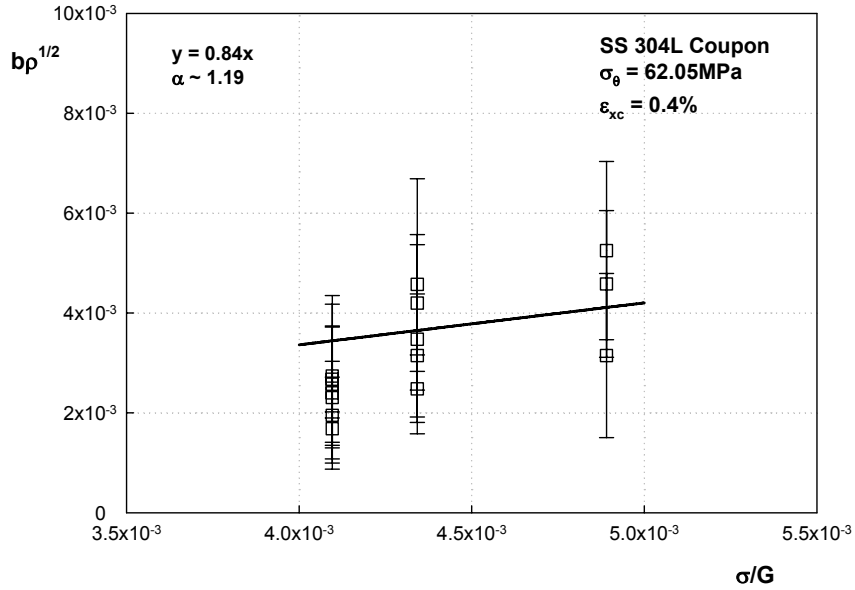


Figure 3.53 Linear relation between dislocation density and stress amplitude in biaxial ratcheting specimens

3.5.2.3 Dislocation Density in Uniaxial Force Controlled Specimens

Dislocation density gathered for uniaxial force-controlled test is shown in Table 3.18. Two types of test specimens, with zero mean stress (non-ratcheting) and with positive mean stress (ratcheting) were used to compare non-ratcheting against ratcheting. The results are summarized in Table 3.18 and are depicted in Figure 3.53.

Table 3.18 Dislocation density of Uniaxial Force-controlled coupons

Non-Ratchetting			Ratchetting		
Region	Dislocation Density (m ⁻²)	Standard Deviation	Region	Dislocation Density (m ⁻²)	Standard Deviation
1_1	1.15E+14	8.72E+13	1_1	1.5E+14	3.02E+13
1_2	1.82E+14	6.32E+13	1_2	2.48E+14	2.18E+13
1_3	1.17E+14	1.2E+13	1_4	2.29E+14	5.74E+13
1_4	1.33E+14	3.11E+13	1_5	1.77E+14	4E+13
1_6	1.12E+14	2.21E+13	1_6	3E+14	2.82E+13
1_7	7.11E+13	1.73E+13	1_7	2.13E+14	7.37E+13
1_10	4.77E+13	1.81E+13	1_8	2.08E+14	5.23E+13
1_11	8.75E+13	5E+13	1_9	2.26E+14	3.45E+13
1_13	1.02E+14	1.91E+13	1_10	1.72E+14	5.68E+13
1_14	4.38E+13	1.34E+13	2_1	1.66E+14	2.48E+13
1_15	8.44E+13	4.5E+13	2_2	7.74E+13	1.41E+13
			2_3	1.45E+14	3.29E+13
			2_4	1.65E+14	7.56E+13
			2_5	1.89E+14	7.22E+13
			2_6	1.48E+14	4.89E+13
			2_8	7.81E+13	1.61E+13
			2_10	1.79E+14	6.57E+13
			2_11	1.57E+14	4.07E+13
			2_12	1.25E+14	4.62E+13
			2_13	1.47E+14	3.58E+13
Mean	9.95E+13	3.44E+13	Mean	1.75E+14	4.34E+13

Figure 3.54 reveals that ratchetting specimen has higher dislocation density than non-ratchetting. From the microstructural observation, dislocation structures have relatively uniform cell structures although walls or boundaries are thick in no ratchetting specimen, while the dislocation structures of ratchetting specimen have poorly formed dislocation cell

structures. Therefore, more dislocations remained in the matrix that caused increasing density of dislocations in ratcheting specimen.

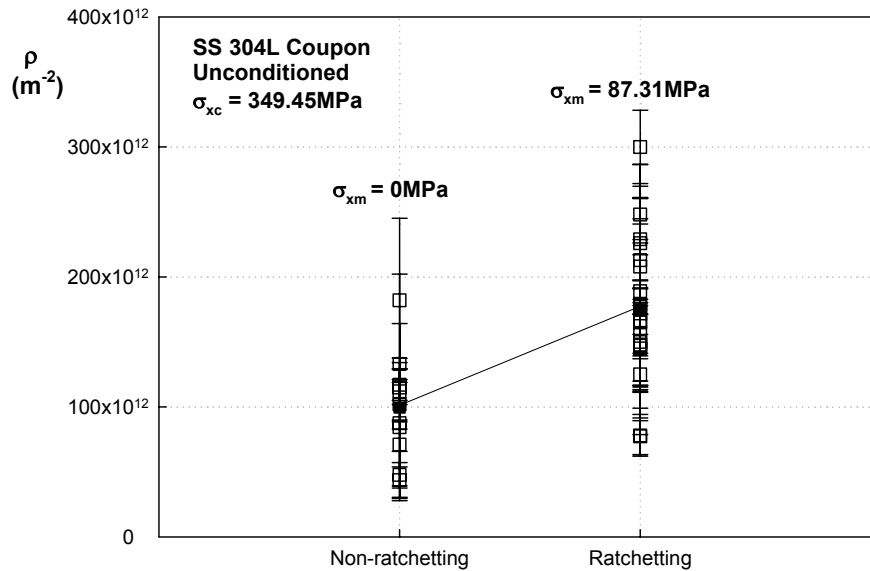


Figure 3.54 Dislocation density (ρ) in unaxial force-controlled (Non-ratchetting vs. Ratchetting) experiments

3.5.2.4 Dislocation Density in Welded Pipe Specimens

Dislocation density of welded pipe specimens with different fatigue cycle is measured at 3mm away from weld toe. Also, welded pipe specimen subjected to 20 cycles test was taken to note the dislocation density at different positions from the weld toe on the top of specimen. Dislocation density was measured in several areas of each specimen. Mean values of measured dislocation density of welded pipe specimens is shown in Table 3.19. Original data of dislocation density measured in every region taken from TEM are included in appendix.

Table 3.19 Dislocation density in welded pipe specimens

Specimen	Cycles	Location (Away from weld toe)	Dislocation density (m^{-2})	Standard Deviation
SSPC4	5	3mm	2.47E+14	5.59E+13
SSPC2	20	3mm	2.56E+14	6.23E+13
		9.8mm	1.86E+14	3.76E+13
		38mm	1.73E+14	5.19E+13
SSPC3	100	3mm	2.46E+14	4.22E+13
SSPC5	2679	3mm	1.38E+14	2.75E+13

Figure 3.55 shows dislocation density measured at 3mm from the weld toe as a function of number of cycles. At 5, 20, and 100 cycles of dislocation density is relatively higher than that following 2679 cycles. This consequence is noted in terms of more cell and wall structures are developed at 2679 cycles, which means dislocations tend to be condensed in the walls and thus the channels become relatively dislocation free (Figure 3.47). Dislocation density at different locations of the welded pipe specimen is graphically noted in Figure 3.56. It is seen that dislocation density decreases for location away from the weld toe due to proportion of tangles and planar slip mentioned in Table 3.11.

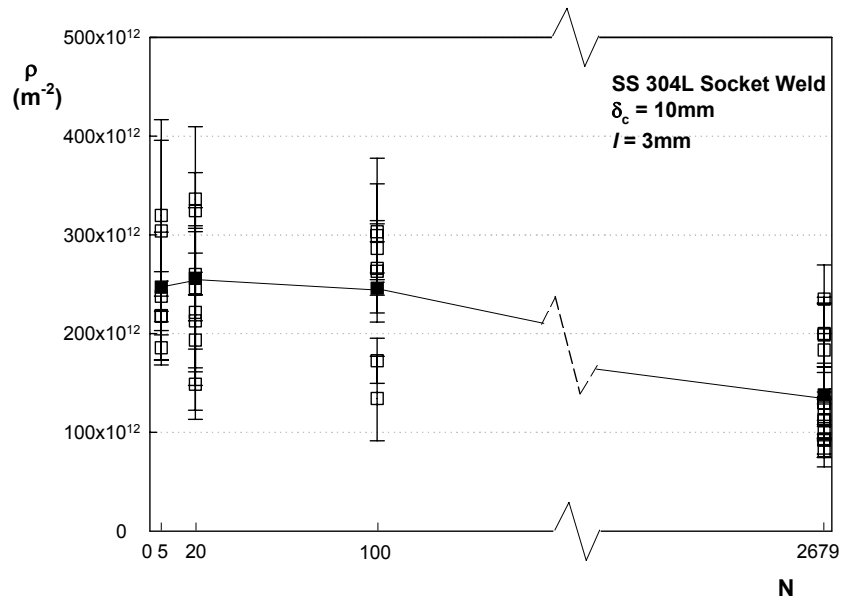


Figure 3.55 Dislocation density (ρ) as a function of the number of cycles (N)

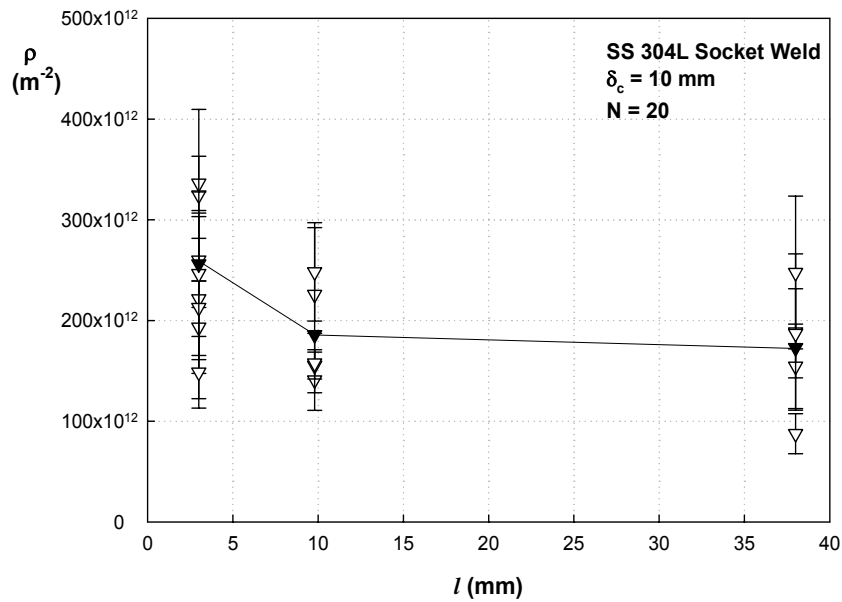


Figure 3.56 Dislocation density (ρ) vs. Location (l) from weld toe

3.5.3 Dislocation Cell Size Measurement

A mean diameter of dislocation cells was calculated by measuring the width of each

cell two times because all of the cell structures do not show equiaxed cell structure. Some of cell sizes were roughly determined from tangles which did not form good cell structure but almost formed cell structure.

3.5.3.1 Dislocation Cell Size in Uniaxial Strain controlled Specimens

Figures 3.57 – 3.59 show cell structure represented in the specimen with different conditions. Mean cell diameters of unconditioned specimen are $0.3\ \mu\text{m}$ after 5 cycles (Figure 3.57 (a)) and $0.27\ \mu\text{m}$ after 20 cycles (Figure 3.57 (b)). At 800°C heat-treatment temperature mean cell diameters of $0.33\ \mu\text{m}$, $0.26\ \mu\text{m}$, and $0.48\ \mu\text{m}$ corresponding to 5, 20, and 100 cycles are measured from Figure 3.58. Figure 3.59 includes cell structures for 1050°C heat-treatment temperature. Each mean cell diameter is $0.26\ \mu\text{m}$ (Figure 3.59 (a)), $0.23\ \mu\text{m}$ (Figure 3.59 (b)), and $0.28\ \mu\text{m}$ (Figure 3.59 (c)). Data collected from all cell structures of uniaxial strain controlled specimen are included in Table 3.20.

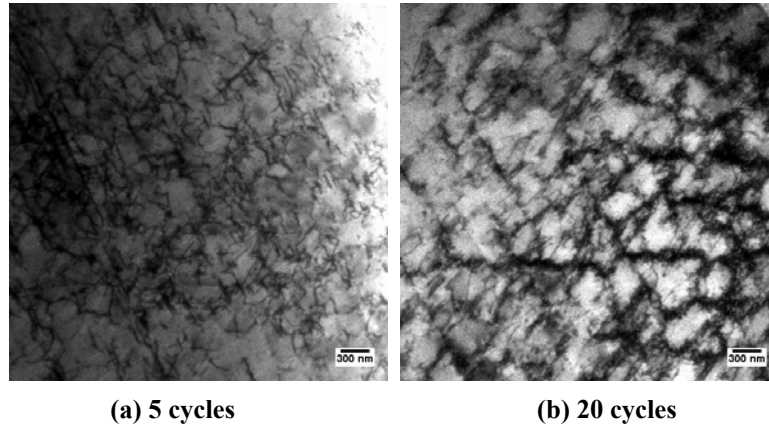
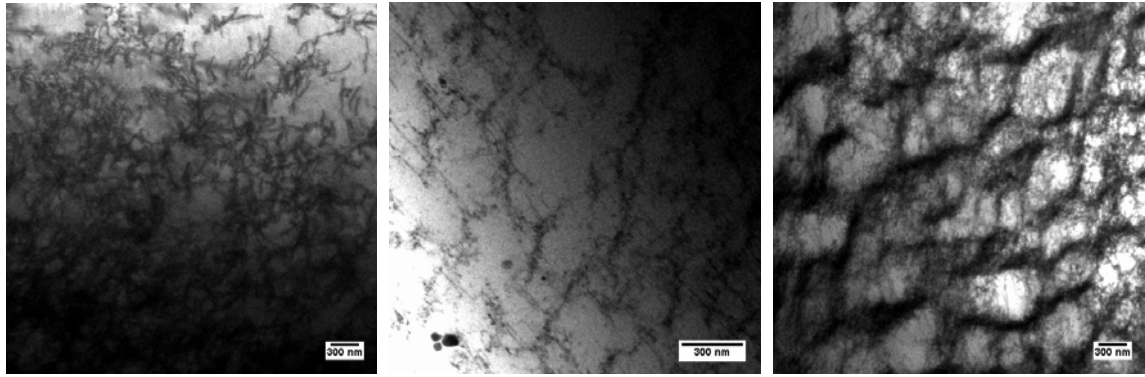


Figure 3.57 Representative cell structure after (a) 5 cycles and (b) 20 cycles in unconditioned specimen

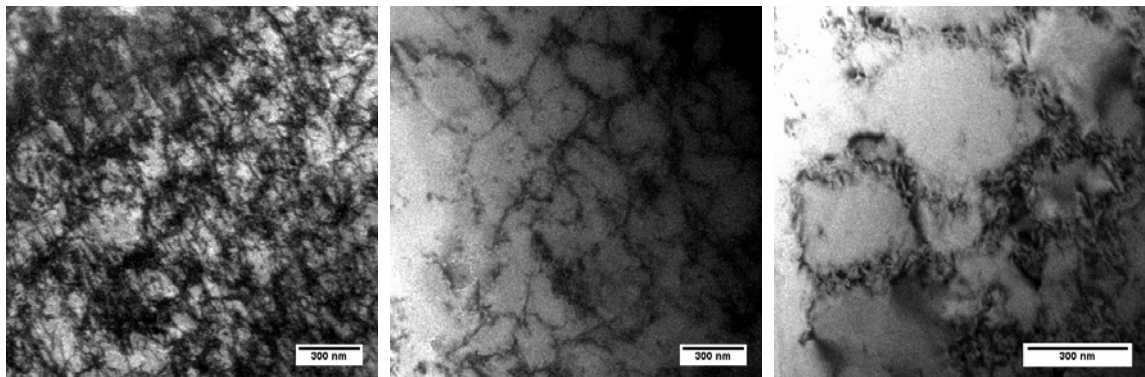


(a) 5 cycles

(b) 20 cycles

(c) 100 cycles

Figure 3.58 Representative cell structure after (a) 5 cycles, (b) 20 cycles, and (c) 100 cycles in 800°C heat-treated specimen



(a) 5 cycles

(b) 20 cycles

(c) 100 cycles

Figure 3.59 Representative cell structure after (a) 5 cycles, (b) 20 cycles, and (c) 100 cycles in 1050°C heat-treated specimen

Table 3.20 Data of dislocation cell diameter for uniaxial strain-controlled tests

	Specimen	Region	Mean cell diameter (μm)	Std. (μm)
Unconditioned temperature	5 cycles	8_2	0.3	0.08
	20 cycles	3_2	0.28	0.06
		3_1	0.3	0.04
		7_1	0.22	0.02
		Mean	0.27	0.04
	100 cycles	N/A	N/A	N/A
Annealed at 800°C	5 cycles	1_1	0.37	0.08
		3_1	0.3	0.03
		Mean	0.33	0.05
	20 cycles	1_5	0.21	0.03
		2_1	0.28	0.06
		2_11	0.3	0.03
		Mean	0.26	0.04
	100 cycles	1	0.48	0.1
		2	0.49	0.11
		Mean	0.48	0.105
Annealed at 1050°C	5 cycles	5_2	0.26	0.06
	20 cycles	2_1	0.23	0.06
	100 cycles	7_1	0.28	0.11

The correlation between mean cell size and the number of cycles is depicted in Figure 3.60. Mean cell size at all temperature conditions decreases until 20 cycles, and then slightly increases at 100 cycles. As mentioned in section 3.1, stress amplitude response of uniaxial strain controlled test shows hardening stage up to 20 cycles and softening stage after 20 cycles. Thus, it can be concluded that cell size decreases with cyclic hardening and increases with cyclic softening. To examine the relationship between cell size and hardening,

cell size as a function of dislocation density is shown in Figure 3.61. It is observed that mean cell size is proportional or almost constant to increasing dislocation density even though dislocation density increases during the hardening where cell size decreases. The inverse relationship between cell size and flow stress in both monotonic and cyclic deformation was reported by Kayali et al. (1982) and established by following equation.

$$\Delta\sigma = \frac{k}{\delta} \quad (5)$$

where $\Delta\sigma$ is flow stress, k is empirical constant for material which is equal to αGb , and d is cell size. The strength constant (α) can be determined using relation between stress and cell size in Figure 3.62. Using this relationship, $\frac{\delta}{b} = \alpha \left(\frac{G}{\sigma} \right) = 6.47x$. The strength constant (α) in uniaxial strain-controlled specimen is about 6.47. It can be also pointed out that mean cell size increases with increasing dislocation density even though dislocation density increases during the hardening where cell size decreases. Figure 3.63 shows mean cell size versus heat-treatment temperature. The mean cell size is almost constant for unconditioned and 800°C but decreases at 1050°C heat-treatment temperature although stress amplitude is the lowest at this temperature.

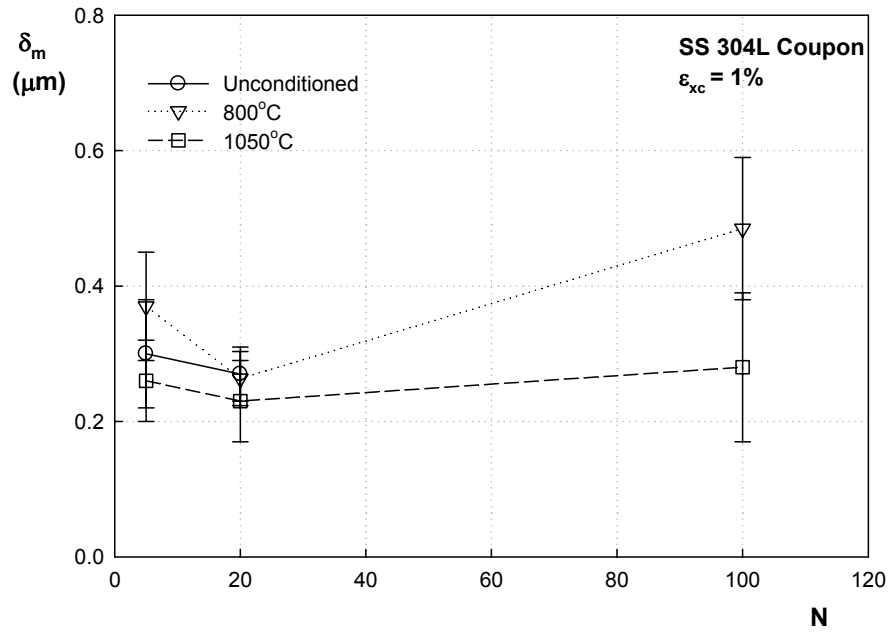


Figure 3.60 Mean cell size (δ_m) vs. Number of fatigue cycles (N)

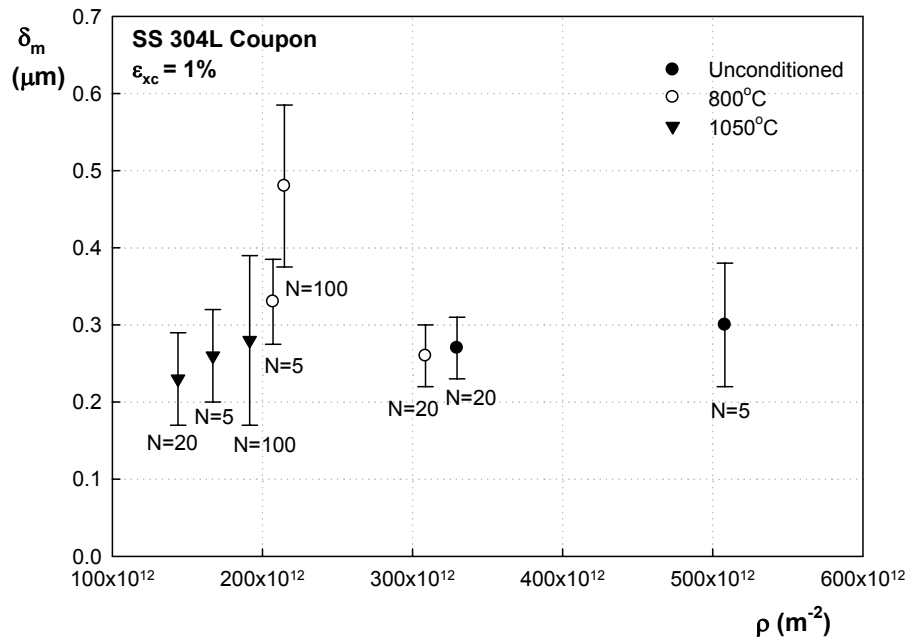


Figure 3.61 Mean cell size (δ_m) as a function of dislocation density (ρ)

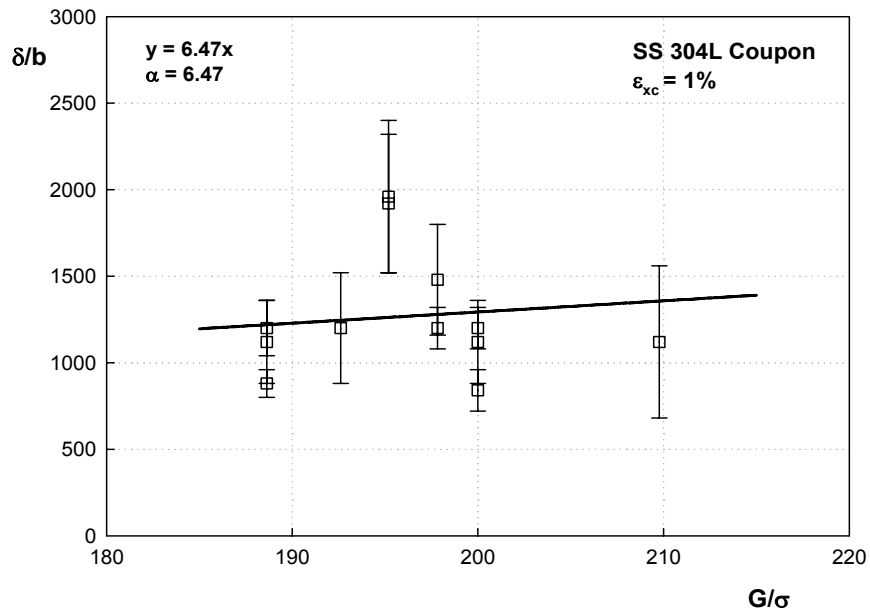


Figure 3.62 Linear relation between stress and cell size in uniaxial strain-controlled specimen

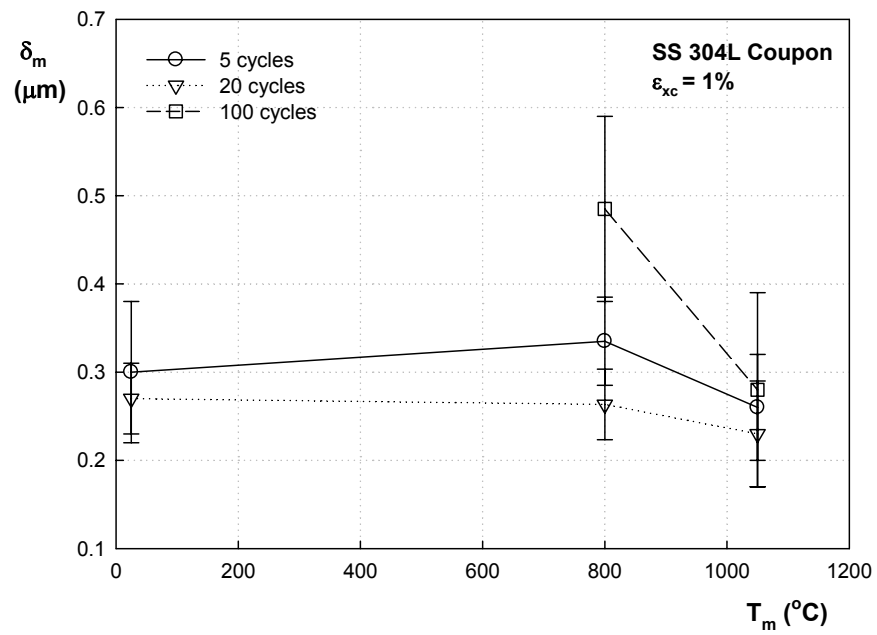


Figure 3.63 Mean cell size (δ_m) vs. Heat-treatment temperature (T_m)

3.5.3.2 Dislocation Cell Size in Biaxial Ratcheting Specimens

Figure 3.64 shows example of cell structure of biaxial ratcheting specimens. Mean cell size is $0.43\mu\text{m}$ for unconditioned material, $0.51\mu\text{m}$ for 800°C heat-treatment temperature, and $0.64\mu\text{m}$ for 1050°C heat-treatment temperature. Mean cell size increases with increasing heat-treatment temperature as shown in Figure 3.65. It is presented in Figure 3.66 that mean cell size is inversely proportional to stress amplitude and dislocation density. In Figure 3.67, the relation between cell size and stress amplitude shows $\frac{\delta}{b} = \alpha \left(\frac{G}{\sigma} \right) = 9.36x$. The strength constant (α) is ~ 9.36 which is slightly different value of uniaxial strain-controlled specimen.

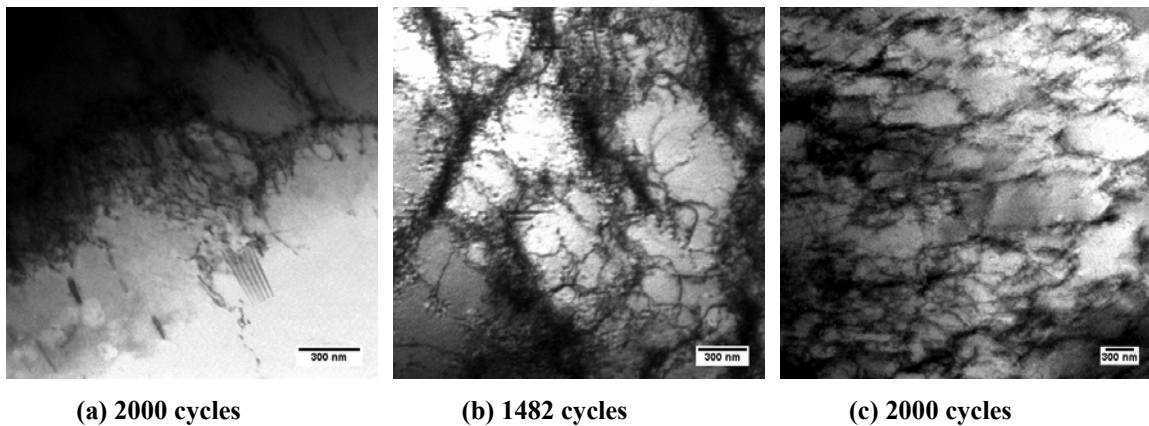


Figure 3.64 Representative cell structure after 2000 cycles in (a) unconditioned material, (b) 800°C heat-treatment temperature, and (c) 1050°C heat-treatment temperature

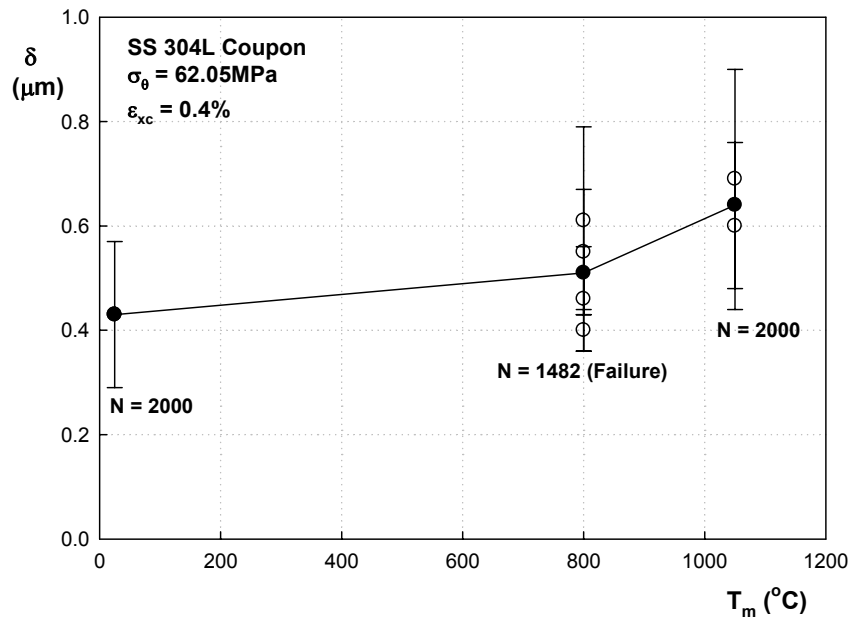


Figure 3.65 Cell size (δ) vs. Heat-treatment temperature (T_m) at 2000 cycles

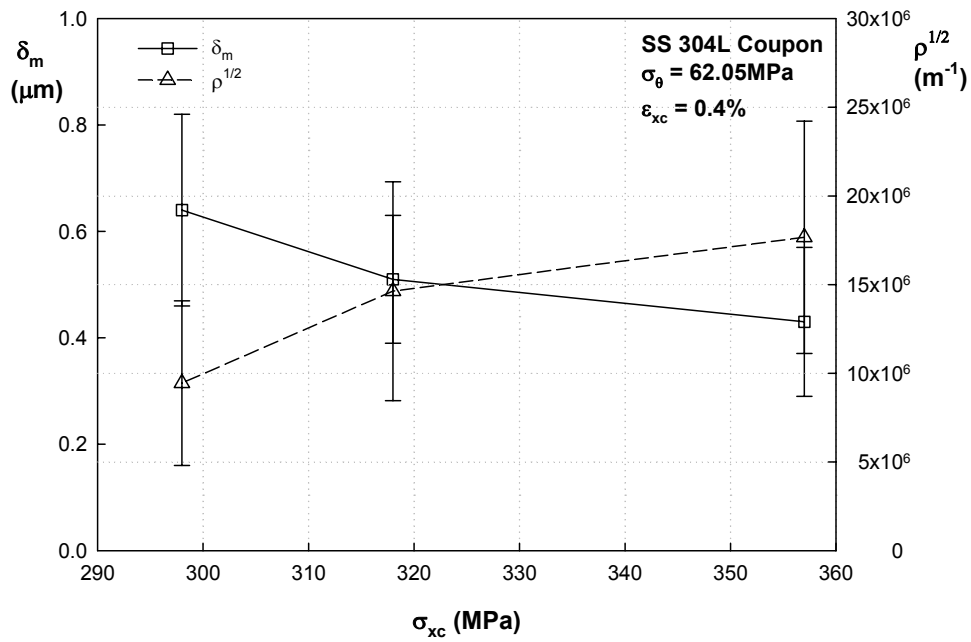


Figure 3.66 Mean cell size (δ_m) as a function of stress amplitude (σ_{xc}) and dislocation density (ρ)

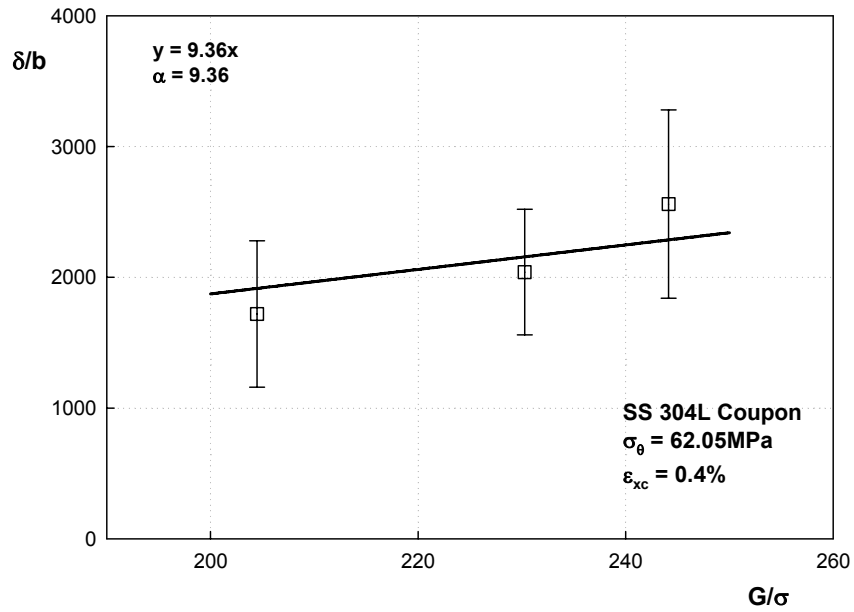
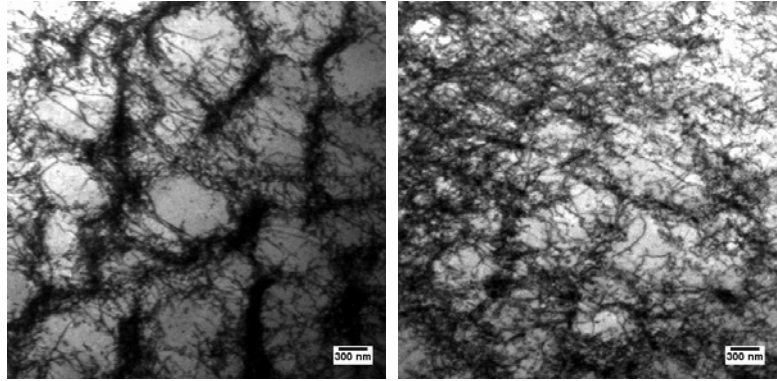


Figure 3.67 Linear relation between stress and cell size in biaxial ratcheting specimen

3.5.3.3 Dislocation Cell Size in Uniaxial Force Controlled Specimens

Figure 3.68 shows representative cell structure of non-ratchetting and ratchetting specimen subjected to uniaxial force controlled test. $0.67\mu\text{m}$ of mean cell size is measured from non-ratchetting specimen. Mean cell size of ratchetting specimen is $0.53\mu\text{m}$. Six regions of non-ratchetting specimen and four regions of ratchetting specimen are taken to measure the cell sizes (Figure 3.69). Mean cell size of non-ratchetting specimen is larger than that of ratchetting specimen because cell structures in non-ratchetting specimen are more uniformly formed, and fewer dislocations remain in channel region than in ratchetting specimen.



(a) No ratchetting

(b) Ratchetting

Figure 3.68 Representative cell structure of (a) non-ratchetting and (b) ratchetting in unconditioned material

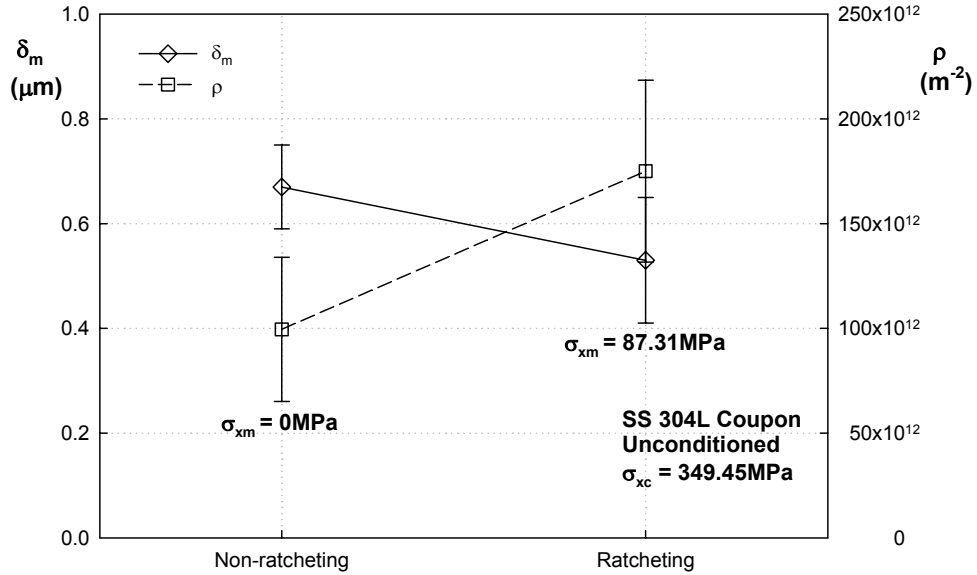


Figure 3.69 Mean cell size (δ_m) in uniaxial force-controlled (Non-ratchetting vs. Ratchetting) experiments

CHAPTER 4 Conclusions and Recommendations

This study made an effort to understand the fatigue failure of socket welded joints of 304L stainless steel pipe. Microstructures of the base metal at weld toe and various locations from the toe are examined. For a better understanding of microstructural observation at the weld toe under fatigue loading, tubular specimens were heat treated to simulate different locations of the weld toe and subjected to various fatigue loading cycles.

Socket welded pipe was subjected to 10mm of displacement-controlled test. Stress response of welded pipe specimen showed cyclic hardening initially until 20 fatigue cycles followed by cyclic softening. Mean and amplitude of strain response data near the weld toe showed ratcheting at the weld toe that is believed to arise from microstructure gradient in the heat affected zone of the welded pipe. Hence, microstructures were examined to determine how ratcheting strain influences dislocation structures in the welded pipe specimen and initiates fatigue cracks. Grain size and hardness at three different locations (3mm, 9.8mm, and 38mm from the weld toe) of the welded pipe specimen did not show significant changes, which indicating that the welding process has minimal influence on the grain size and hardness.

In order to investigate the microstructure evolution of ratcheting fatigue phenomenon fatigue tests of welded pipe specimens were made with different cycles at the weld toe. At the microstructure level, different welded pipe specimens subjected to different fatigue cycles showed varied dislocation microstructures near the weld toe. As the number of fatigue cycles is increased, increased number of dislocation cell and wall structures are formed and in contrast planar slip decreased. After 5 cycles no cell structure is noted, but tangles and high

percentage of planar slip are observed. After 20 cycles, tangles are predominant, and structure started to form dislocation cells. After 100 cycles, planar slip and tangles decrease with increasing cell structure. After 2679 cycles, when fatigue crack initiated, not only cell but also wall structure is observed. However, these cell and wall structures are not well defined because walls were poorly formed while dislocations remained in the channel. At 3mm from the weld toe, dislocation density gradually increases up to 20 cycles and then decreases until 2679 cycles. This could be explained by the cyclic stress response that showed initial cyclic hardening followed by cyclic softening.

Then for a specimen subjected to 20 cycles, we studied microstructure evolution at different locations with respect to the weld toe of the specimen. Small proportion of cell structure and high proportion of tangles are observed near the weld toe. At locations far from the weld toe, cells are not visible, but reduced tangle and increased planar slip are observed. Thus, dislocation density decreases far away from the weld toe. Relatively more heterogeneous dislocation microstructures such as tangles, cells and walls are noted as number of fatigue cycles increases and also close to the weld toe.

The coupon specimens were subjected to different cycles of uniaxial strain-controlled, uniaxial force-controlled, and biaxial ratcheting tests following different heat-treatments. Stress response of uniaxial strain-controlled test shows cyclic hardening and softening dependent on the number of fatigue cycles. In addition, maximum stress amplitude decreases with increasing heat-treatment temperature. Grain size became larger and elongated at 1050°C. However, fatigue loading did not affect the grain size. Hardness increased with number of cycles, but short heat-treatment time (5 minutes) did not change

hardness. Before applying cyclic loading, dislocation structure of all coupons showed very high percentage of randomly distributed dislocations with a small amount of stacking faults. Various kinds of dislocation structures were observed during fatigue cycle tests. Planar slip and tangles decrease with increasing number of cycles, and cell structures increased at the same time for unconditioned and 800°C heat-treated coupons. However, relatively high percentage of planar dislocations remained although cell structures increased when fatigue cycles increased for 1050°C heat-treated coupon. Dislocation density increased with increasing maximum stress amplitude but reduced as heat-treatment temperature increased. According to the relationship between dislocation density and maximum stress amplitude, dislocation density increased during cyclic hardening and decreased during cyclic softening. Cell size decreased with hardening and increased with softening. However, the coupon heat-treated at 800°C showed cell size decreasing with increasing maximum stress amplitude proportionally with the square root of dislocation density.

Strain response of uniaxial force-controlled test showed axial ratcheting strain when positive mean stress is imposed on the coupon, while no ratcheting strain is observed under zero mean stress case. Ratcheting and non-ratcheting coupons of uniaxial force-controlled tests showed similar proportion of dislocation structures. However, cell and wall structures of non-ratcheting coupons were well defined, while dislocations of ratcheting coupons were not well condensed into walls and cell boundaries. This is mainly because of the significantly more mobile dislocations under uniaxial ratcheting. For the specimen of uniaxial ratcheting, more dislocations are observed in the channel and hence the higher dislocation density.

In the biaxial ratcheting tests, ratcheting strain in hoop direction was observed in

unconditioned, 800°C, and 1050°C heat-treated coupons. In the 1050°C heat-treated coupon under biaxial ratcheting test, grain growth was noted with increased ratcheting strain. However, there is no significant difference in hardness following different heat-treatment temperatures. Dislocation cells and walls dominated structures of biaxial ratcheting coupons. A significant observation made was high percentage of dislocation wall structures in 1050°C heat-treated coupon. Dislocation density decreased as heat-treatment temperature increased. Cell size decreased with increasing maximum stress amplitude and dislocation density.

New observation related to uniaxial ratcheting needs to be further studied for different cycles and temperatures in order to understand its influence on crack initiation. For biaxial ratcheting we have studied different temperature but only at large cycle, and thus more studies at different cycles 0, 5, 20, and 100 and at different temperatures need to be conducted. For welded joints, the closest location to weld toe that we studied is 3mm. However, it was observed that all the fatigue cracks initiated exactly at the weld toe. Hence, dislocation microstructure studies of welded joints should focus at or very close to the weld toe materials.

REFERENCES

- Altenberger, I., Scholtes, B., Martin, U., Oettel, H., 1999, *Cyclic Deformation and Near Surface Microstructures of Shot Peened or Deep Rolled Austenitic Stainless Steel AISI 304*, Material Science and Engineering A, 264, 1-16.
- Bocher, L., Delobelle, P., Robinet, P., Feaugas, X., 2001, *Mechanical and Microstructural Investigations of an Austenitic Stainless Steel under Non-proportional Loadings in Tension-torsion-internal and External Pressure*, International Journal of Plasticity, 17, 1491–1530.
- Chiu, P.K., Wang, S.H., Yang, J.R., Weng, K.L., Fang, J., 2006, *The Effect of Strain Ratio on Morphology of Dislocation in Low Cycle Fatigued SAF 2205 DSS*, Material chemistry and physics, 98, 103-110.
- Choi, Y.H., Choi, S.Y., 2007, *Socket Weld Integrity in Nuclear Piping under Fatigue Loading Condition*, Nuclear Engineering and Design, 237, 213-218.
- Dieter, G. E., 1986, *Mechanical metallurgy*, McGraw-Hill series in material Science and engineering, New York.
- EPRI, 1998, *Reactor Piping Failures at U.S. Commercial LWRs; 1961-1997*, EPRI TR-110102.
- Feaugas, X., 1999, *On the Origin of the Tensile Flow Stress in the Stainless Steel AISI 316 L at 300 K: back stress and effective stress*. Acta Mater., 47, 3617–3632.
- Gerland, M., Mendez, J., Violan, P., Ait Saadi, B., 1989, *Evolution of Dislocation Structures and Cyclic Behaviour of a 316L-type Austenitic Stainless Steel Cycled in vacuo at Room Temperature*, Materials Science and Engineering A, 118, 83-95.
- Gosselin, S., 2008, *Fatigue in Operating Nuclear Power Plants Components after 60 years*, Workshop on U.S. Nuclear Power Plant Life Extension Research and Development Issues, February 19-21, Bethesda, Maryland.

Ham, R.K., 1961, *The Determination of Dislocation Densities in Thin Films*, Philosophical Magazine, 6, 1183 – 1184.

Hassan, T., Lu, X., 2005, *A Fatigue Failure Mechanism of Welded Piping Joints*, ASME Pressure Vessels and Piping Division Conference, July 17-21, Denver, Colorado.

Humphreys, A.E., 2004, *Influence of Residual Stress on the Initiation of Fatigue Cracks at Welded Piping Joints*, MS Thesis, North Carolina State University.

Kang, G., Liu, Y., Li, Z., 2006, *Experimental Study on Ratcheting-fatigue Interaction of SS304 Stainless Steel in Uniaxial Cyclic Stressing*, Material Science and Engineering A 435-436, 396-404.

Kang, G., Gao, Q., Cai, L., Sun, Y., 2002, *Experimental Study on Uniaxial and Nonproportionally Multiaxial Ratcheting of SS304 Stainless Steel at Room and High temperatures*, Nuclear Engineering and Design, 216, 13-26

Kayali, E.S., Plumtree, A., 1982, *Stress-Substructure Relationship in Cyclically and Monotonically Deformed Wavy Slip Mode Metals*, Metallurgical and Materials Transactions A, 13, 1033-1041.

Kulkarnia, S.C., Desai, Y.M., Kanta, T., Reddy, G.R., Parulekar, Y., Vaze, K.K., 2003, *Uniaxial and Biaxial Ratchetting Study of SA333 Gr.6 Steel at Room Temperature*, International Journal of Pressure Vessels and Piping, 80, 179–185.

Laird, C., Wang, Z., Ma, B.T., Chai, H.F., 1989, *Low Energy Dislocation Structures Produced by Cyclic Softening*, Material Science and Engineering A, 113, 245-257.

Llanes, L., Laird, C., 1993, *Substructure Evolution of Copper Polycrystals under Different Testing Conditions: Conventional Strain Control and Ramp Loading*, Material Science and Engineering A, 161, 1-12.

Lee, W., Lin, C., 2001, *Impact Properties and Microstructure Evolution of 304L Stainless Steel*, Materials Science and Engineering A, 308, 124-135.

Lu, X., 2003, *Influence of Residual Stress on Fatigue Failure of Welded Joints*, PhD Dissertation, North Carolina State University.

Maddox, S.J., 1991, *Fatigue Strength of Welded Structures*, Woodhead Publishing Ltd. Abington Hall, Abington.

Mayama, T., Sasaki, K., Kuroda, M., 2008, *Quantitative Evaluations for Strain Amplitude Dependent Organization of Dislocation Structures due to Cyclic Plasticity in Austenitic Stainless Steel 316L*, Acta Materialia, 56, 2735-2743.

Mughrabi, H., 1983. *Dislocation wall and cell structures and long-range internal stresses in deformed metal crystals*, Acta Metall. Mater. 31, 1367–1385.

Obertlík, K., Kruml, T., Polak, J., 1994, Dislocation Structures in 316L Stainless Steel Cycled with Plastic Strain Amplitudes over A Wide Interval , Material Science and Engineering A, 187, 1-9.

Vecchio, R.S., 1996, *Fatigue Evaluation of Socket Welded Piping in A Nuclear Power Plant*, ASME PVP 338, 25-41.

Xia, Y.B., Wang, Z.G., 1992, Low Cycle Fatigue Behaviour of New Type of Stainless Steel, Materials Science and Engineering A, 151, 29-35.

Xia, Z., Kujawski, D., Ellyin, F., 1996, *Effect of Mean Stress and Ratcheting Strain on Fatigue Life of Steel*, International Journal of Fatigue, 18, 335-341.

Yamashita, T., Hattori, T., Iida, K., Nomoto, T., Sato, M., 1997, *Effects of Residual Stress on Fatigue Strength of Small-Diameter Welded Pip Joint*, ASME Journal of Pressure Vessel Technology, 119, 428-434.

APPENDICES

A.1 Original data of dislocation density in uniaxial strain-controlled coupons unconditioned (See Table 3.16)

	Region	Dislocation density (m^{-2})	Standard deviation
0 cycles	1	2.16E+14	1.11E+13
	2	2.41E+14	1.59E+13
	3	2.94E+14	5.01E+13
	4	2.45E+14	9.59E+13
	5	1.9E+14	5.30E+12
	6	2.44E+14	4.33E+13
	7	4.23E+14	2.21E+13
	8	2.29E+14	3.12E+13
	Mean	2.6E+14	3.44E+13
5 cycles	7_2	4.46E+14	0
	8_2	5.39E+14	5.85E+13
	Mean	4.93E+14	2.92E+13
20 cycles	1_2	2.61E+14	3.83E+13
	2_1	1.66E+14	0
	2_2	4.46E+14	1.38E+14
	3_2	2.87E+14	7.96E+13
	4_2	4.21E+14	2.48E+13
	5_2	2.76E+14	2.77E+13
	6_2	3.51E+14	8.50E+13
	8_1	3.02E+14	1.16E+14
	9_1	2.95E+14	5.08E+13
	Mean	3.12E+14	6.23E+13

A.2 Original data of dislocation density in uniaxial strain-controlled coupons heat-treated at 800°C (See Table 3.16)

	Region	Dislocation density (m ⁻²)	Standard deviation
0 cycles	2_1	9.5E+13	2.87E+13
	2_2	1.08E+14	2.51E+13
	3_1	1.03E+14	4.1E+13
	Mean	1.02E+14	3.16E+13
5 cycles	1_1	2.06E+14	3.24E+13
	3_1	2.13E+14	4.2E+13
	2_1	1.87E+14	0
	Mean	2.02E+14	2.48E+13
20 cycles	1_3	1.4E+14	2.11E+13
	2_4	3.19E+14	4.81E+13
	2_5	2.76E+14	2.14E+13
	2_6	3.41E+14	6E+13
	2_7	4.23E+14	8.2E+13
	2_8	2.35E+14	5.07E+13
	2_10	3.25E+14	8.04E+13
	2_11	4.12E+14	4.37E+13
	Mean	3.09E+14	5.09E+13
100 cycles	1	3.85E+14	2.7E+13
	2	1.32E+14	3.63E+13
	1_1	1.23E+14	1.36E+12
	Mean	2.14E+14	2.16E+13

A.3 Original data of dislocation density in uniaxial strain-controlled coupons heat-treated at 1050°C (See Table 3.16)

	Region	Dislocation density (m ⁻²)	Standard deviation
0 cycles	7	6.89E+13	1.29E+13
	4	4.25E+13	6.77E+12
	Mean	5.57E+13	9.83E+12
5 cycles	1_2	1.72E+14	2.69E+13
	2_2	2.25E+14	1.69E+13
	3	7.51E+13	2.53E+13
	4	8.64E+13	2.34E+13
	4_2	2.31E+14	5.67E+13
	5	8.3E+13	2.76E+13
	6_2	2.26E+14	3.26E+13
	7	1.31E+14	1.7E+13
	7_2	1.35E+14	1.06E+13
	8	2E+14	4E+13
	5_2	4.67E+14	2.94E+13
	Mean	1.85E+14	2.79E+13
20 cycles	2_1	1.34E+14	3.79E+13
	3_1	1.51E+14	4.9E+13
	2	1.44E+14	4.71E+13
	Mean	1.43E+14	4.47E+13
100 cycles	11_2	1.78E+14	3.96E+13
	12_2	1.92E+14	7.52E+12
	13_2	1.96E+14	3.49E+13
	14_2	2.03E+14	7.41E+13
	Mean	1.92E+14	3.9E+13

A.4 Original data of dislocation density in welded pipe specimens (See Table 3.19)

Specimen	Cycles	Location	region	Dislocation density (m ⁻²)	Standard deviation
SSPC4	5	3mm	1_1	2.18E+14	1.95E+13
			1_2	2.38E+14	6.49E+13
			1_3	2.18E+14	4.45E+13
			3_1	3.04E+14	9.19E+13
			3_2	3.2E+14	9.7E+13
			3_3	1.86E+14	1.74E+13
			Mean	2.47E+14	5.59E+13
SSPC2	20	3mm	1_2	2.6E+14	4.69E+13
			3_2	3.36E+14	2.69E+13
			3_3	1.93E+14	4.58E+13
			3_1	3.24E+14	8.51E+13
			4_1	2.21E+14	6.02E+13
			5_1	2.13E+14	9.04E+13
			1_1	2.46E+14	8.11E+13
			Mean	2.56E+14	6.23E+13
		9.8mm	1_1	1.41E+14	3.01E+13
			1_2	1.55E+14	1.33E+13
			1_3	2.26E+14	6.62E+13
			1_4	1.58E+14	2.94E+13
			1_5	2.48E+14	4.88E+13
			Mean	1.86E+14	3.76E+13
		38mm	1_1	1.89E+14	7.76E+13
			1_2	2.48E+14	7.59E+13
			2_1	8.77E+13	1.98E+13
			2_2	1.55E+14	4.19E+13
			2_3	1.87E+14	4.42E+13
			Mean	1.73E+14	5.19E+13
		SSPC3		3mm	1_1

			1_2	2.99E+14	7.83E+13
			1_3	1.34E+14	4.28E+13
			1_4	3.03E+14	4.85E+13
			1_5	2.63E+14	5.13E+13
			2_2	1.72E+14	2.28E+13
			2_5	2.66E+14	2.7E+13
			Mean	2.46E+14	4.22E+13
SSPC5	2679	3mm	1_1	1.13E+14	2.12E+13
			1_2	2E+14	3.01E+13
			1_3	1.99E+14	3.8E+13
			2_1	9.34E+13	1.87E+13
			2_2	9.2E+13	1.4E+13
			2_3	1.12E+14	1.71E+13
			2_4	8.15E+13	1.65E+13
			3_1	1.3E+14	3.64E+13
			3_2	1.24E+14	1.64E+13
			3_3	1.04E+14	2.93E+13
			3_4	1.83E+14	4.76E+13
			3_4(10kx)	2.35E+14	3.48E+13
			3_5	1.3E+14	3.67E+13
			Mean	1.38E+14	2.75E+13

A.5 List of coupon specimens for fatigue test

Fatigue test type	Annealing temperature	Specimen ID	Number of cycle	Prescribed loading
Uniaxial strain controlled	Unconditioned	SS_uncond	0	Before fatigue
		SS_sn11	5	$\varepsilon = 1\%$
		SS_sn12	20	$\varepsilon = 1\%$
		SS_sn01	234	$\varepsilon = 1\%$
	800C	SS_800	0	Before fatigue
		SS_sn13	5	$\varepsilon = 1\%$
		SS_sn14	20	$\varepsilon = 1\%$
		SS_sn05	100	$\varepsilon = 1\%$
	1050C	SS_1050	0	Before fatigue
		SS_sn15	5	$\varepsilon = 1\%$
		SS_sn16	20	$\varepsilon = 1\%$
		SS_sn07	100	$\varepsilon = 1\%$
Biaxial ratchetting	Unconditioned	SS_bi01	2000	P = 6.89MPa $\varepsilon_x = 0.4\%$
	800C	SS_bi04	1482	P = 6.89MPa $\varepsilon_x = 0.4\%$
	1050C	SS_bi05	2000	P = 6.89MPa $\varepsilon_x = 0.4\%$
Uniaxial force controlled	Unconditioned	SS_uni11	400	$F_m = 0$ $F_a = 0.8F_{1\%}$
		SS_uni01	400	$F_m = 0.2F_{1\%}$ $F_a = 0.8F_{1\%}$

A.6 List of welded pipe specimens for fatigue test

Specimen	Number of cycle	Welding type	Welding sequence	Prescribed loading amplitude, δ_c
SSPC4	5	Socket	Quarter	10mm
SSPC2	20	Socket	Quarter	10mm
SSPC3	100	Socket	Quarter	10mm
SSPC5	2679	Socket	Quarter	10mm

Figure A.1 TEM images of SS_uncond coupon

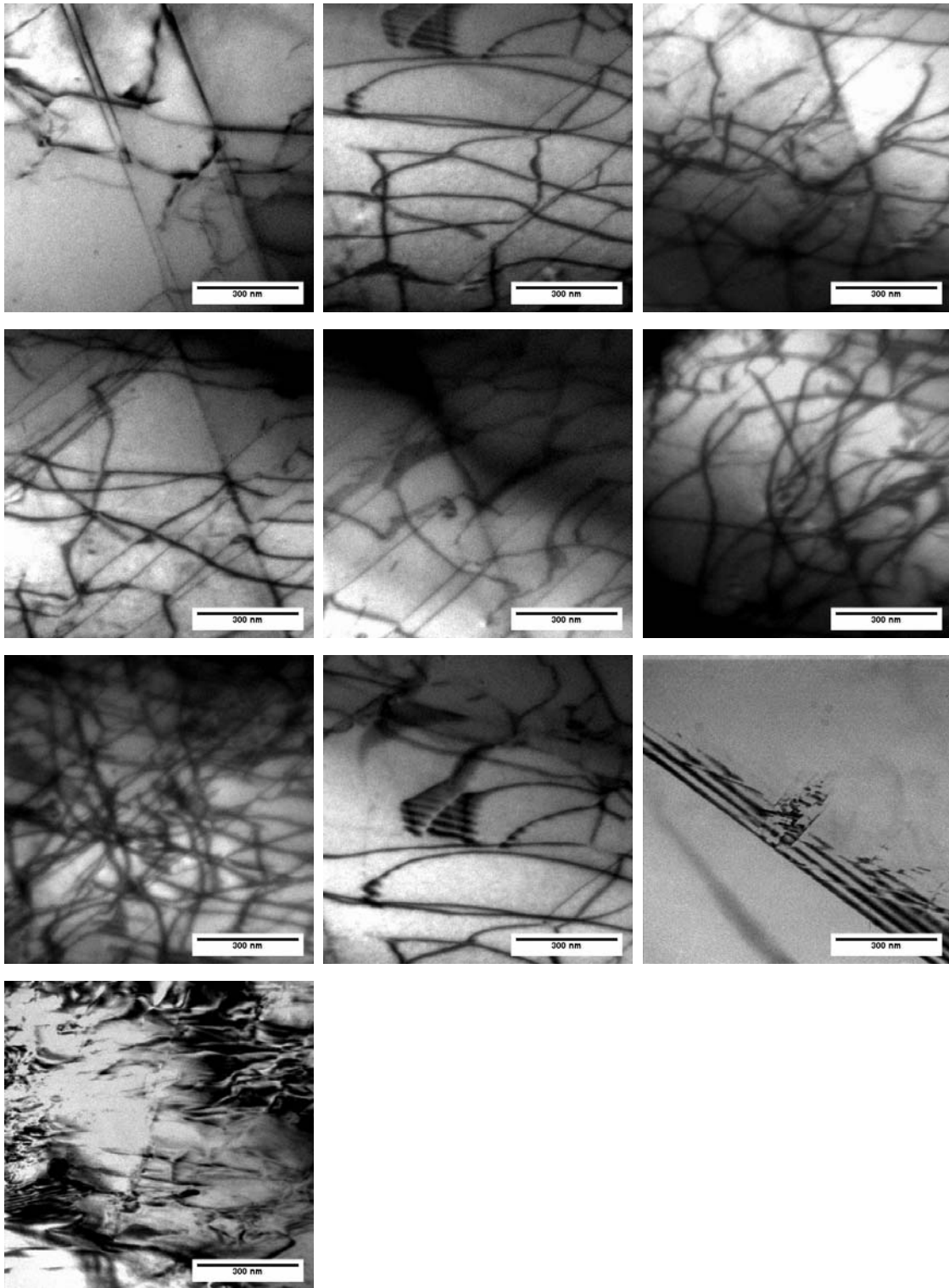


Figure A.2 TEM images of SS_sn11 coupon

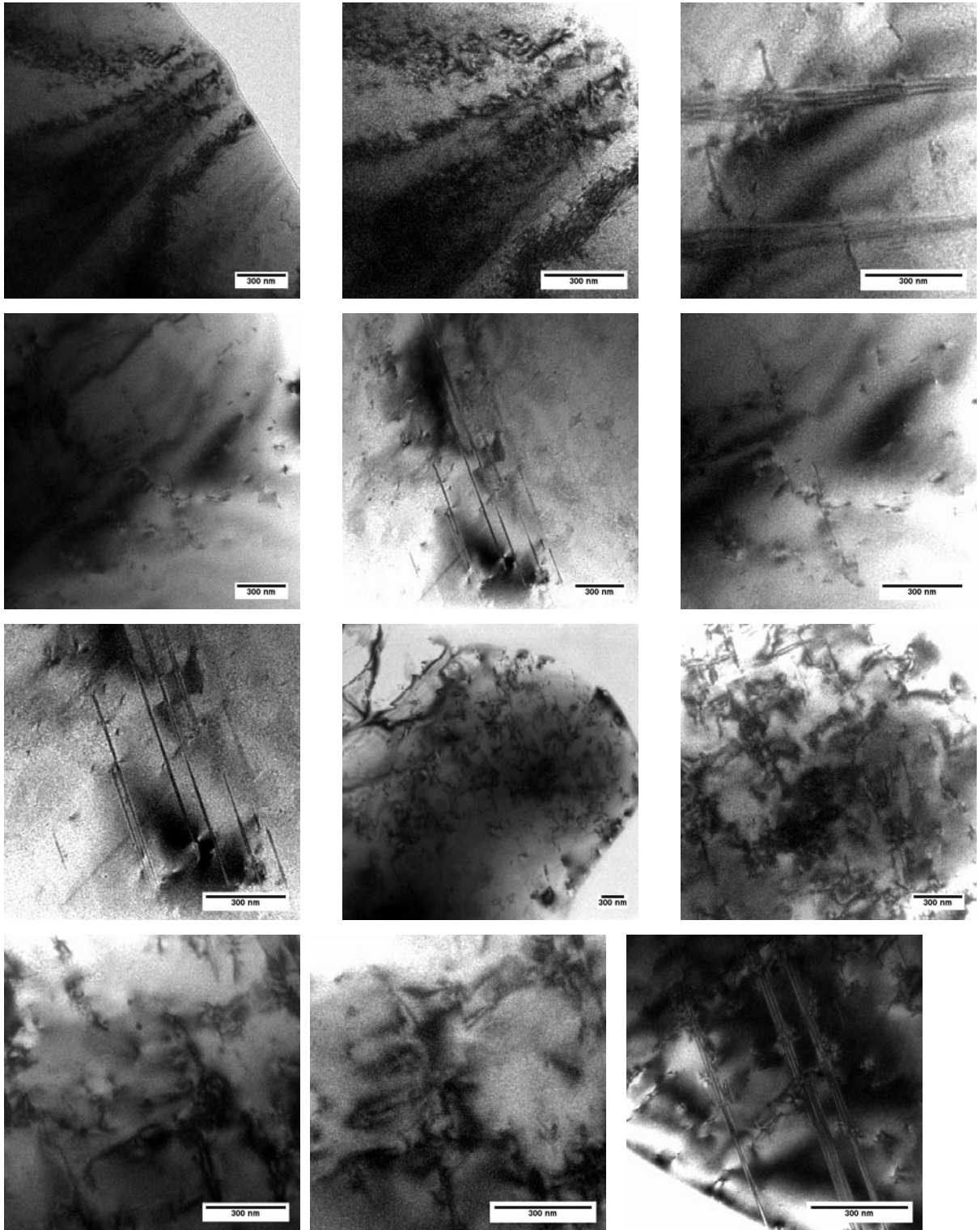


Figure A.2 (Continued)

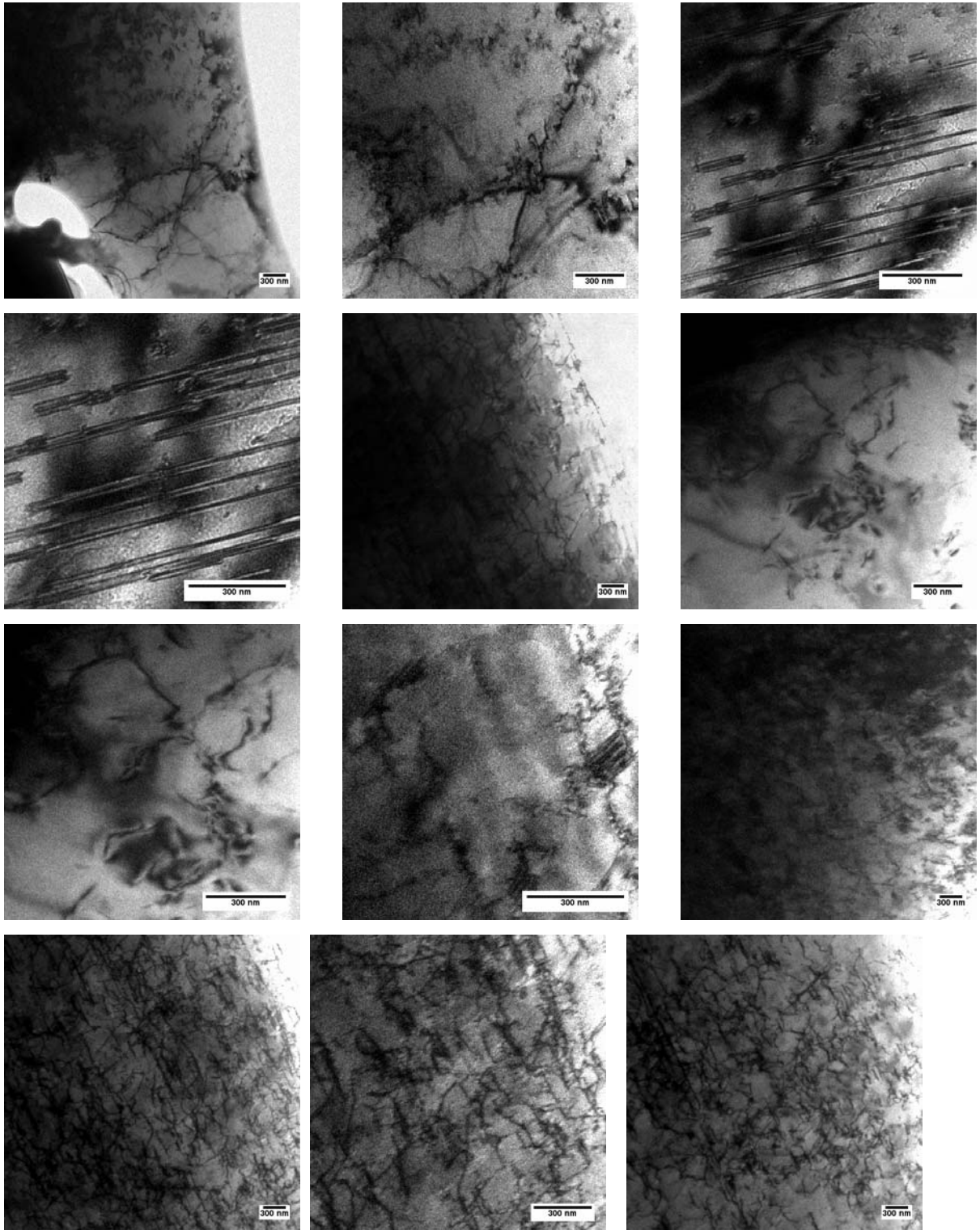


Figure A.2 (Continued)

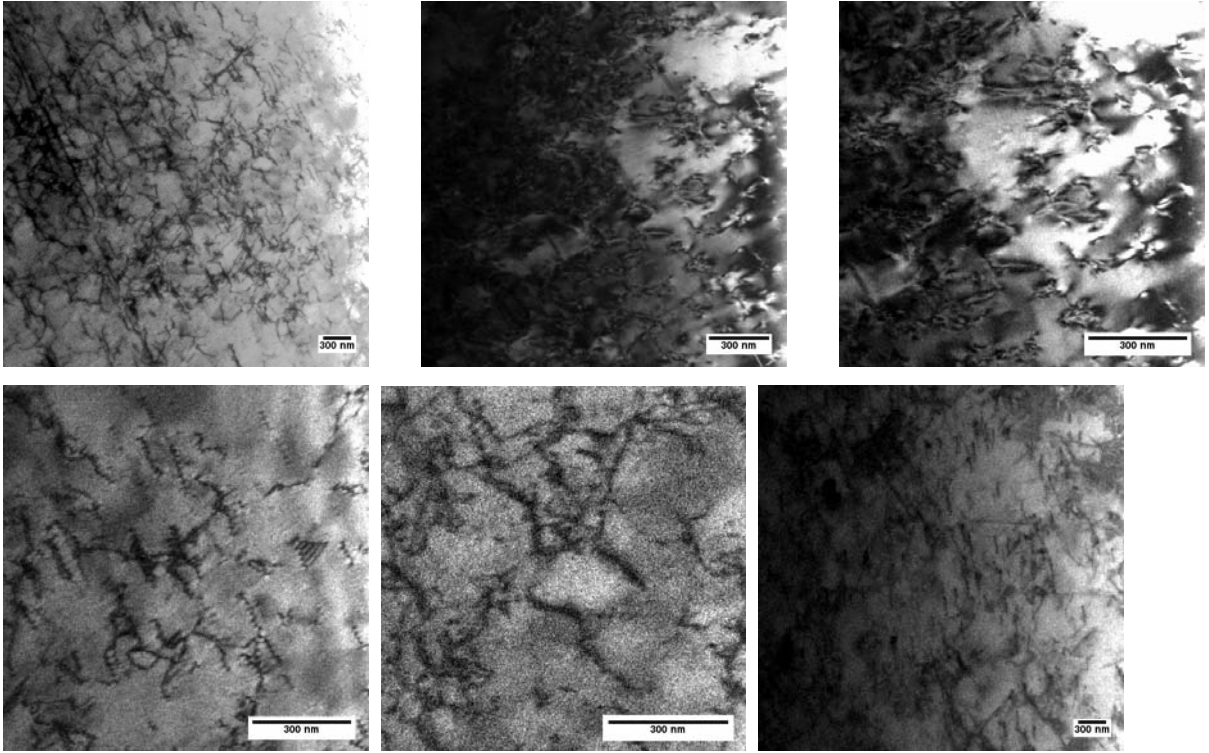


Figure A.3 TEM images of SS_sn12 coupon

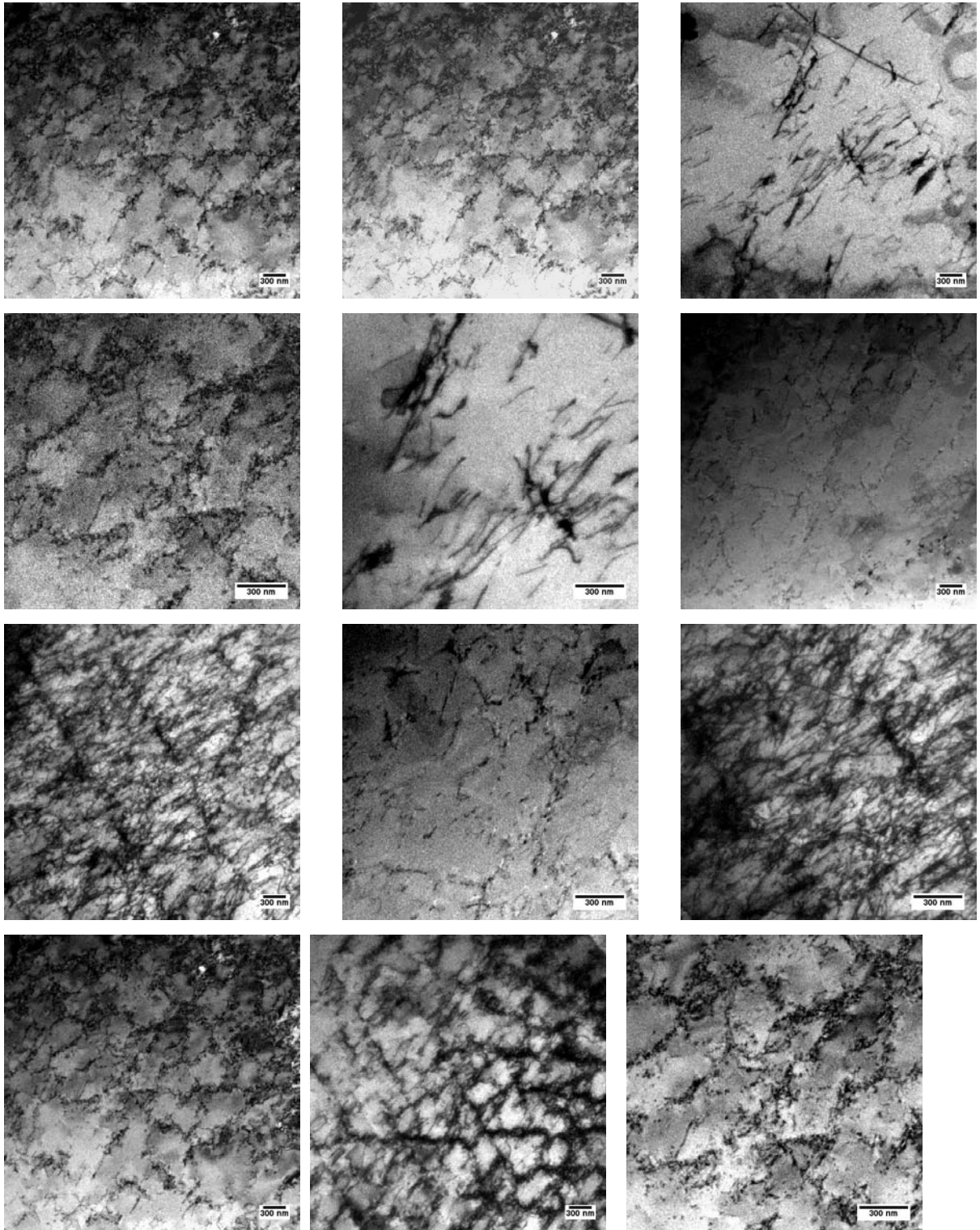


Figure A.3 (Continued)

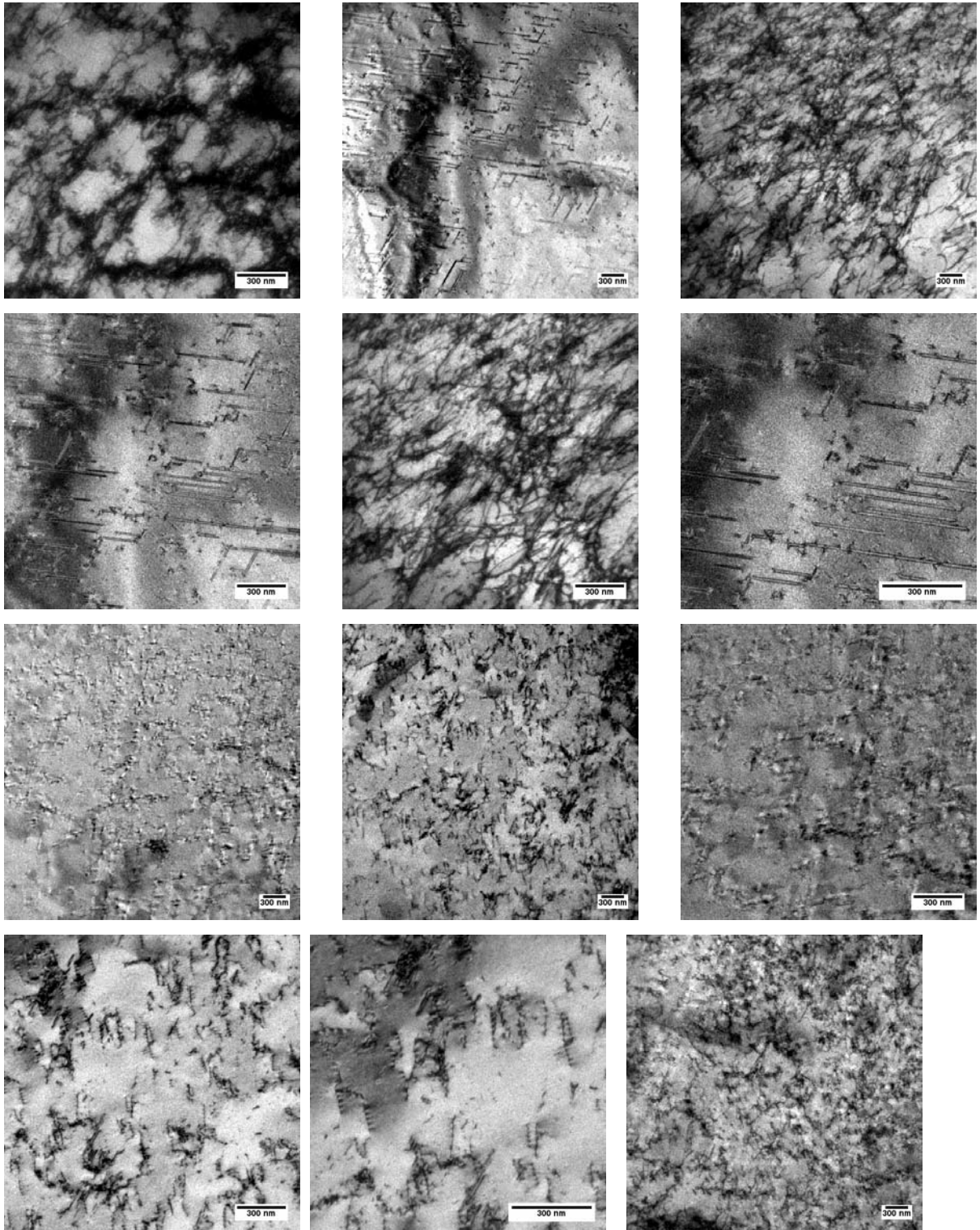


Figure A.3 (Continued)

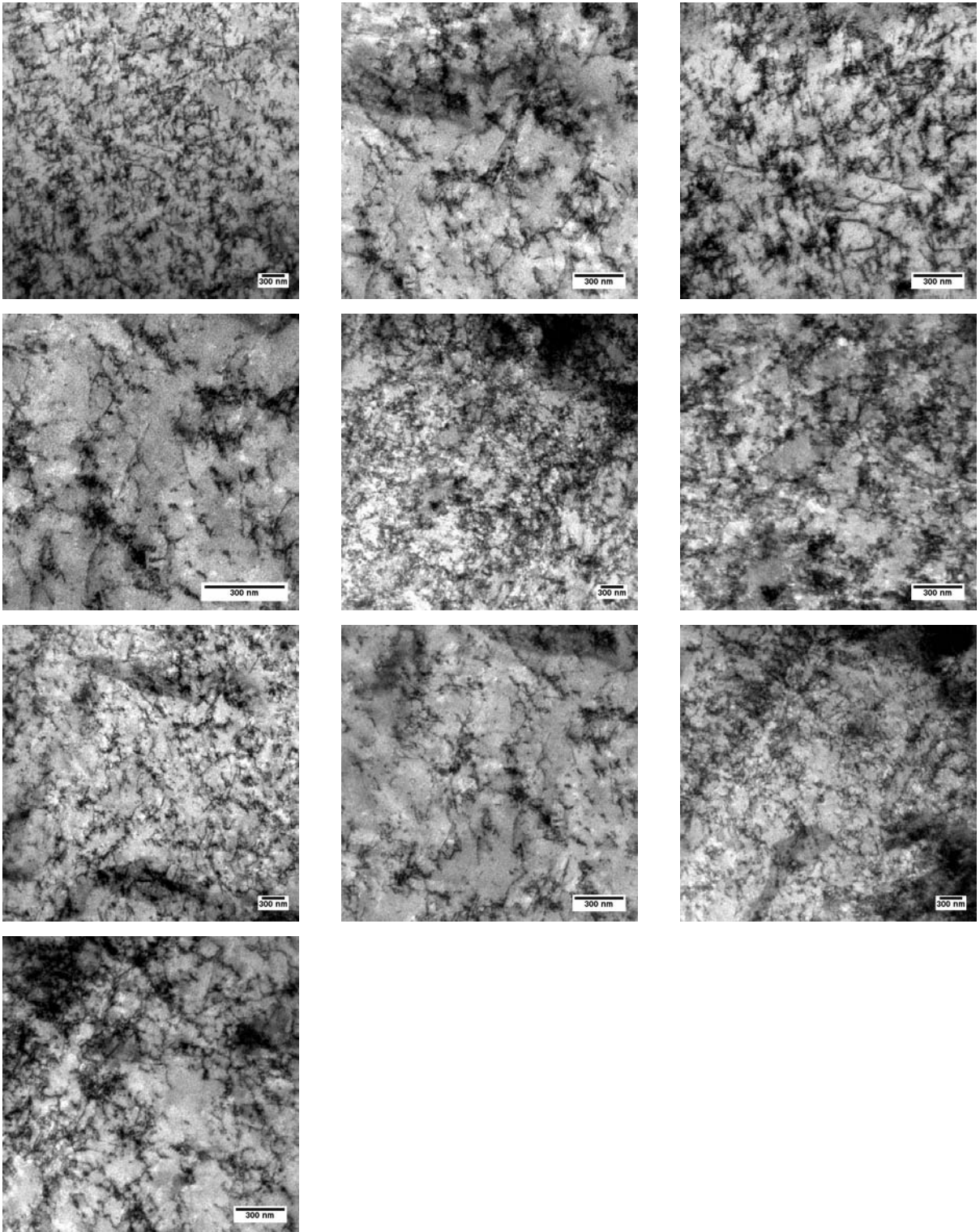


Figure A.4 TEM images of SS_sn01 coupon

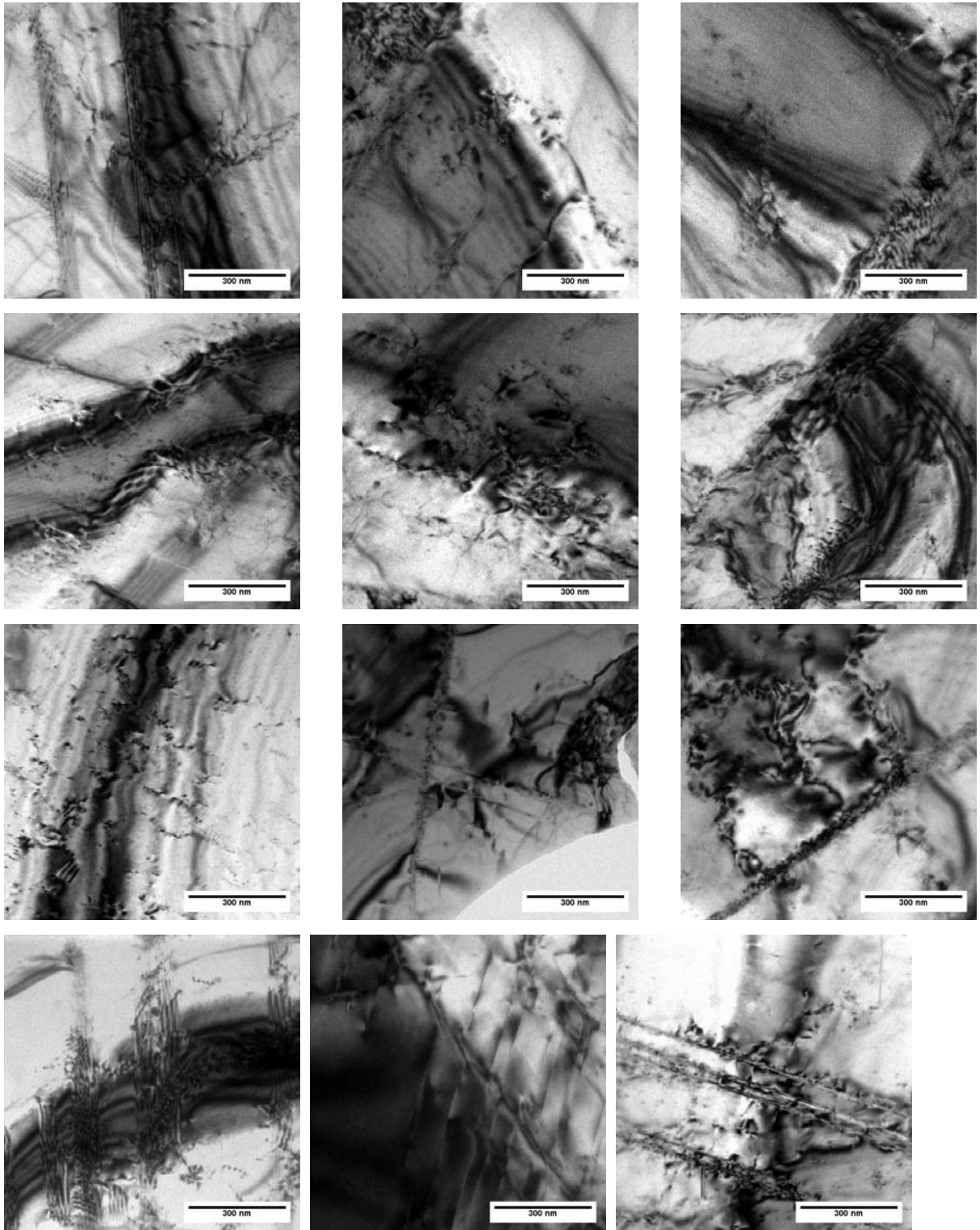


Figure A.5 TEM images of SS_800 coupon

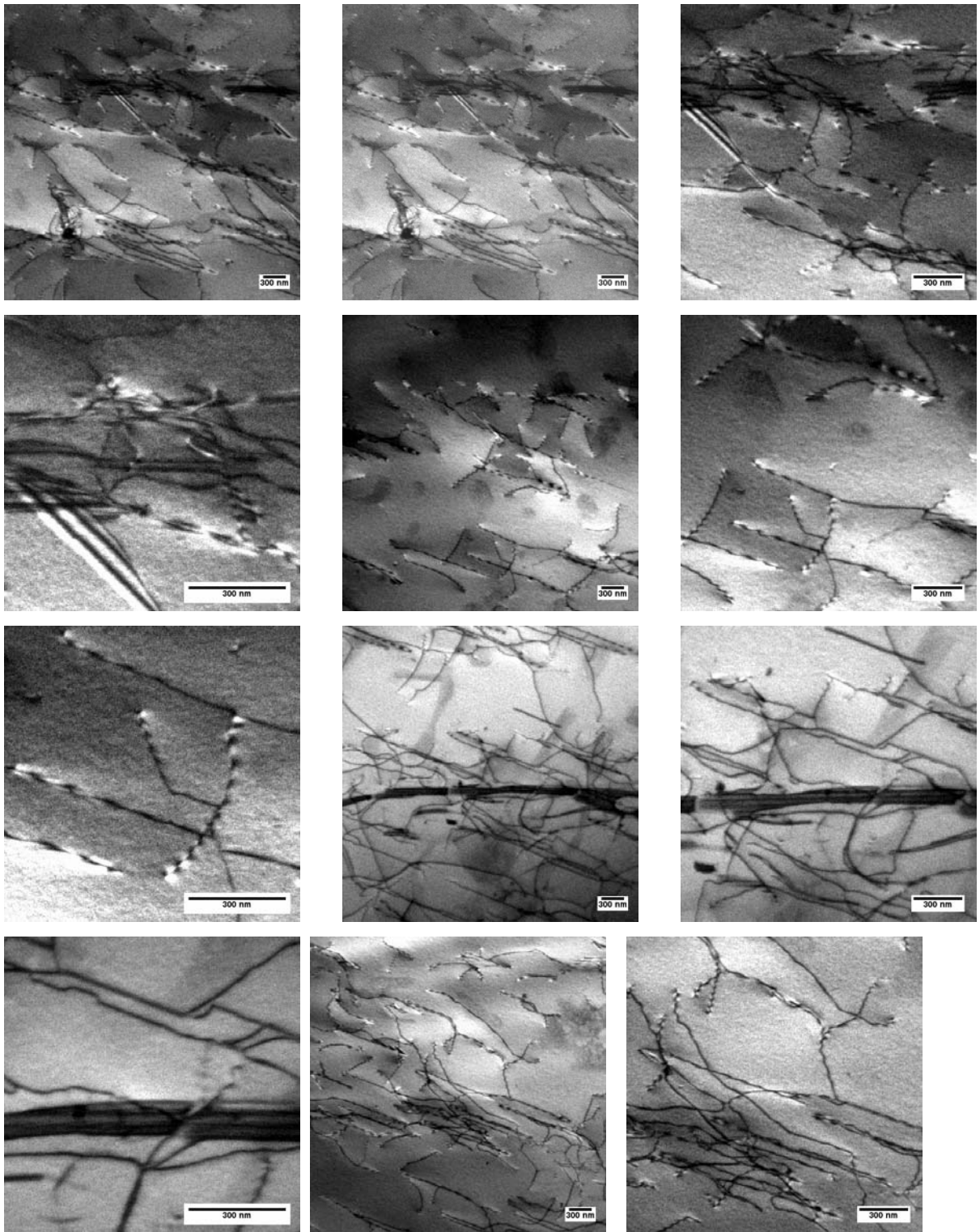


Figure A.5 (Continued)

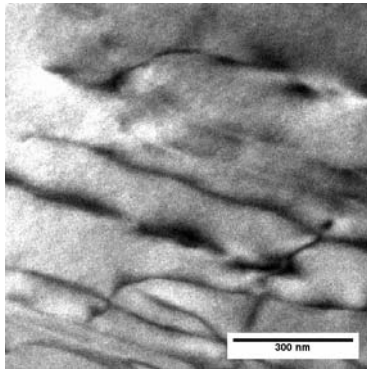
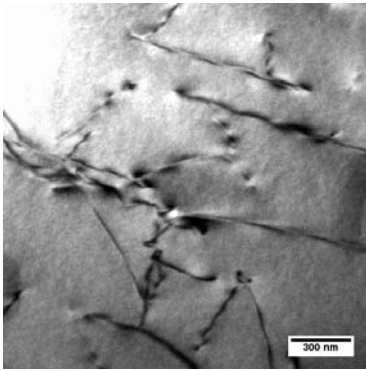
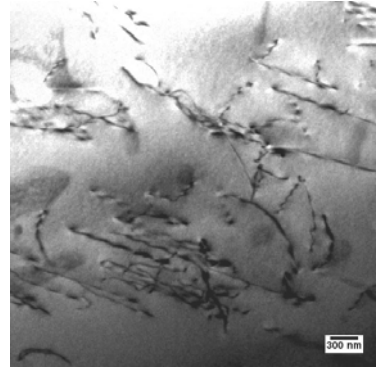
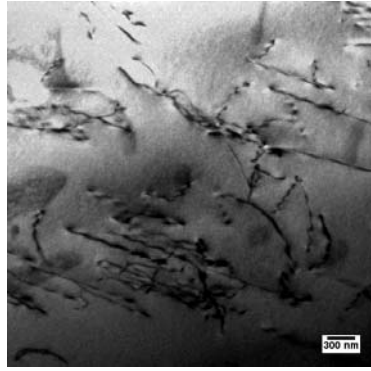
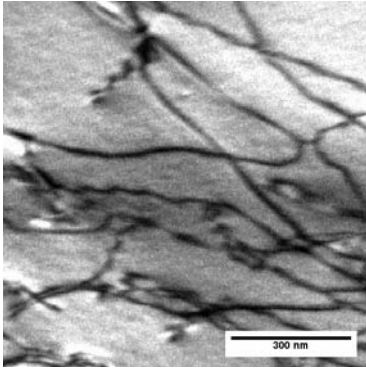


Figure A.6 TEM images of SS_sn13 coupon

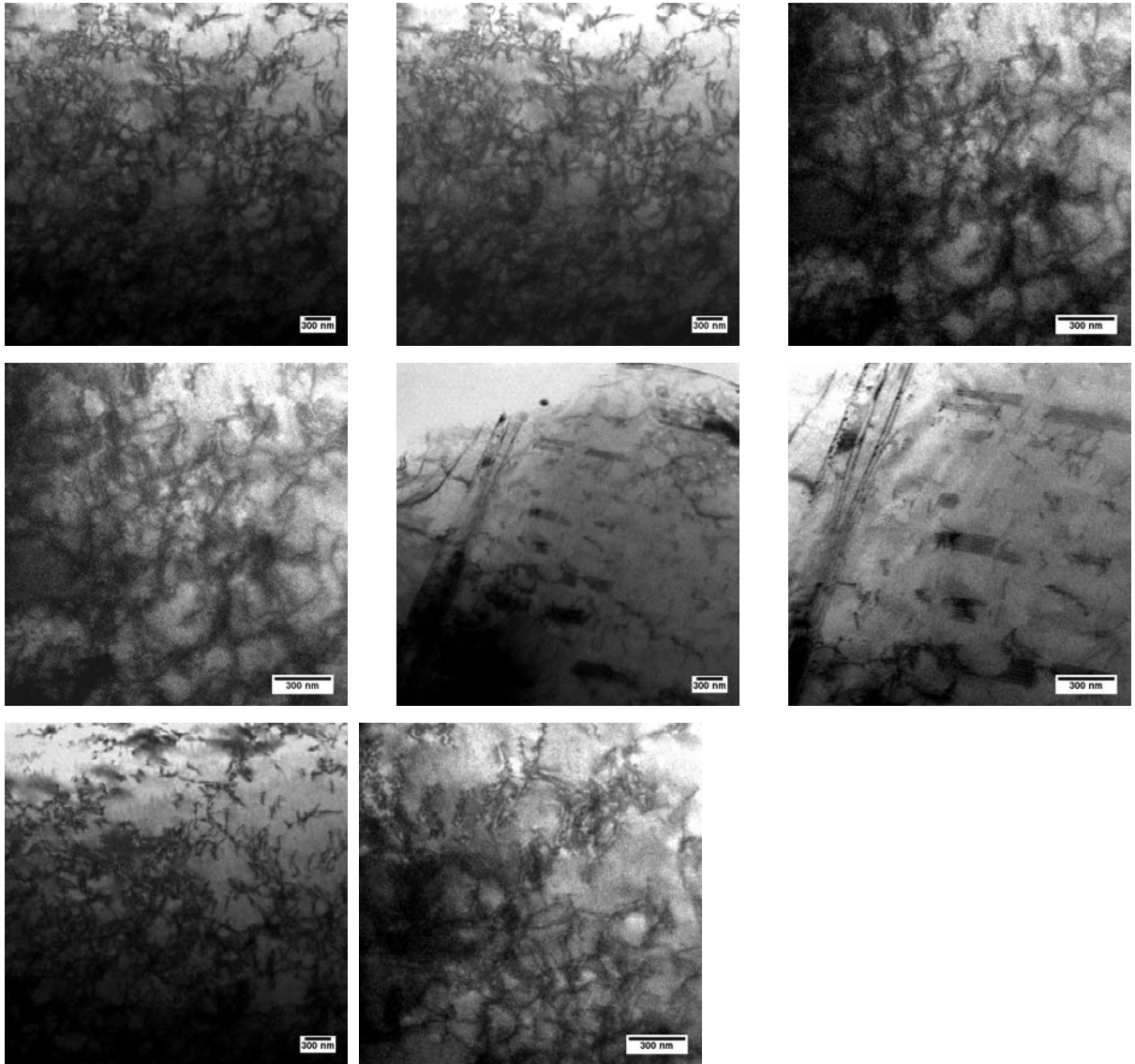


Figure A.7 TEM images of SS_sn14 coupon

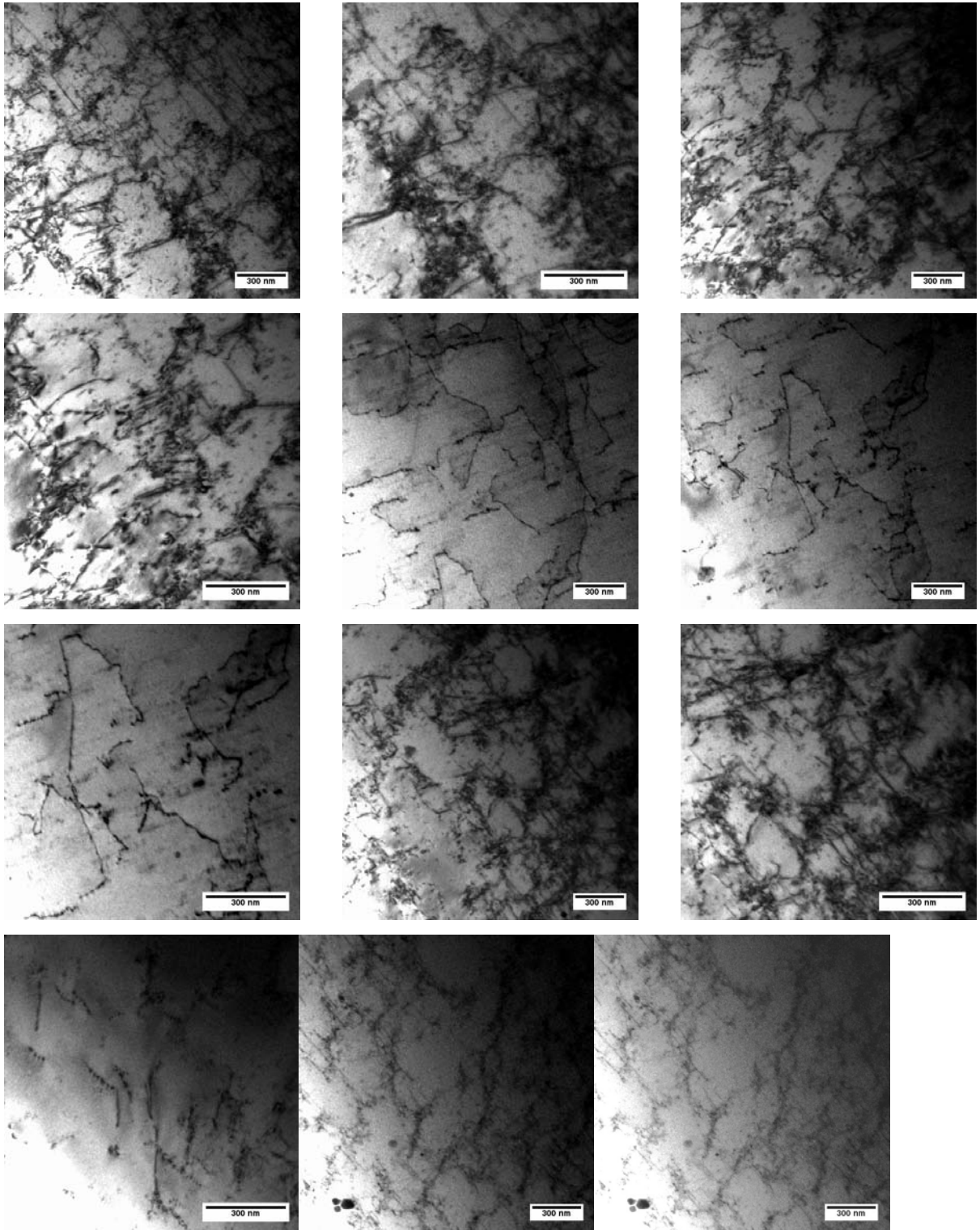


Figure A.7 (Continued)

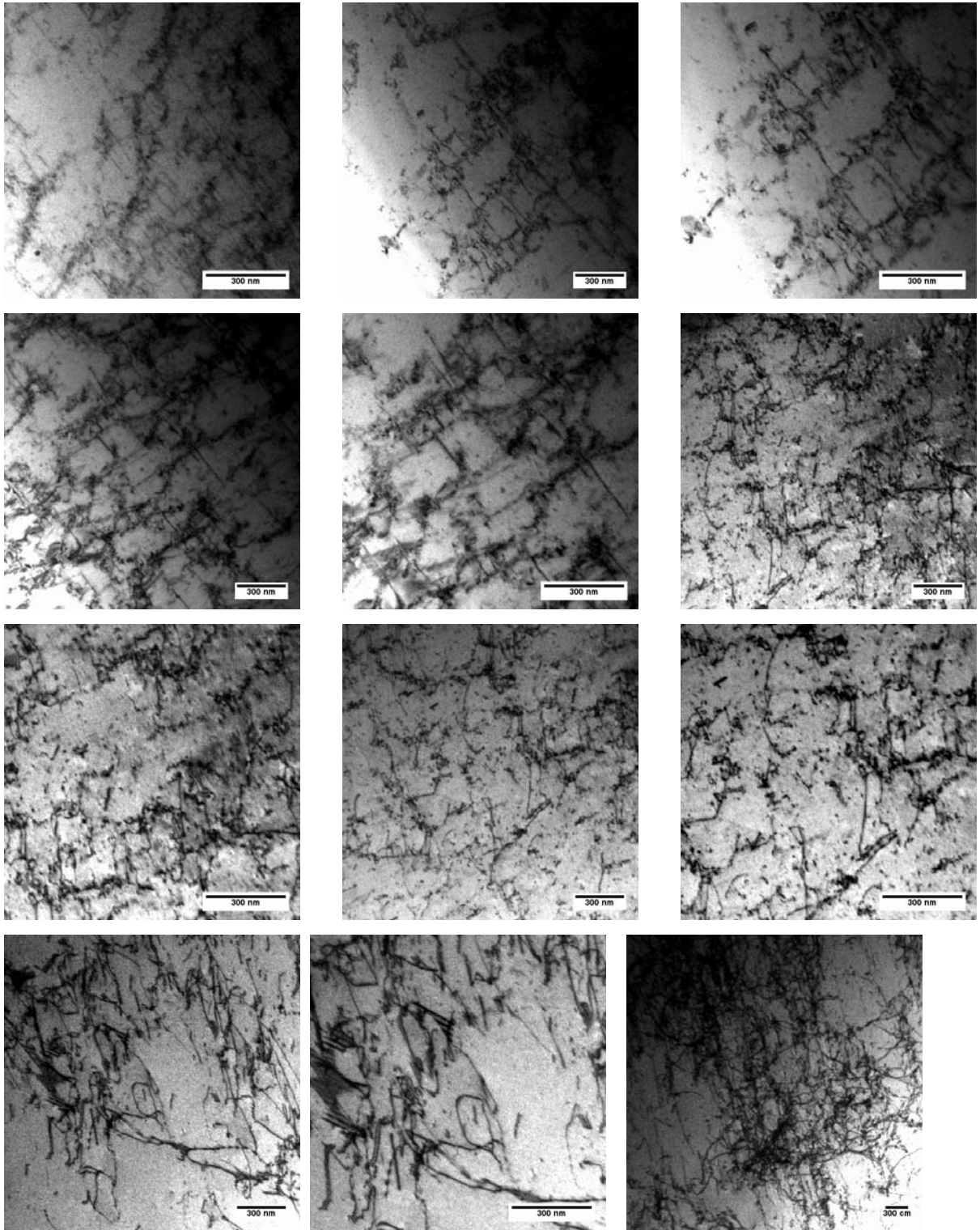


Figure A.7 (Continued)

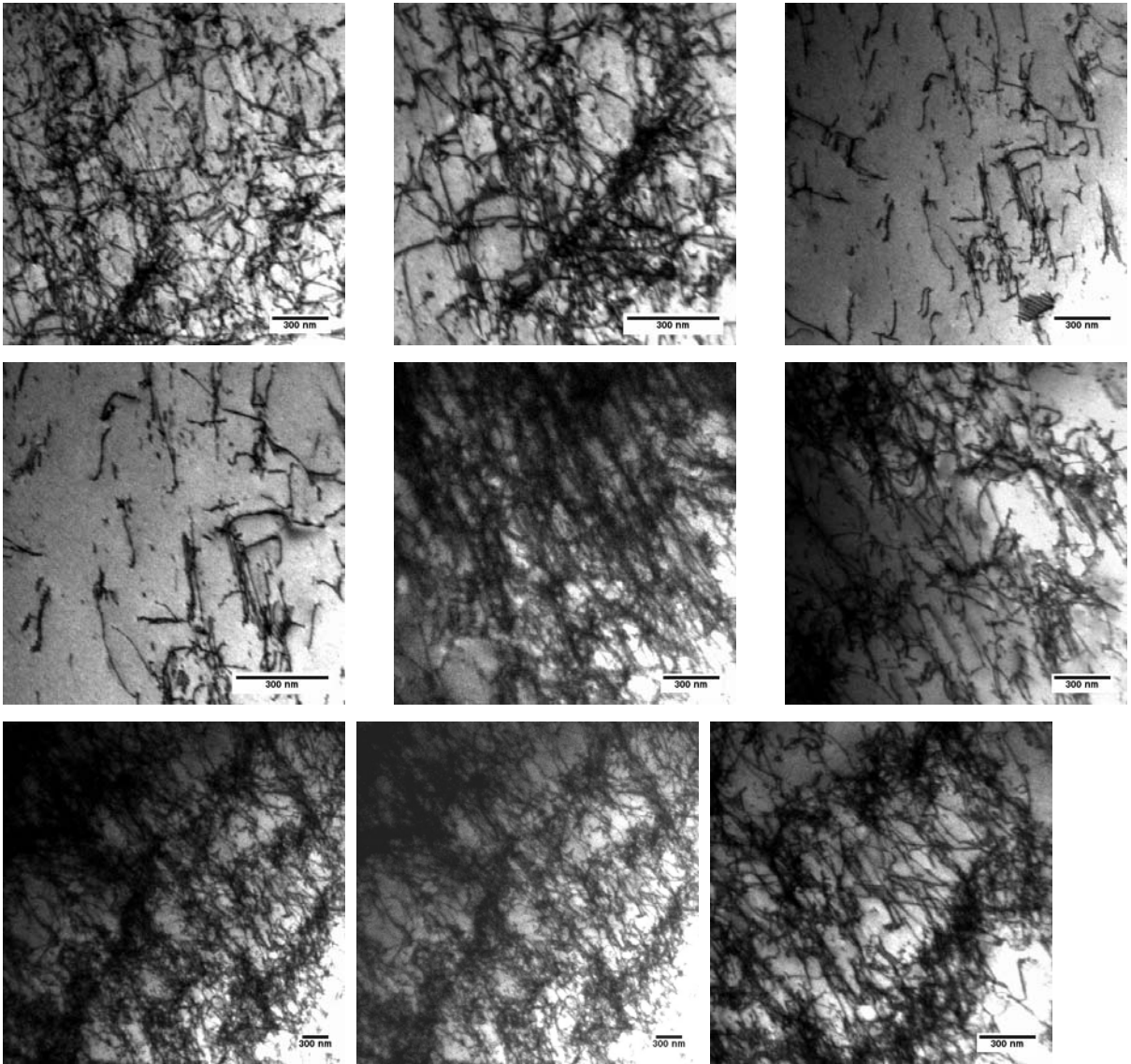


Figure A.8 TEM images of SS_sn05 coupon

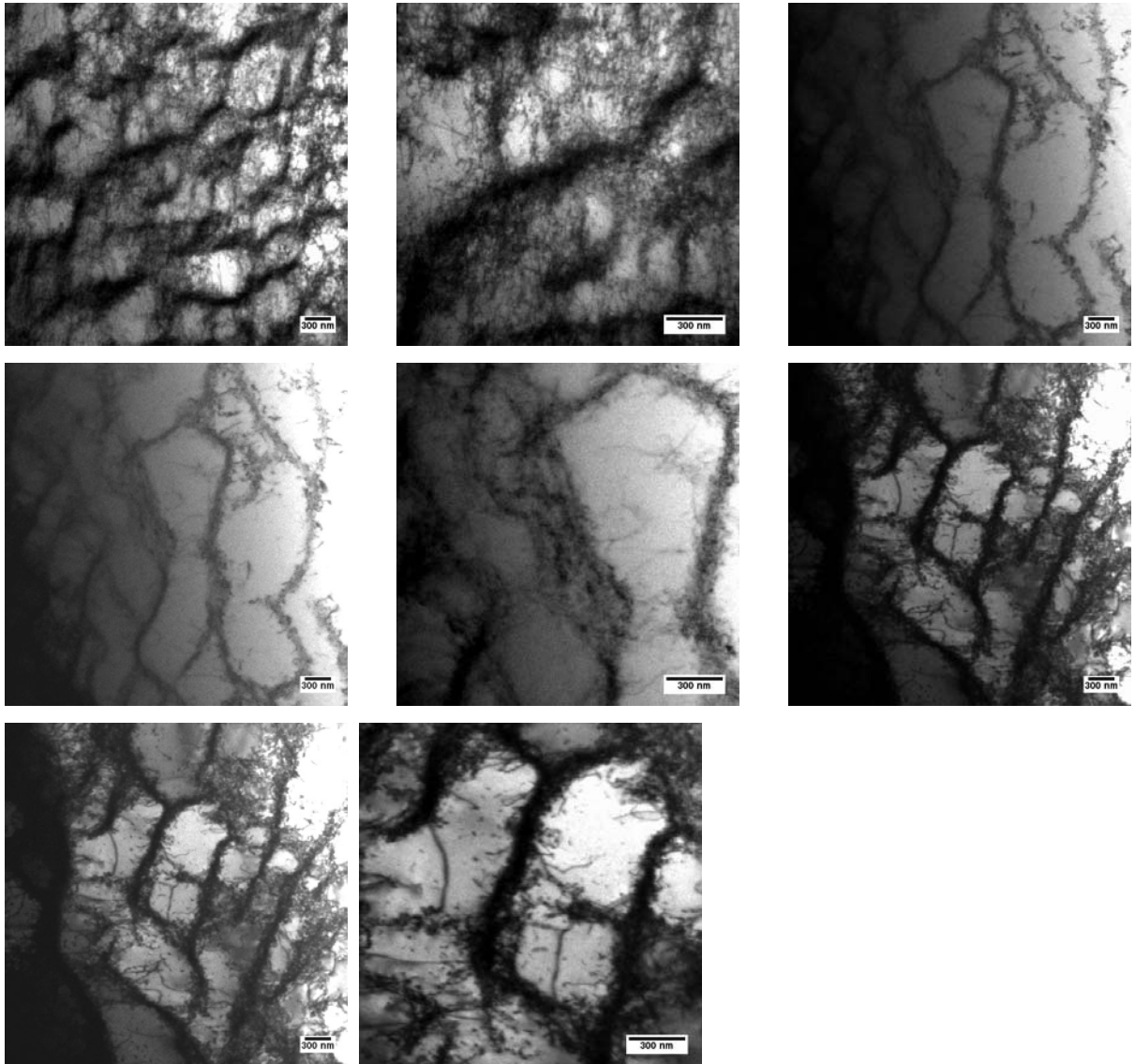


Figure A.9 TEM images of SS_1050 coupon

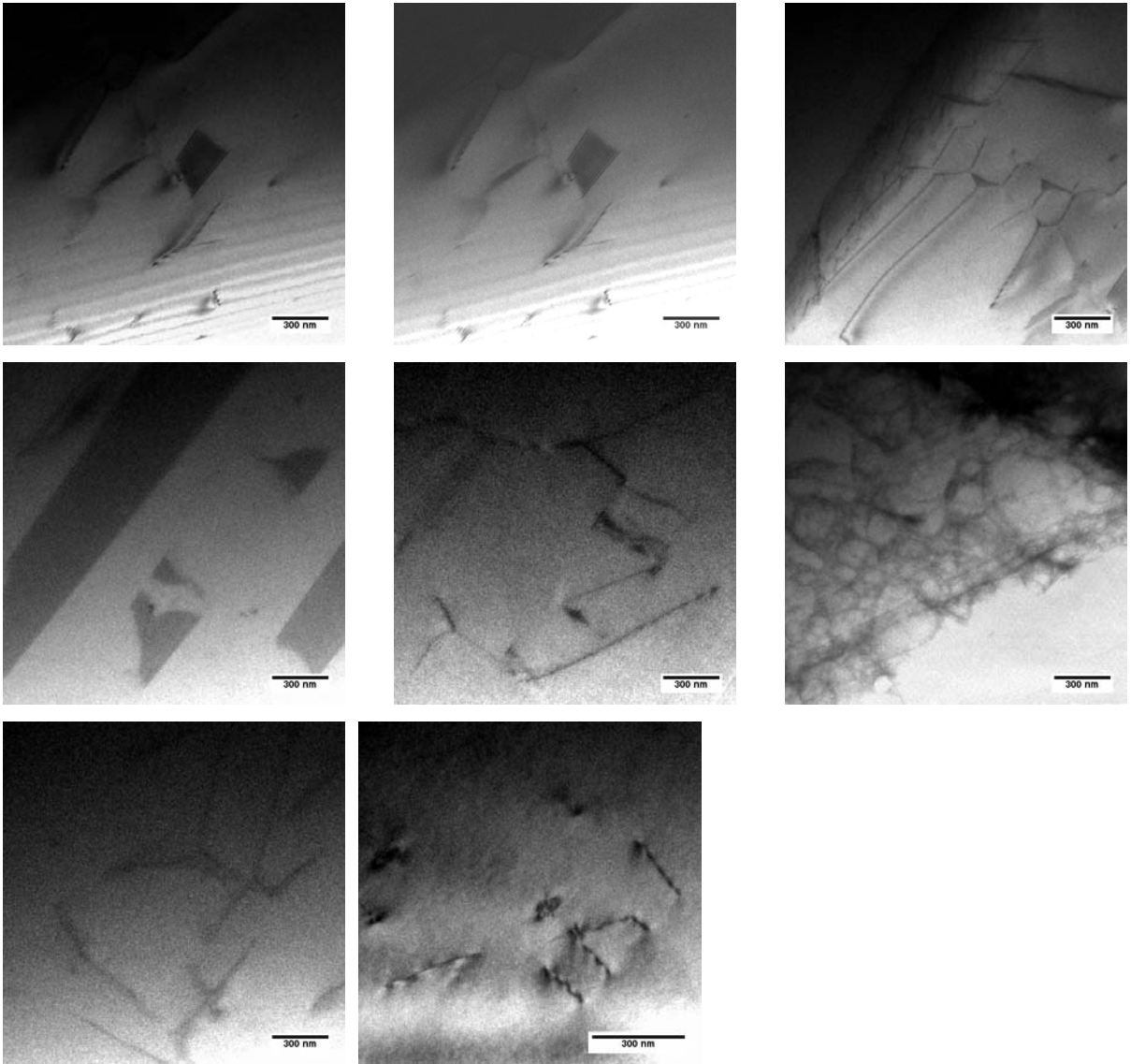


Figure A.10 TEM images of SS_sn15 coupon

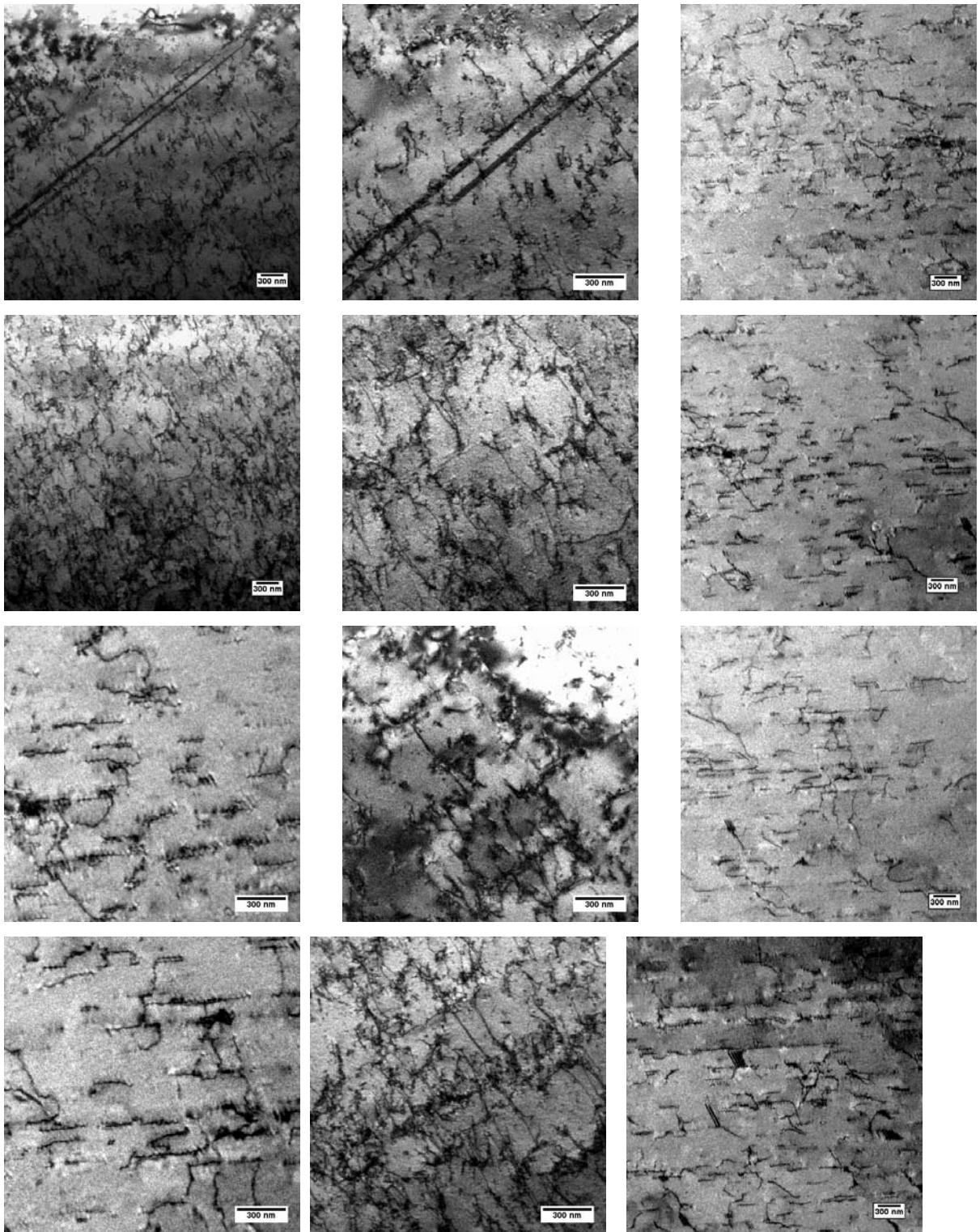


Figure A.10 (Continued)

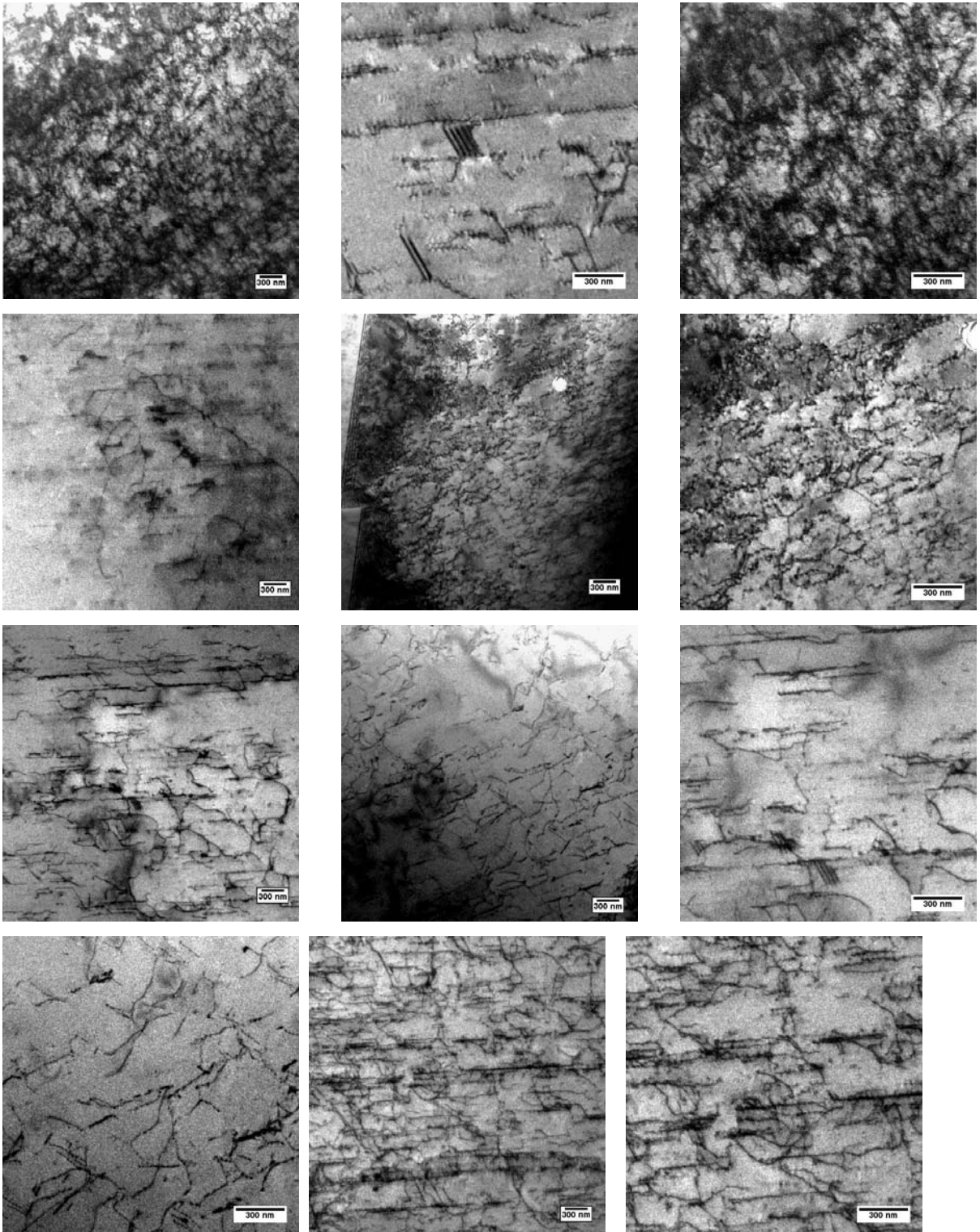


Figure A.11 TEM images of SS_sn16 coupon

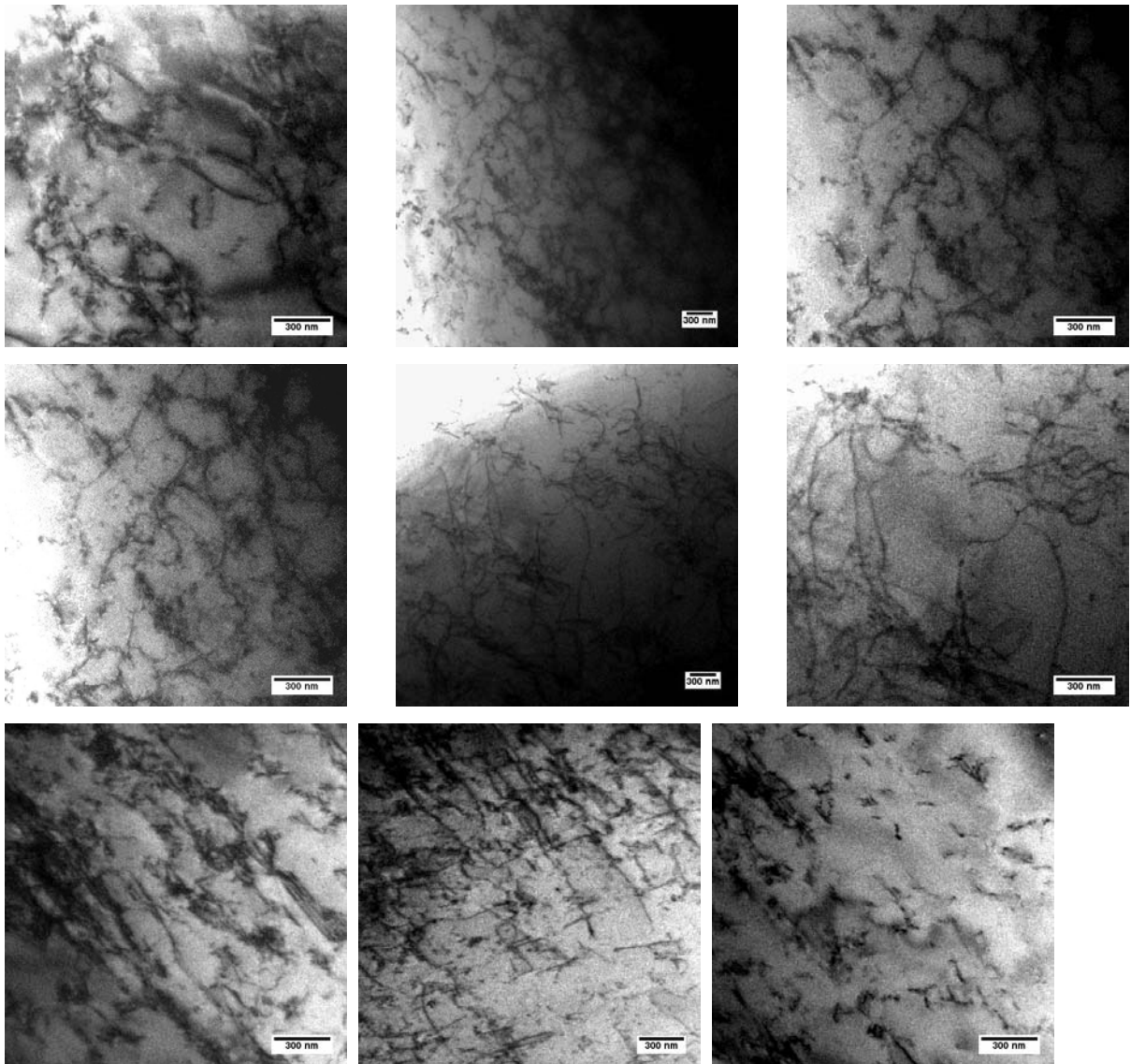


Figure A.12 TEM images of SS_sn07 coupon

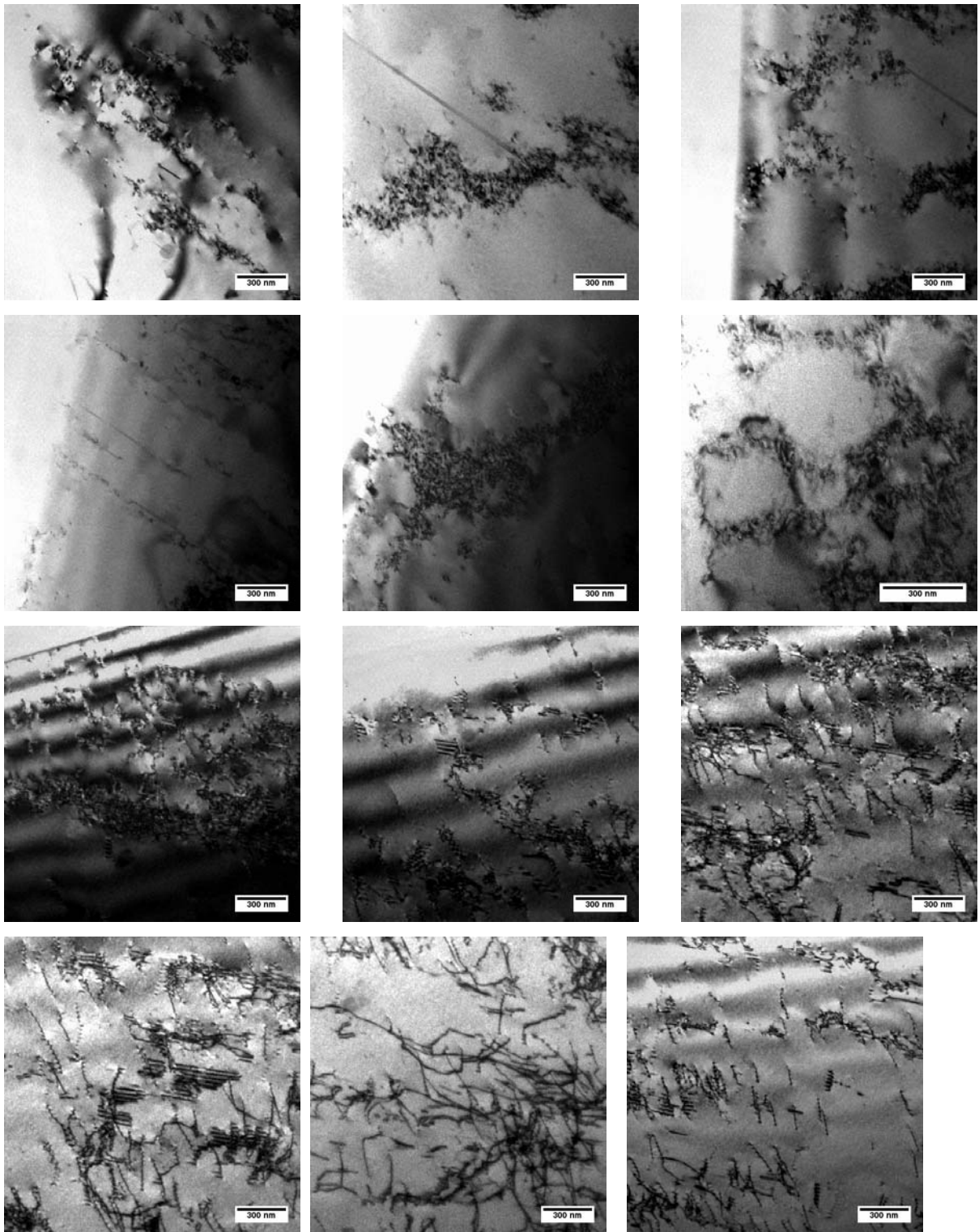


Figure A.12 (Continued)

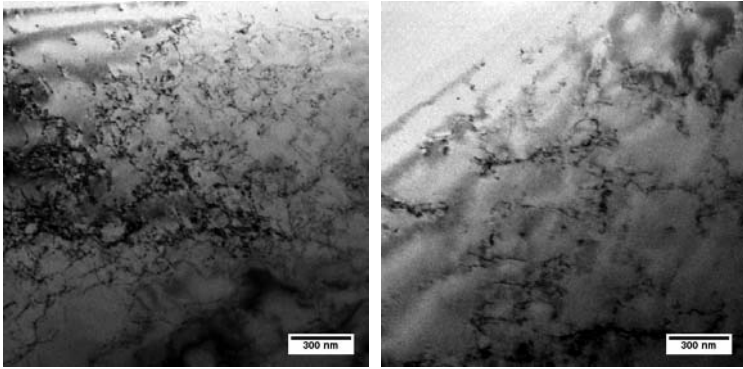


Figure A.13 TEM images of SS_bi01 coupon

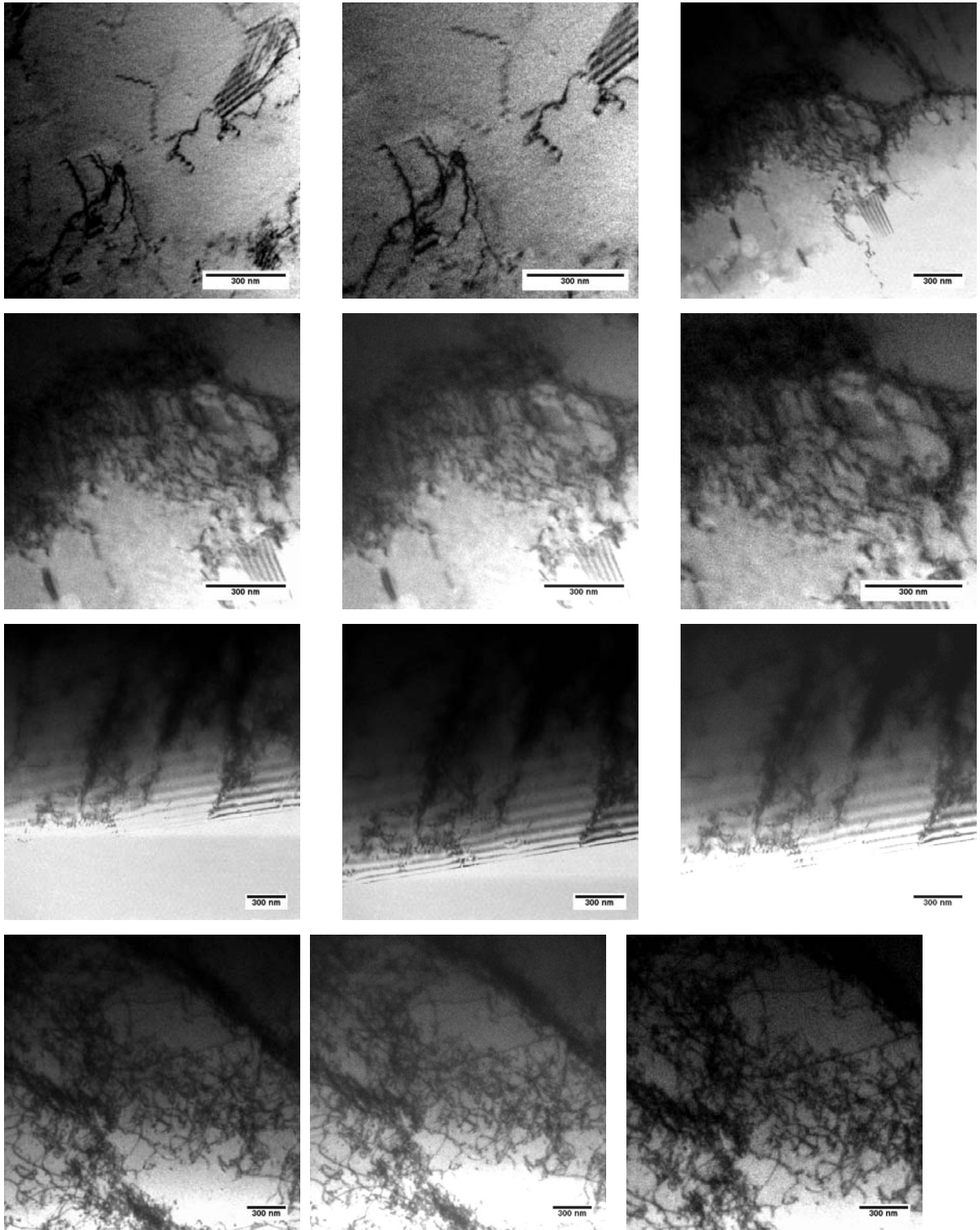


Figure A.13 (Continued)

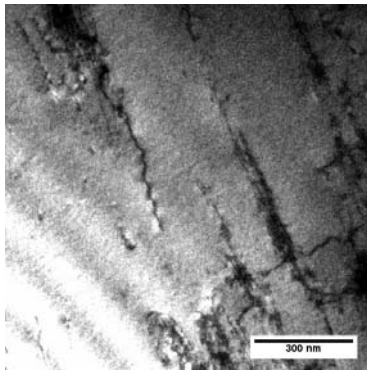
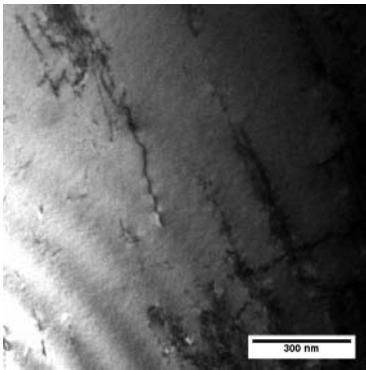
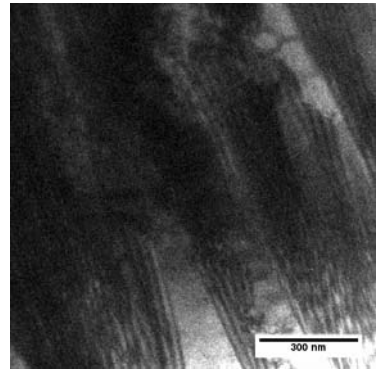
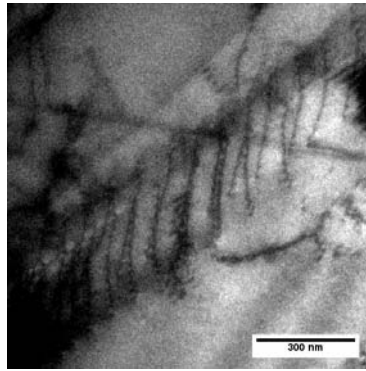
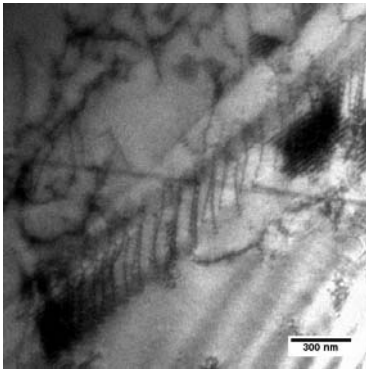
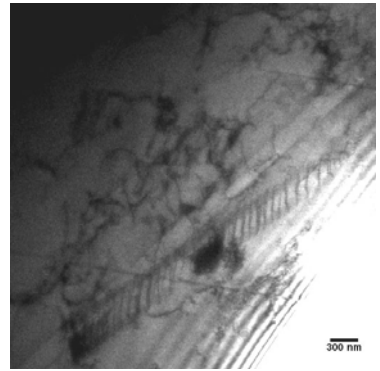
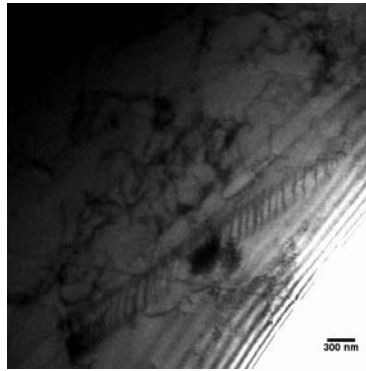
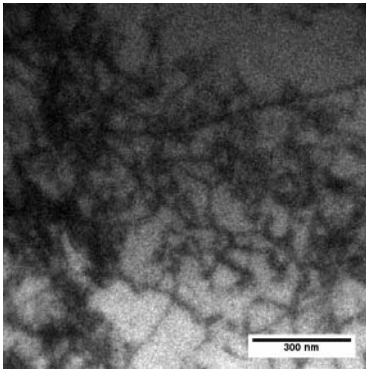


Figure A.14 TEM images of SS_bi04 coupon

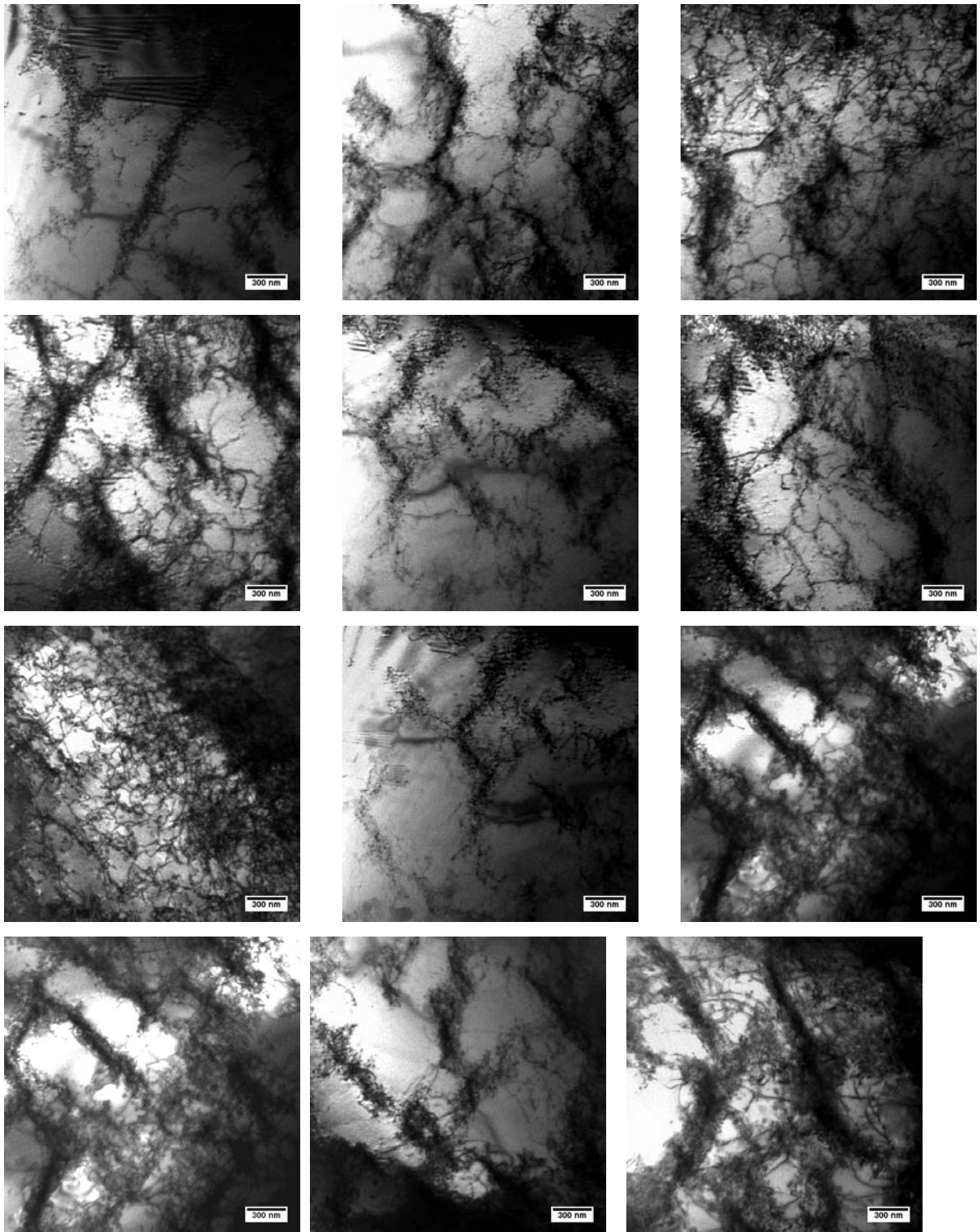


Figure A.14 (Continued)

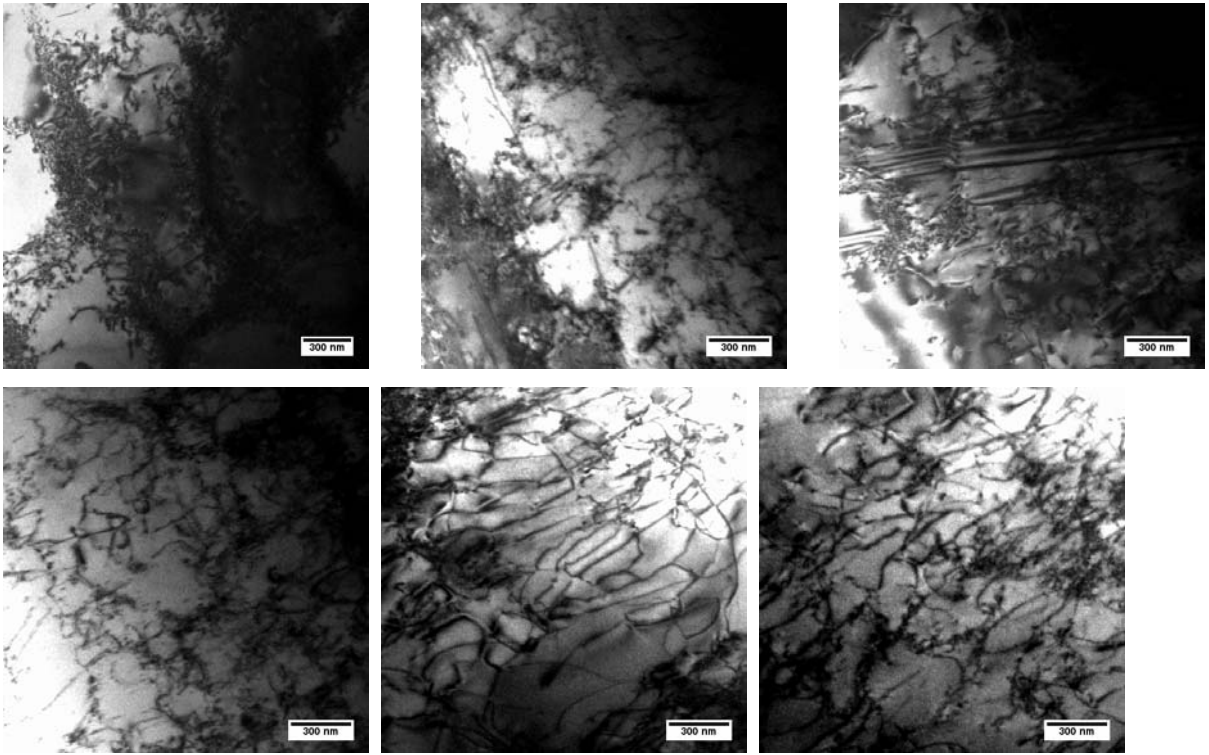


Figure A.15 TEM images of SS_bi05 coupon

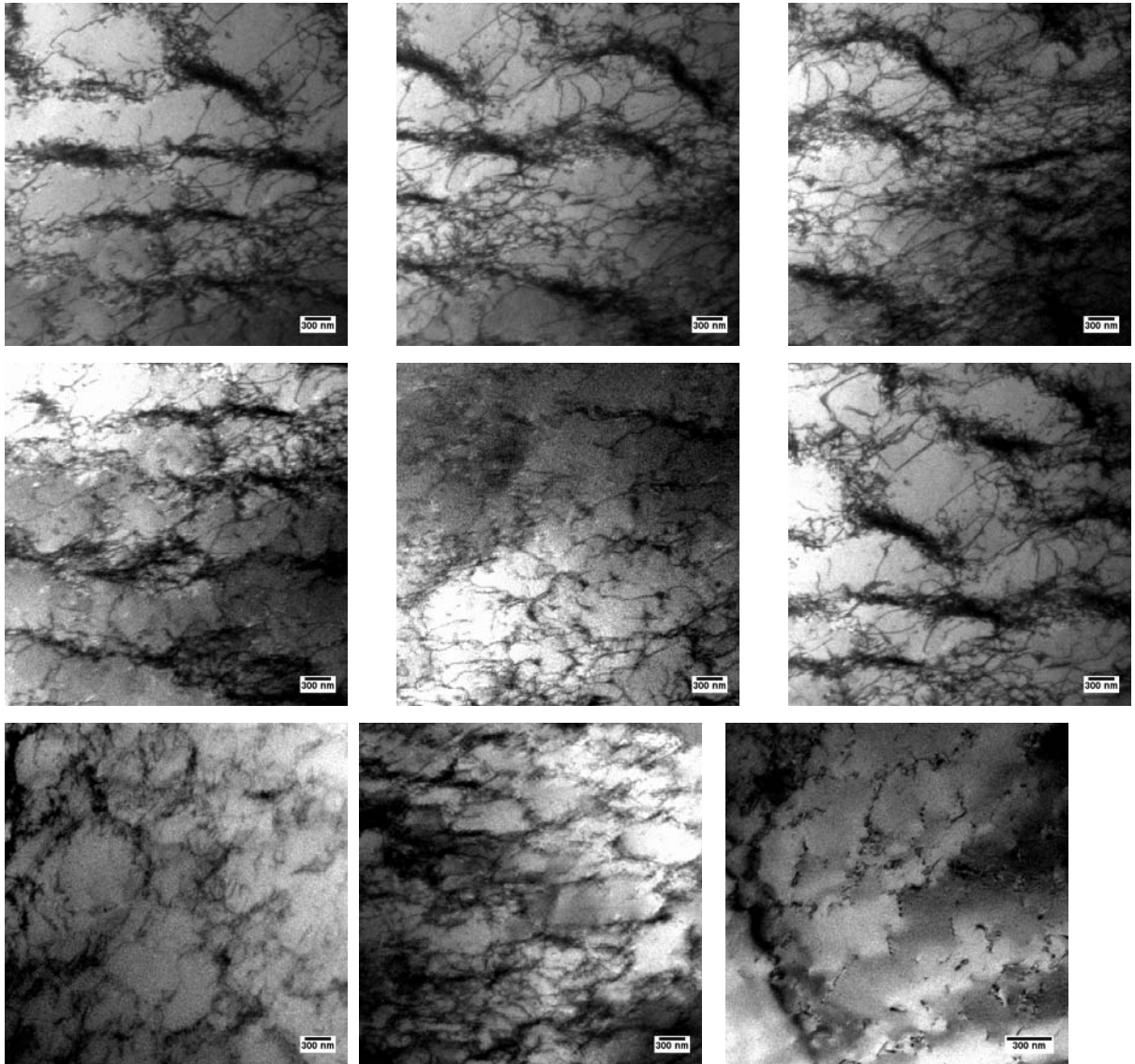


Figure A.16 TEM images of SS_uni01 coupon

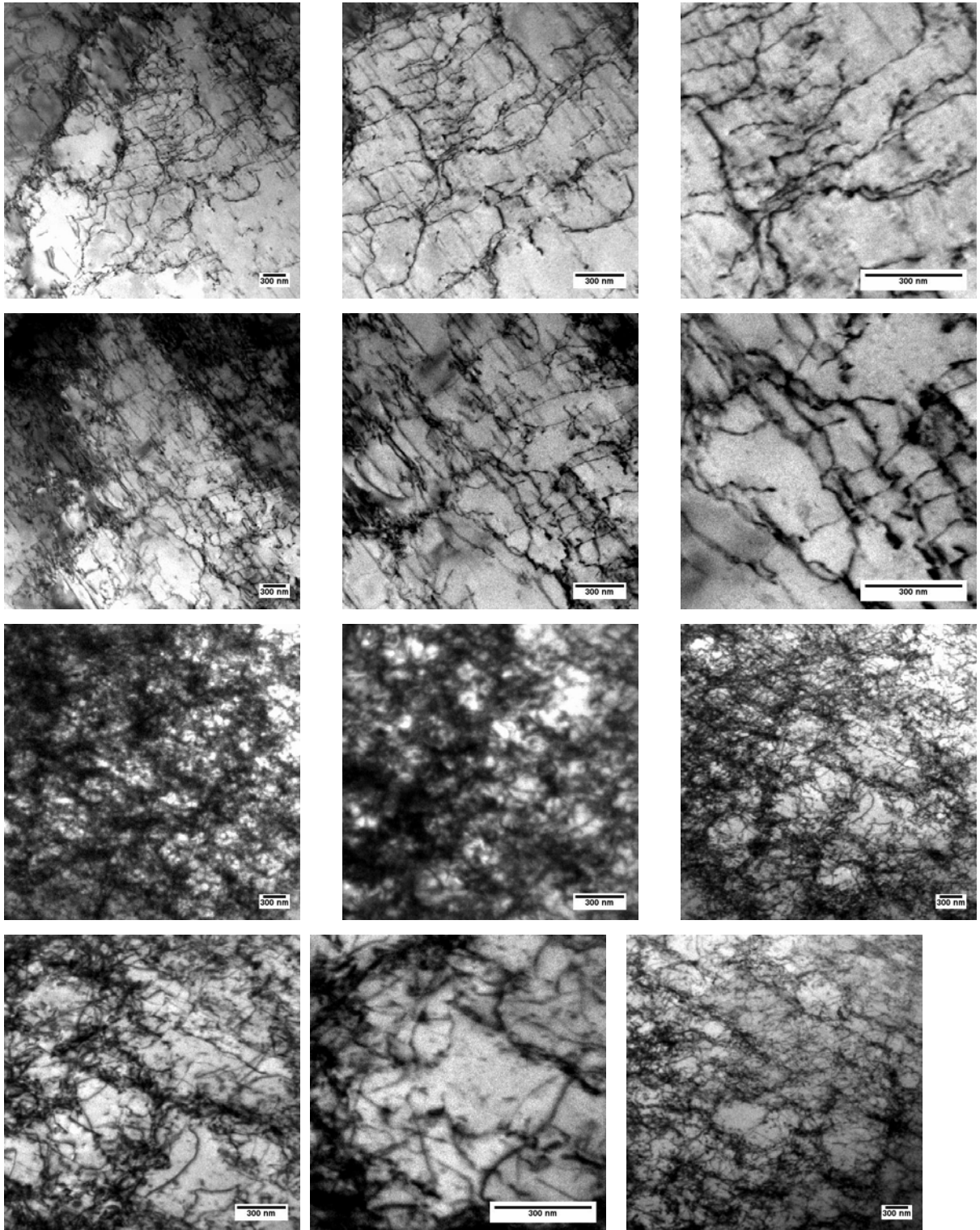


Figure A.16 (Continued)

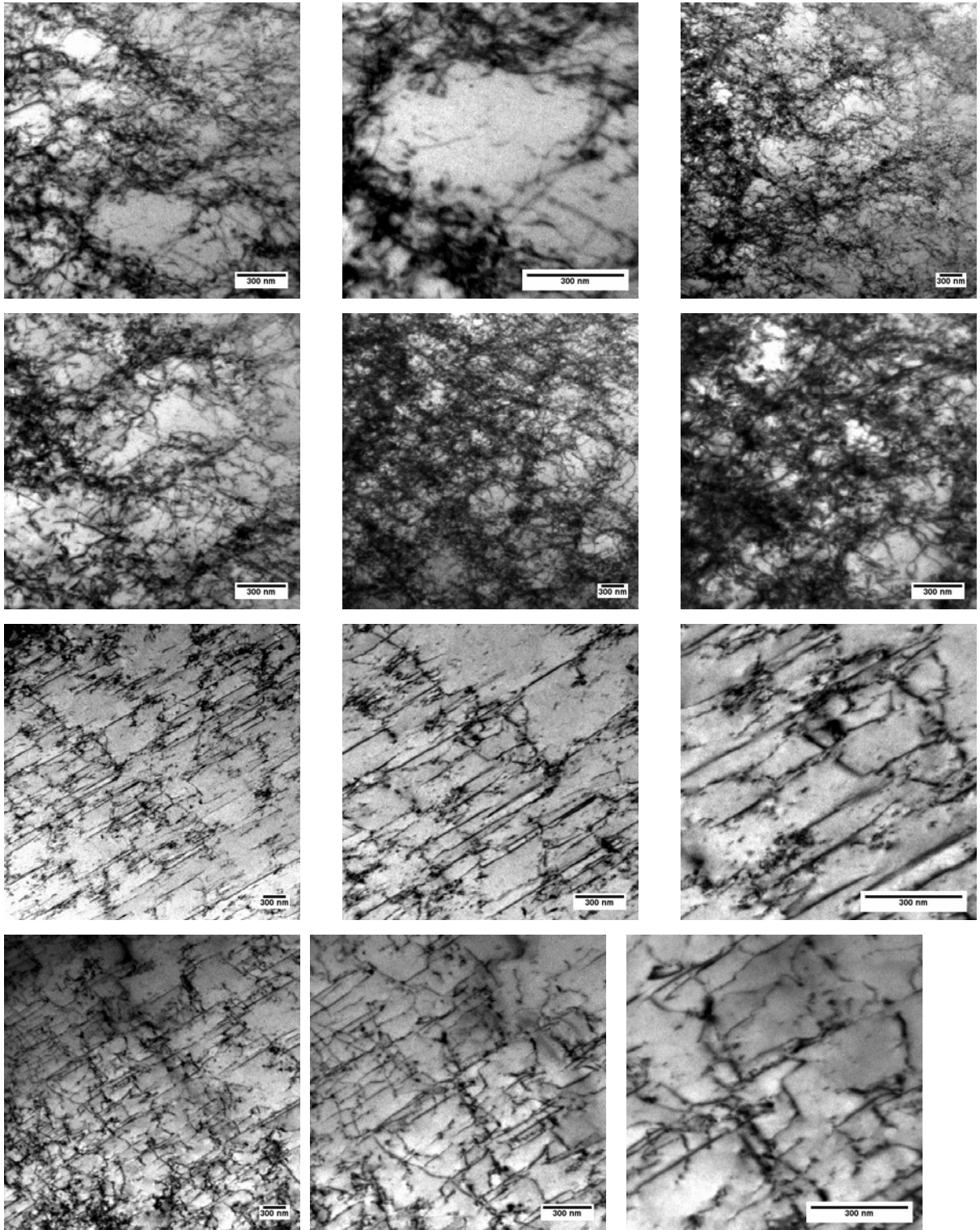


Figure A.16 (Continued)

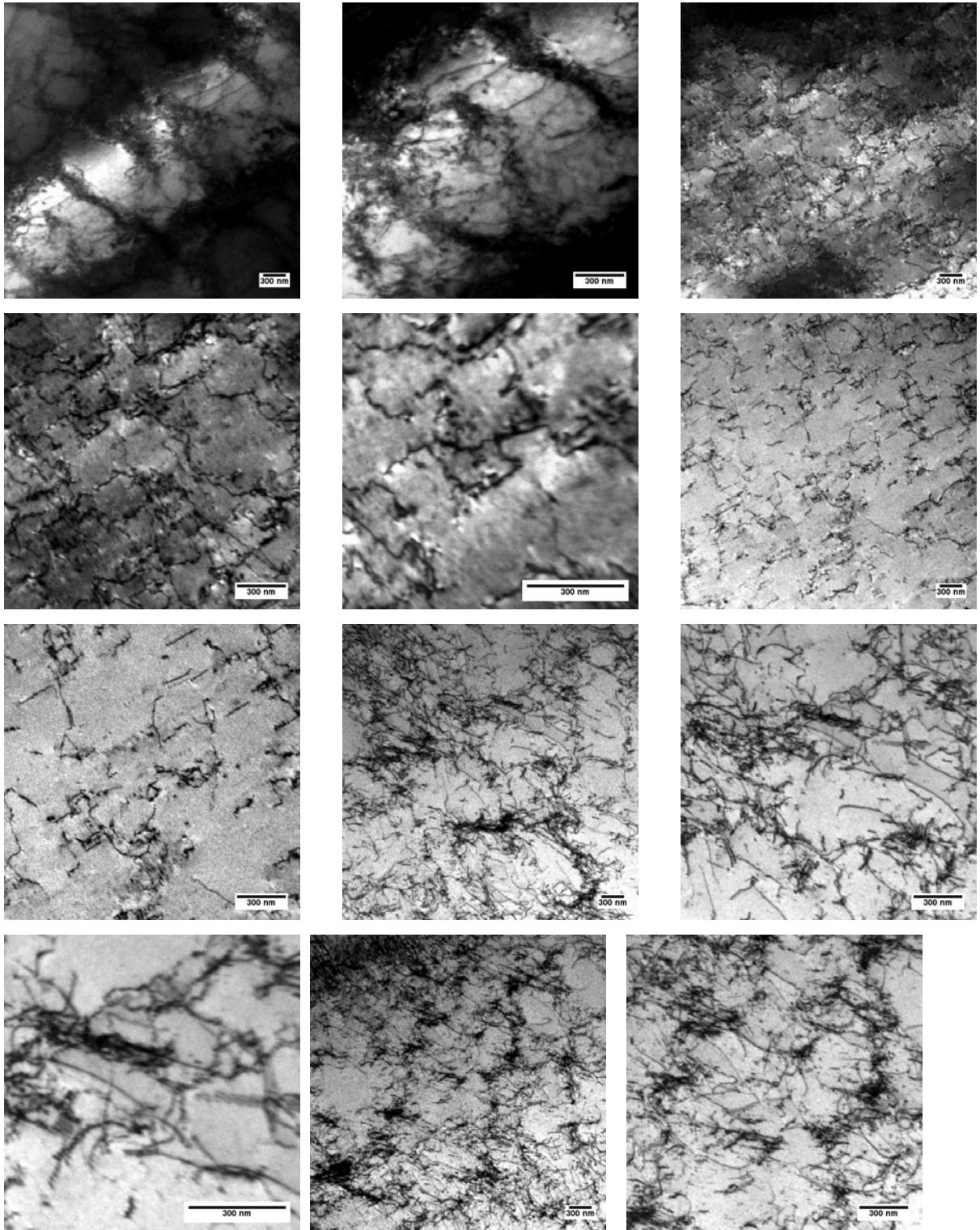


Figure A.16 (Continued)

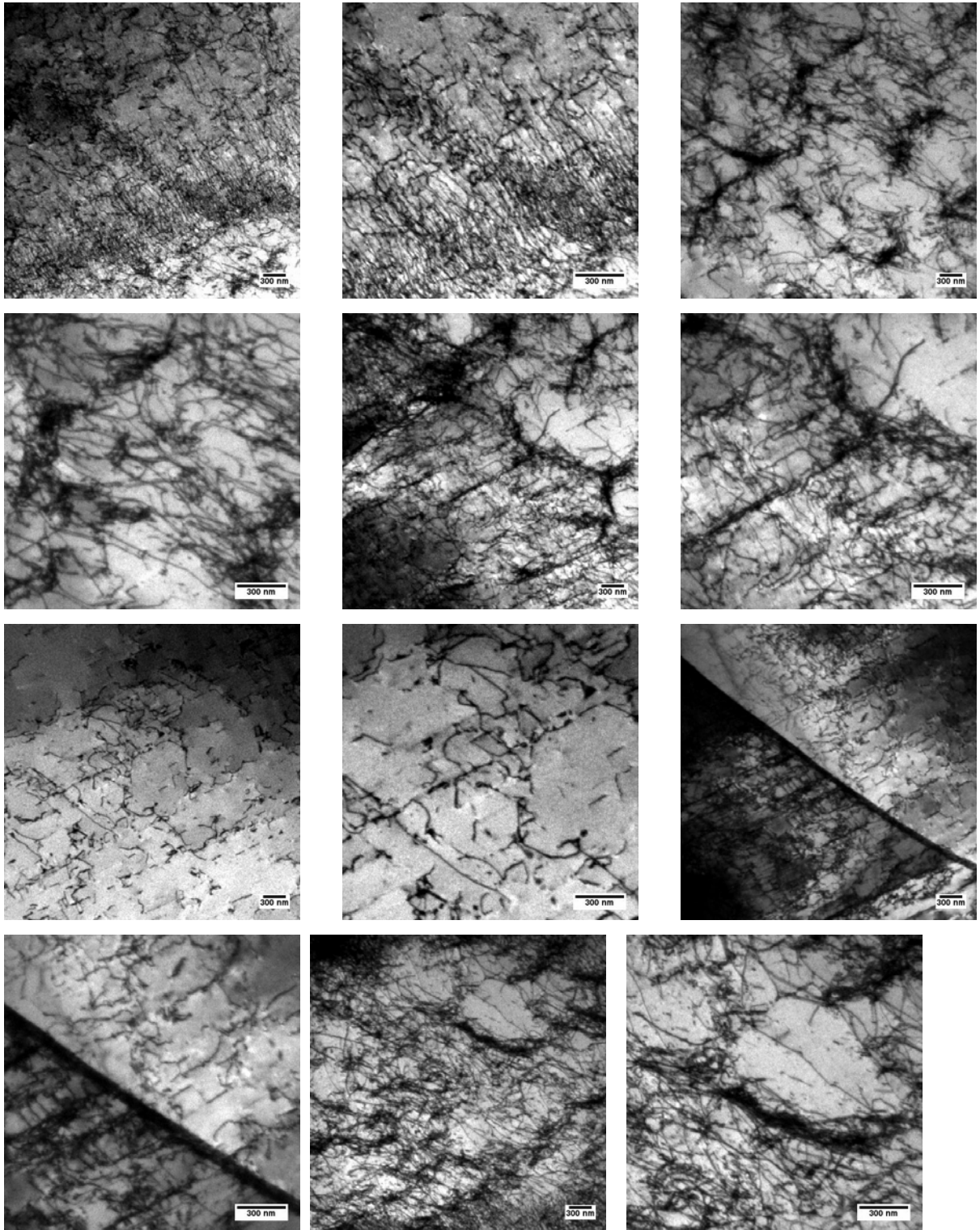


Figure A.16 (Continued)

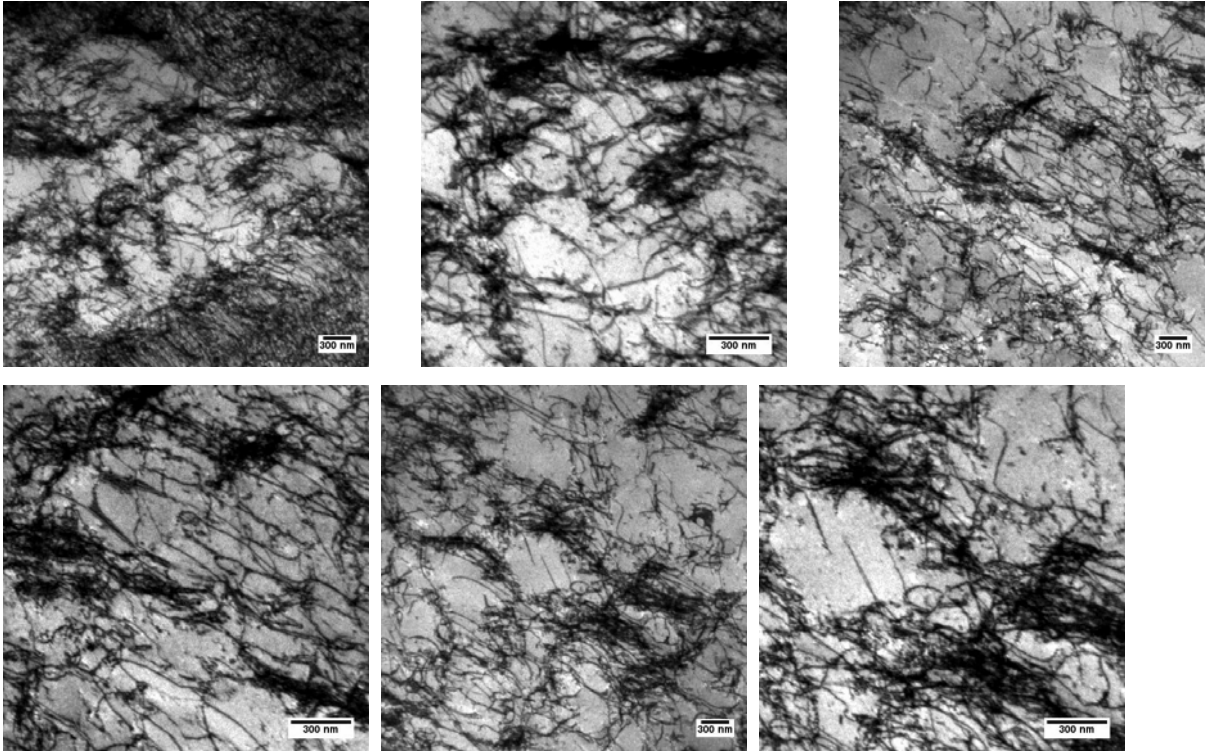


Figure A.17 TEM images of SS_uni11 coupon

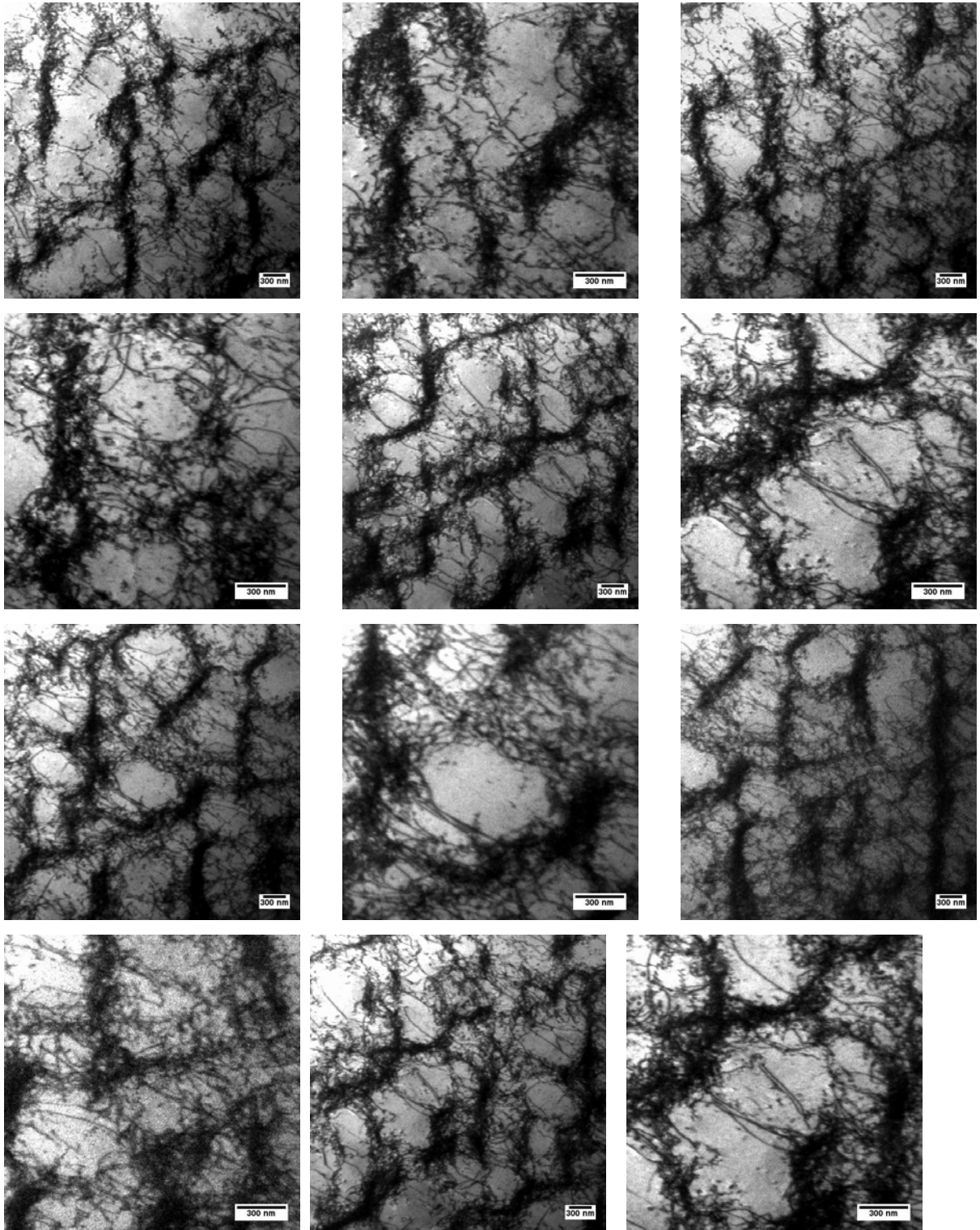


Figure A.17 (Continued)

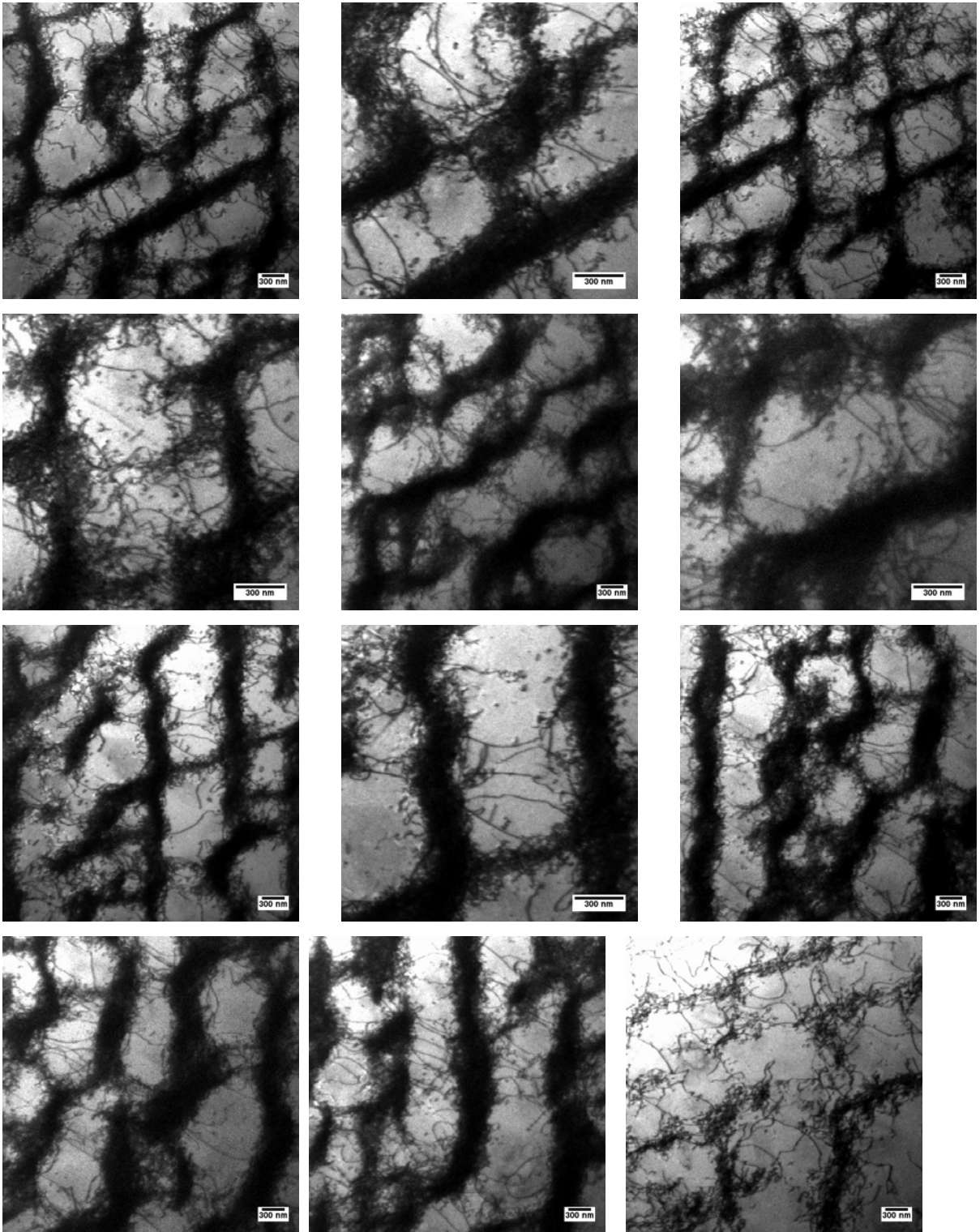


Figure A.17 (Continued)

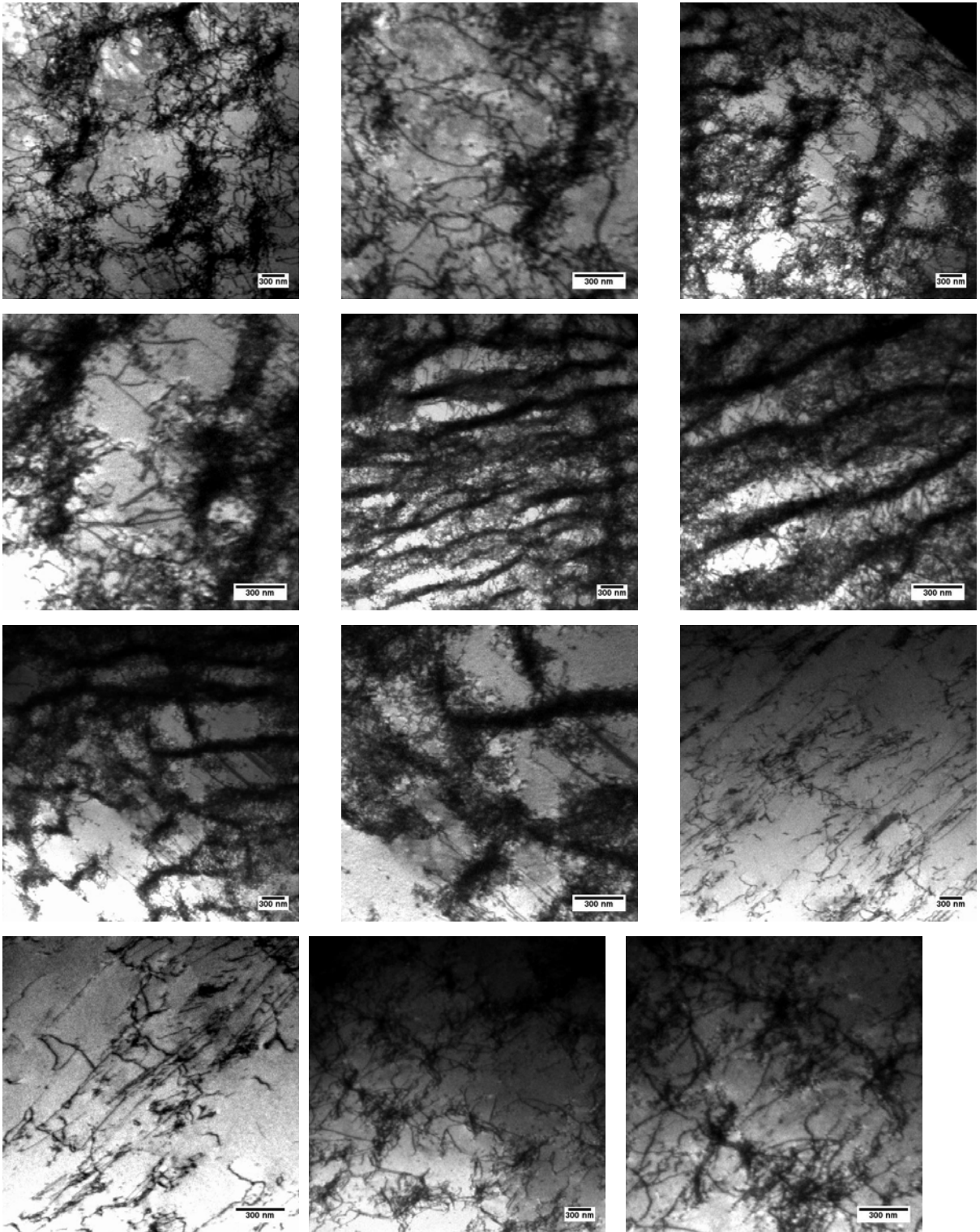


Figure A.17 (Continued)

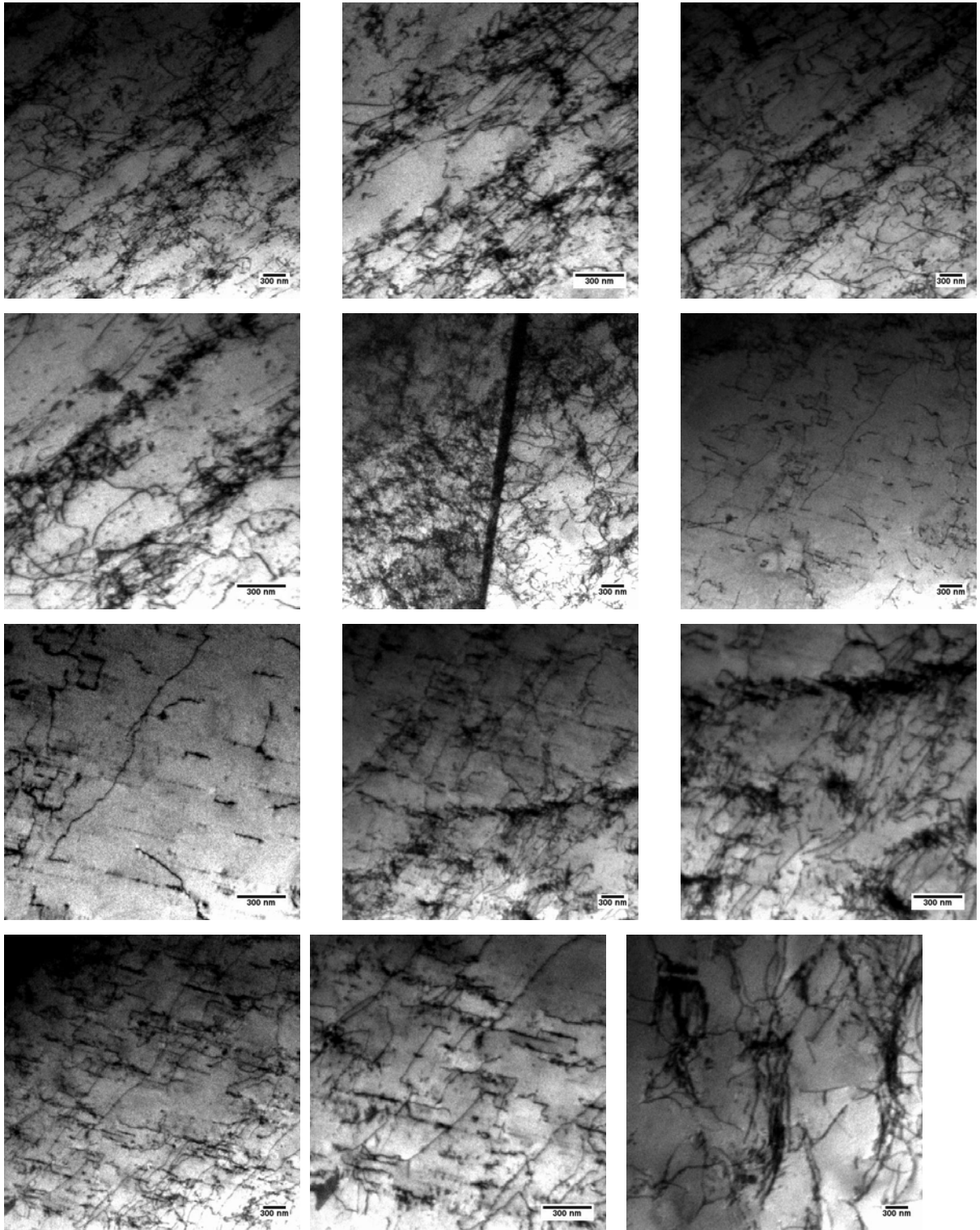


Figure A.17 (Continued)

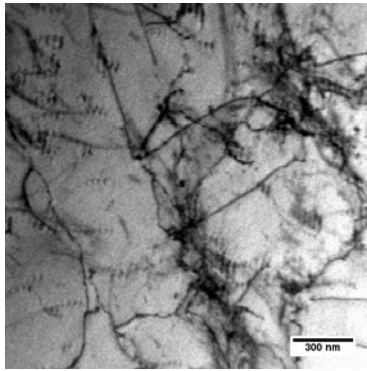
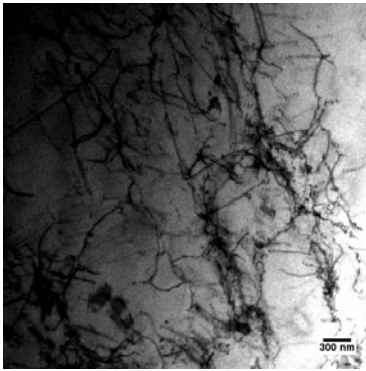
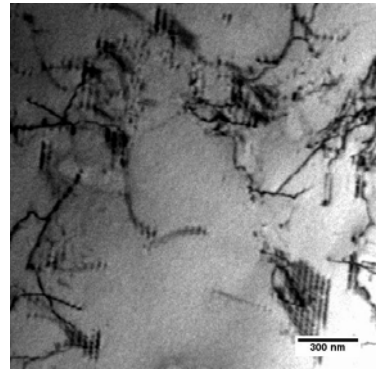
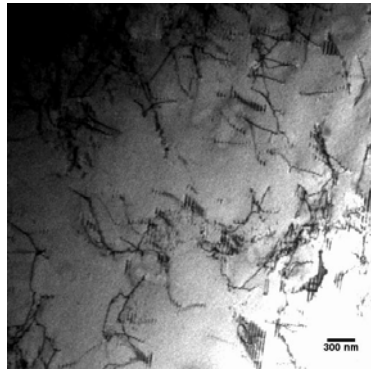
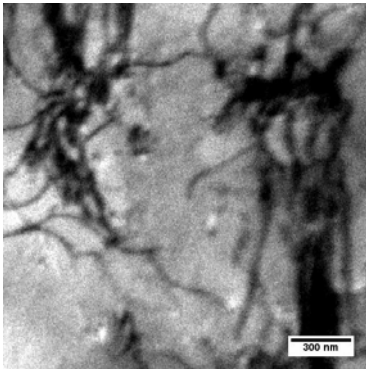


Figure A.18 TEM images of SSPC4 welded pipe (3mm)

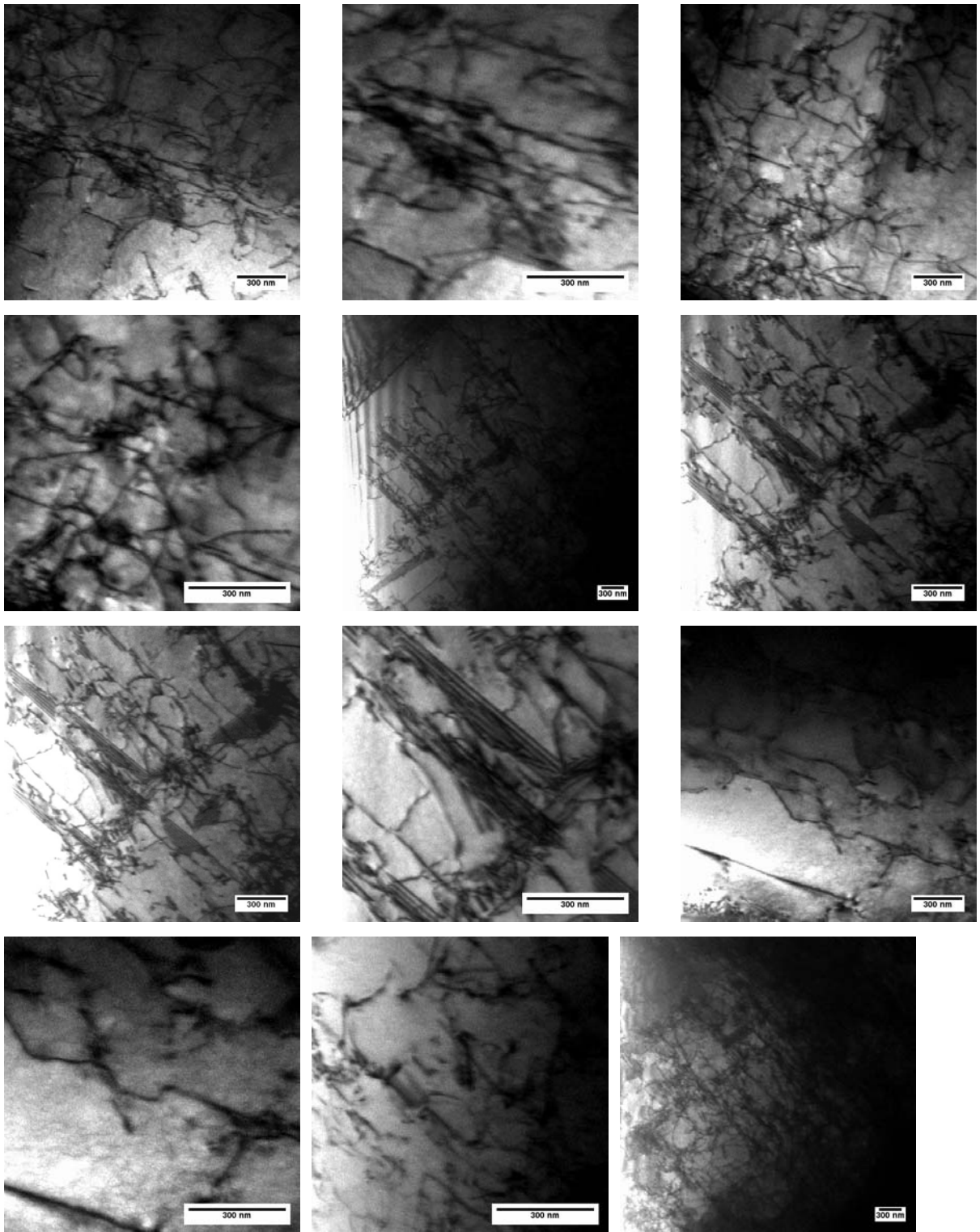


Figure A.18 (Continued)

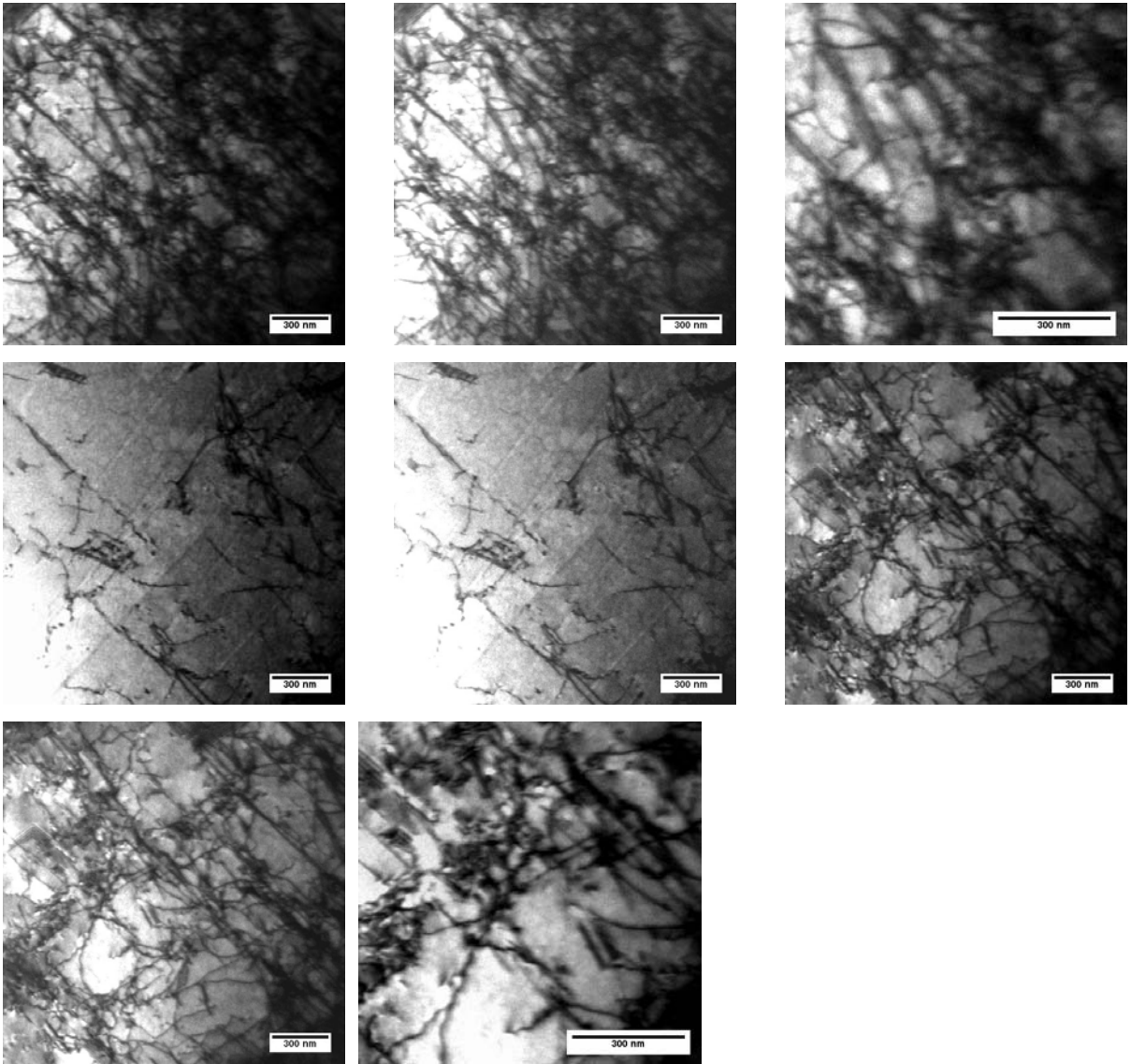


Figure A.19 TEM images of SSPC2 welded pipe (3mm)

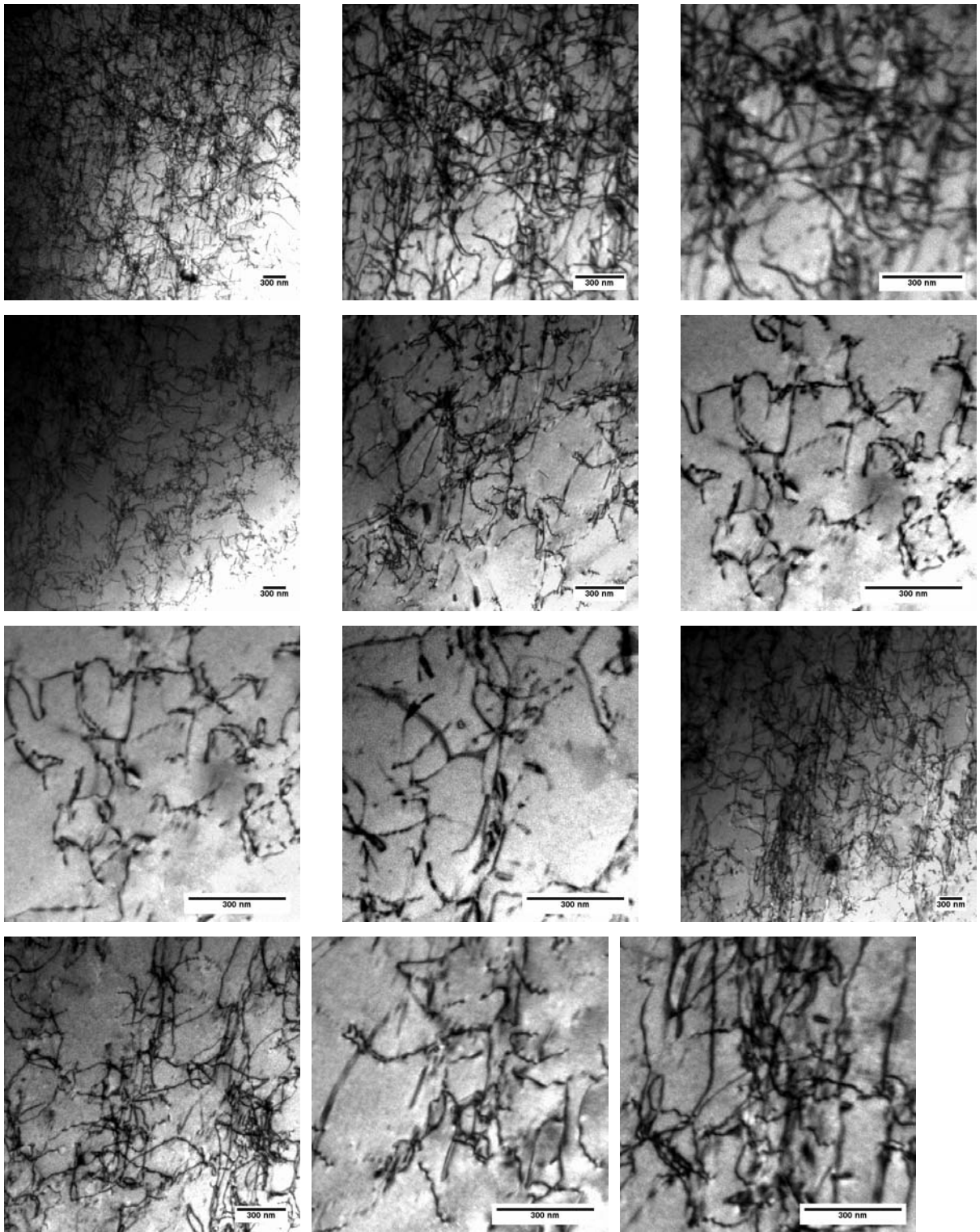


Figure A.19 (Continued)

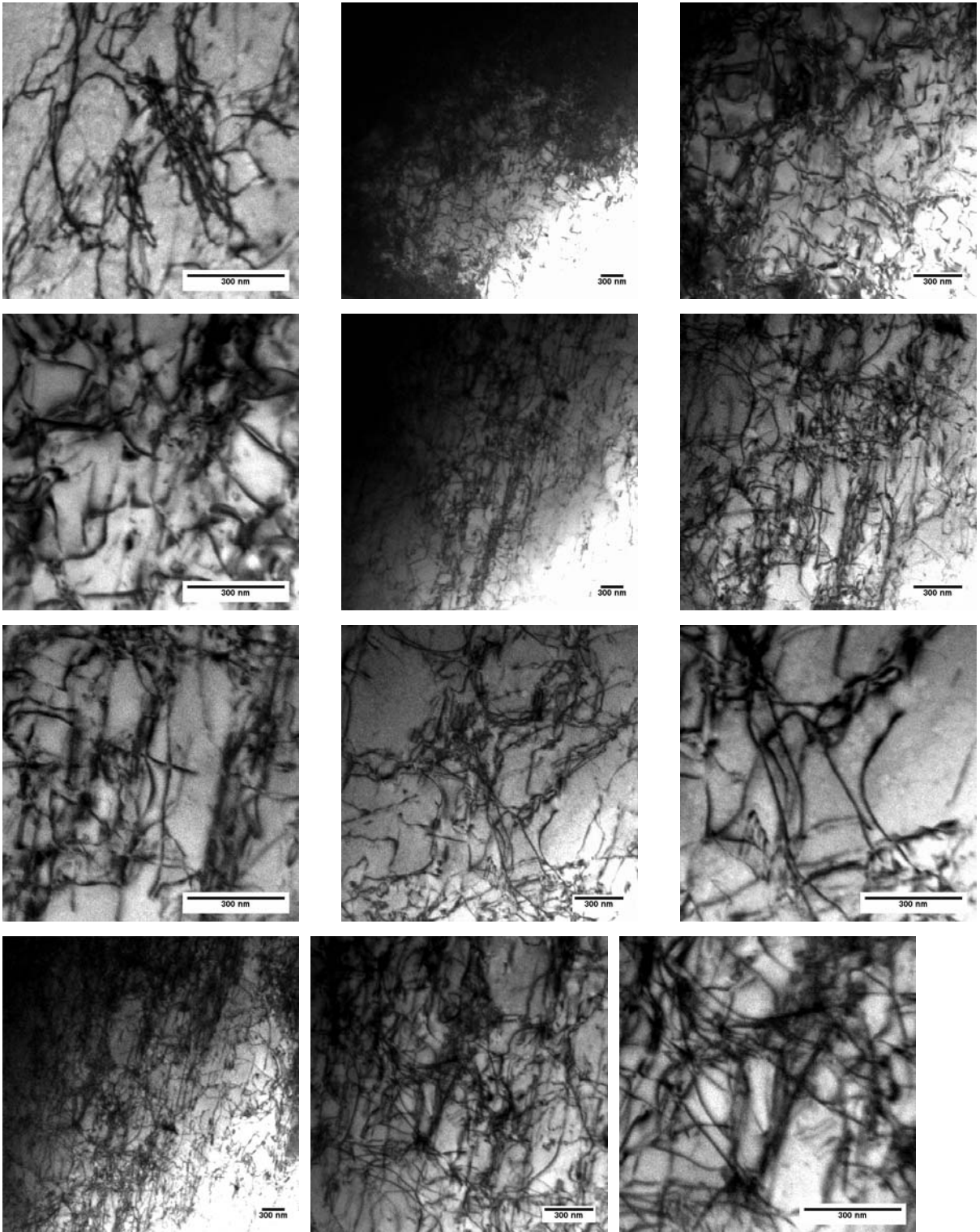


Figure A.20 TEM images of SSPC2 welded pipe (9.8mm)

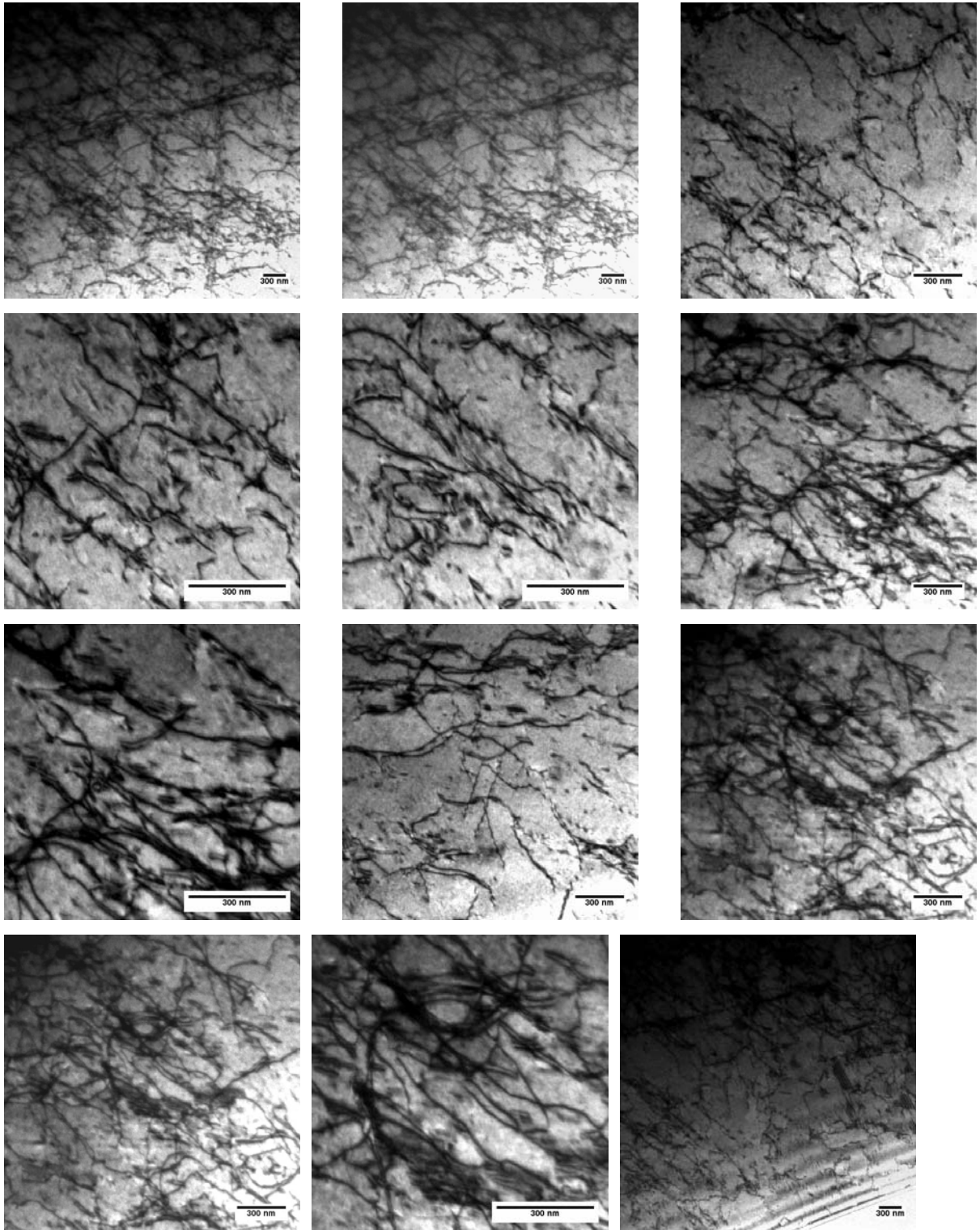


Figure A.20 (Continued)

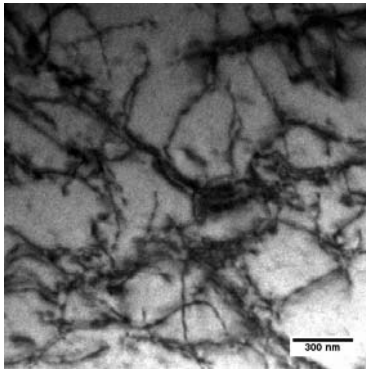
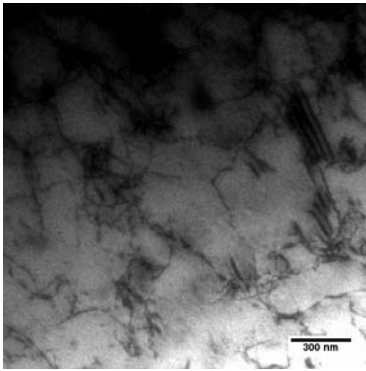
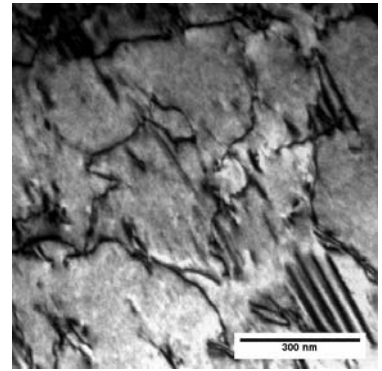
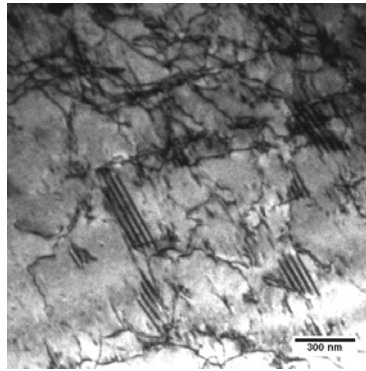
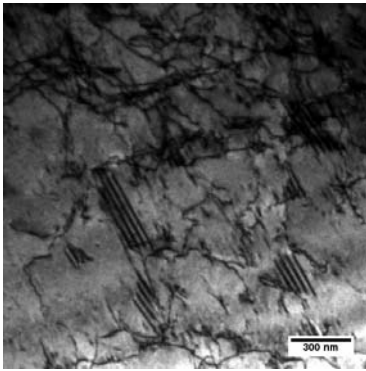


Figure A.21 TEM images of SSPC2 welded pipe (38mm)

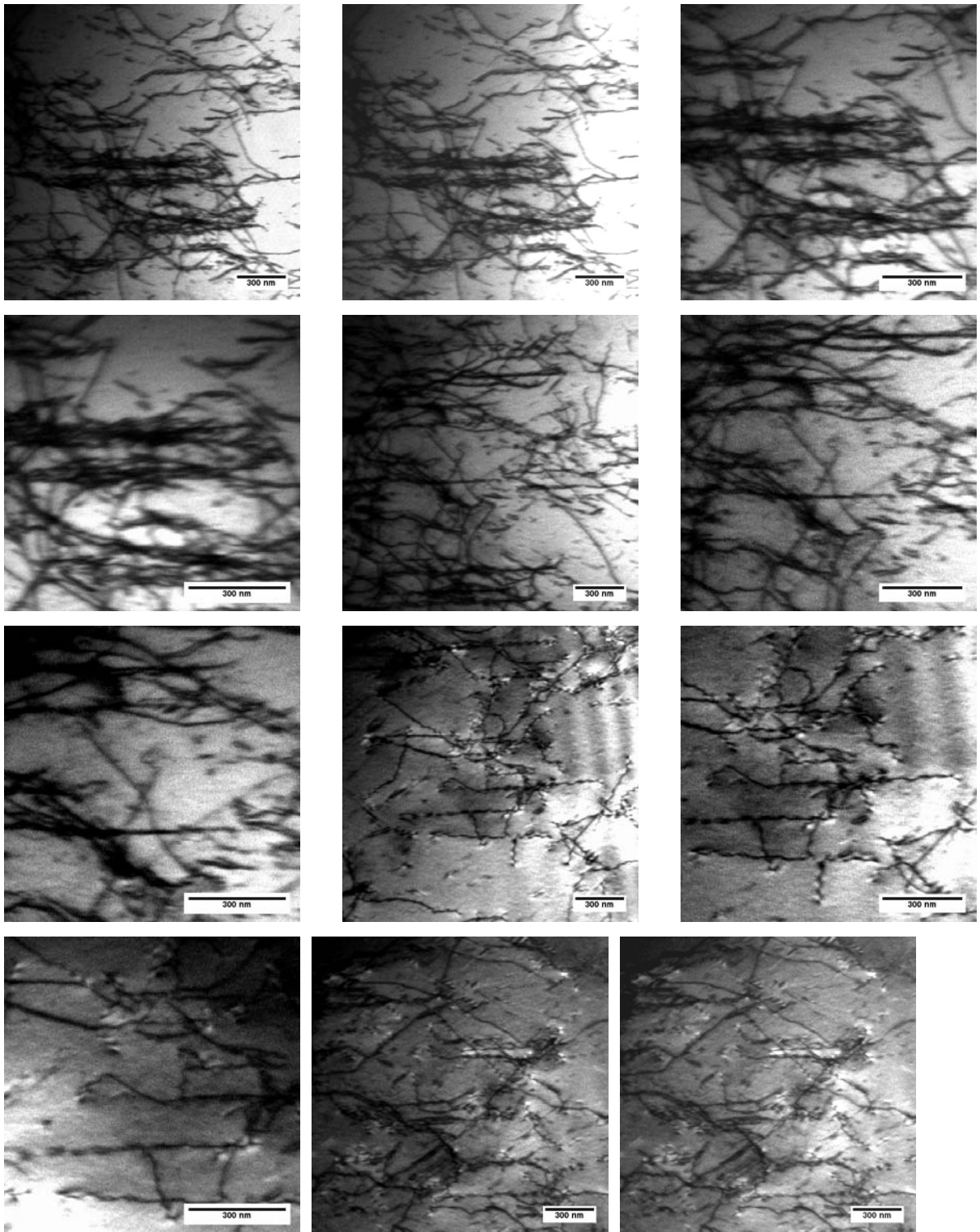


Figure A.21 (Continued)

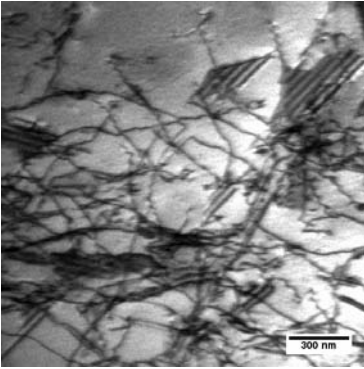


Figure A.22 TEM images of SSPC3 welded pipe (3mm)

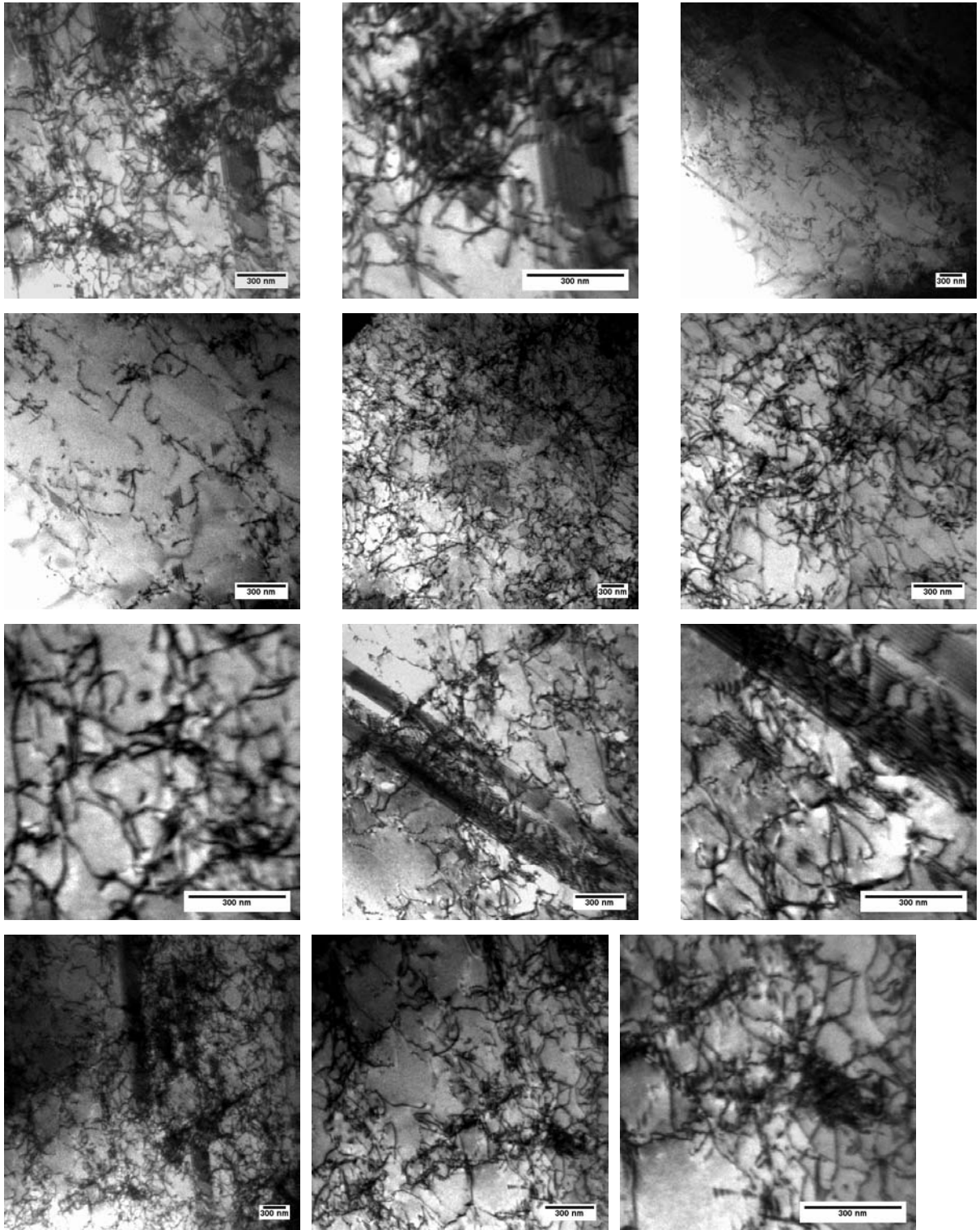


Figure A.22 (Continued)

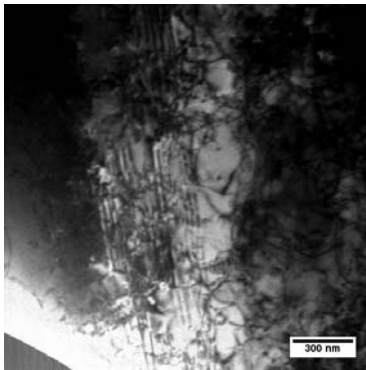
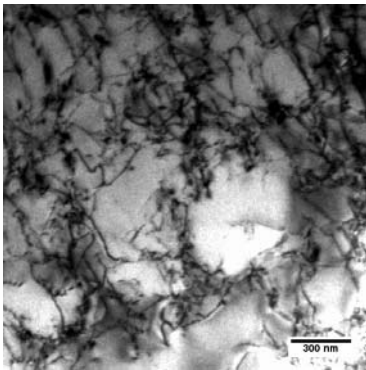
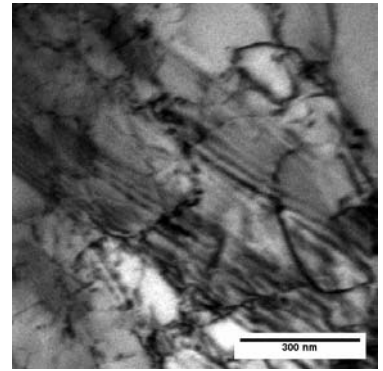
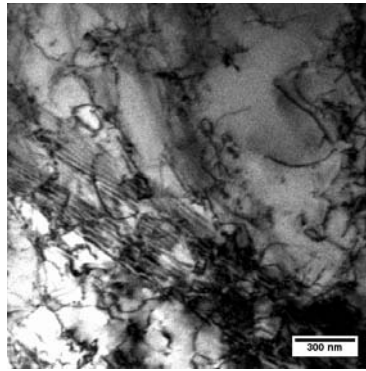
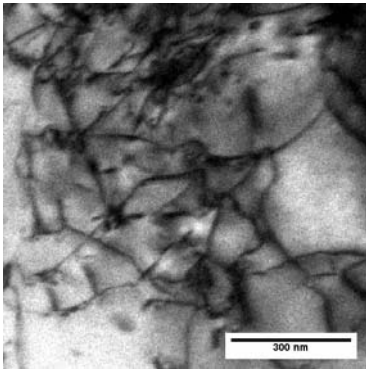
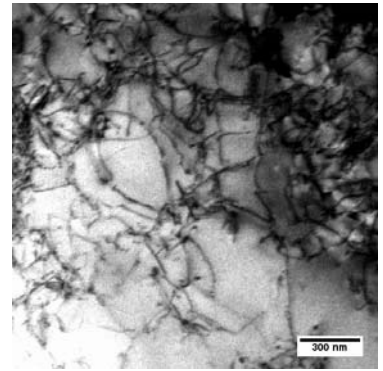
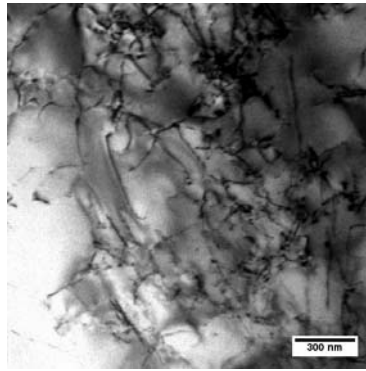
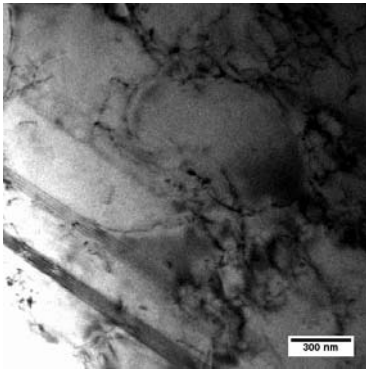


Figure A.23 TEM images of SSPC5 welded pipe (3mm)

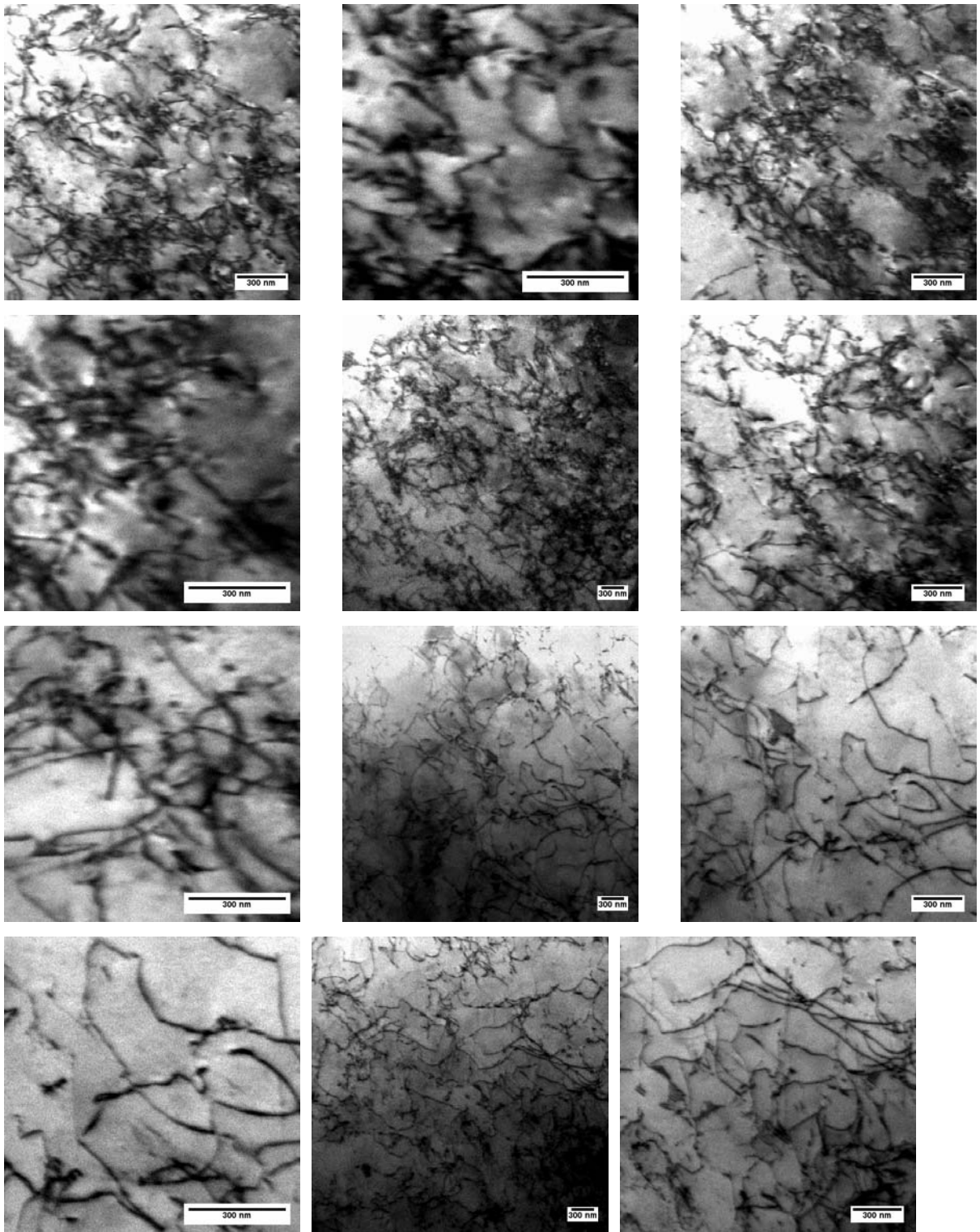


Figure A.23 (Continued)

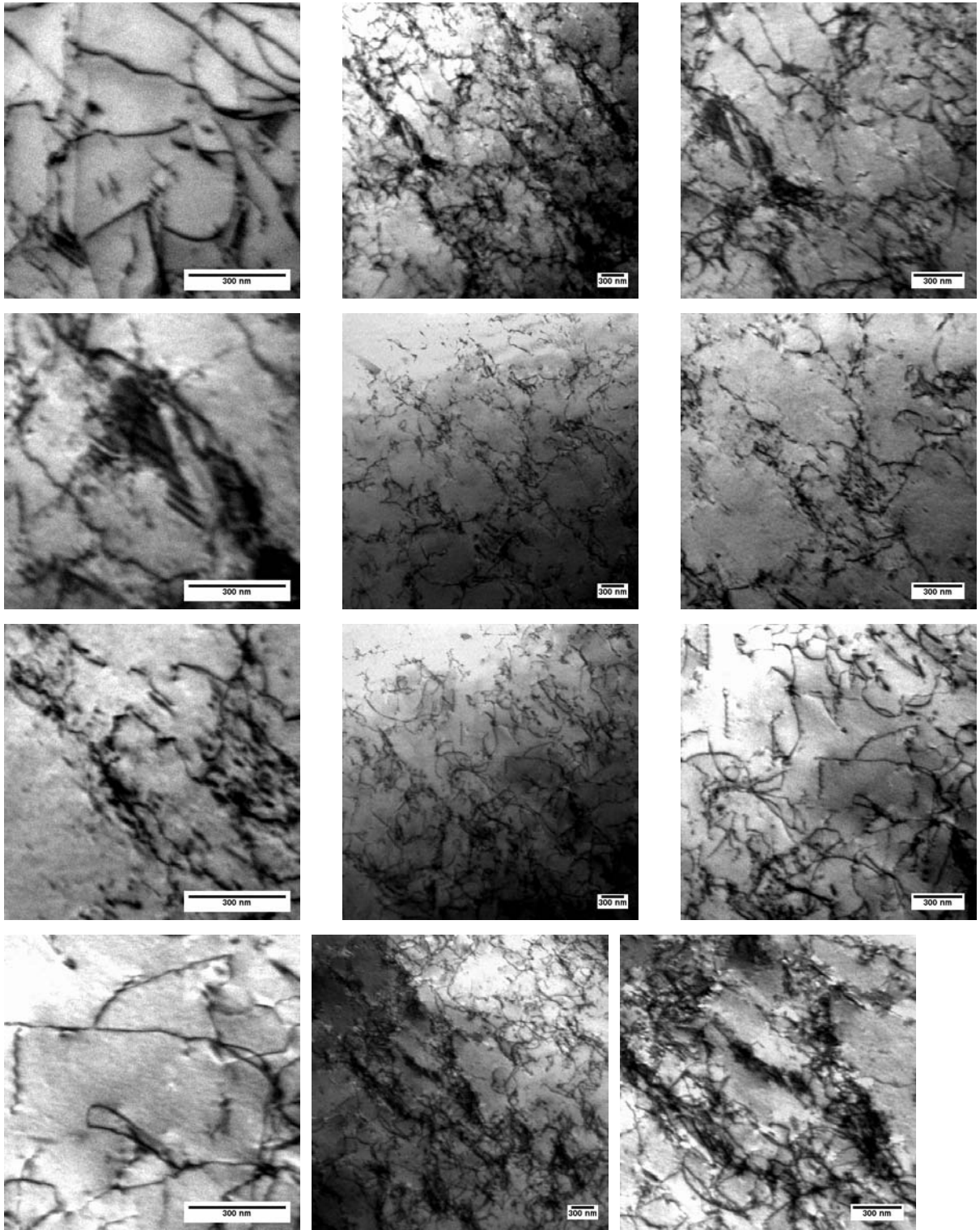


Figure A.23 (Continued)

